University of Szeged
Department of Mineralogy, Geochemistry and Petrology

Krisztián Fintor

Postmetamorphic palaeofluid evolution of the Baksa Gneiss Complex

PhD Thesis

Supervisors: Dr. Tivadar M. Tóth, Dr. Félix Schubert

Szeged

2010

Table of contents

Table of figures

Table of tables

Introduction

Palaeohydrological investigation of basement crystalline rocks, especially Variscan crystalline basement complexes, has become very important in the last decades from the perspective of both basic and applied geological research (e.g. NORTON & KNAPP 1977; RUMMEL 1978; KOZLOVSKY 1984; EDMUNDS et al. 1985; STOBER 1986, 1996; BEHR & GERLER 1987; SITTLER et al. 1995; EMMERMAN et al. 1995; BANKS et al. 1996; LODEMANN 1998; BUCHER & STOBER 2000; FRAPE et al. 2005). The hydrodynamic importance of crystalline basement rocks is inherent in the advanced state of their secondary porosity and special characteristics of their flow permeability (MAZUREK 2000). Advanced researches of the upper crust through deep boreholes (e.g. KTB, Urach-3, Soultz, and Kola Peninsula, e.g. MÖLLER et al. 1997; STOBER & BUCHER 2000) have shown that crystalline basement rocks can have significant fracture permeability down to depths of ~9 km. The significant role of the fracture porosity of crystalline rocks is obvious in the case of many applied geological problems of fluid mining, such as fractured hydrocarbon reservoirs (MUNZ et al. 1995; MUNZ et al. 1998; MUNZ 2001), exploration for geothermal energy (RUMMEL 1978; EDMUNDS et al. 1985; STOBER 1986, 1995; BEHR & GERLER 1987; BENDERITTER & ELSASS 1995; SITTLER et al. 1995; LODEMANN 1998) or in the case of deep rock burial sites as the solution to radioactive waste disposal (CHAPMAN & MCKINLEY 1987; GASCOYNE et al. 1995; WALLIN & PETERMAN, 1999; BLYTH et al. 2000; BLYTH 2001).

The area which will be investigated in this study is the Baksa Complex (BC), a fragment of the crystalline basement of the SW part of the Pannonian Basin (*Fig. 1.1*). This subsurface formation approaches the surface in a small area called Görcsöny Ridge located between the Mecsek and Villány mountains (red box in *Fig. 1.1*) and is penetrated by a deep borehole, Baksa-2, which reveals the basement of more than 1000 m thickness. The crystalline basement of the SW Pannonian Basin has few outcrops, and hence deep penetration boreholes – such as Baksa-2 – have key importance in understanding the metamorphic basement. Baksa-2 develops the rocks of the crystalline basement with almost 100% core recovery, and hence this rock section is the most detailed exploration of the crystalline basement of the SW Pannonian Basin. This exploration gives an excellent opportunity to investigate and understand the metamorphic and postmetamorphic evolution of the crystalline basement of this part of the Tisza Megaunit. Nowadays rock formations of the Mecsek-Villány area have become very important from the point of view of environmental geology because low- and medium-level (Mórágy Granite Formation) and high-level (Boda

Claystone Formation) radioactive waste depository sites are proposed in this region. During the complex research on the potential host formations of the depository sites, understanding the recent and palaeohydrological behaviour of these formations has great importance. In the case of palaeohydrological examinations, the analysis of fractured porosity not only in the host rocks but also in their neighbouring formations can be important. Hence knowledge of the postmetamorphic palaeohydrological evolution of BC – which is located in the vicinity of the abovementioned formations – can provide important information for understanding the hydrogeological evolution of the area.

In this study the complex mineralogical and palaeohydrological analysis and possible interpretation of the postmetamorphic fracture, cementation of the BC will be presented in detail. I try to distinguish the different fracture filling types occurring in the rock body and to determine a relative formation sequence of the types distinguished. By detailed petrographical investigation of fracture filling mineral phases I try to determine the exact cementation sequence of the analysed veins and to establish the paragenetic mineral succession of the different vein types. I make an attempt to determine the physicochemical conditions of cementation of veins by using detailed mineral chemical and fluid inclusion analysis of the different mineral phases of the veins. With the help of microthermometric and Raman spectroscopic investigations I try to make a model of the *P-T-X* evolution of palaeofluids which have migrated in the veins. Summarizing the results I make an attempt to sketch a detailed model of postmetamorphic palaeofluid evolution that occurred in the fracture system of the BC.

The dissertation is separated into different chapters which focus on parts of the problem to be solved. After the first chapter, which focuses on the geological background and preliminary studies of the area, the next chapters (*CHAPTERS 2*, *3*, and *4*) contain original scientific papers that have already been accepted or submitted. In *CHAPTER 5* a summary of the whole thesis will be outlined. In the following the guiding principles of the aims of the single chapters are to be summarized briefly:

CHAPTER 1: In this chapter the location, geological relationships, and structural evolution of the BC will be presented in detail. At the beginning of the chapter the tectonic evolution and structural development of the Pannonian Basin and Tisza Megaunit will be summarized. Afterwards, a description of the location, lithology, and metamorphic evolution of the BC will be sketched briefly, followed by a detailed presentation of the post-metamorphic evolution of the Complex.

CHAPTER 2: This chapter deals with the oldest vein generation of the BC. The paragenetic sequence of the vein generation will be determined by detailed petrographical analysis. Thermobarometric calculations are made using mineral chemical data and, in conjunction with the results of microthermometry, the results are used to determine the possible *P-T-X* properties of the cementation fluids.

CHAPTER 3: The metasomatic effect of the fluid migration detailed in the earlier chapter will be analysed here by detailed petrographical, whole rock chemical, and fluid inclusion investigation.

CHAPTER 4: In this chapter the youngest pervasive fracture filling generation will be studied in detail. A petrographical mineral chemical and fluid inclusion study will be carried out to fulfil this purpose. To reveal the physicochemical character of the palaeofluid which migrated in the vein, microthermometric Raman spectroscopic methods and a combination of these techniques will be used.

CHAPTER 5: A short summary of the postmetamorphic palaeohydrological evolution of the BC will be described here to reflect the findings of the previous chapters.

REFERENCES

BANKS, D., ODLING, N., E., SKARPHAGEN, H., ROHR-TROP, E. (1996): Permeability and stress in crystalline rocks. *Terra Nova*, 8, 223-235.

BEHR, H. J., & GERLER, J. (1987): Inclusions of Sedimentary Brines in Post-Variscan Mineralizations in the Federal republic of Germany - A Study by Neutron Activation Analysis. *Chemical Geology*, 61, 65-77.

BENDERITTER, Y., & ELSASS, P. (1995): Structural control of deep fluid circulation at the Soultz HDR site. France: a review. *Geoterm. Sci. Tech.*, 4, 227-237.

BLYTH, A., FRAPE, S., BLOMQVIST, R., NISSINEN, P. (2000): Assessing the past thermal and chemical history of fluids in crystalline rock by combining fluid inclusion and isotopic investigations of fracture calcite. *Applied Geochemistry*, 15, 1417-1437.

BUCHER, K., & STOBER, I. (2000): The composition of groundwater in the continental crystalline crust. *Hydrogeology of Crystalline Rocks*, BUCHER, K., & STOBER, I., Dordrecht, Kluwer Academic Publishers, 34, 141-176.

CHAPMAN, N., A., & MCKINLEY, I., G. (1987): The Geological Disposal of Nuclear Waste., New York, Wiley, 280.

EDMUNDS, W., M., KAY, R., L., & MCCARTNEY, R., A. (1985): Origin of saline groundwaters in the Carnmenellis granite (Cornwall, England): natural processes and reaction during hot dry rock reservoir circulation. *Chemical Geology*, 49, 287-301.

FRAPE, S. K., & BLYTH, A. (2005): Deep Fluids in the Continents: II. Crystalline Rocks. *Treatise on Geochemistry*, HOLLAND, H., D., & TUREKIAN, K., K., Oxford, Elsevier Science, 5, 541-580.

GASCOYNE, M., STROES-GASCOYNE, S., & SARGENT, F., P. (1995): Geochemical influences on the design, construction and operation of a nuclear water vault. *Applied Geochemistry*, 10, 657-671.

KOZLOWSKY, Y., A. (1984): The worlds deepest well. *Scientific Am.*, 251, 106-112.

LODEMANN, L., FRITZ, P., WOLF, M., IVANOVICH, M., HANSEN, B. T., & NOLTE, E. (1998): On the origin of saline fluids in the KTB (continental deep drilling project of Germany. *Applied Geochemistry*, 12, 831-849.

MAZUREK, M. (2000): Geological and hydraulic properties of water-conducting features in crystalline rock. *Hydrogeology of Crystalline Rocks*, STOBER, I. B., K., Dordrecht, Kluwer Academic Publishers, The Netherlands, 3-26.

MÖLLER, P., WEISE, S., M., ALTHAUS, E., BACK, W., BEHR, H., J., BORCHARDT, R., BRÄUER, K., DRESCHER, J., ERZINGER, J., FABER, E., HANSEN, B., T., HORN, E., E., HUENGES, E., KÄMPF, H., KESSELS, W., KIRSTEN, D., LANDWEHR, D., LODEMANN, M., MACHON, L., PEKDEGER, A., PIELOW, H., U., REUTEL, C., SIMON, K., WALTHER, J., WEINLICH, F., H., & ZIMMER, M. (1997): Paleofluids and recent fluids in the upper continental crust: results from the German continental deep drilling program (KTB). *Journal of Geophysical Research*, 102, 18233-18254.

MUNZ, I. A., YARDLEY, B. W. D., BANKS, D. A., & WAYNE, D. (1995): Deep penetration of sedimentary fluids in basement rocks from southern Norway: Evidence from hydrocarbon and brine inclusion in quartz veins. *Geochimica et Cosmochimica Acta*, 59, 2, 239-254.

MUNZ, I. A. (2001): Petroleum inclusions in sedimentary basins: systematics analytical methods and application. *Lithos*, 55, 195-212.

NORTON, D., & KNAPP, R. (1977): Transport phenomena, in hydrothermal systems: the nature of porosity. *American Journal of Science*, 277, 913-936.

SITTLER, C., BAUMGÄRTNER, J., GÉRARD, A., & BARIA, R. (1995): Natürliche Energiegewinnung in Unter-Elsass (Frankreich): Erdöl, Erdwärme, und Wasserkraftwerke am Rhein (Exkursion A). *Jahresbericht Mittellungen, oberrheinischen geologischen Vereinigung*, 47-102.

STOBER, I. (1986): Strömungsverhalten in Festgesteinsaquiferen mit Hilfe von Pump- und Injektionversuchen. *Geol. Jahrbuch.*, REIHE, C., 204.

STOBER, I. (1995): Die Wasserführung des kristallinen Grundgebirges., Stuttgart, Enke-Verlag, 191.

STOBER, I. (1996): Hydrogeological investigations in crystalline rocks of the Black Forest, Germany. *Terra Nova*, 8, 255-258.

WALLIN, B., PETERMAN, Z. (1999): Calcite fracture fillings as indicators of paleohydrology at Laxemar at the Aspö Hard Rock Laboratory, southern Sweden. *Applied Geochemistry*, 14, 953-962.

CHAPTER 1

Localisation, geological relationships, and structural evolution of the Baksa Complex in the Pannonian Basin

An Overview

1. Localisation, geological relationships, and structural evolution of the Baksa Complex in the Pannonian Basin

An Overview

1.1. Geological setting and structural evolution of the Pannonian Basin

The Pannonian Basin is located in Central Europe and is surrounded by the Eastern and Southern Alps, the Carpathians, and the Dinarides (*Fig. 1.1*). The central part of the Pannonian Basin is situated in Hungary, but the marginal areas stretch to Slovakia, Ukraine, Romania, Serbia, Croatia, Slovenia, and Austria (*Fig. 1.1*). The Pannonian Basin is located on the area of two microplates that are adjoined along the Middle Hungarian Lineament (M. H. L. on *Fig. 1.1*) (WEIN 1969, 1978; GÉCZY 1973, 1984; KÁZMÉR & KOVÁCS 1985; CSONTOS et al., 1992). North of this line is the so-called ALCAPA (Alpine-Carpathian-Pannonian system) unit, which has an African (southern Tethys) origin and is correlated with the Southern Alps, the inner Eastern Alps, the inner Western Carpathians, and the Dinarides. On the southern part of the Middle-Hungarian Lineament lies the Tisza-Dacia microplate, which has a European affinity (northern Tethys) and is correlated with the outer Eastern Alps as well as the outer Western- Eastern- and Southern Carpathians (*Fig. 1.2/a*) (GÉCZY 1972, 1973a, 1973b). The Tisza-Dacia microplate can be subdivided into a western part, called Tisza Megaunit, and an eastern block, called the Dacia unit (*Fig. 1.2/a*). The two microplates were adjoined as a consequence of the closure of the East Vardar Ocean during the Cretaceous-Early Paleogene, which led to the formation of the internal Tisza-Dacia block (SCHMID et al. 2008). The present-day geological setting of the Pannonian Basin is the result of a multi-stage, complex evolution that has been occurring since the early Miocene. Most studies agree on this evolution's subdivision into three major phases (CSONTOS et al. 1992; HORVÁTH 1988; TARI et al. 1992).

1.1.1. Early Miocene continental escape (pre-rift phase)

The distribution of the mentioned tectonostratigraphic units is best explained by a north-eastward movement of the ALCAPA unit along the Middle Hungarian Lineament (GÉCZY 1973b, 1984). This event is termed the early Miocene continental escape event. Based on the continental sedimentation in late Eggenburgian-Ottnangian time, TARI (1994) and VAKARCS (1997) determined this age as the time of the escape event, with an offset of about 200 km (TARI 1994).

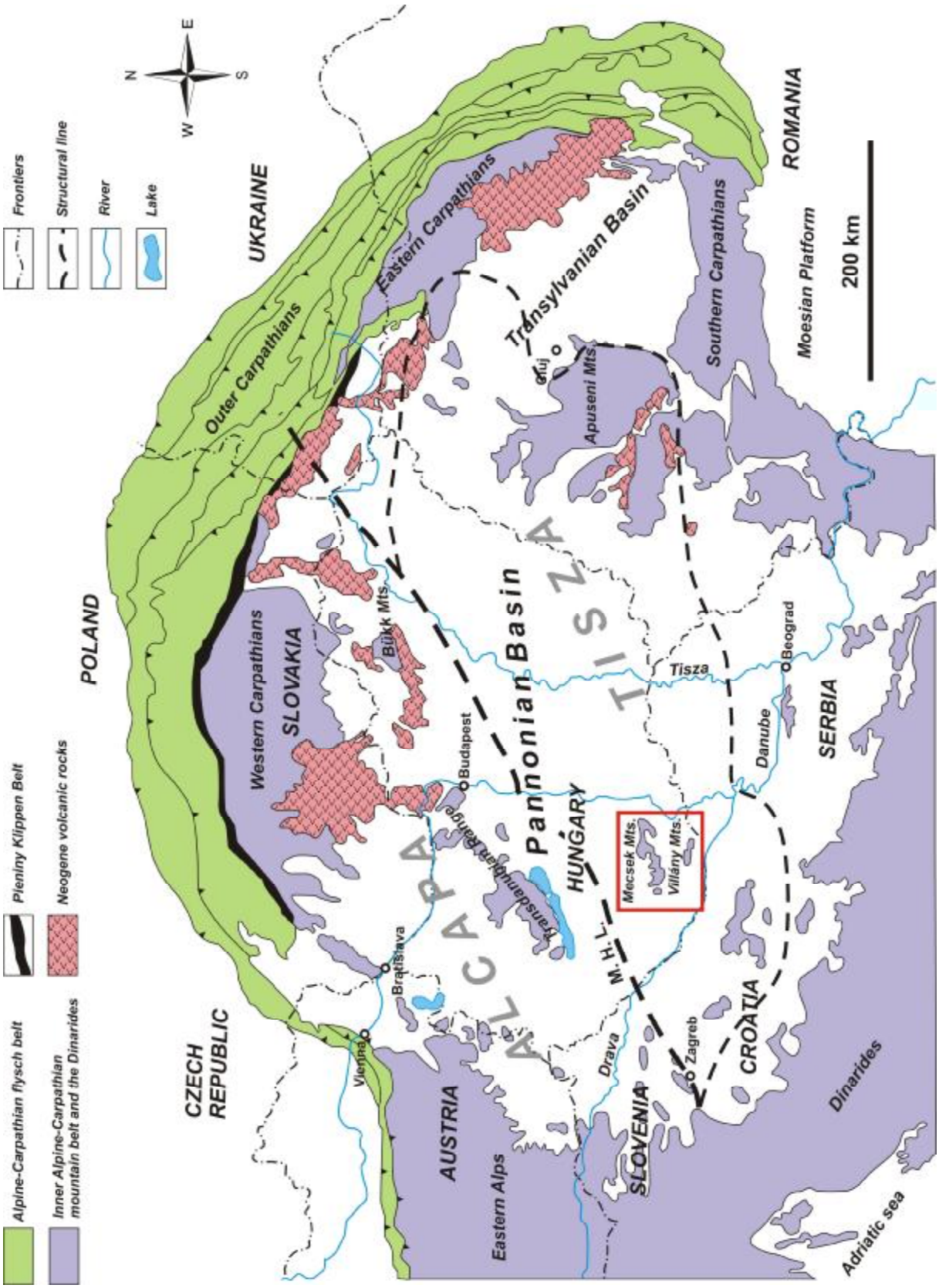

Figure 1.1. *Geological framework of the Pannonian Basin and its immediate environment (modified after CSONTOS et al. 2002). The red box indicates the approximate position of the study area.*

1.1.2. Middle Miocene subsidence (syn-rift phase)

To describe the syn-rift tectonics of the Pannonian Basin, TARI (1994) applied the model of DEWEY (1988), in which the initial extension of the intra-Carpathian area is the consequence of an extensional collapse of the over-thickened, and therefore unstable, lithosphere (DEWEY 1988; HORVÁTH & BERCKHEMMER 1982). The syn-rift phase is characterised by a rapid tectonic subsidence, and it commenced at around 18-20 Ma BP (before present) within the entire Pannonian Basin region (ROYDEN et al. 1983; TARI et al. 1999). During the syn-rift phase, compressional structural evolution was dominant in the central part of the Eastern Alps by a progressive movement of the Adria microplate. The expression of the ALCAPA microplate was driven by a sinistral movement along the Salzach-Ennstal-Mariazell-Puchberg (SEMP) and Mura-Mürz-Zsolna (MMZ) lineaments (LINZER et al. 2002; DECKER 2007) as well as a dextral lateral movement along Middle-Hungarian lineament. Transpression associated with the dextral lateral movement along Periadriatic-Lineament (PAL) occurred at the Dinarides (ILIĆ & NEUBAUER 2005). Meanwhile, the ALCAPA unit moved anticlockwise while the Tisza-Dacia unit had a clockwise rotation (MÁRTON 1981; BALLA 1984; CSONTOS & NAGYMAROSI 1998). The total amount of syn-rift extension across the Pannonian Basin was estimated by TARI (1994) to be 200-250 km.

1.1.3. Late Miocene – Pliocene subsidence (post-rift phase)

The gradually diminishing rate of extension during the late Miocene/Pliocene could not focus the extension into a narrow rift zone in the Pannonian basin. However, in some deep subbasins, the extension continued with a decreasing rate. In contrast to the syn-rift subsidence, the late subsidence has affected the entire basin, but different rates of subsidence occurred in different basins. During the post-rift phase, a general down-wrapping of the lithosphere manifested itself in a phase of thermal subsidence (e.g., SCLATER et al. 1980; ROYDEN & DÖVÉNYI 1988).

1.1.4. Pliocene/Quaternary uplift

High-resolution seismic data (HORVÁTH 1993; VAKARCS 1997), kinematic and paleostress data (BECKER 1993; GERNER et al. 1995; PERESSON & DECKER 1996; HORVÁTH et al. 2006; BADA et al. 2007) indicate a late Miocene transient, E-W compressive event in the Pannonian Basin. There is a considerable debate about the onset of this late compressional phase. This compressional cycle of basin evolution was characterised by the gradual structural inversion

of the Pannonian Basin system during Late Pliocene-Quaternary times (HORVÁTH & CLOETINGH 1996). This feature is commonly termed "Pliocene/Quaternary uplift" (HORVÁTH et al. 1996) in the literature because it was the most widespread during this time.

1.2. Geological framework of the metamorphic basement of Tisza Megaunit

The Tisza Megaunit/Tisia Composite Terrane is a large lithosphere block of complex internal structure that is bounded by the Mid-Hungarian Lineament to the northwest, the Száva, Zombor-Óbecse and Maros lineaments to the south and the Szamos Lineament to the northeast (*Fig. 1.2/a, b*). It is made up of Variscan crystalline complexes in the basement and post-Variscan–Alpine overstep sequences. The correlation of the crystalline complexes and Variscan granitoid occurrences of the Tisza Megaunit with the European Variscan orogenic belt (NEUBAUER & RAUMER 1993; BUDA 1996; KOVÁCS et al. 2000) indicates that during the Variscan Orogeny (Carboniferous), the Tisza Megaunit was an integral part of the Variscan Mountain Range. GÉCZY (1972) established by paleontological evidence that the Tisza Megaunit was originally part of European margin of Neo-Tethys. In the Middle Jurassic (Bathonian), the Tisza Microplate broke off from the European plate due to the opening of the Penninic Ocean (KÁZMÉR & KOVÁCS 1985; HAAS & PÉRÓ 2004). The significant Early Cretaceous rotation of the Tisza Microplate (MÁRTON 2000) can be explained by the asymmetric opening of Vahic oceanic basin, while its movement away from European plate led to a gradual closure of the westernmost segment of Neo-Tethys (TARI & PAMIC 1998). The Tisza Megaunit gradually welded onto the ALCAPA unit along the Mid-Hungarian Lineament during the Early Burdigalian (TISCHLER et al. 2007).

Beneath the molasse-type post-Variscan formations of the Megaunit, crystalline complexes with variable characteristics and evolutionary history occur. These are the Slavonia-Dravia, Kunságia, and Békésia Units/Terranes (*Fig. 1.2/b*) (SZEDERKÉNYI 1996; KOVÁCS et al. 1997, 2000). By definition, a "Terrane" is a crust fragment (block) bordered by considerable fractures, lineaments or accretional complexes or (crypto) sutures. A Terrane is characterised by a diverse evolution from the adjacent block(s) and is based upon non-horizontal lithofacial changes and stratigraphic-, paleontological-, structural-, deformational-inner continuities, among others (after KEPPIE & DALLMEYER 1990). Although the main description of the "Terrane concept" is known, the independence of individual terranes and subterranes of the Tisza Megaunit is rather problematic. In spite of the uncertainties, we have used the terminology and description of KOVÁCS et al. (2000) in this study.

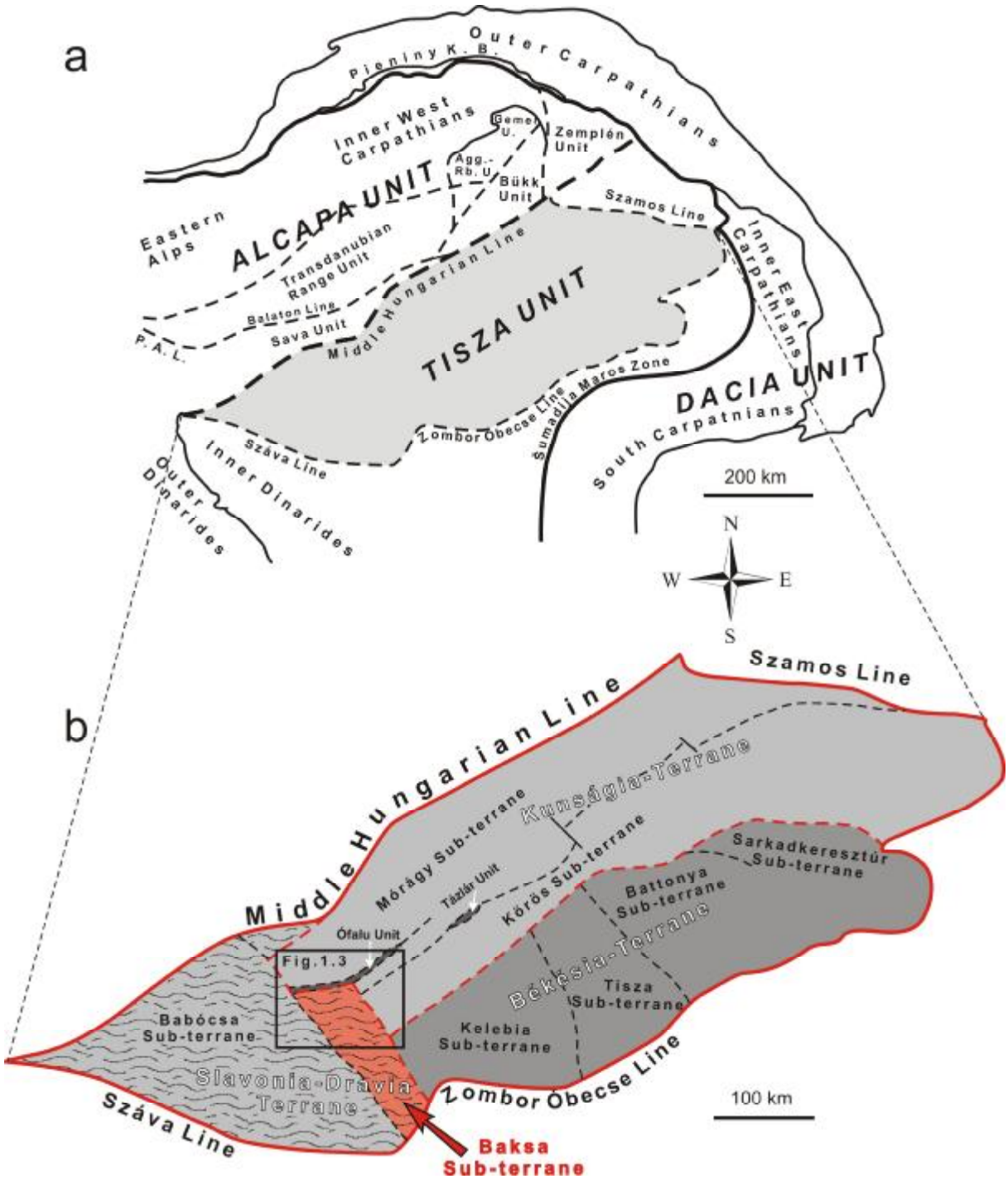

Figure 1.2. *Structural sketch of the Carpathian Pannonian region with special regard to the Tisza Megaunit*
a) Structural units of the Pannonian Basin (grey-shaded area refers to Tisia Composite Terrane, (modified after SZEDERKÉNYI, 1996 and HAAS & PÉRÓ, 2001)); b) Detailed structural map of Tisza Megaunit (box refers to area of Fig. 1.3)

The three terranes (Slavonia-Dravia, Kunságia, Békésia) can be divided into sub-terranes (*Fig. 1.2/b*) based on tectonically determined boundaries and extensions with their characteristic lithostratigraphic columns (LELKES-FELVÁRI in: CSÁSZÁR (ed.), 1997) and evolution. The Kunságia terrane is located between the Middle Hungarian Lineament and the

northern border of the Békésia terrane, and it can be divided to the Mórágy and Körös subterranes (*Fig. 1.2/b*). To its south is the Békésia Terrane, which can be subdivided into the Kelebia, Tisza, Battonya, and Sarkadkeresztúr subterranes (*Fig. 1.2/b*).

At the south-western corner of the pre-Alpian part of the Megaunit is the Slavonia-Dravia Terrane. This terrane can be subdivided into two subunits, namely, the Babócsa and Baksa subterranes (*Fig. 1.2/b*). The Slavonian Mountains and their immediate environments show petrographical characteristics that differ from the Babócsa and Baksa subterranes. This area can therefore be designated the "Slavonian Subterrane". The borders of this area are not yet determined, so it is not designated on the map shown in *Fig. 1.2/b*.

1.3. Geological framework and evolution of the Baksa Complex

1.3.1. Location and lithology

The investigated study area, the Baksa Complex/Baksa Subterrane (BC), is located in the eastern part of the Slavonia-Dravia Terrane within the Tisza Megaunit (*Fig. 1.2/b*). The metamorphic formations of this complex do not outcrop; instead, they are covered by thin (50-100 m) Tertiary and Quaternary sediments in the area of Görcsöny Ridge. The crystalline schists of the Babócsa Complex form the western border of the BC (*Fig. 1.3*). The Villány deep fracture zone (KASSAI 1972), which has a NW-SE strike, separates the Baksa metamorphic block from the Mórágy Granite Complex and the Permo-Triassic sediments to the east (*Fig. 1.3*). The Mecsekalja Tectonic Zone borders the complex in the north (*Fig. 1.3*). This zone separates metamorphic rocks and non-metamorphic Mesozoic sediments that are built by sandstone, conglomerate, and limestone with evaporite (anhydrite, gypsum) intercalations on the Permian-Triassic border (Magyarürög Anhydrite Member of the Hetvehely Dolomite Formation, KONRÁD 1997). The rocks of this complex are overlain by the Carboniferous Téseny Sandstone Formation and the Mesozoic rocks of the Villány Mountains (*Fig. 1.3*). Further to the south, formations in the complex can be traced over the Slavonian regions in the Papuk and Krndija Mountains.

The Baksa-2 exploratory well (bottom-hole: 1200 m) gives the most detailed investigation of the BC. The well exposes the crystalline basement formation with a total thickness of over 1,100 m and a nearly 100% core recovery. Rocks in this complex are mostly built by gneiss and mica schists that are intercalated by marble, dolomite-marble, and amphibolite bodies.

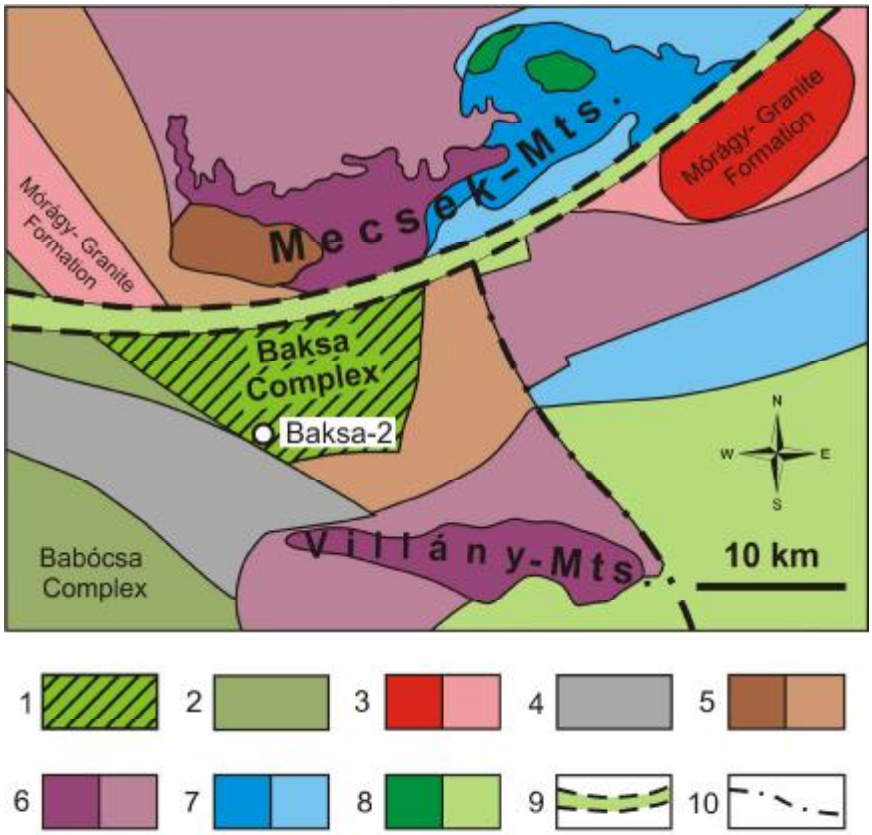

Figure 1.3. *Geologic map of the Baksa Complex and its geological environment presented without Tertiary and Quaternary sediments*
Legend: 1. Baksa Complex (study area); 2. Babócsa Complex; 3. Mórágy Complex (Carboniferous); 4. Carboniferous sediments; 5. Permian formations; 6. Triassic formations; 7. Jurassic formations; 8. Cretaceous formations; 9. Ófalu shear zone; 10. Villány-Szalatnak deep fracture zone.

Microgranite (aplite) dykes crosscut the entire drill section, occurring most frequently in the marble and dolomite-marble parts of the drill section. Based on petrographic considerations, the drilled rock body can be distributed to the following sections (SZEDERKÉNYI 1979):

1.3.1.1. Upper marble section (57 – 224 m)

Marble and dolomite marble are the predominant rock types in this section, with gneiss and mica-schist intercalations. The Aplite dykes that frequently occur in this section caused alterations in carbonate rocks that are accompanied by the formation of calc-silicate hornfels with epidote and diopside. Ore deposits are also characteristic of this section, from the hydrothermal alternation produced by the dikes. The most significant ore deposit is a 6-7-cm thick polymetallic vein that penetrates the borehole at depth of 186.4 m.

1.3.1.2. Chloritic two-mica gneiss (224 – 822 m)

This section is composed of two-mica gneiss and schist with some amphibolite. Significant chloritisation (after biotite) is observed in some parts of the rocks (SZEDERKÉNYI, 1979). Aplite dykes are rare in this section, and a cross-cutting biotite-andesite dyke is observed in a fault zone at a depth of approximately 460 m.

1.3.1.3. Lower marble section (822 – 867 m)

This section is composed of amphibolites, although marble intercalations are the most important rock type. The marble bands are almost pure dolomite. This section is very rich in aplite dykes, which have caused alterations similar to those found in the upper marble section.

1.3.1.4. Garnetiferous two-mica gneiss (867 – 922 m)

This rock section is dominated by gneiss with some mica schist intercalations. Large garnet grains (> 2 cm in diameter) are a common occurrence throughout the section. Aplite dykes do not occur in this section.

1.3.1.5. Garnetiferous two-mica schist (922 - 1200 m)

This is the second-thickest section in the core and is two-thirds mica schist and one-third gneiss. This section also contains abundant garnet, and it locally contains thin amphibolite intercalations.

1.3.2. Metamorphic evolution

The metamorphic evolution of the BC has been investigated by many researchers (RAVASZ-BARANYAI 1969; SZEDERKÉNYI 1976, 1981, 1983; ÁRKAI 1985; ÁRKAI et al. 1999; KIRÁLY 1996; HORVÁTH et al. 2003; NAGY & M. TÓTH 2009). The metamorphic events can be interpreted as individual deformation periods of a single $P - T$ path (ÁRKAI et al. 1999; ÁRKAI 1985). The earliest detectable metamorphic effect is indicated by an eclogite sample, which was exposed by the Görcsöny-1 well. From the mineral assemblages of the eclogite samples, RAVASZ-BARANYAI (1969) concluded there were earlier progressive and later retrograde alteration phases. HORVÁTH et al. (2003) investigated the eclogite and amphibolite pebbles of the Miocene conglomerate that covers the crystalline basement. They determined a 1300-1500 MPa pressure and 600-650 °C temperature values for the progressive phase and ~ 800 MPa pressure and ~ 500 °C temperatures for the retrograde phase. The subsequent

progressive middle pressure and temperature alteration resulted in a Barrow-type mineral zonation in the formations of the crystalline basement (SZEDERKÉNYI 1976). This is the oldest metamorphic event detectable in nearly all of the basement rocks of Southeast Transdanubia (ÁRKAI 1984; ÁRKAI et al. 1985; KIRÁLY 1996; ÁRKAI et al. 1999). ÁRKAI et al. (1999) calculated the peak conditions of this phase as P_{max}: 750±50 MPa and T_{max}: 660±20 °C, while KIRÁLY (1996) noted values of P_{max}: 500-700 MPa and T_{max}: 540-650 °C.

The next retrograde process – following the Barrovian phase – caused secondary albitisation. This event was followed by a close to isothermal decompression with parameters of 440±20 MPa and 650±40 °C (ÁRKAI et al. 1999). According to KIRÁLY (1996), the decompression parameters were <200 MPa and 400-560 °C. According to ÁRKAI et al. (1999) the mentioned event can be associated with a Variscan granitoid magmatism that occurred in the geological environment of the Baksa Complex. KOVÁCH et al. (1985) and BALOGH et al. (1983) place the age of the mentioned events, including the Barrovian event, between 307 and 270 Ma with significant uncertainty. The latest research gives a 307-312 Ma interval to the age of the Barrovian event and the isothermal decompression (LELKES-FELVÁRI & FRANK 2006). According to NAGY & M. TÓTH (2009), the two lowermost sections (garnetiferous two-mica gneiss; garnetiferous two-mica schist) underwent a rather different *P-T* history than the rest of the drilled rock body. These rocks show a *P-T* path ranging from >800 MPa/700-750 °C to ~ 500 MPa/~ 620 °C.

The isothermal decompression was followed by contact metasomatism related to late orogenic aplite dykes that penetrated the rock body. As these aplite dykes can be found in the whole borehole, they only caused significant alterations in the carbonate rock types. The most significant alterations are the skarn formations, which include epidote, garnet, diopside, and in lesser amounts, sulphides. In addition to the aplite dikes, hydrothermal ore indications are also observable in the rock body. These indications have been divided genetically into two groups: one group is related to the aplite dykes, the other is independent of them (SZEDERKÉNYI 1979). TARNAI (1997, 1998) gave a 240-300 °C temperature to the ore formation phase independent of the aplite. This temperature was inferred from fluid inclusions that can be found in quartz crystals cogenetic with ore minerals. A retrograde greenschist facies event that caused chloritisation and secondary albitisation is the youngest event detectable in the rocks of the complex (SZEDERKÉNYI 1979). The temperature of this low grade alteration was established to be around 200-400 °C by ÁRKAI et al. (1985), while the age of this phase was placed around the Alpine orogeny by SZEDERKÉNYI (1984).

1.3.3. "Postmetamorphic" evolution

Although the main details of the regional metamorphic evolution of the Baksa Complex is known, their retrograde metamorphic evolution (briefly reviewed in section 1.3.2.), post-metamorphic fracture deformation, and fracture cementation processes are only marginally known. In this section, these events and their petrographical characteristics will be represented in detail. These events are younger or are independent of the main periods of the regional metamorphic events. The following short review of these events is based on the report of SZEDERKÉNYI (1979).

1.3.3.1. Subvolcanic bodies (aplite, andesite dikes) and contact metamorphic rocks

Evidence of subvolcanic activity is one of the most characteristic features of the rocks of the Baksa Complex. Patterns of two types of subvolcanic activity can be found in the metamorphic column. The predominant pattern is made by several aplite dikes (micro granite veins) that intrude the rocks mostly along fault zones or joints. In case of mica schist, they penetrate among the cleavages of the rocks as intrusive sheets (SZEDERKÉNYI 1979). The most characteristic contact metasomatic patterns occur along the boundaries of the aplite dikes and the carbonate rocks (marble and dolomite marble). These alterations can appear in various forms. Narrow bands (<1 cm) on the contact zones show *grs±ep+di±an+qtz±mc+cal+dol* mineral paragenesis (mineral abbreviations after SIIVOLA & SCHMID 2007). These can be subdivided to three sub-zones: epidote endoskarn in an aplite dike; epidote exoskarn between aplite and marble; and diopside-grossular exoskarn in the marble. Epidote in the endoskarn occurs as a fracture-filling mineral in the aplite bodies.

The most effective contact metasomatic effects are observable in the marble rock types that suffered intensive brittle deformation, resulting in a cataclastic texture. Here, contact zones can reach several centimetres (~5-7 cm) in thickness. In these domains, epidote is the main rock-forming mineral; in some places, 1-3-cm thick "epidosite" rims are observable in the marble beside the aplite bodies. Additionally, epidote frequently occurs in veins as a fracture-filling mineral even several metres from the contact zone. The dominant mineral assemblage of the contact is *cal+ep+qtz±tr±pl±chl*.

Where the aplite penetrates into gneiss or mica schist, the alteration halo is smaller in dimension and the alteration paragenesis is poorer, but it is not so various that it is visible in the carbonate host rocks. Epidote can be consistently found, but albite is also very common in

these contact domains and this latter mineral formed by retrogressive processes. Characteristic mineral assemblage of these contact domains is: *or+mc+qtz±ms+ep+ab*.

Aplite dikes penetrating the rocks of the Baksa Complex can be found in many parts of the granitoid rock bodies of South Transdanubia. These dikes can also be found in the serpentinite bodies of Helesfa and Gyód or in the crystalline rocks of the Ófalu Phyllite Formation.

The formation of the aplite dikes has been dated to 270±20 Ma. This date was obtained using Rb-Sr geochronology (SVINGOR & KOVÁCH, 1981), and it indicates a younger age for this event than the Barrovian progressive metamorphism (307-312 Ma in LELKES-FELVÁRI & FRANK, 2006).

The other detected pattern of subvolcanic activity is a single biotite andesite dike, which can be found at a ~469-m depth in the drilled section. The ~6-cm-thick vein shows a perlitic microtexture with euhedral andesine crystals. The dike is related to andesitic rock based on the main element distribution. The absolute age of the volcanic activity is unknown, but the formation is presumably younger than Mesozoic (SZEDERKÉNYI 1979).

1.3.3.2. Hydrothermal events and their mineralisation

Traces of hydrothermal effects can be observed in each section of the penetrated rock body. Characteristic hydrothermal mineral assemblages have formed in joints or diaclases and/or in thin veinlets that are parallel to or crosscut the cleavage of the rock. Generally, there are two hydrothermal processes that can be distinguished based on the time and type of formation (SZEDERKÉNYI 1979).

The earlier process is connected to the penetration of the aplite dikes detailed in the former section. This hydrothermal process occurred after the intrusion and consolidation of the aplite mass at the relaxation stage of the tectonocycle, and it caused the cementation of the fractures occurring in the rigid aplite body and the adjacent rocks. These fracture infillings make thin (~1 mm to ~1 cm-thick) green-coloured veins with a steep or often zigzagged shape. Epidote, adularia, and quartz are the most significant fracture-filling minerals, but plagioclases, chlorite, tremolite, and calcite also occur in several places. Although, this fracture cementation is the most frequent in the drilled rock section, it is accompanied almost exclusively with non-ore mineralisation. Beyond the disseminated ore phase, including some tiny pyrite grains, no other ore accumulation is observable.

Several ore-rich quartz veinlets occur in the rock columns, frequently reaching a ~0.5-mm thickness. These veins crosscut the mentioned epidote-rich veins; hence, they are younger and must have been formed in a subsequent tectonocycle. The joints and shear planes that include the ore veins were able to expand into the Upper Marble section because of the more rigid behaviour of the adjacent rock, which allowed the formation of several-cm-thick ore veins with a massive sulphide fracture-filling mineralisation. The ore mineral paragenesis of the massive sulphide mineralization is the following: pyrite, marcasite, sphalerite, chalcopyrite, pyrrhotite, galena, hematite, pentlandite, covellite (TARNAI, 1997). The non-ore minerals occur to a lesser degree and quartz, calcite, and feldspar are the most characteristic of them. The hydrothermal origin of the ore minerals is indicated by the ore mineral paragenesis with their morphological and textural features (TARNAI, 1997, 1998). The petrographical and mineralogical characteristics of a 7-cm-thick massive sulphide vein, which is one of the best developed ore veins in the drilled section, were investigated in detail by TARNAI (1998). The ore veins are not homogeneous, there are two clearly separated parts having quite different ore mineral parageneses. Therefore, the outer and inner (main) ore phases are easily distinguished. Both fluid inclusions of the quartz cogenetic with ore minerals and ore microscopical analyses suggest that two phases can be distinguished in the formation of the vein.

The paragenesis of the first (outer phase) is galena, sphalerite, and pyrite (marcasite), and it was formed at a lower temperature (250-270 °C). The ore paragenesis of the main or inner phase is pyrite, marcasite, sphalerite, pyrrhotite, and chalcopyrite. It was formed at a higher temperature (290-310 °C). Both assemblages were formed from a low salinity (T_m(Ice)=-1.6 – -2.8 °C → 4-5% *w*NaCl eq.) H_2O-CO_2-NaCl-($CaCl_2$) composition fluid. The ore mineral paragenesis can be characterised by a Fe, Zn, Cu, Pb, and Ni sulphide mineralisation. The results of fluid inclusion analyses and the presence and habit of the main non-ore minerals (quartz, calcite, feldspar) show that the fluids were connected with the real magmatic activity and not from the mobilisation of metamorphic fluid in a wider sense. Accurate geological dating and determination of the regional connections of the hydrothermal activity is quite difficult. On the basis of geological closeness and an analogy of the mineralisation features, the hydrothermal processes can be related to the Lower Permian rhyolitic volcanism (Gyűrűfű Rhyolite Formation). Traces of the subsequent post-volcanic activity of this rhyolitic volcanism can be found as a hydrothermal ore indication in the borehole Szava-1, which is 10-15 km to the east of borehole Baksa-2 (FAZEKAS & VINCE, 1991).

1.3.3.3. Postmetamorphic tectonic movements in the Baksa Complex

Our knowledge of the postmetamorphic structural evolution of the Baksa Complex is largely incomplete. The only information about the movements of the crystalline basement from the Carboniferous up to now is based on the study of CSÁSZÁR (2004). He constructed a subsidence curve of the surface of the crystalline basement of the Mórágy Complex and its vicinity. Using the results of this study, significant consequences can be deduced from the Alpine structural evolution of the Baksa Complex. A significant uplift of the BC occurred after the Barrovian event at the end of the Carboniferous. A relaxation of the crystalline block took place concurrently with the uplift of the area. At the end of the Permian age, an intensive subsidence of the Tisza mega-unit occurred, and the area was a base level of erosion until the late Cretaceous-Palaeogene uplift. The most recent results concerning the tertiary structural history of the Mecsek-Villány area are related to the study of CSONTOS et al. (2002). The Mecsek-Villány area has suffered a very complicated Tertiary tectonic history that is dominated by transpression. The most important tectonic process that operated at Görcsöny Ridge (Baksa Complex) was the uplift in the Ottnangian stage that elevated the crystalline basement above the erosion level. This elevation, caused by transpression, continued until the late Miocene, and it led to significant denudation of the crystalline block. Tectonic activity caused the brittle deformation of the rigid metamorphic mass of the crystalline basement, which lead to the development of significant fault zones penetrating the rocks of the Baksa Complex. These fault zones are marked by a crumbled rock structure where the fault breccia is embedded in a significant amount of yellowish- or greenish-coloured clay gouge (SZEDERKÉNYI 1979). In the Baksa-2 borehole, fourteen major fault zones are detectable, and eleven of them can be found between a 410 and 570-m depth in the drilled section. In some fault zones, the carbonate cementation is observable and the characteristic chloritisation of the biotite is observable in the wall rock along each fault zone. According to SZEDERKÉNYI (1979), a recent seepage of water occurs in the fault zones where limonitic bands or patches are observable.

REFERENCES

ÁRKAI, P. (1984): Polymetahmorphism of the crystalline basement of the Somogy-Dráva basin (southwestwern transdanubia, Hungary. *Acta Mineralogica-Petrographica, Szeged*, 2, XXVI, 129-153.

ÁRKAI, P. (1985): Polymetamorphic evolution of the South-Hungarian crystalline basement, Pannonian basin: geothermometric and geobarometric data. *Acta Geologica Hungarica*, 3-4, 23, 165-190.

ÁRKAI, P., HORVÁTH, P., NAGY, G. (1999): A clockwise *P-T* path from the Variscan basement of the Tisza Unit, Pannonian basin Hungary. *Geologica Croatica*, 2, 52, 109-117.

BADA, G., HORVÁTH, F., DÖVÉNYI, P., SZAFIÁN, P., WINDHOFFER, G., & CLOETINGH, S. (2007): Present-day stress field and tectonic inversion in the Pannonian basin. *Global and Planetary Change*, 58, 165-180.

BALLA, Z. (1982): Development of the Pannonian Basin basement trough the Cretaceous-Cenozoic collision: a new synthesis. *Tectonophysics*, 88, 61-102.

BALLA, Z. (1984): The Carpathian loop and the Pannonian basin: a kinematic analysis. *Geophysical Transactions*, 30, 4, 313–353.

BALOGH, K., ÁRVA-SÓS, E., BUDA, GY. (1983): Chronology of granitoid and metamorphic rocks of Transdanubia (Hungary). *Anuarul Institului de Geologie şi Geofizică*, 61, 359-364.

BECKER, A. (1993): Contemporary state of stress and neotectonic deformation in the Carpathian-Pannonian region. *Terra Nova*, 5, 375-388.

BUDA, G. (1996): Correlation of Variscan Granitoids occurring in Central Europe. *Acta Mineralogica-Petrographica*, 37 (Supplementum), 1-24.

CSÁSZÁR, G. (2004): Alpine burial history of the Mórágy Block and its environs. *Annual Report of the Geological Institute of Hungary*, 395-401.

CSONTOS, L., NAGYMAROSY, A., HORVATH, F., & KOVAC, M. (1992): Tertiary evolution of the Intra-Carpathian area: a model. *Tectonophysics*, 208, 221-241.

CSONTOS, L., & NAGYMAROSY, A. (1998): The Mid-Hungarian line: a zone of repeated tectonic inversions. *Tectonophysics*, 297, 1-4, 51-71.

CSONTOS, L., BENKOVICS, L., BERGERAT, F., MANSY, J., L., & WÓRUM, G. (2002): Tertiary deformation history from seismic section study and fault analysis in a former European Tethyan margin (the Mecsek–Villa´ny area, SW Hungary). *Tectonophysics*, 357, 81-102.

DECKER, K. (2007): Miocene to present tectonics at the Alpine-Carpathian-Pannonian junction, *Collision and extension in the Alpine-Carpathian-Pannonian system*, Siófok, Hungary,

DEWEY, J., F. (1988): Extensional collapse of orogens. *Tectonics*, 7, 6, 1123-1139.

FAZEKAS, V., & VINCZE, J. (1991): Hidrotermás ércindikációk a Villány-hegység északi előtere mélyfúrásaiban. *Földtani Közlöny*, 91, 1-4, 23-56.

GÉCZY, B. (1972): The origin of the Jurassic faunal provinces and the Mediterranean plate tectonics. *MTA X. Oszt. Közl.*, 5, 297-311.

GÉCZY, B. (1973a): The origin of the Jurassic faunal provinces and the Mediterranean plate tectonics. *Ann. univ. Sci. Budapest R. Eötvös Nom. Sect. Geol.*, 16, 99-114.

GÉCZY, B. (1973b): Plate tectonics and paleogeography in the East- Mediterranean Mesozoic. *Acta Geol. Hung.*, 27, 379-389.

GÉCZY, B. (1984): Provincialism of Jurassic ammonites: examples from Hungarian faunas. *Acta Geol. Hung.*, 27, 34, 379-389.

GERNER, P., DÖVÉNYI, P., HORVÁTH, F., & MÜLLER, B. (1995): State of recent stress and seismotectonics in the Pannonian Basin and surroundings areas. *Terra Abstracts*, 7, 1, 173.

HAAS, J., & PÉRÓ, CS. (2004): Mesosoic evolution of the Tisza Mega-unit. *International Journal of Earth Sciences*, 93, 297-313.

HORVATH, F., BADA, G., SZAFIAN, P., TARI, G., ADAM, A., & CLOETINGH, S. (2006): Formation and deformation of the Pannonian Basin: constraints from observational data. *European Lithosphere Dynamics.*, GEE, D. G., & STEPHENSON, R., London, Geological Society, 32, 191-206.

HORVÁTH, F., & BERCKHEMER, H. (1982): Mediterranean back-arc basins. *Alpine Mediterranean geodynamics.*, BERCKHEMER, H., & HSÜ, K., J., American Geophysical Union, 7, 141-173.

HORVÁTH, F. (1988): Neotectonic behavior of the Alpine-Mediterranean Region. *The Pannonian basin - A study in basin evolution.*, ROYDEN, L., H., & HORVÁTH, F., Tulsa, Oklahoma, Amer. Assoc. Petrol. Geol., 45, 49-55.

HORVÁTH, F. (1993): Towards a mechanical model for the formation of the Pannonian Basin. *Tectonophysics*, 226, 333-357.

HORVÁTH, F., CSONTOS, L., CLOETINGH, S., GERNER, P., & DÖVÉNYI, P. (1996): Compression during extension in the Pannonian Basin and its bearing on hydrocarbon exploration. *Oil and Gas in Alpidic Thrustbelts and basins of Central and Eastern Europe*, WESSELY, G., & LIEBL, W., EAGE Special Publication, 5, 415-416.

HORVÁTH, F., & CLOETINGH, S., (1996): Stress-induced late-stage subsidence anomalies in the Pannonian basin. *Tectonophysics*, 266, 287-300.

HORVÁTH, P., KOVÁCS, G., SZAKMÁNY, GY. (2003): Eclogite and garnet amphibolite pebbles from niocene conglomerates (Pannonian basin Hungary): implications for the variscab metamorphic evolution of the Tisza Megaunit. *Geologica Catpathica*, 6, 54, 355-366.

ILIĆ, A., & NEUBAUER, F. (2005): Tertiary to recent oblique convergence and wrenching of Central Dinarides: constrains from a palaeostress study. *Tectonophysics*, Special Issue: Carpathians/Pannonian System.,

KASSAI, M. (1972): A Villány-Szalatnaki pleozóos mélytörés. (The Paleozoic Deep Fracture of Villány-Szalatnak.). *MTA X. Oszt. Közl.*, 6, 1, 351-354.

KÁZMÉR, M., KOVÁCS, S. (1985): Permian–Paleogene paleogeography along the Eastern part of the Insubric–Periadriatic Lineament system: evidence for continental escape of the Bakony-Drauzug unit. *Acta Geol. Hung.*, 28, 1-2, 71-84.

KEPPIE, J., D., & DALLMEYER, R., D. (1990): Introduction to terrane analysis and the tectonic map of Pre-Mesosic terranes in Circum Atlantic Phanerozoic orogens., *IGCP Project*, Göttingen, 24-27

KIRÁLY, E. (1996): Adalékok a délkelet-dunántúli polimetamorf aljzat megismeréséhez. *Földtani Közlöny*, 1, 126, 1-23.

KONRÁD, G. (1997): A DK-dunántúli alsó - és középső triász képződmények szedimentológiai vizsgálatának eredményei, Kandidátusi éertekezés,

KOVÁCH, A., SVINGOR, E., & SZEDERKÉNYI, T. (1985): Rb-Sr Dating of basement rocks from the southern foreland of the Mecsek mountains, southeastern transdanubia, Hungary. *Acta Mineralogica-Petrographica, Szeged*, XXVII, 51-57.

KOVÁCS, S., SZEDERKÉNYI T., ÁRKAI, P., BUDA GY., LELKES-FELVÁRI GY., NAGYMAROSY A. (1997): Explanation to the terrane map of Hungary. *Ann. Géol. des Pays Hell*, PAPANIKOLAOU, D., 37, 271-330.

KOVÁCS, S., HAAS, J., CSÁSZÁR G., SZEDERKÉNYI T., BUDA GY., NAGYMAROSY A. (2000): Tectonostratigraphic terranes in the pre-Neogene basement of Hungarian part of the Pannonian area. *Acta Geol. Hung.*, 43, 225-328.

LELKES-FELVÁRI, G., & FRANK, W. (1997): Geochronology of the metamorphic basement, Transdanubian part of the Tisza Mega-Unit. *Acta Geologica Hungarica*, 49, 3, 189-206.

LELKESNÉ FELVÁRI, GY. (1997): Formáció leírások. – In: CSÁSZÁR, G. (ed): Magyarország litosztratigráfiai egységei, táblázatok és rövid leírások. Basic lithostratigraphic units of Hungary. Charts and short descriptions. *MÁFI Alkalmi Kiadványai* 192, pp. 26–29; 100–104.

LINZER, H., G., DECKER, K., PERESSON, H., DELL' MOUR, R., & FRISCH, W. (2002): Balancing lateral orogenic float of the Eastern Alps. *Tectonophysics*, 354, 211-237.

MÁRTON, E. (1981): Tectonic implication of paleomagnetic data for the Carpatho-Pannonian Region. *Earth Evol. Sci.*, 1, 34, 257–264.

MÁRTON, E. (2000): The Tisza Megatectonic Unit in the light of paleomagnetic data. *Acta Geol. Hung.*, 43, 329-343.

NEUBAUER, F., & RAUMER, J., F. (1993): The Alpine Basement. Linkage between Variscides and East Mediterranean Mountain Belts. *Pre-Mesosoic geology in the Alps.*, RAUMER, J., F., & NEUBAUER, F., Berlin, Heidelberg, New York, Springer, 641-664.

PERESSON, H., & DECKER, K. (1996): From extension to compression: Late Miocene stress inversion in the Alpine-Carpathian-Pannonian transition area. *Mitt. Ges. Geol. Bergbaustud. Österr.*, 41, 75-86.

RAVASZ BARANYAI, L. (1969): Eclogite from the Mecsek Mountains, Hungary. *Acta Geologica Academiae Scientiarum Hungaricae*, 13, 315-322.

ROYDEN, L. H., HORVÁTH, F., NAGYMAROSY, A., & STEGENA, L. (1983): Evolution of the Pannonian Basin System. Subsidence and thermal history. *Tectonics*, 2, 91-137.

ROYDEN, L. H., & DÖVÉNYI, P. (1988): Variations in extensional styles at depth across the Pannonian basin system. *The Pannonian Basin: a Case Study in Basin Evolution.*, ROYDEN, L. H., & HORVÁTH, F., American Association of Petroleum Geologists, Memoirs., 45, 235-255.

SCHMID, S. M., BERNOULLI, D., FUGENSCHUH, B., MATENCO, L., SCHAEFER, S., SCHUSTER, R., TISCHLER, M., & USTASZEWSKI, K. (2008): The Alps–Carpathians–Dinarides-connection: a compilation of tectonic units. *Swiss J. Geosci.*, 101, 139-183.

SCLATER, J., ROYDEN, L., HORVÁTH, F., BURCHFIEL, B., SEMKEN, S., & STEGENA, L. (1980): The formation of the intra-Carpathian basins as determined from subsidence data. *Earth and Planetary Science Letters*, 51, 139-162.

SIIVOLA, J., & SCHMID, R. (2007): List of Mineral Abbreviations, A classification and glossary of terms., FETTES, D., & DESMONS, J., New York, Cambridge University Press: 93-110.

SVINGOR, É., & KOVÁCH, Á. (1981): Rb-Sr isotopic studies on granodioritic rocks from the Mecsek Mountains, Hungary. *Acta Geol. Ac. Sci. Hung.*, 24, 2-4, 295-307.

SZEDERKÉNYI, T. (1974): A DK-Dunántúli ópaleozóos képződmények ritkaelem kutatása, Kézirat. Kandidátusi értekezés MTAK,

SZEDERKÉNYI, T. (1976): Barrow -type metamorphism int he crystalline basement of South-East Transdanubia. *Acta Geol. Ac. Sci. Hung.*, 20, 47-61.

SZEDERKÉNYI, T. (1979): A mecseki ópaleozóos-prekambriumi alapszelvények komplex földtani feldolgozása.,

SZEDERKÉNYI, T. (1983): Origin of amphibolites and metavolcanics of crystalline complexes of south transdanubia, Hungary. *Acta Geologica Hungarica*, 1-2, 26, 103-136.

SZEDERKÉNYI, T. (1996): Metamorphic formations and their correlation in the Hungarian part of Tisia Megaunit (Tisia Composite Terrane). *Acta Mineralogica-Petrographica, Szeged*, XXXVII, 143-160.

SZEDERKÉNYI, T., & LELKES-FELVÁRI GY. (1997): CSÁSZÁR, G.,

TARI, G., HORVÁTH, F., & RUMPLER, J. (1992): Styles of extension in the Pannonian Basin. *Tectonophysics*, 208, 203-219.

TARI, G., DÖVÉNYI, P., DUNKEL, I., HORVÁTH, F., LENKEY, L., STEFANESCU, M., SZAFIÁN, P., & and TÓTH, T. (1999): Lithospheric structure of the Pannonian basin derived from seismic, gravity and geothermal data. *The Mediterranean Basins: Tertiary Extension within the Alpine Orogen.*, DURAND, B., JOLIVET, L., HORVÁTH, F., and SÉRANNE, M., (eds.) London, Geological Society Special Publications, 156, 215-250.

TARI, V., & PAMIĆ, J (1998): Geodynamic evolution of the northern Dinarides and South Pannonian Basin. *Tectonophysics*, 297, 269-281.

TARNAI, T. (1997): Ore minerals from the key section of the Baksa Complex (W Baranya hills, Hungary). *Acta Mineralogica-Petrographica*, XXXVIII, Supplementum, 119-133.

TARNAI, T. (1998): Mineralogical-petrological study on ore vein penetrated by the key-borehole Baksa No. 2 SE Transdanubia, Hungary. *Acta Mineralogica-Petrographica*, XXXIX, 21-34.

TISCHLER, M., GRÖGER, H.R., FÜGENSCHUH, B., SCHMID, S.M. (2007): Miocene tectonics of the Maramures area (Northern Romania): implications for the Mid-Hungarian fault zone. *International Journal of Earth Sciences*, 96, 473-496.

WEIN, G. (1969): Tectonic review of the Neogene covered areas of Hungary. *Acta Geol. Hung.*, 13, 399-436.

WEIN, G. (1978): A Kárpát medence alpi tektogenezise. *Annual Report of the Hungarian Geological Survey from 1976*, 245-256.

CHAPTER 2

Hydrothermal paleofluid circulation in the fracture network of the Baksa Gneiss Complex, SW Pannonian Basin, Hungary[*]

[*] K. FINTOR, T. M. TÓTH, F. SCHUBERT (2010): Hydrothermal paleofluid circulation in the fracture network of the Baksa Gneiss Complex SW Pannonian Basin Hungary, International Journal of Earth Sciences (submitted manuscript)

2. Hydrothermal palaeofluid circulation in the fracture network of the Baksa Gneiss Complex of SW Pannonian Basin, Hungary

ABSTRACT

A well developed fracture filling system can be found in the rock body of the Baksa Gneiss Complex (SW Hungary) which is mostly built up by Ca-Al-silicate dominant veins. Detailed investigation of this vein network was carried out here by accurate mineralogical and fluid inclusion analyses. In the investigated veins a well defined mineral succession can be derived: *di→ep→sph→ab±kfp→chl1±prh±adu→chl2→chl3→pyr→cal1→cal2→cal3*, which is similar to those that can be observed in wall-rocks that have suffered propylitic alteration. The mineral assemblage, mineral chemistry data, and fluid inclusion analyses indicate that vein formation occurred during low *P-T* conditions in a cooling hydrothermal system. The calculated temperature range of the formation of cogenetic feldspars is between 230 and 336 °C, while in the case of chlorites a temperature cooling trend (T_{chl1}: 260 ± 32 °C → T_{chl2}: 222 ± 20 °C → T_{chl3}: 154 ± 13 °C) is assignable. The observed homogenization temperatures of D_1 inclusions in diopside (T_h: 276–362 °C) and E_1 inclusions in epidote (T_h: 181–359 °C) can be fit into the cooling trend. The almost identical salinity (0.2–1.5% *w*NaCl eq.) of these inclusions in each host is related to the dominance of the same fluid regime during the hydrothermal phase. The high trace element content (in respect of As, Cu, Zn, Mn) and Co/Ni ratio ~1–5 of pyrite grains support the post-magmatic hydrothermal origin of the veins. The vein microstructure and identical fluid composition indicate that vein mineralization occurred in an interconnected fracture system where crystals grew in fluid filled cracks. Diopside and epidote were precipitated during a temperature decrease from ~480 °C to ~236 °C, estimated from the nearly constant regional pressure condition (~100 MPa). The cooling rate of the fluid was influenced mainly by the ambient rock temperature, which was around 154 °C, based on thermometry data of the last chlorite phase (chlorite 3), and ~37 °C/km was assumed for the regional thermal gradient. The rather different fluid characteristics (T_h: 75–124 °C; 17.5–22.6% *w*$CaCl_2$ eq.) of C_1 inclusions of the subsequent calcite 1 phase and the special $\delta^{18}O$ signature of fluid from which this mineral phase precipitated indicate the occurrence of externally derived fluid in the fracture system.

2.1. Introduction

Investigations of fracture cementations of crystalline basement complexes can contribute to better understanding the paleohydrological processes of continental crust (WILKINSON et al. 1995; WALLIN & PETERMAN 1999; JUHÁSZ et al. 2002; GLEESON et al. 2003; STOBER & BUCHER, 2004, 2005). Many of these investigations were made connected to the crystalline basement of European continent (WILKINSON et al. 1995; WALLIN & PETERMAN 1999; JUHÁSZ et al. 2002). The most detailed results were originated from the area of the European Variscan belt (BOIRON et al. 2003; LODEMANN et al. 1997; WILKINSON et al. 1995; STOBER & BUCHER 2005). The Baksa Gneiss Complex which is a part of the Variscan crystalline rocks of the Tisza microplate is located on the SW part of the Pannonian Basin. The Baksa-2 exploratory well which is deepening into the Baksa Complex with almost 100% core recovery developing the Variscan basement rocks of the Tisza microplate close to 1200m in thickness. This is the most detailed exploration of the crystalline basement of the Pannonian Basin.

There are many evidences can be found in the explored section of Baksa Complex which is refer to well developed fracture cementation processes. TARNAI (1997; 1998) gave a detailed study of hydrothermal ore veins including a thick base-metal sulfide vein and many sulfide veinlets can be found in the metamorphic block, while FINTOR et al. (2008) made a detailed fluid inclusion study about quartz-carbonate veins cross cutting the rock body. Nevertheless the most important fracture cementation process can be observe in a veins are filled by mostly calc-silicate minerals with a small amount of feldspar chlorite and carbonate, and this type of veining can found very often in the penetrated rock section. SZEDERKÉNYI (1979) related the origins of this vein formation to those unknown originated sub-volcanic (granite-aplite) dykes are occurring frequently in the drilled section. The comprehensive investigation of this type of calc-silicate veins can give essential information about the *P-T-X* condition of fluids during pegmatitic-hydrothermal transitions and through the period of the hydrothermal stage (BAKKER 2006) or in case of evolution of skarn ore deposits (BAKER et al. 2004).

In this study we make petrographic and mineral chemical analysis of the mentioned calc-silicate fracture infillings of the Baksa Complex, in conjunction with detailed fluid inclusion analysis of these minerals including diopside, epidote and carbonate phases. The aim of this research is to interpret the evolution of the fracture filling mineralization, and to make a sketch about *P-T-X* evolution of fluids were dominant during the fracture cementation process.

2.2. Geological setting

The Baksa Complex (BC) is found in the SW part of the Tisza Megaunit (*Fig. 2.1*) a microplate, which forms the basement of South Hungary. The Tisza Megaunit was originally part of the Northern European margin of the Tethys and was separated by predominatly Meso-Alpine horizontal displacements of microplates (GÉCZY 1973; HAAS & PÉRÓ 2004). KOVÁCH et al (2000) divided the pre-Alpine basement complexes of the Tisza Megaunit into three major parts: the Kunságia terrane, the Békésia terrane and the Dravia-Slavonia terrane. According to SZEDERKÉNYI (1996) the BC belongs to the Dravia-Slavonia Terrane accompanied with the Babócsa Complex (sub terrane).

The metamorphic formations of the complex do not outcrop; they are covered by thin (50-100 m) Tertiary and Quaternary sediments in the area of Görcsöny Ridge. The crystalline schist's of the Babócsa Complex form the Western border of the BC (*Fig. 2.1*). The Villány deep fracture zone (KASSAI 1972) with a NW-SE strike separates the Baksa metamorphic block from the Mórágy Granite Complex and Permo-Triassic sediments to the East. The Mecsekalja Tectonic Zone borders the complex in the North; it separates metamorphic rocks and non-metamorphic Mesozoic sediments of the Mecsek Mountains (*Fig. 2.1*). Further to the South formations of the complex can be traced over the Slavonian regions, in the Papuk and Krndija Mountains.

The petrographical development and metamorphic evolution of the BC has been investigated by many researchers (RAVASZ-BARANYAI 1969; SZEDERKÉNYI 1976, 1983; ÁRKAI 1985, ÁRKAI et al. 1999; KIRÁLY 1996; HORVÁTH et al. 2003). Petrographically the complex consists of polymetamorphic rocks, mainly gneiss, mica-schist containing marble dolomarble and amphibolite intercalations. There are five metamorphic events detectable in the rocks of the Baksa Complex. RAVASZ-BARANYAI (1969) detected a high pressure phase was followed by a significant decompression. The peak conditions of this *P-T* path was around 1300-1500 MPa and 600-650 °C down to approximately 800 MPa and 500 °C (HORVÁTH et al. 2003). Peak conditions of the Barrovian event (SZEDERKÉNYI 1976) subsequent to the previous high pressure phase was around 750±50 MPa, and 660±20 °C by ÁRKAI et al.(1999) and KIRÁLY (1996) with conditions of 500-700 MPa and 540-650 °C. After the Barrovian event the area underwent secondary albitization and closely isothermal decompression down to 440±20 MPa, 650±40 °C according to ÁRKAI et al. (1999) and < 200 MPa, 400-560 °C by KIRÁLY (1996).

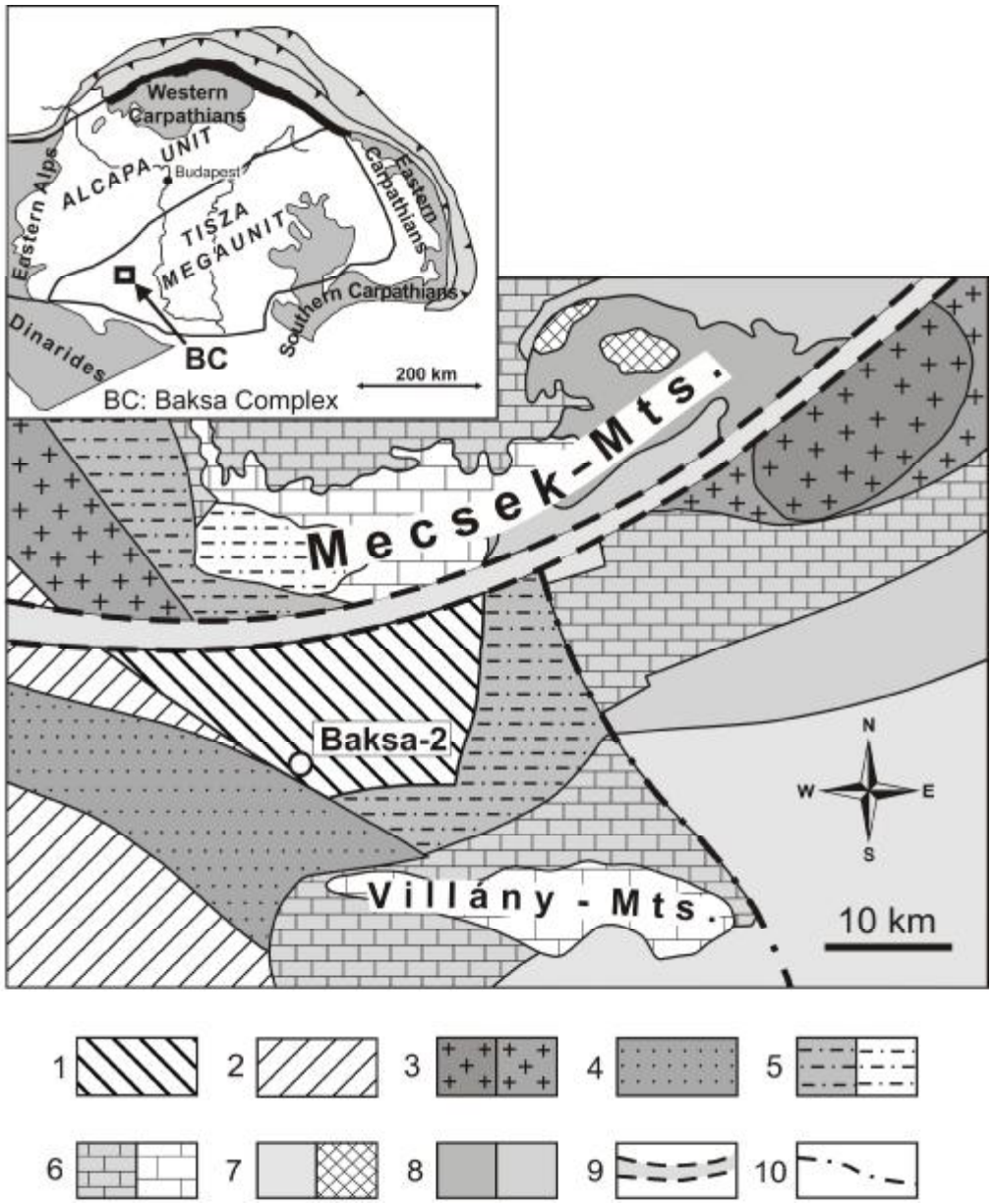

Figure 2.1. *The geological map of the Baksa Complex and its environs is presented without Tertiary and Quaternary sediments.*
Legend: 1. Baksa Complex (study area), 2. Babócsa Complex, 3. Mórágy Complex (Carboniferous), 4. Carboniferous sediments, 5. Permian formations, 6. Triassic formations, 7. Jurassic formations, 8. Cretaceous formations, 9. Mecsekalja Tectonic Zone,, 10. Villány-Szalatnak deep fracture zone. Inset: Location of the study area (BC) in the Pannonian Basin (ALCAPA and Tisza mega unit are also represented on the map); Inset legend: 1. Flysch Belt, 2. Pieniny Klippen Belt, 3. Inner Carpathian Mountain Belt.

The isothermal decompression was followed by contact metasomatism related to aplite intrusions. These aplite dykes caused considerable alteration only in the carbonate rocks of the complex. The significant alteration products contain epidote, diopside, garnet and a wide spectrum of sulfide minerals. In addition to the aplite dykes, hydrothermal ore indications also occur in the rock body. These hydrothermal ore indications were attributed to an earlier event

related to the aplites and a latter one independent from the aplites (SZEDERKÉNYI 1979). In the earlier phase minor amounts of pyrite, chalcopyrite and sphalerite grew sporadically in the veins mostly filled by non-ore minerals, like epidote, diopside, chlorite, quartz, and calcite. The latter ore phase form veins with different dimensions from thin pyrite-pyrrhotite veinlets till several cm thick polymetallic sulfide veins. The detailed mineralogical and ore genetic investigation of the thick ore veins was carried out by TARNAI (1997; 1998) who determine pyrite+pyrrhotite+sphalerite+hematite+chalcopyrite+galena+pentlandite ore paragenesis from these veins. In a study of fluid inclusions of the quartz cogenetic with the later ore minerals he got T_t: 240 to 300 °C and P_t: 15 – 30 MPa for the trapping conditions (TARNAI 1998). The youngest alteration phase which can be investigated in the rocks is a retrograde greenschist facies event, which caused chloritization and secondary albitization (SZEDERKÉNYI 1979). Its temperature range is assumed to be 200-400 °C by ÁRKAI et al. (1985). The beginning of this event is related to alpine orogeny (SZEDERKÉNYI 1984). FINTOR et al. (2008) detected traces of high salinity fluids (~20-25% *w*NaCl eq.) in the postmetamorphic quartz-carbonate veins are penetrating the rock body. They obtained approximately 80-180 °C and 20-100 MPa for the formation parameters of the quartz-carbonate veins by microthermometry.

The Baksa-2 exploratory well (bottom-hole: 1200 m) gives the most detailed discovery of the Baksa Complex. It exposes the crystalline basement formation with a total thickness of over 1100 m and near 100% core recovery. The metamorphic mass could be divided (SZEDERKÉNYI 1979; 1981) into the following lithostratigraphic units:

1. *Upper marble section (57 – 224 m)*
2. *Chloritic two-mica gneiss (224 – 822 m)*
3. *Lower marble section (822 – 867 m)*
4. *Garnetiferous two-mica gneiss (867 – 922 m)*
5. *Garnetiferous two-mica schist (922 - 1200 m)*

2.2.1. Upper marble section

Marble and dolomite marble are predominant rock types in this section with gneiss and mica-schist intercalations. Aplite dykes can be found very frequently in the section and caused significant alterations only in carbonate rocks. These alterations are accompanied by formation of calc-silicate hornfels with epidote and diopside. Ore indications caused by hydrothermal fluids also can be found very frequently.

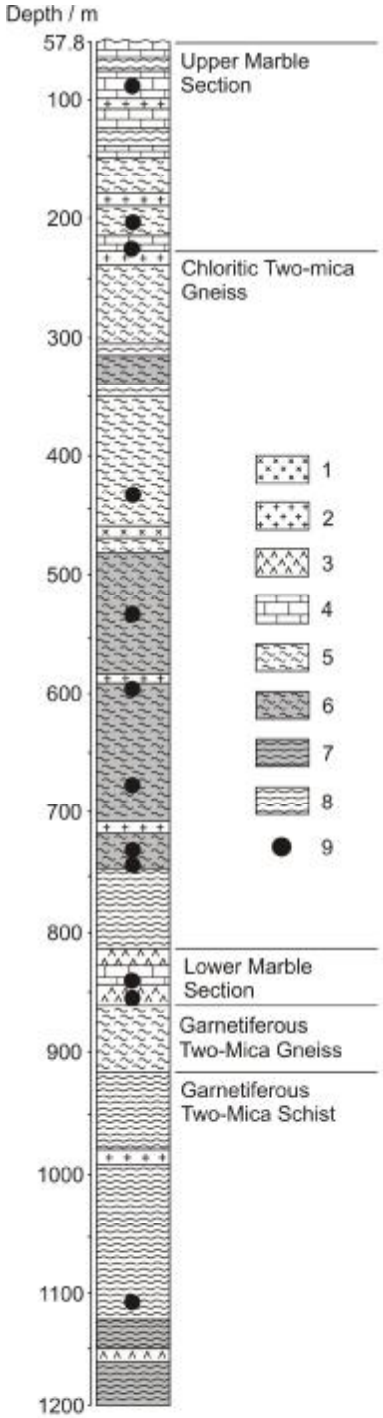

Figure 2.2. *Lithological profile of the Baksa-2 borehole (after SZEDERKÉNYI 1979) Legend: 1: Biotite-andesite dyke; 2: Aplite dykes; 3: Amphibolite; 4: Marble and dolomite marble; 5: Two-mica gneiss; 6: Chloritic gneiss; 7: Chloritic schist; 8: Two-mica schist; 9: Samples used for investigations.*

The most significant ore vein (6-7 cm thick) is found at 186.4 m depth. Formation conditions and ore mineral paragenesis (pyrite, pyrrhotite, sphalerite, chalcopyrite, galenite, pentlandite, hematite, covelline, marchazite) of the vein were investigated in detail by TARNAI

(1997; 1998) and he related it to rhyolitic volcanism that occurred near the northern margin of Villány Mountains (FAZEKAS & VINCZE 1991).

2.2.2. Chloritic two-mica gneiss

This section is comprised of two-mica gneiss and schist with some amphibolite intercalations. Significant chloritization (after biotite) are observable in some parts of the rocks (SZEDERKÉNYI 1979). Aplite dykes occur rarely in this section; however a young biotite-andesites dyke is observable in a fault zone at approximately 460 m depth.

2.2.3. Lower marble section

This section is comprised of amphibolites however; the marble intercalations are the most important rock type of the section. The marbles bands are almost pure dolomite marbles. This section is very rich in aplite dykes which caused alterations similar to those are found in upper marble section.

2.2.4. Garnetiferous two-mica gneiss

This rock section is dominated by gneiss with some mica schist intercalations. Garnets occur in considerable amounts throughout the section. These garnets are mostly almandines and can reach 2 centimetres in diameter.

2.2.5. Garnetiferoust two-mica schist

The section is predominantly mica schist and in lesser amounts gneiss with some amphibolite intercalations. Garnets with similar characteristics to those of the Garnetiferous two-mica gneiss can also be found in considerable amount.

2.3. Samples and methods

2.3.1. Sampling, mineral chemistry and SEM imaging

Samples necessary for the analysis were selected from the Baksa-2 drill cores (*Fig. 2.2*). Mineral paragenesis of vein minerals was determined by microscopic examination. Quantitative analyses of minerals were made in the Eugen F. Stumpfl electron microprobe laboratory at the Montanuniversität Leoben. A JEOL JXA 8200 Superprobe was used for the analysis. The instrument working with five WDS and can measure each element from boron till uranium. It can measure 30 elements simultaneously. High resolution digital X-ray

mapping can be making with using both WDS and EDS. All analytical modes are fully automated. Quantitative analyses were carried out at 10nA beam current and 15 kV accelerating voltage. The beam diameter was 1μm but 5 μm during feldspar analyses. Accumulation time was 10 sec. for the peaks and 4 sec for the backgrounds. Detection limit was 0.1-0.02% in case of Si, Al, Ti, Fe, Mg, Ca, Na, K, Mn, and Cr, while 0,2-0,07% in case of Ba. For the quantitative interpretation of elements international mineral standards were used. ZAF correction was used for the correction of each measurement. Minfile 5.1 program package (AFIFI & ESSENE 1988) was used for the calculation of mineral formulae and calculations based upon charge balance method. Some of the SE and BSE images were made by the above mentioned instrument. The other SE, BSE pictures were made by using a Hitachi S4700 scanning electron microscope at the Institute of Environmental Protection of University of Szeged. The beam conditions of this instrument were 25 kV and 10 μA.

2.3.2. Cathodoluminescence microscopy

The cathodoluminescence images were made at the Geochemical Institute of MTA using a Reliotron cold cathode cathodoluminescence instrument mounted on a Nikon Eclipse E600 optical microscope. The applied beam current was 0.3–0.8 mA with 8–9 kV electron energy. The measurements were made on polished thin sections which had been cleaned by distilled water and acetone previously.

2.3.3. Stable isotope studies

Stable isotope analyses were made at the Geochemical Institute of MTA using a Finnigan delta plus XP mass spectrometer in He carrier gas. The sampling was done by micro drilling of crack filling calcite, obtaining 0.1–0.3 mg calcite powder. These samples were reacted with purified phosphoric acid, producing CO_2 gas which was analysed by the mass spectrometer. The isotopic compositions $\delta^{13}C$ (vs. V-PDB) and $\delta^{18}O$ (vs. V-SMOW) of each sample are averages of replicate analyses. Precision of the measurements was ± 0.1–0.2‰ in cases of $\delta^{13}C$ and $\delta^{18}O$. The ^{13}C and ^{18}O isotope results are reported in the standard δ notation of the difference in isotope ratio between the sample and a standard expressed in per mil (‰), where: $\delta = [(R_{sample}/R_{standard}) - 1] * 1000$.

2.3.4. Fluid inclusion studies

Fluid inclusions were studied in 75-150 μm double polished thick sections prepared from the vein materials. A low speed sawing machine was used for cutting the samples in order to avoid changes in the volume of the fluid inclusions. Microthermometric measurements were carried out with a Linkam THMSG 600 heating-freezing stage operating over a temperature range from -190 to 600 °C. Synthetic fluid inclusions were used for the calibration at -56.6, 0.0 and 374.0 °C. The accuracy of the data is approximately ±0.2 °C under freezing and ±0.5 °C under heating conditions. An LMPlanFI 100X objective lens (Olympus) was used to analyze the inclusions. The measurements of inclusions trapped in epidote and diopside began with freezing while in case of calcite the heating experiments were carried out first. In the latter case, inclusions are able to suffer permanent deformation during the freezing experiment (OXTOBY 2000; GOLDSTEIN & REYNOLDS 1994). The cycling method (GOLDSTEIN & REYNOLDS 1994) was used to determine the last ice melting temperature of fluids trapped in calcite. Determinations of volume fractions of vapor bubbles (φ_{vap}) were obtained from area analysis in a two dimensional projection of fluid inclusions. Terms and symbols defined by DIAMOND (2003) have been used during the investigations. The computer package *FLUIDS* (BAKKER 2003) was used to calculate fluid properties. A calculation of salinities is based on the equivalent *w*% principle. Generally these calculations use NaCl (ROEDDER 1984), but this study uses NaCl to express ice melting temperatures only in case of D_1, E_1, and C_2 fluid types, while in case of D_2, E_2, and C_2 types use $CaCl_2$ in order to express ice melting temperatures below the H_2O-NaCl eutectic point(-21.2 °C). The program *AqSo2e* was used to calculate salinities in the NaCl-H_2O and H_2O-$CaCl_2$ systems (NADEN 1996). The program *BULK* (BAKKER 2003) enabled the calculation of bulk fluid properties (molar volume (V_m), and bulk composition) of individual fluid inclusions. The calculation was accomplished using a purely empirical thermodynamic model, the equation of state for electrolyte bearing aqueous solutions of KRUMGALZ et al. (1996) and the volume fractions of the liquid phase of the inclusions at room temperature. The isochore slopes were calculated by means of the program *LONER 38* (BAKKER 2003; ZHANG & FRANTZ 1987) whose requirement is the knowledge of homogenization temperature (T_h) and salinity of the inclusions.

2.3.5. Raman microspectrometry

A Jobin Yvon LABRAM confocal Raman spectrometer equipped with a frequency doubled Nd-YAG laser (100 mW, 532.2 nm) with a 100X/0.80 objective lens was used to identify fluid phases in inclusions. Calibration of the spectrometer was made by using a silicon chip.

The spectral resolution of the instruments was 4 cm^{-1} while the spatial resolution was a few μm^3. Acquisition time was 100 s with 20 s accumulation periods in each spectrum.

2.3.6. Combined Raman spectroscopy and microthermometry

During Raman spectroscopy assisted microthermometry the Linkam THMSG 600 heating-freezing stage was mounted on the Raman spectrometer, in order to make analyses at different temperature conditions. In order to make accurate identification of ice and salt hydrates, spectra were recorded at temperature condition lower than -170 °C. This method is applicable with great efficiency to determine last melting temperature of salt hydrates, and to distinguish the different type of salt hydrates from ice and each other.

2.4. Results

2.4.1. Petrography of the veins

The investigated veins of the BC belong to the same group according to their mineral paragenesis and succession. However, it is noticeable that not every mineral occurs in each vein. Vein types can be distinguished based on the dominant minerals occurring in the paragenesis. In this way clinopyroxene dominant (V_{cpx}) (*Fig. 2.3/a, b*), feldspar dominant (V_{fp}) (*Fig. 2.3/c, d*), and epidote dominant (V_{ep}) (*Fig. 2.3/e, f*) vein types can be distinguished. Each type is characterized by about 1–10 mm thick and very steep (70°–90°) veins (*Fig. 2.3*).

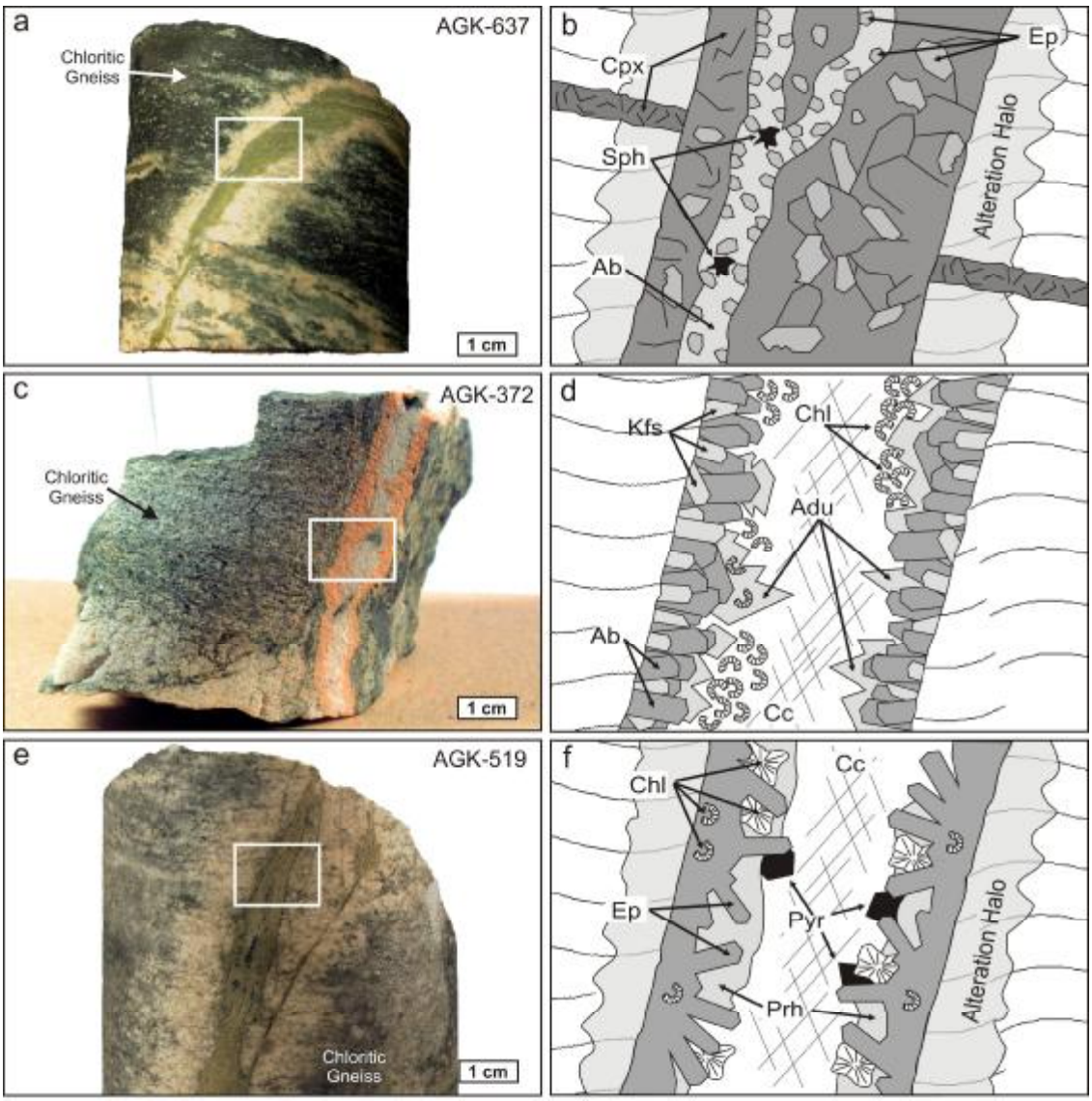

Figure 2.3. *The three investigated vein types*
a) clinopyroxene-epidote dominant vein (V_{cpx}); b) sketch of the localization of the vein filling minerals in V_{cpx}; c) feldspar dominant vein type (V_{fp}); d) sketch of the localization of the vein filling minerals in V_{fp}; e) epidote-chlorite dominant vein type; f) sketch of the localization of the vein filling minerals in V_{ep}.

The main type of V_{cpx} forms 0.5–1 cm thick veins, and along them a characteristic alteration halo is observable which appears as a 1–3 cm thick bleached pinkish coloured band without any macroscopic internal zonation (*Fig. 2.3/a, b*). These veins are pre-dated by thin (~1–2 mm thick) monomineralic clinopyroxene veins filled by anhedral clinopyroxene crystals (*Fig. 2.3/b; 2.4/a, b*). The main type does not show symmetrical fracture filling mineralization; however they show a complex vein filling texture where clinopyroxene and epidote are the dominant minerals (*Fig. 2.3/b; 2.4/a, b*). Clinopyroxene grows on the vein wall and appears as subhedral elongated and/or bulky crystals (*Fig. 2.4/c, d*).

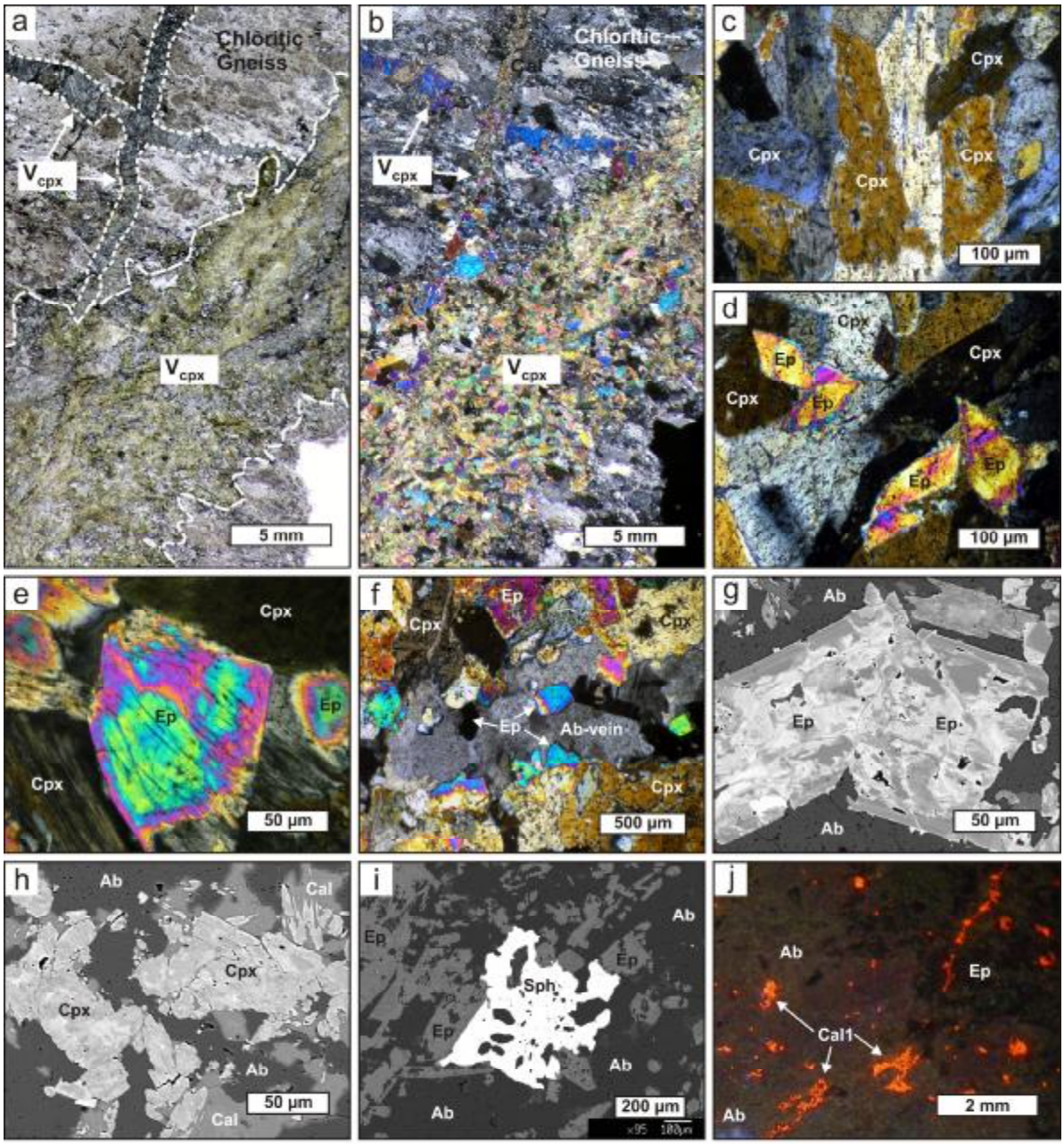

Figure 2.4. *Microscope images from V_{cpx}*

a, b) clinopyroxene veinlets are post dated by a thick clinopyroxene dominant vein (1N, +N); c) subhedral clinopyroxene crystals (+N); d) euhedral epidote crystals in subhedral clinopyroxene matrix (+N); e) epidote crystal with well developed growth zonation (+N); f) subsequent albite vein with epidote crystals on the vein walls (+N); g) epidote crystals with characteristic patchy internal zonation (BSE); h) anhedral clinopyroxene aggregates with calcite in subsequent albite vein (BSE); i) anhedral sphalerite crystal with dissolution patterns in subsequent albite vein (BSE); j) orange cathodoluminescence colour calcite in rest of the pore space

Epidote occurs as euhedral to subhedral crystals that are distributed irregularly in a matrix of clinopyroxene crystals (*Fig. 2.4/d*). Epidote crystals show a well developed growth zonation pattern with sharp crystal boundaries (*Fig. 2.4/e*). The veins were crosscut subsequently by 1–5 mm thick albite dominant veins (*Fig. 2.4/f*) containing epidote, clinopyroxene, sphalerite, and calcite vein filling minerals beside albite. Epidote is deposited directly onto the vein walls as euhedral to subhedral crystals (*Fig. 2.4/f*). Most of the crystals show significant irregular internal inhomogeneity and at some places irregular crystal boundaries (*Fig. 2.4/g*). In lesser amounts than epidote, anhedral aggregates of clinopyroxene crystals also can be found among epidote crystals and they show patchy internal inhomogeneity (*Fig. 2.4/h*). Tiny anhedral sphalerite crystals appear sporadically among pyroxene and epidote crystals (*Fig. 2.4/i*). The rest of the pore space was filled fully by bulky albite phase. Small amounts of calcite (calcite 1) occur in small irregular patches in the feldspar phase, principally around anhedral clinopyroxene (*Fig. 2.4/h,*), and this calcite phase shows an orange cathodoluminescence colour (*Fig. 2.4/j*). The paragenetic sequence of the vein type is: *cpx+ep+sph+ab+cal1*.

In the V_{fp} type, two characteristic subtypes can be distinguished. Pure albite veins with 1–2 mm maximum thickness can be found very frequently in the penetrated rock section of BC. At some places these veins contain elongated epidote and radial chlorite crystals too.

Symmetric veins with *fp-chl-cal* mineral assemblages of about 1 cm thickness give the most abundant subtype of V_{fp} (*Fig. 2.3/c, d*). In these veins euhedral albite and K-feldspar crystals grew directly on the fracture wall (*Fig. 2.5/a, b, c*). In some places the two feldspar phases contain each other as inclusions (*Fig. 2.5/d*). Both phases contain a myriad of tiny (1–2 μm) fluid and solid (muscovite, biotite) inclusions which give them a turbid appearance (*Fig. 2.5/e*). These feldspar phases are followed by a green euhedral chlorite (chlorite 1), which is made up of vermiform crystal aggregates (*Fig. 2.5/e*). Adularia-habit clear alkali feldspars occur as overgrowth on the albite-K-feldspar assemblage (*Fig. 2.5/f*) and contain a high amount of vermiform chlorite grains as inclusions (*Fig. 2.5/g*). A calcite phase occurs (*Fig. 2.5/a, c, f, h*) subsequent to chlorite, giving a bulky appearance, and frequently contains

deformation lamellas (*Fig. 2.5/h*). In the cathodoluminescence images it has a homogenous appearance with a uniform orange colour (*Fig. 2.5/i*). Similar cathodoluminescence colour can be observed in patchy calcite of V_{cpx} veins (*Fig. 2.4/j*). The paragenetic sequence of the V_{fp} type is: *ab+kfp+chl1+adu +cal1*.

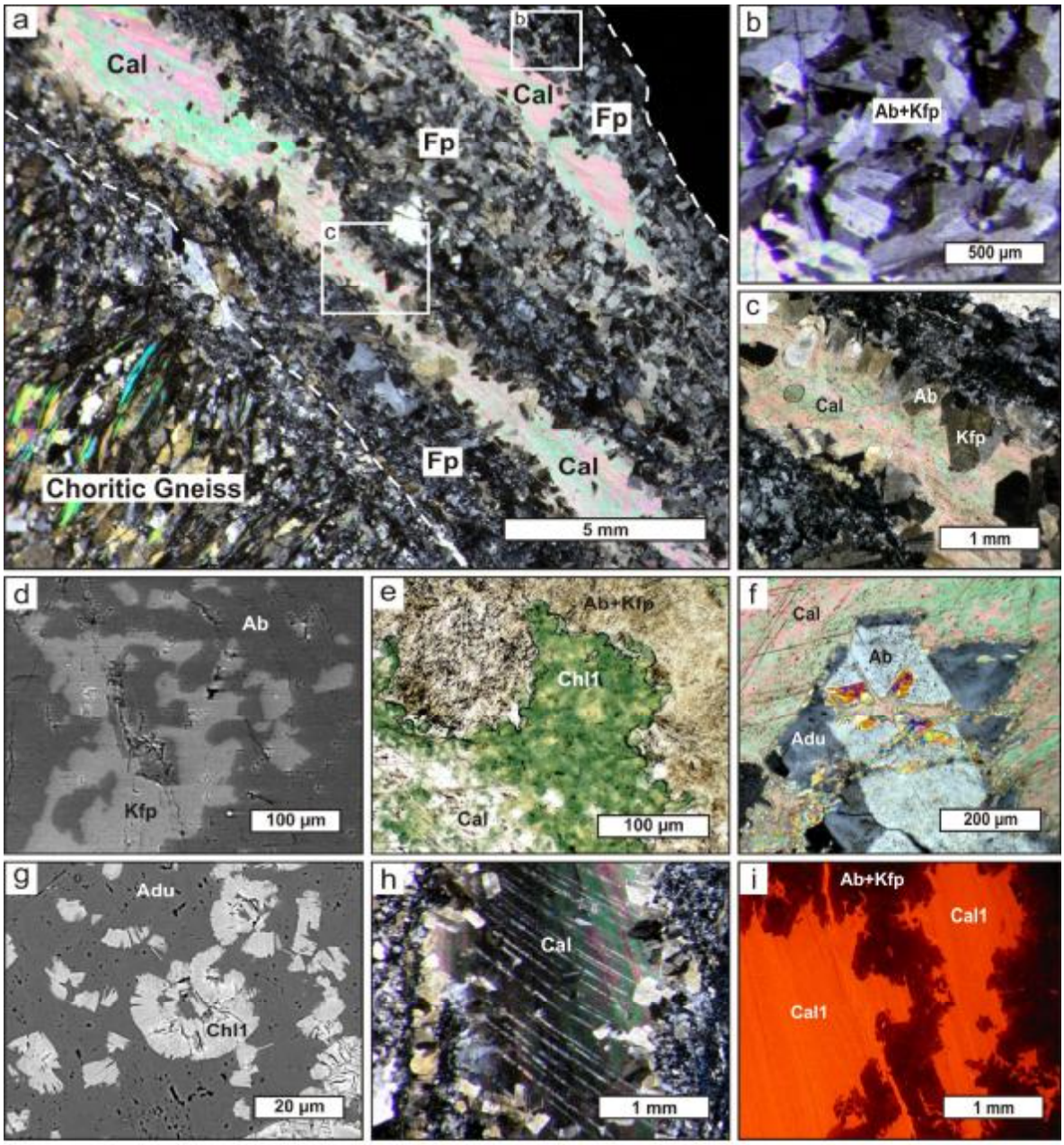

Figure 2.5. *Microscope images from V_{fp}*
a) feldspar dominant vein in chloritic gneiss with subsequent calcite phase (+N); b) assemblage of albite and K-feldspar crystals in the vein margin (+N); c) euhedral albite and K-feldspar crystals growth into the pore space filled by calcite (+N); d) occurrence of albite and K-feldspar crystals as inclusions in each other (BSE); e) green vermiform aggregate of chlorite (chl1) following feldspar assemblage (1N); f) euhedral adularia growths on euhedral albite crystal surrounded by calcite (+N); g) vermiform structured chlorite in adularia, (notice the micropores occur in adularia) (BSE); h) twin lamellae of fracture filling calcite (+N); i) orange cathodoluminescence colour calcite 1 phase with homogenous internal structure

V_{ep} makes 0.2–1.5 cm thick veins surrounded by a characteristic alteration halo which is made by 2–3 cm thick bleached selvage along the veins (*Fig. 2.3/e, f*). It is clearly identifiable that V_{ep} veins postdate V_{fp} veins based on their cross cutting relationship (*Fig. 2.6/a, b*). In the V_{ep}, epidote-clinozoisite crystals show two characteristic appearances. Euhedral crystals with characteristic growing zonation patterns are dominant (*Fig. 2.6/c*).

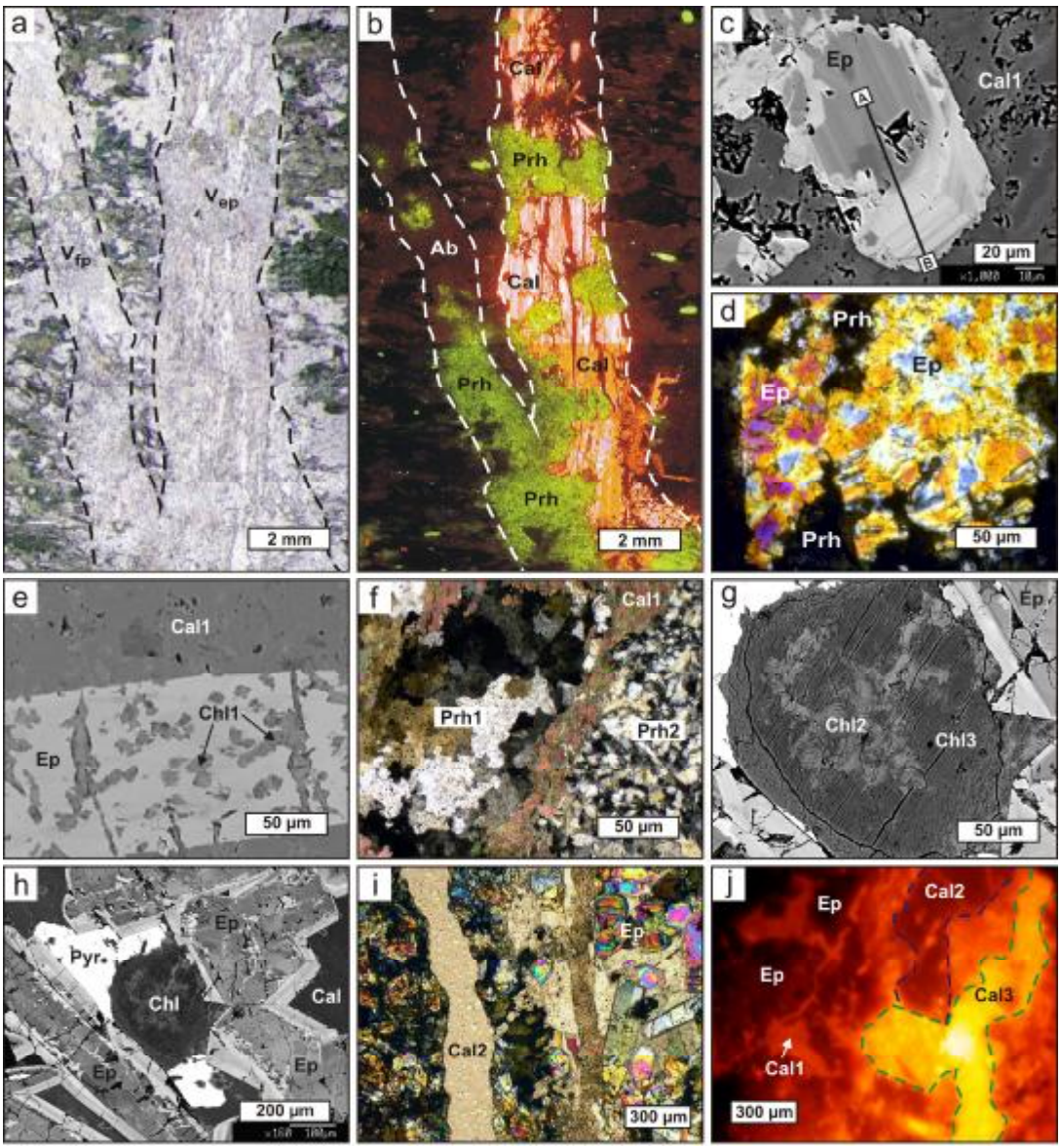

Figure 2.6. *Microscope images from V_{ep}*
a) relationship between V_{fp} and V_{ep} veins (V_{ep} postdating V_{fp}) (1N); b) cathodoluminescence image of the area on picture (a) (calcite: different shade of orange; prehnite: light green-yellow; albite: reddish brown); c) well-developed growth zonation in an epidote grain (section AB denotes the location of EMPA line-scan) (BSE); d) aggregates of anhedral epidote grains surrounded by prehnite (+N); e) chl1 phase as inclusion in an elongated epidote crystal (BSE); f) two crystallization types of prehnites, a graphic textured (left), and a very fine grained aggregate (right) (+N); g) chl2 is overgrown by chl3 among epidote (BSE); h) pyrite grains among epidote and chlorite phases (BSE);i) epidote crystals in cal1 cross cut by a cal2 vein; j) cathodoluminescence image showing calcite filling the rest of the pore space of fracture filling minerals (orange: calcite 1, deep claret: calcite 2, yellow: calcite 3)

Subordinately, epidote-clinozoisite assemblage can occur as very fine grained lamellar structured aggregates (*Fig. 2.6/d*). Both of them contain vermiform aggregates of green euhedral chlorite similar to chlorite 1 (*Fig. 2.6/e*), which can be found in V_{fp}. The anhedral epidote-clinozoisite assemblage is overgrown by prehnite which shows two different structural patterns. Tabular crystal prehnite shows irregular sub-grain boundaries (*Fig*. 2.*6/b, f*) and was overgrown by very fine grained fan shaped prehnite crystals (*Fig*. 2.*6/f*). Prehnite is totally missing from domains where euhedral epidote-clinozoisite crystals are predominant. At certain places adularia subsequent to the euhedral epidote and clinozoisite can be observed. Among the euhedral crystals, brownish radial habit chlorite (chlorite 2) (*Fig. 2.6/g*) can be found and has been overgrown by lamellar structured chlorite (chlorite 3) (*Fig. 2.6/g*). Sporadically, fine grained subhedral pyrite crystals occur subsequently to the chlorite 3 (*Fig. 2.6/*h). The remaining pore space was occupied by calcite which can be subdivided into three phases. Most of the pore spaces filled by calcite 1 (*Fig. 2.6/i*) show orange colour on the cathodoluminescence image (*Fig*. 2.*6/j*) similar to those observed in cases of V_{cpx} and V_{fp}. Calcite 2 occurs as thin veinlets cross cutting the V_{ep} subsequently (Fig. 2.6/i) or filling the rest of the pore space remaining among calcite 1. This phase (calcite 2) shows a deep brownish-red colour on the cathodoluminescence image (*Fig*. 2.*6/j*). The youngest calcite phase (calcite 3) occurs only as thin veinlets cross cutting all former vein filling mineral phases (*Fig*. 2.*6/j*). The paragenetic sequence of this vein type is: *chl1+ep+czo±prh±adu+ chl2+chl3+pyr+ cal1+cal2+cal3.*

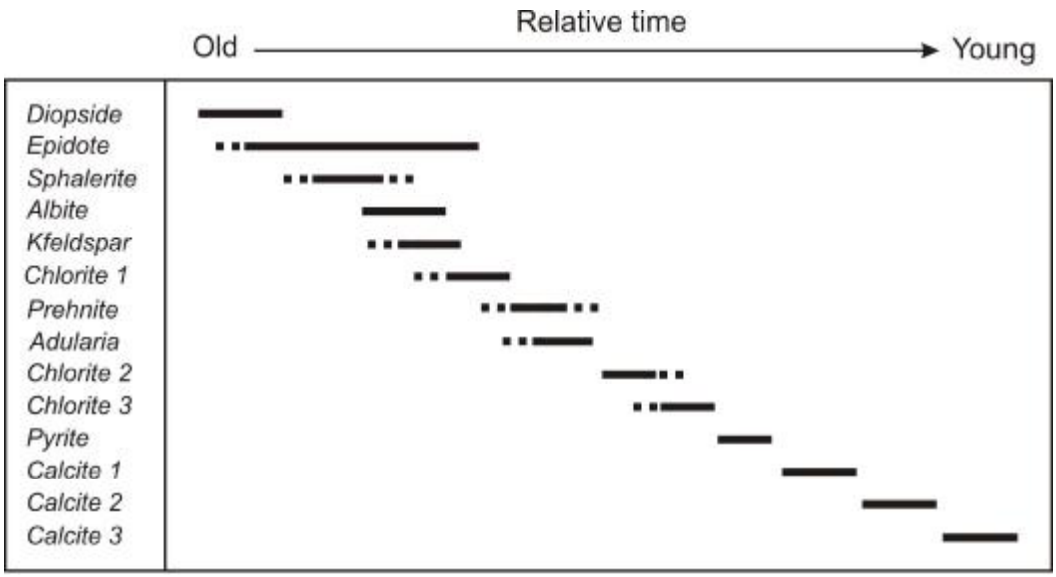

Figure 2.7. *Paragenetic sequence of the vein filling minerals*

Based on the many overlaps between the paragenetic sequences of the three vein types distinguished, the veins detailed above can be interpreted as periods of a comprehensive mineral precipitation process based on similar mineral assemblages and mineral successions. The paragenetic sequence of the vein mineralization can be seen in *Fig. 2.7*.

2.4.2. Mineral chemistry

2.4.2.1. Clinopyroxene

The composition of clinopyroxene in the veins corresponds to the diopside-hedenbergite solid-solution series with high Ca^{2+} content (*Fig. 2.8*). The X_{Mg} = Mg/(Mg + Fe_{tot} + Mn) values are between 0.48 and 0.55 in the case of subhedral pyroxenes, while in the anhedral pyroxene, aggregates in the 0.66 – 0.78 range are observable. In the anhedral pyroxene crystals, Mg- and Fe-rich domains are distinguishable.

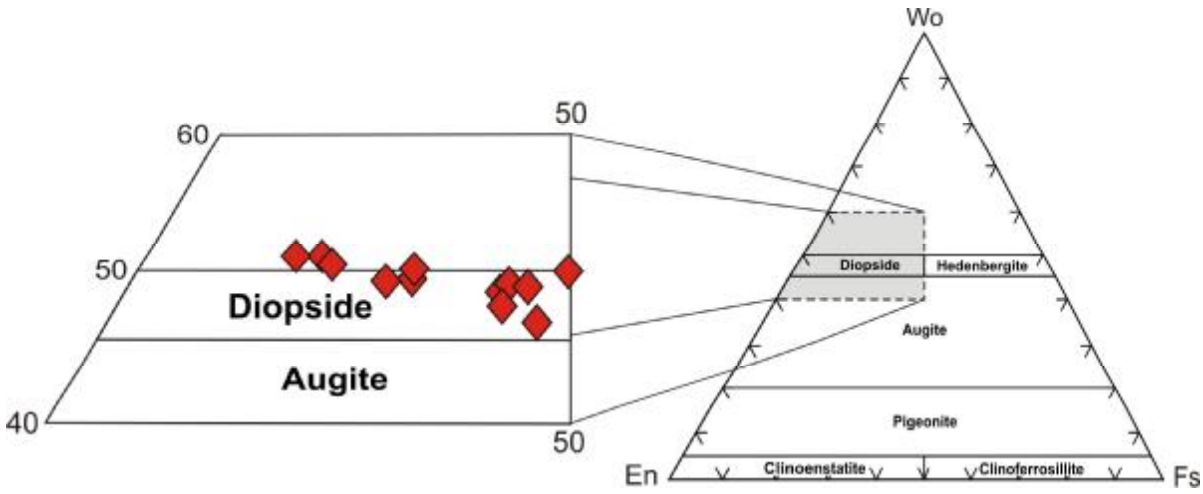

Figure 2.8. *Composition of vein filling clinopyroxenes*

2.4.2.2. Epidote/clinozoizite

The majority of the analysed grains related to epidote solid solution series and their chemical composition vary in a broad range (X_{Fe} = 0.17–0.4) (*Fig. 2.9/a; Table 2.1*). Clinozoisite occurs only in very few cases as its composition shows X_{Fe} = 0.13–0.17 variation (*Fig. 2.9/a; Table 2.1*). Growth zonation and other intracrystalline inhomogeneities in individual epidote crystals appear very frequently. This phenomenon appears characteristically in the mineral chemical data (*Table 2.1*). The observed textural patterns are caused by the difference in Al^{3+} and Fe^{3+} content on the three different octahedral sites, M1, M2, and M3, of the epidote structure. In the grains showing concentric growing zonation, an Al^{3+} rich core and an Fe^{3+} rich rim are

characteristic (*Fig. 2.9/b*). In other cases the internal inhomogeneity is caused by an irregular distribution of Al^{3+}- and Fe^{3+}-rich domains in a single grain (*Fig. 2.9/c, d, e*).

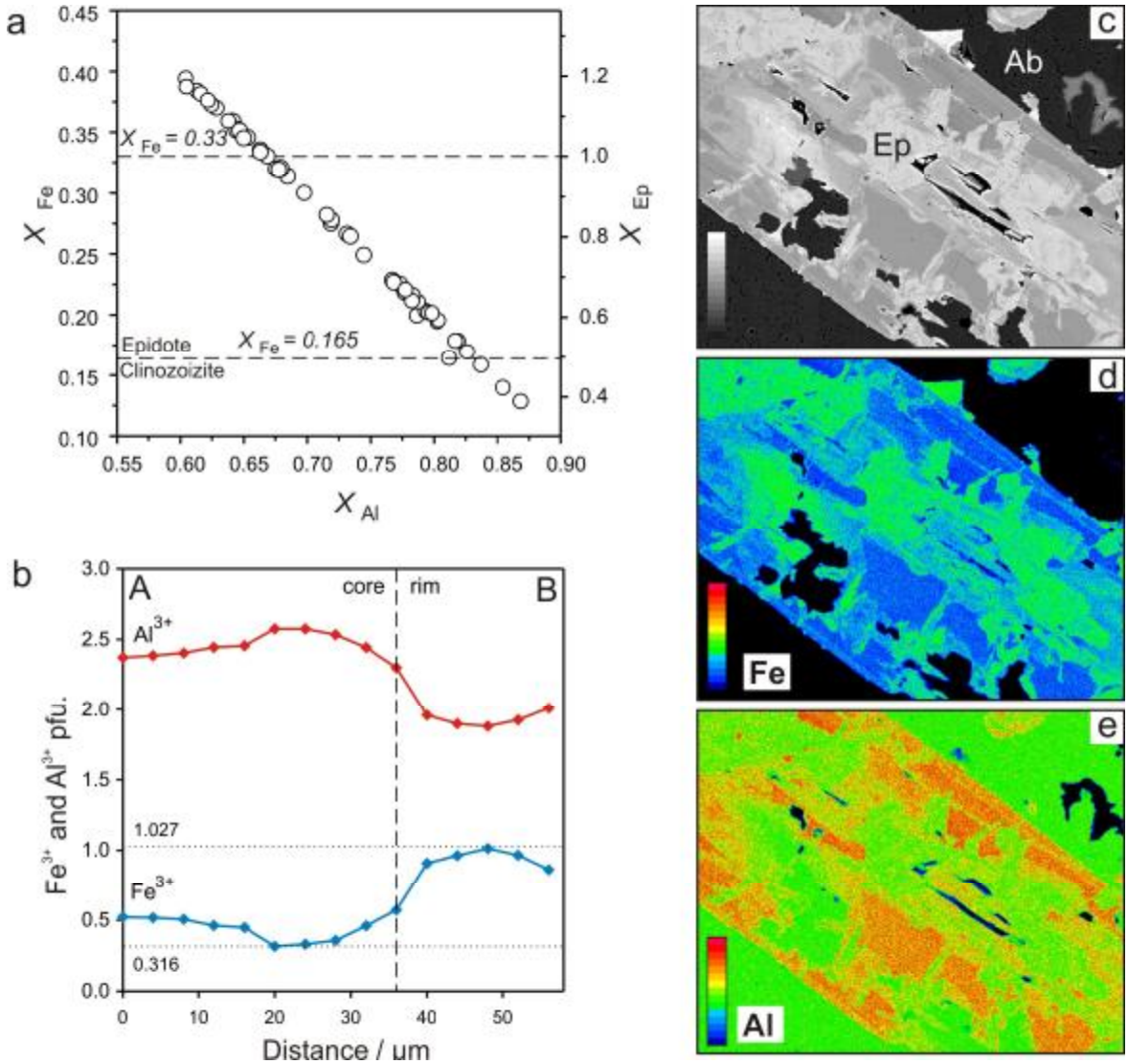

Figure 2.9. *Mineral chemistry characteristics of vein filling epidote*
a) XAl3+, XFe3+ and XEp content of the vein filling epidotes and clinozoisites; b) changing of Al3+ and Fe3+ content from core to rim in an epidote grain from V_{ep} (a BSE picture of the grain and the AB section of the line scan can be seen in Figure 6/c); c) a BSE image of an epidote crystal shows an irregular patchy internal zonation pattern; d) Fe distribution X-ray map of the epidote crystal; e) Al distribution X-ray map of the epidote crystal

Table 2.1. *Mineral chemistry data were obtained from the most characteristic epidote phases Measurements obtained from crystal cores and rims are also indicated at the heads of the columns.*

	EPIDOTES									
Oxides	702 ep9	702 ep6	699 ep16	699 ep9	637 ep4	637 ep5	519 ep11 core	519 ep6 rim	284 ep9 core	284 ep12 rim
SiO_2	39.25	37.64	36.97	39.44	38.03	39.25	40.17	37.57	39.08	38.57
TiO_2	0.05	0.00	0.00	0.05	0.03	0.08	0.12	0.11	0.09	0.00
Al_2O_3	27.99	20.67	21.77	27.99	21.68	26.31	28.85	22.63	26.15	22.06
Fe_2O_3	7.43	17.51	17.32	7.43	15.04	8.17	4.60	14.89	8.30	13.47
MnO	0.25	0.15	0.05	0.25	0.00	0.13	0.21	0.03	0.14	0.17
CaO	23.47	22.20	22.83	23.47	23.30	23.32	24.20	22.77	24.10	23.56
Na_2O	0.07	0.00	0.00	0.07	0.08	0.00	0.00	0.00	0.01	0.01
Total	98.51	98.17	98.94	98.70	98.17	98.15	98.18	98.00	97.90	97.87
Structural formula on a basis of 12.5 oxygen pfu										
Si^{IV}	3.014	2.984	2.913	3.014	3.004	3.057	3.073	2.961	3.036	3.043
Al^{IV}	0.000	0.016	0.087	0.000	0.000	0.000	0.000	0.039	0.000	0.000
T-site	3.014	3.000	3.000	3.014	3.004	3.057	3.073	3.000	3.036	3.043
Al^{VI}	2.533	1.915	1.934	2.533	2.018	2.415	2.601	2.064	2.395	2.051
Fe^{3+}	0.474	1.158	1.139	0.474	0.991	0.532	0.294	0.979	0.539	0.889
Mn^{3+}	0.000	0.000	0.000	0.000	0.000	0.000	0.000	0.000	0.000	0.000
Ti	0.003	0.000	0.000	0.003	0.002	0.005	0.007	0.006	0.005	0.000
Fe^{2+}	0.002	0.001	0.001	0.002	0.001	0.000	0.000	0.002	0.000	0.000
Mn^{2+}	0.008	0.005	0.001	0.008	0.000	0.008	0.013	0.007	0.008	0.010
M-site	3.020	3.079	3.076	3.020	3.012	2.960	2.915	3.058	2.947	2.950
Mn^{3+}	0.000	0.000	0.000	0.000	0.000	0.000	0.000	0.000	0.000	0.000
Mn^{2+}	0.008	0.005	0.002	0.008	0.000	0.001	0.001	0.008	0.001	0.001
Fe^{2+}	0.001	0.001	0.001	0.001	0.001	0.000	0.000	0.001	0.000	0.000
Ca	1.931	1.885	1.927	1.931	1.972	1.946	1.983	1.923	2.006	1.992
Na	0.010	0.000	0.000	0.010	0.000	0.000	0.000	0.000	0.002	0.002
A-site	1.950	1.891	1.930	1.950	1.973	1.947	1.984	1.932	2.009	1.994
O	12.000	12.000	12.000	12.000	12.000	12.000	12.000	12.000	12.000	12.000
OH	0.997	0.998	0.998	0.997	0.998	1.000	1.000	0.997	1.000	1.000
Total	20.981	20.968	21.004	20.981	20.986	20.964	20.972	20.987	20.992	20.988
X_{Fe}	0.16	0.38	0.37	0.16	0.33	0.18	0.10	0.32	0.18	0.30
X_{Ep}	0.47	1.16	1.06	0.47	0.99	0.53	0.32	0.97	0.57	0.94
X_{Al}	0.84	0.62	0.63	0.84	0.67	0.82	0.89	0.68	0.81	0.70

2.4.2.3. Feldspar

Analyzed feldspars are very close to pure albite and orthoclase endmember compostition (*Fig. 2.10/a*). Albite which occurs cogenetically with K-feldspar shows a low anorthite content ($Or_{0.1–1.2}\,Ab_{98.5–99.8}\,An_{0.0–0.4}$) (*Fig. 2.10/b; Table 2.2*) while K-feldspar that is cogenetic with albite shows an almost pure orthoclase composition ($Or_{97.7–99.0}\ \ Ab_{1.1–2.2}\ \ An_{0.0–0.15}$) (*Fig. 2.10/c; Table 2.2*) with very low anorthite content. Albite occurring in pure albite veins shows the highest anorthite content ($Or_{0.2–0.6}\,Ab_{97.9–99.6}\,An_{0.2–1.5}$) (*Fig. 2.10/b; Table 2.2*). The composition of adularia ($Or_{97.5–98.9}\ \ Ab_{1.1–2.1}\ \ An_{0.0–0.4}$) (*Fig. 2.10/d; Table 2.2*) exhibits a little anorthite contamination.

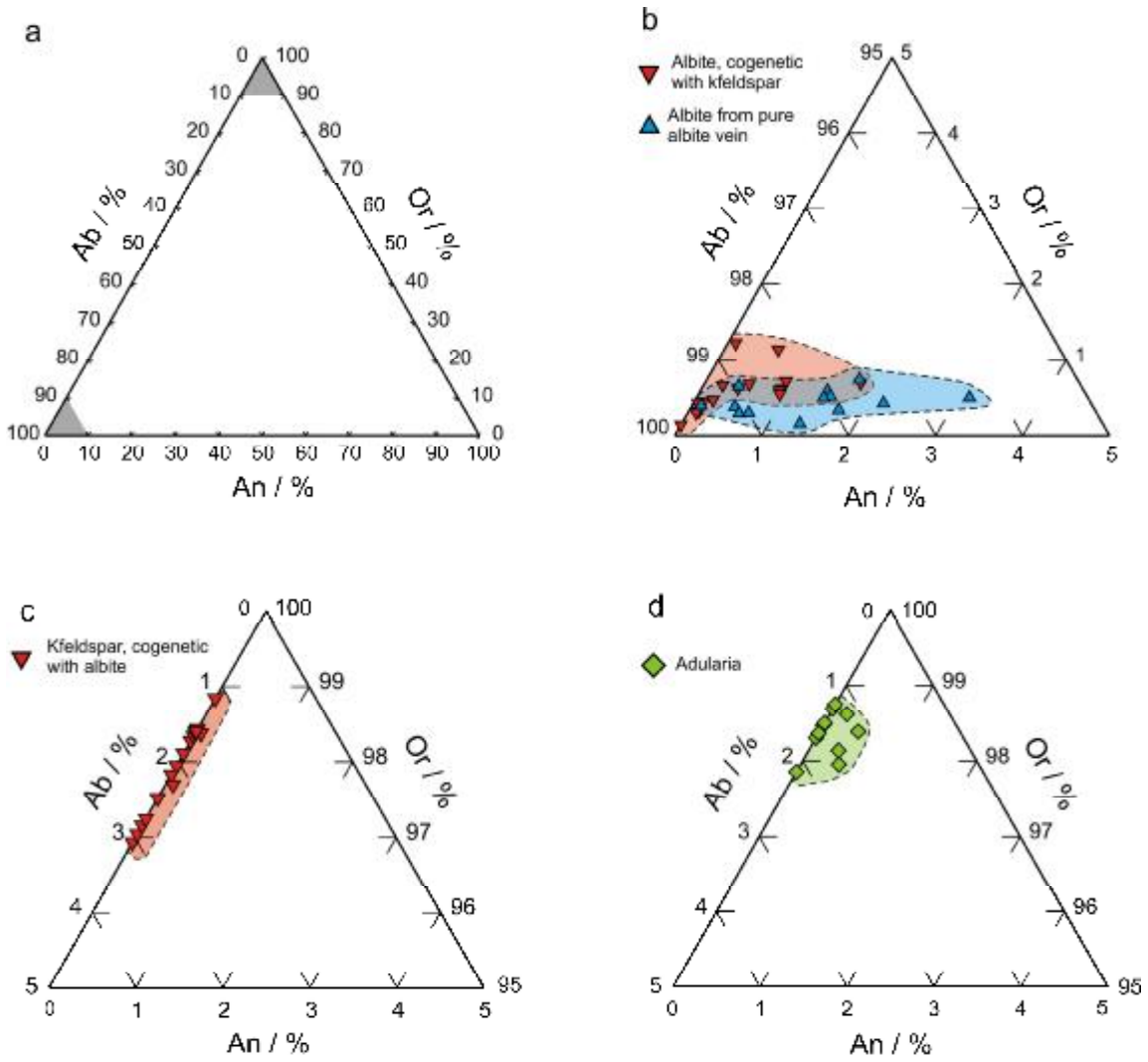

Figure 2.10. *Ab-Or-An ternary diagram of feldspars*
a) compositional field of analyses are designated by grey shaded triangles; b) composition of the vein filling albites (a red triangle represents albite growth cogenetic with K-feldspar, a blue triangle represents albite from albite veins); c) composition of K-feldspar crystallized cogenetically with albite; d) composition of adularia

Table 2.2. *Mineral chemistry data were obtained from the most characteristic feldspar phases Column heading titles are marked with asterisks (*) and refer to feldspar phases that are cogenetic with each other.*

	FELDSPARS								
Oxides	702 ab1	699 ab1	637 ab3	*870 ab1	*870 kfp1	*372 ab1	*372 kfp1	870 adu1	372 adu5
SiO_2	69.72	69.65	69.75	68.98	65.23	67.13	63.30	65.33	62.25
TiO_2	0.09	0.03	0.08	0.00	0.00	0.04	0.04	0.04	0.00
Al_2O_3	19.03	18.90	18.93	19.78	17.92	20.41	19.32	17.09	20.55
FeO	0.03	0.07	0.26	0.04	0.00	0.12	0.12	0.03	0.07
MnO	0.08	0.03	0.03	0.00	0.00	0.00	0.00	0.05	0.00
MgO	0.02	0.00	0.00	0.00	0.00	0.00	0.00	0.01	0.00
CaO	0.33	0.10	0.43	0.02	0.00	0.08	0.00	0.09	0.00
Na_2O	10.45	10.96	10.58	11.08	0.26	11.15	0.33	0.19	0.32
K_2O	0.06	0.06	0.07	0.05	15.53	0.11	15.96	16.75	16.01
BaO	0.00	0.00	0.00	0.00	0.21	0.00	0.00	0.00	0.00
Total	99.81	99.80	100.13	99.96	99.15	99.04	99.07	99.58	99.20
Structural formula on a basis of 8 oxygen pfu.									
Si	2.970	2.971	2.967	2.938	2.963	2.959	2.954	3.039	2.905
Ti	0.003	0.001	0.003	0.000	0.000	0.001	0.001	0.001	0.000
Al	1.041	1.035	1.034	1.081	1.045	1.061	1.063	0.937	1.130
Fe	0.001	0.003	0.010	0.002	0.000	0.004	0.005	0.001	0.003
Mn	0.003	0.001	0.001	0.000	0.000	0.000	0.000	0.002	0.000
Mg	0.001	0.000	0.000	0.000	0.000	0.000	0.000	0.001	0.001
Ca	0.016	0.005	0.021	0.001	0.000	0.004	0.000	0.004	0.000
Na	0.940	0.987	0.950	0.997	0.025	0.953	0.030	0.017	0.029
K	0.003	0.004	0.004	0.003	0.980	0.006	0.950	0.994	0.953
Ba	0.000	0.000	0.000	0.000	0.004	0.000	0.000	0.000	0.000
Total	4.979	5.006	4.991	5.022	5.017	4.989	5.003	4.997	5.021
Endmember composition									
X_{Ab}	0.979	0.991	0.974	0.996	0.025	0.990	0.031	0.017	0.030
X_{Or}	0.017	0.005	0.022	0.003	0.975	0.006	0.969	0.979	0.970
X_{An}	0.003	0.004	0.004	0.001	0.000	0.004	0.000	0.004	0.000

2.4.2.4. Chlorite

The analysed chlorites related to the tri-trioctahedral chlorites based on the procedure by ZANE & WEISS (1998). If we represent the Mg, Al, and Fe content of the chlorites in an X_{Mg}–X_{Al}–X_{Fe} ternary diagram it appears that each chlorite is in the lower part of the triangle (*Fig. 2.11/a*), which means that they are low Al containing type I chlorites ($X_{Mg}+X_{Fe} < X_{Al}+X_{\square}$, where X is the number of atoms per formula unit – pfu). In chlorite 1 the Fe/(Fe + Mg) is in the 0.42–0.63 range, while in contrast 0.32–0.45 values are observable in chlorite 2 and 0.34–0.40 values can be seen in chlorite 3. In the Al^{IV} plotted against the Fe/(Fe + Mg) diagram (*Fig. 2.11/b*) it can be seen that Al^{IV} increases with increasing Fe/(Fe + Mg) ratios. The Al^{IV} varies from 1.99 to 2.66 in chlorite 1 while it shows values of 1.78–2.14 in chlorite 2 and 1.17–1.44 in the case of chlorite 3. The Al^{VI} shows values of 1.68–3.16 in chlorite 1, while 1.92–2.33 intervals can be observed in chlorite 2 and 1.84–2.24 in chlorite 3.

The Al^{VI}/Al^{IV} ratios are close to unity in the cases of chlorite 1 and chlorite 2 (*Fig. 2.11/c*); however Al^{VI}/Al^{IV} values are much higher than unity in the case of chlorite 3 (*Fig. 2.11/c*). Classification of the three chlorites is based on the nomenclature of BAILEY (1980) according to the dominant divalent octahedral cation present. Thus chlorite 1 is chamosite due to its high Fe content, while chlorite 2 and chlorite 3 are designated as clinochlore due to their higher X_{Mg}. Mineral chemical measurements were carried out from crystal cores and rims in cases of chlorite 1 and chlorite 2 and the results indicate a decreasing Al^{IV} content from core to rim in each of the measured crystals (*Table 2.3*).

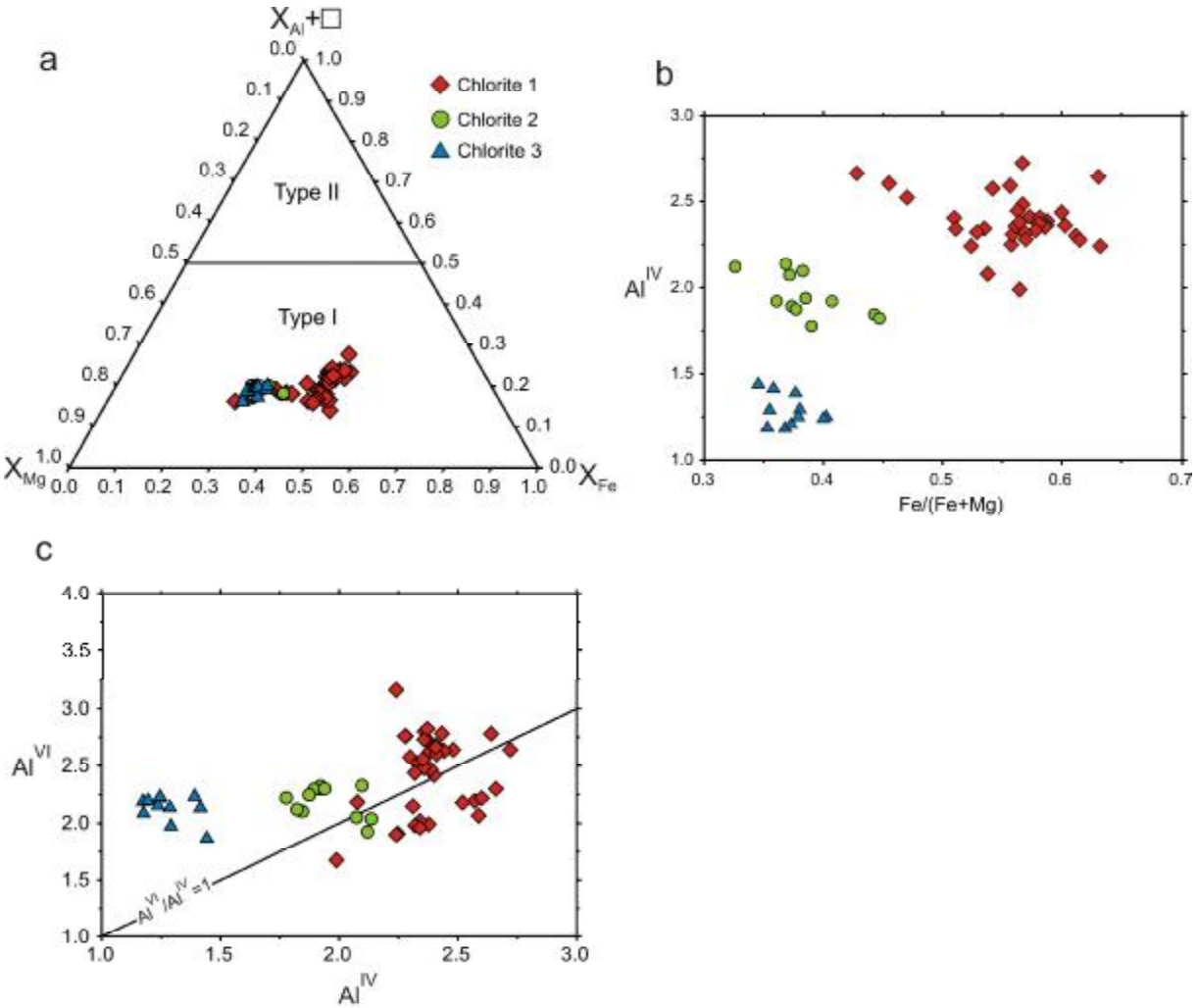

Figure 2.11. *Composition diagrams of the distinguished vein filling chlorite types*
a) localization of the three chlorites in the representation triangle of the compositional fields of type I and type II chlorites; b) plot of Al(IV) contents vs Fe/(Fe + Mg) ratios of chlorites; c) plot of Al(VI) vs Al(IV) contents of chlorites.

Table 2.3. *Mineral chemistry data were obtained from the most characteristic chlorite phases Measurements made from crystal cores and rims are also indicated in the column headings.*

	CHLORITES									
Oxides	870 chl6 core	870 chl4 rim	702 chl3	702 chl7	372 chl3 core	372 chl2 rim	519 chl1 core	519 chl6 rim	284 chl2	284 chl7
SiO_2	24.95	27.14	26.11	27.18	26.11	28.04	29.29	29.91	33.31	34.19
TiO_2	0.05	0.00	0.02	0.05	0.02	0.00	0.11	0.01	0.00	0.00
Al_2O_3	21.33	21.60	18.98	16.60	17.07	14.43	17.04	17.64	15.14	14.16
FeO	31.95	29.45	26.29	29.77	30.37	31.52	18.85	22.12	19.98	19.63
MnO	0.10	0.17	0.44	0.44	0.53	0.72	0.47	0.66	0.19	0.18
MgO	10.47	9.56	16.67	15.14	13.54	13.93	22.35	18.07	20.16	18.95
CaO	0.04	0.33	0.40	0.64	0.28	0.57	0.67	0.09	0.27	0.48
Na_2O	0.00	0.00	0.00	0.00	0.20	0.00	0.00	0.04	0.00	0.03
K_2O	0.12	0.15	0.00	0.00	0.01	0.04	0.03	0.03	0.03	0.02
Total	89.00	88.41	88.92	89.82	88.12	89.25	88.81	88.56	89.08	87.64
	Structural formula on a basis of 28 oxygen pfu.									
Si	5.360	5.760	5.480	5.760	5.622	6.011	5.881	6.079	6.584	6.826
Al^{IV}	2.640	2.240	2.520	2.240	2.378	1.989	2.119	1.921	1.416	1.174
T-site	8.000	8.000	8.000	8.000	8.000	8.000	8.000	8.000	8.000	8.000
Al^{VI}	2.780	3.160	2.180	1.900	1.991	1.676	1.924	2.324	2.137	2.193
Ti	0.000	0.000	0.000	0.000	0.003	0.000	0.017	0.002	0.000	0.000
Fe^{+3}	0.000	0.000	0.060	0.180	0.000	0.000	0.000	0.217	0.403	0.567
Fe^{+2}	5.740	5.220	4.560	5.080	5.655	5.783	3.234	3.544	2.900	2.711
Mn	0.020	0.040	0.080	0.080	0.097	0.131	0.080	0.113	0.032	0.030
Mg	3.360	3.020	5.220	4.780	4.346	4.452	6.690	5.475	5.940	5.640
Ca	0.000	0.080	0.080	0.140	0.065	0.131	0.144	0.019	0.057	0.103
Na	0.000	0.000	0.000	0.000	0.167	0.000	0.000	0.031	0.000	0.023
K	0.040	0.040	0.000	0.000	0.005	0.022	0.015	0.014	0.015	0.010
O-site	11.940	11.560	12.180	12.160	12.329	12.194	12.104	11.738	11.485	11.277
OH	16.000	16.000	16.000	16.000	16.000	16.000	16.000	16.000	16.000	16.000
Total	35.940	35.560	36.180	36.160	36.329	36.194	36.104	35.738	35.485	35.277
X_{Fe}	0.481	0.452	0.379	0.433	0.459	0.474	0.267	0.320	0.288	0.291
X_{Mg}	0.281	0.261	0.429	0.393	0.353	0.365	0.553	0.466	0.517	0.500
X_{Al}	0.233	0.273	0.179	0.156	0.161	0.137	0.159	0.198	0.186	0.194
Fe/(Fe+Mg)	0.631	0.633	0.470	0.524	0.423	0.565	0.326	0.407	0.357	0.368

2.4.2.5. Prehnite

The composition of prehnite in the veins does not show any significant variation except a minor difference in Fe^{3+} content (X_{Fe} = 0.01–0.13), which can substitute alumina on the octahedral site of the prehnite crystal structure. The enrichment of iron content is not detectable in prehnite crystals located near to epidote crystals.

2.4.2.6. Pyrite

Thirty-three pyrite analyses were made from different pyrite crystals from the Ca-Al silicate veins. In order to compare this pyrite phase to those that can be found in the polymetallic vein investigated by TARNAI (1998), measurements (25) were made from this phase also. Samples were analysed for S, Fe, Cu, As, Mn, Zn, Cd, Co, and Ni and the representative analyses are presented in *Table 2.4*. A similar chemical composition is observable in the two pyrite phases

(*Table 2.4*). The Mn, Zn, and Cd contents of pyrite were below the detection limit of the microprobe except in the case of Zn, where few measurements are in the 940–1170 ppm range. The concentration of these elements is most probably very low in the investigated pyrite crystals. Pyrite grains show significant As content that varies between 2020 and 6360 ppm, while their Cu content is in the 680–3380 ppm range in Ca-Al silicate veins but mostly below detectability in polymetallic veins (*Table 2.4*). The Ni content is very low and its values vary in the 390–920 ppm range. Pyrites contain a much higher content of Co than Ni; the amount of Co is in a broad range of 460–3610 ppm but most of the data exceed 1000 ppm.

Table 2.4. *Mineral chemistry data were obtained from the most characteristic pyrites from the Ca-Al-silicate- and the sulfide veins*

PYRITES														
	Ca-Al-Silicate veins							Sulfide veins						
Elements	284 pyr1	284 pyr2	284 pyr3	284 pyr4	284 pyr8	284 pyr9	284 pyr10	362 pyr1	362 pyr3	362 pyr4	362 pyr6	362 pyr7	362 pyr12	362 pyr13
Fe	46.78	44.92	46.84	46.75	46.97	46.65	46.30	47.55	47.59	46.89	47.71	47.54	47.36	47.25
S	52.23	52.56	52.19	52.29	52.62	52.49	52.16	52.50	52.05	52.20	52.76	52.93	52.50	52.30
Trace elements in ppm														
Co	1470	3610	1670	1270	850	1310	660	400	1380	2420	980	1480	670	730
Ni	920	730	390	250	850	810	390	480	670	530	440	760	740	550
As	1580	1310	0	1670	0	1740	2830	330	730	1050	0	720	0	0
Cu	200	1750	3380	1430	680	680	0	910	0	40	0	0	0	0
Zn	940	0	10	110	0	610	1170	1680	0	410	0	0	0	250
Cd	0	0	0	0	0	0	0	0	0	0	0	0	0	0
Mn	0	0	640	0	690	0	900	0	920	10	0	470	610	0
Total	99.52	98.22	99.64	99.52	99.89	99.65	99.05	100.43	100.01	99.53	100.61	100.80	100.06	99.70
Co/Ni	1.6	4.9	4.3	5.1	1.0	1.6	1.7	0.8	2.1	4.6	2.2	1.9	0.9	1.3

2.4.3. Stable isotope geochemistry

Only in the case of the calcite 1 phase from the carbonate phases was it possible to separate material sufficiently for analysis. The preceding cathodoluminescence study of carbonate phases indicated that a considerable amount of homogenous calcite suitable for sampling by micro drilling occurs in calcite 1. Five measurements were made from calcite 1 at three different depth levels of the bore hole. Data summarized in *Table 2.5* show that $\delta^{13}C$ (V-PDB) values are in the range –4.9 to –8.2‰ while $\delta^{18}O$ (V-SMOW) values are in the range 7–10.8‰ in all fracture filling calcite 1 phase.

Table 2.5. *Stable isotope values of calcite 1*

Detph / m	$\delta^{13}C$ (V-PDB)	$\delta^{18}O$ (V-SMOW)
208.4	-8.2	8.8
	-8.0	7.1
679.7	-4.9	9.7
733.1	-6.3	10.8
	-6.3	7.0

2.4.4. Geothermometry

2.4.4.1. Two feldspars thermometry

The cogenetic alkali and plagioclase feldspars offer the opportunity to determine the approximate temperature range of formation of feldspar assemblages. We applied two thermometry methods to determine the formation temperature of feldspars. The binary methods (WHITNEY & STORMER 1977) are based on the alkali feldspar (Ab-Or) binary (ORVILLE 1963; BACHINSKY & MÜLLER 1971), while ternary methods (NEKVASIL & BURNHAM 1987) work with a ternary solvus (SECK 1971), where An-content is also taken into account. In our case the mineral chemistry dataset indicates crystallization under low *P-T* parameters. The most relevant binary thermometer for these conditions is related to WHITNEY & STORMER (1977). This thermometric calculation is based on microcline-low-albite solvus was determined by BACHINSKY & MÜLLER (1971) and is valid in systems with conditions below 400 °C. Temperatures of about 296 ± 33 °C are calculated by this method at 5, 50, 100, 150, 200 MPa pressure conditions. We used the program SOLVCALC 2.0 (WEN & NEKVASIL 1994) to calculate temperatures in ternary systems. We applied thermometers according to NEKVASIL & BURNHAM (1987) at 5, 50, 100, 150, 200 MPa pressure conditions to obtain estimates of temperature. Values are around 283 ± 53 °C (15 cases), which is a broader range than in the case of a binary model. Lower values occurred in only one case (~180 °C), where considerable differences were observable between concordant temperatures at the same pressure (188–281 °C/150 MPa). Obtaining appraisable values was not successful in the case of one feldspar pair.

2.4.4.2. Chlorite geothermometry

A chlorite solid-solution geothermometer was proposed by CATHELINEAU & NIEVA (1985), based on a systematic investigation of the relation between chlorite composition and temperature in the Los Azufres geothermal system (Mexico). In this empirical approach, they noted that Al^{IV} is strongly correlated with the precipitation temperature, following a linear relation. The Al^{IV} content depends not only on the temperature but also on the Fe/(Fe + Mg) ratio, as noted by many authors (HEY 1954; FOSTER 1962; MCLEOD & STANDON 1984). In the newer geothermometers the Fe/(Fe + Mg) ratio is also taken into consideration to correct the Al^{IV} content of the chlorites. During thermometry calculation we did not take into consideration analyses where total CaO, Na_2O, and K_2O contents exceeded 0.5 wt%. With this consideration, 41 analyses (29 from chlorite 1, 9 from chlorite 2, and 7 from chlorite 3)

were used to estimate the temperature range. Thermometric calculation based on the considerations of ZHANG & FYFE (1995) was used to evaluate the precipitation temperature of chlorites. The calculated formation temperatures are 260 ± 32 °C in the case of chlorite 1, 222 ± 20 °C for chlorite 2, and 154 ± 13 °C for chlorite 3 (*Fig. 2.12*).

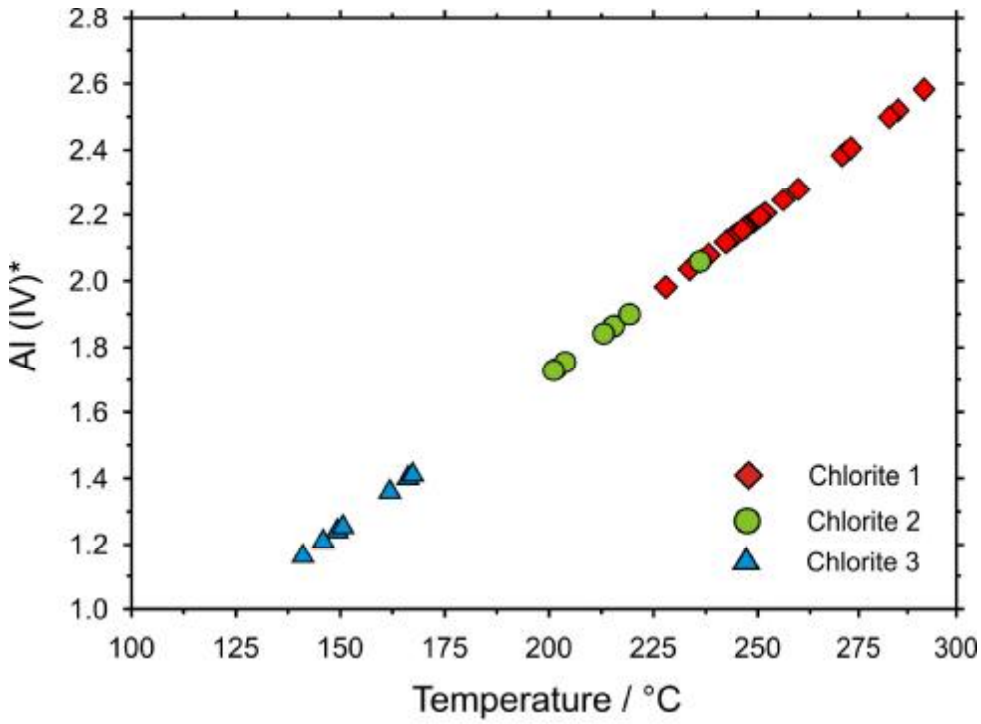

Figure 2.12. *Calculated crystallization temperatures of different chlorite types (thermometer: Zhang & Fyfe (1995); Al^{IV}* refers to the tetrahedral alumina content corrected after Zhang & Fyfe (1995))*

2.4.5. Fluid inclusion study

2.4.5.1. Fluid inclusion petrography

The fluid inclusion study was made of diopside, epidote, and calcite host minerals of the Ca-Al-silicate dominant veins. Each mentioned phase contains primary pseudosecondary and secondary aqueous fluid inclusion assemblages. Secondary and pseudosecondary assemblages occur very rarely in the studied host minerals. They are located along trails and contain one liquid phase; most of their inclusions are in the sub-micrometer size range, and hence they are inappropriate for further analysis. Definitive evidence for the primary origin of fluid inclusions is the occurrence of inclusions along growth zones (GOLDSTEIN & REYNOLDS 1994; BODNAR 2003). Less conclusive is the occurrence of one or a few inclusions in the interiors of minerals, as is the case for most inclusions in this study. Even if the inclusions are not primary, we can determine their relative timing in the overall fracture-filling evolution of the

veins based on mineral paragenetic succession (*Fig. 2.13/a*). Combining information related to the timing of mineral precipitation in veins with types of fluid inclusions contained in minerals from different stages of the mineral precipitation process has been used successfully by other researchers to determine fluid evolution (BEANE & TITLEY 1981; PREECE & BEANE 1982; BEANE & BODNAR 1995; FALL et al. 2007).

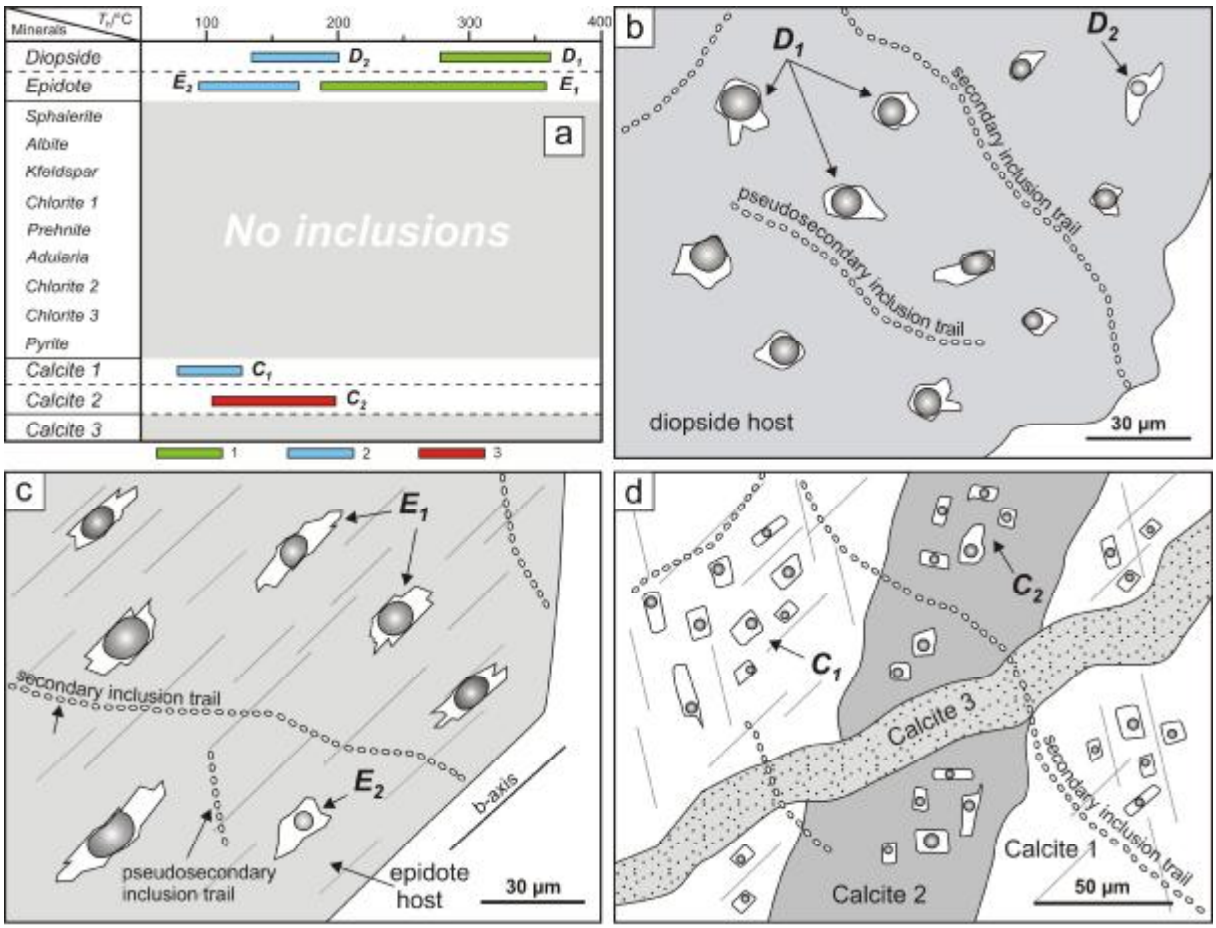

Figure 2.13. *Results of fluid inclusion petrography in the investigated host minerals*
a) Distribution of the different fluid types in the investigated host minerals. 1: refers to D_1 and E_1 fluids; 2: refers to D_2, E_2, and C_2 fluids; 3: refers to C_2 fluid type; b) characteristic distribution of the different fluid inclusion types in the diopside host crystal; c) distribution of the different fluid inclusion types in the epidote host mineral; d) distribution of the different fluid inclusion types in the calcite 1 and calcite 2 host mineral phases.

Diopside

Each inclusion deemed primary in diopside contains two phases, a vapour and a liquid (L + V), and shows liquid dominancy (*Fig. 2.13/b; 2.14/a, b, c*). They occur randomly or in small clusters in the crystals. Their sizes vary between 5 and 40 µm (*Fig. 2.13/b; 2.14/a, b, c*). In certain inclusions the negative crystal shape is dominant, while in other cases a combination of irregular shape with negative crystal geometry can be observed (*Fig. 2.14/a, b*). The

majority of the inclusions show φ_{vap}: 0.3–0.5 values (designated D_1 in *Fig. 2.13/a, b; 2.14/a,b*) while in some cases inclusions with lower values of φ_{vap}: 0.1–0.2 (designated D_2 on *Fig. 2.13/a, b*) can also be found (*Fig. 2.13/b; 14/a, c*).

Figure 2.14. *Representative fluid inclusion types of the vein filling minerals*
a) D1 type irregular shape fluid inclusion in diopside; b) close to negative crystal shaped D1 inclusions in diopside; c) D2 type fluid inclusion from diopside at room temperature and during reheating after freezing procedure; d, e) elongated rod shaped E1 type fluid inclusions in epidote (note the different fluid-vapour ratio); f) irregularly shaped isolated single E1 inclusion in epidote; g) E2 type fluid inclusion in epidote; g) negative crystal shape C1 inclusions in calcite 1; h) negative crystal shape C1 fluid inclusion assemblage in calcite 1;i) C1 type fluid inclusion from calcite 1 at room temperature j) C1 type fluid inclusion in calcite 1 during reheating after freezing (containing ice + hydrohalite crystals); j) small cluster of C2 type fluid inclusions from calcite 2; l) negative crystal shaped C2 fluid inclusion (note the higher vapour fraction).

Rarely, pseudosecondary and secondary inclusion trails can be observed containing inclusions of sub-micrometer size (*Fig. 2.13/b*).

Epidote

In epidote three characteristic fluid inclusion groups can be observed. Elongated, close to rod shaped inclusions, always parallel with the *b* crystallographic axis of epidote crystal, form the most frequent type (*Fig. 2.13/c; 2.14/d, e*). They contain two-phase liquid and vapour (L + V) liquid dominant inclusions with their longest dimension having a 5–35 μm range (*Fig. 2.13/c; 2.14/d, e*). Irregularly shaped single inclusions also occur in several places in the crystals, but in lesser amounts than the former ones (*Fig. 2.14/f*). Their longest dimensions vary in the 15–35 μm range and each of them are liquid dominant and show L + V character at room temperature (*Fig. 2.13/c; 2.14/d, e, f*). These inclusions are considered to be primary based on their distribution within crystals (BODNAR 2003). Their volume fraction varies in a very broad range between values of φ_{vap}: 0.3 and 0.5 (designated E_1 in *Fig. 2.13/a, c; 2.14/d, e, f*), while a smaller group occurs in the range φ_{vap}: 0.1–0.2 (designated E_2 in *Fig. 2.13/a, c; 2.14/g*). The third fluid inclusion class can be seen in epidote appearing as trails of minor sized (< 1 μm) one-phase liquid (L) inclusions considered to be secondary in origin and occurring very rarely in the crystals (*Fig. 2.13/c*).

Calcite phases

Only the calcite 1 and calcite 2 phases contain fluid inclusions available for microthermometric analysis; calcite 3 is almost free of fluid inclusions but in some domains sub-micrometer sized fluid inclusions can be found (*Fig. 2.13/d*). Inclusions in calcite 1 are grouped in 3D clusters, which show almost uniform extension into the three directions of space and can be found in random domains of the host calcite 1 phase (designated C_1 in *Fig. 2.13/a, d*). These clusters contain close to negative crystal shaped two-phase (L + V) liquid dominant inclusions (*Fig. 2.13/d; 2.14/h, i*) where the φ_{vap} values are below 0.1. The longest dimensions of the individual inclusions are in the 5–15 μm range. Based on their distribution this fluid inclusion assemblage is considered primary in origin (BODNAR 2003). In the calcite 2 fluid inclusions a similar distribution can be observed in the case of calcite 1 (designated C_2 in *Fig. 2.13/a, d; 2.14/k*). Two phase (L + V) liquid dominant negative crystal shaped inclusions (*Fig. 2.14/k*) arranged in equidimensional clusters can be found in different parts of the host calcite 2, and their longest dimensions vary between 5 and 20 μm (*Fig. 2.13/d; 2.14/k*). The φ_{vap} values are in a short range of ~0.1. Based on their distribution within the

host mineral these inclusions are most probably primary in origin. Fluid inclusions typified as secondary occur very rarely in each calcite phase; they are arranged along trails and contain sub-micrometer sized one-phase (L) fluid inclusions (*Fig. 2.13/d*).

2.4.5.2. Microthermometry and Raman spectroscopy

Diopside

Both the liquid and the vapour phases were analysed by Raman micro spectroscopy at T_{lab} in primary (D_1, and D_2) inclusions. No gases (such as CO_2, CH_4, O_2, N_2, and H_2) were detected in either the vapour bubbles or the liquid phase. The observed characteristics indicate that the fluid captured in these inclusions is a pure aqueous-electrolyte solution. During freezing of D_1 inclusions, ice nucleation (T_n (Ice)) occurred between –36 and –34 °C (*Table 2.6*). Initial ice melting temperatures (T_i) could not be detected during reheating of the inclusions; therefore the salt composition of the inclusion fluid could not be determined exactly. No type of salt hydrate was detectable in the inclusion during the freezing procedure. Hence the salinity of the fluid was calculated using the last ice melting temperatures (T_m(Ice): –1.7 to –0.4 °C; *Fig. 2.15/a; Table 2.6*) in the H_2O-NaCl model system resulting in a 0.7–2.9% *w*NaCl eq. (*Table 2.6*) range. In the heating procedure the inclusions homogenize into a liquid phase ($L + V \Rightarrow L$) in the range of T_h: 276–362 °C (*Fig. 2.15/a, b; Table 2.6*) corresponding to a molar volume (V_m) of 24.1–33.5 $cm^3\ mol^{-1}$ (*Table 2.6*). D_2 inclusions are characterized by rather different physicochemical conditions. Ice nucleation in these inclusions occurred at around –80 °C (*Table 2.6*) during the freezing procedure. The first melting temperature of ice was observed at around –52 °C (*Table 2.6*), and hydrohalite ($NaCl*H_2O$) crystals (*Fig. 2.14/c*) were detected in the inclusions by Raman spectroscopy. The final ice melting temperatures occurred in a range between –25.2 and –22.2 °C (*Fig. 2.15/a; Table 2.6*). Final melting of hydrohalite (T_m(Hh)) could not be detected even if Raman spectroscopy combined with microthermometry was used. The T_i data indicate dissolved alkali earth metals (Ca^{2+} or Mg^{2+}) in the fluid, which can most probably be characterized by the H_2O-NaCl-$CaCl_2$ model composition. In the absence of T_m(Hh) data the salinity has been expressed in equivalent % *w*$CaCl_2$ eq. which is between 22 and 21% *w*$CaCl_2$ eq. (*Table 2.6*) Homogenization occurred into the liquid phase ($L + V \Rightarrow L$) between 135 and 200 °C (*Fig. 2.15/a, b, Table 2.6*), corresponding to a molar volume of 19.6–20.5 $cm^3\ mol^{-1}$ (*Table 2.6*).

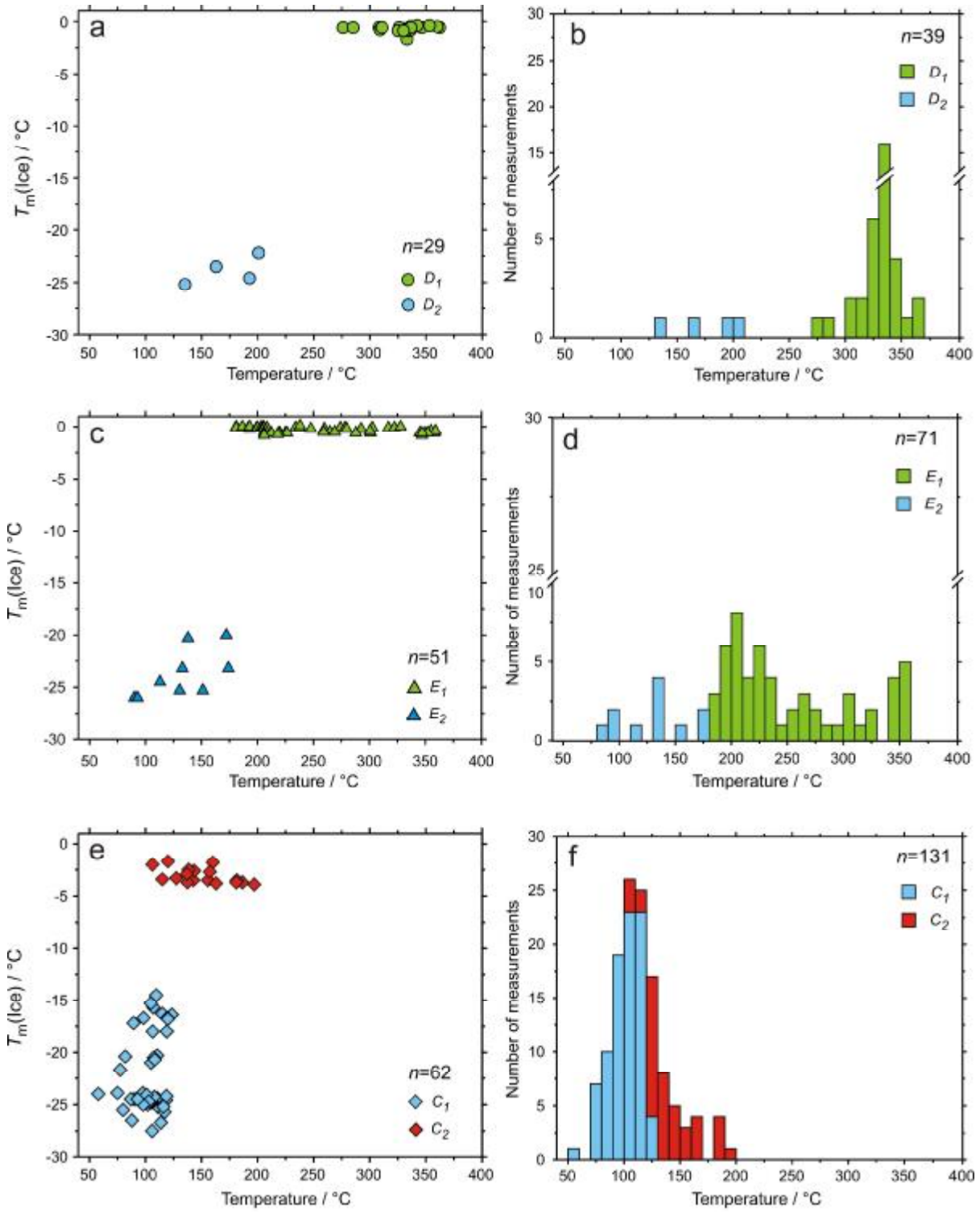

Figure 2.15. *Results of fluid inclusion microthermometry*
a) Diagrams representing microthermometry results: T_h vs T_m(Ice) plot of D_1 and D_2 fluid inclusions of diopside; b) T_h histograms of D_1 and D_2 fluid inclusions of diopside; c) T_h vs T_m(Ice) plot of fluid E_1 and E_2 inclusions of epidote; d) T_h histograms of E_1 and E_2 fluid inclusions from epidote; e) T_h vs T_m(Ice) plot of C_1 and C_2 fluid inclusions of calcite 1 and calcite 2 mineral phases; f) T_h histograms of C_1 and C_2 fluid inclusions from calcite 1 and calcite 2

Epidote

Raman spectra recorded at T_{lab} conditions do not indicate the presence of any amount of gaseous components either in the liquid or in the vapour phases in both E_1 and E_2 inclusions. In the E_1 primary fluid inclusions, nucleation of ice occurred in the range T_n(Ice): –43.2 to –31.5 °C (*Table 2.6*) during the freezing procedure. The initial melting phenomenon was not detectable during reheating of inclusions even with Raman spectroscopy; hence T_i values could not be measured. No type of salt hydrate was detectable by Raman spectroscopy either during freezing or in the reheating cycle. The final melting of ice occurred between –0.8 and –0.1 °C (*Fig. 2.15/c; Table 2.6*). The observed characteristics indicate the pure aqueous-electrolyte character of the fluid in type E_1; however the exact salt composition of the fluid could not be determined in the absence of T_i. Salt concentration was calculated in a H_2O-NaCl model system and the values are in the range 0.2–1.6% *w*NaCl eq. (*Table 2.6*). Each inclusion of the E_1 type homogenizes into the liquid phase ($L + V \Rightarrow L$) in a very wide range of 181–359 °C (*Fig. 2.15/c, d; Table 2.6*), corresponding to a molar volume of 20.3–33.1 cm^3 mol^{-1} (*Table 2.6*).

Table 2.6. *Summary of the results of the fluid inclusion study*

Host mineral	Type	*n*	φ_V	T_n(Ice) (°C)	T_e (°C)	T_m(Ice) (°C)	T_h (°C)	V_m (cm^3/mol)	Salinity	
									% *w*NaCl eq.	% *w*$CaCl_2$ eq.
Diopside	D_1	38	0.3-0.5	-36– -34	–	-1.7– -0.4	276-362	24.1-33.5	0.7-2.9	–
	D_2	4	0.1-0.2	~-80	~-52	-25.2– -22.2	135-200	19.6-20.5	–	22-21
Epidote	E_1	61	0.3-0.5	-43.2– -31.5	–	-0.8– -0.1	181-359	20.3-33.1	0.2-1.6	–
	E_2	11	0.1-0.2	-86.5– -75.5	55.6±2.9	-26– -20	87-170	19.1-20	–	20.6-23.2
Calcite 1	C_1	78	<0.1	-92– -52	-56±2	-25– -17	75-124	18.8-19.3	–	22.6-17.5
Calcite 2	C_2	45	0.1-0.2	47.4– -31.6	–	-1.7– -3.9	106-197	19-20.5	2.9-6.3	–

In E_2 type inclusions the Raman spectroscopy also could not detect any gaseous species in either the vapour or liquid phases. In the case of these inclusions T_n(Ice) values are between –86.5 and –75.5 °C (*Table 2.6*), a much lower range than in the case of type E_1. The first melting temperatures were detected in the interval T_i: –58.5 to –52.7 °C (*Table 2.6*), which is typical in fluids that can be modelled with a H_2O-NaCl-$CaCl_2$ composition. Salt hydrate crystals can be observed visually in some fluid inclusions during the reheating process and Raman spectroscopy confirmed that these crystals are hydrohalites. The final melting of hydrohalite can be measured only in one case with T_m(Hh)= –24.3 °C. The final melting of ice occurred in the range –26 to –20 °C (*Fig. 2.15/c; Table 2.6*). Since T_m(Hh) data were not detectable, salinities were calculated in the H_2O-$CaCl_2$ model system and were found to be in

the range 20.6–23.2% *w*$CaCl_2$ eq. (*Table 2.6*). Homogenization occurred into the liquid phase ($L + V \Rightarrow L$) between 87 and 170 °C (*Fig. 2.15/c, d; Table 2.6*) and the calculated molar volumes are 19.1–20 $cm^3\ mol^{-1}$ (*Table 2.6*).

Calcite

Raman spectroscopic analysis of the fluid inclusions could not be accomplished in the cases of C_1 and C_2 inclusions because of the high fluorescence of the host mineral. In C_1, nucleation of ice occurred at low temperatures between –92 and –52 °C (*Table 2.6*). During reheating the first melting phase appeared between –58 and –54 °C (*Table 2.6*). No phenomena related to the formation, presence, and decomposition of gas hydrate could be observed in the FIA, and hence the inclusion fluid was supposed to be an aqueous-electrolyte solution. From the T_i values of H_2O-NaCl-$CaCl_2$, the character of the trapped fluid can be deduced. Hydrohalite crystals large enough for visual identification could be grown in only a few cases during the cooling procedure (*Fig. 2.14/j*); however T_m(Hh) values were not determinable by the optical method during the reheating phase and hence we have no information about these values. The final melting of ice crystal was the last phase transition during the reheating process which took place at a very low temperature range of T_m(Ice): –25 to –17 °C (*Fig. 2.15/e; Table 2.6*) in each inclusion. Salinities of the fluid in the range 22.6–17.5% *w*$CaCl_2$ eq. (*Table 2.6*) can be calculated in the H_2O-$CaCl_2$ system by using T_m(Ice) values. Each fluid inclusion homogenizes into the liquid phase ($L + V \Rightarrow L$) and the T_h values are in the range 75–124 °C (*Fig. 2.15/e, f; Table 2.6*). The calculated molar volumes are in the range 18.8–19.3 $cm^3\ mol^{-1}$ (*Table 2.6*).

Analysis of C_2 inclusions reflects a fluid character quite different from that which can be observed in C_1. In the absence of useful Raman spectra we have no information about the gas content of the inclusions. Phenomena related to the presence of gas components in inclusions were not observable during microthermometry and hence this FIA most probably contains aqueous-electrolyte solution. Ice nucleation occurred between –47.4 and –31.6 °C (*Table 2.6*), and during the reheating procedure the initial melting phenomenon was not observable; hence T_i values could not be measured. The last melting of ice occurred between –3.9 and –1.7 °C (*Fig. 2.15/e; Table 2.6*); no solid phase (salt hydrate) beyond ice could be observed in the reheating process. The fluid was modelled in the H_2O-NaCl model system and the calculated salinity using T_m(Ice) data was found to be 2.9–6.3% *w*NaCl eq (*Table 2.6*). Each inclusion homogenizes into the liquid phase ($L + V \Rightarrow L$) during the heating process in

a 106–197 °C temperature range (*Fig. 2.15/e, f; Table 2.6*). The molar volumes of these inclusions – calculated from the measured data – are in the range 19–20.5 cm^3 mol^{-1} (*Table 2.6*).

2.5. Discussion

2.5.1. Post-magmatic origin of the Ca-Al silicate veins

The observed fracture filling minerals and their paragenesis (*Fig. 2.7*) are very similar to those that can be found worldwide in fractured metamorphic basement complexes (HUBER et al. 2007; RUGGIERI et al. 1999; COX & BROWNE 1998), different types of magmatic intrusions (DILLES & EINAUDI 1992; PREECE & BEANE 1982), and subvolcanic-volcanic rock assemblages (e.g. PENNACCHIONI et al. 2006; MARTÍNEZ SERRANO 2002; GIANELLI et al. 1998). The processes that resulted in the formation of the analysed vein types can be coupled to greenschist facies retrograde evolution of metamorphic terranes (MILLER & CARTWRIGHT 2006; HUBER et al. 2007) or can be linked to post-magmatic hydrothermal fluid circulation in cooling plutonic bodies and volcanic rocks (DILLES & EINAUDI 1992; TARRIELA 2004; GONZÁLEZ-PARTIDA et al. 1997) or even contact metamorphic interaction of magmatic stocks and different adjacent rocks (DILLES & EINAUDI 1992).

Diopside as a vein filling mineral can be found in regional metamorphic terranes (TSUJIMORI 1997), although it is more frequent in contact metamorphic rocks (VAN MARCKE DE LUMMEN & VERKAEREN 1986; WANG & WILLIAMS 2001) and in hydrothermal systems (BIRD et al. 1984; MAGDE et al. 1995; BAKKER & ELBURG 2006). Clinopyroxene grains similar in composition to ours (highly calcic, X_{Mg}: ~0.5–0.8) can be found in many skarn deposits (NAKANO et al. 1994; NAKANO 1989); however the observed high Ca content (*Fig. 2.8*) is rather characteristic of continental post-magmatic hydrothermal systems too (MARTÍNEZ SERRANO 2002; BIRD et al. 1984; CAVARETTA et al. 1982). The detected subhedral/anhedral unoriented pyroxene crystals (*Fig. 2.4/c, d*) and fine grained aggregates (*Fig. 2.4/h*) are very typical features of diopside occurring in hydrothermal veins (BIRD et al. 1984; CAVARETTA et al. 1982), while the well-crystallized form is usually observed in other metamorphic rocks, like skarns or calc-silicate hornfelses (BIRD et al. 1984). Epidote as a vein infilling and wall-rock alteration minerals commonly occur together with clinopyroxene in different geological environments (as can be seen above) (e.g. GIANELLI et al. 1998; MARTÍNEZ SERRANO 2002; CATHELINEAU et al. 1985). The sharp difference in composition (Al and Fe at the M3 site) (*Table 2.1*) occurring within a single crystal (*Fig. 2.9/a, b, Table*

2.1) or between different grains is a typical feature of epidote in greenschist facies metamorphic terranes (e.g. GRAPES & WATANABE 1984; MARUYAMA et al. 1983; RAITH 1976). However, this kind of broad chemical difference is also a typical feature of epidote formed due to hydrothermal alteration in different geothermal areas (e.g. ARNASON et al. 1993; SHIKAZONO 1984; CAVARETTA et al. 1982). Fractures filled by pure feldspar phase, especially pure albite veins, are commonly associated with the greenschist facies overprint in high-pressure metamorphic rocks. This vein type usually forms following regional retrogression in response to continued decompression and exhumation of metamorphic terranes (HUBER et al. 2007; MILLER et al. 2001; 1998). In contrast, pure albite veins are frequently associated with pegmatites (ALFONSO & MELGAREJO 2003) or can be coupled to Na-metasomatism in hydrothermally altered rocks (DEER ET AL. 2001). The presence of cogenetic plagioclase and K-feldspar with almost pure compositions ($\sim Or_{1.0} Ab_{99}$ $An_{0.0}$ and $\sim Or_{99} Ab_{1.0} An_{0.0}$, respectively) is typical in feldspathic rocks that have been hydrothermally altered at low *P-T* (PARSONS & LEE 2000; LEE & PARSONS 1997) and can also be found as authigenic feldspar phases in geothermal areas (MCDOWELL 1986). Chlorites occurring in the investigated veins can be found in a wide variety of geological environments including metamorphic terranes and active or fossil geothermal provinces. Distinguishing chlorites formed due to metamorphic fluid–rock interaction from those resulting from post-magmatic hydrothermal fluids is very difficult and in many cases cannot be done with certainty on a mineral chemical and crystal morphological basis. In the case of pyrite grains following the chlorite phases, mineral chemical data can be used to identify the origin of the ore phase.

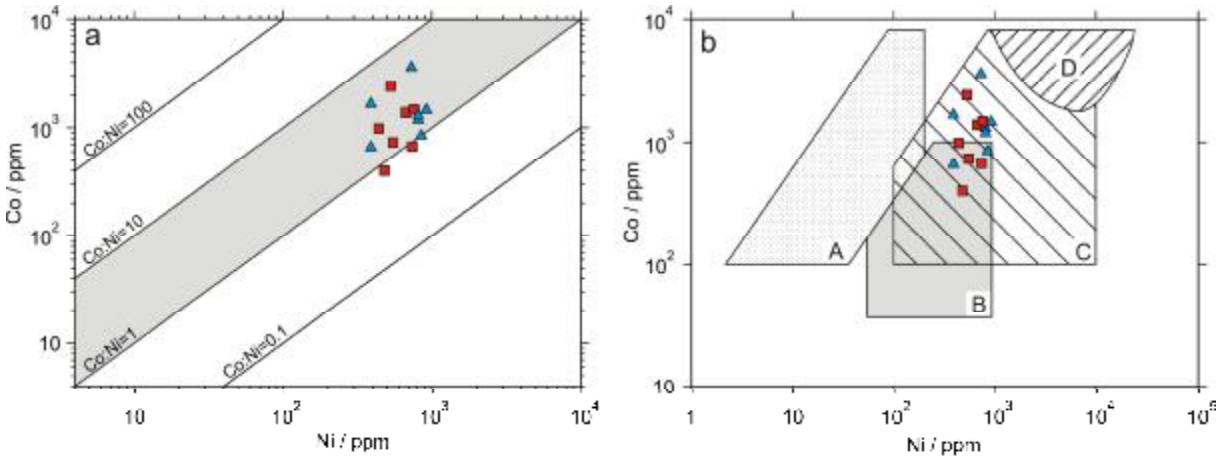

Figure 2.16. *Distribuition of Co/Ni ratio in pyrite from the Ca-Al-silicate dominant veins and the polymetallic sulphide veins*

a) Co vs Ni plot of average values of pyrites in this study (blue triangle) and from polymetallic veins investigated by Tarnai (1998) (red square); b) distribution of Co/Ni values of pyrites in the diagram of the approximate compositional fields (in terms of Co/Ni ratios) of pyrites from different varieties of ore deposits (modified after Price 1972). Legend: A) Massive (volcanic exhalative) sulfide deposits; B) Hydrothermal gold-vein deposits; C) Hydrothermal tin-molybdenum-tungsten vein deposits; D) Magmatic segregation deposits

Similarly high amounts of As, Co, and Ni (*Table 2.4*) are characteristic of post-magmatic hydrothermal pyrites both in Ca-Al-silicate and in polymetallic veins. In the analysed case, the Co/Ni ratio of pyrites is ~1–5 in Ca-Al silicate veins, while this ratio varies in a quite similar range of ~0.8–4.6 in the case of the polymetallic veins (*Fig. 2.16/a; Table 2.4*). These Co/Ni values are in the Co/Ni range of pyrites from post-magmatic hydrothermal veins (Co/Ni: 1–10, grey shaded area in *Fig. 2.16/a*, BRAILA et al. 1979; PRICE 1972).

If we represent the Co/Ni values on the diagram of the approximate compositional fields (in terms of Co/Ni ratios) of pyrites (*Fig. 2.16/b*) from different varieties of ore deposits it can be seen that pyrites of both studied vein types are within the field of hydrothermally originated vein deposits (*Fig. 2.16/b, B and C fields*, PRICE 1972). Based on the above considerations (especially the Co/Ni ratio of pyrite) about the possible origin of the studied veins, the detailed fracture filling mineralization must be due to post-magmatic hydrothermal fluid circulation rather than being an effect of metamorphically originated fluids. This assessment is in accordance with the opinion of SZEDERKÉNYI (1979), who in his early work related the widespread calc-silicate vein mineralization of the BC to the aplite dykes that can be found very frequently in the drilled rock section of the complex. The local dominance of the different vein filling minerals in different parts of the drilled rock body is very similar to those situations where rock domains (mostly neutral volcanic rocks) suffer propylitic alteration due to intense circulation of nearly neutral to weakly alkaline post-magmatic hydrothermal fluids (ZHARIKOV et al. 2007).

2.5.2. Formation conditions of the Ca-Al-silicate veins

2.5.2.1. Interpretation of vein mineralization

Diopside with X_{Mg} = 0.66–0.78 associated with Ca-Al silicate veins can be found in amphibolite host rock next to the dolomite marble intercalations, while lower X_{Mg} (0.48–0.55) diopside occurs rather in connection with high iron content biotite gneiss. This suggests that the quality of the host rock has some influence on the composition of the fracture filling diopside.

The textural position of diopside and epidote phases (*Fig. 2.4/a, b, d; Fig. 2.7*) clearly supports the chronologically superimposed participation of the two minerals. Although many papers deal with the temperature–pressure constraints of epidote solid solution composition (e.g. BIRD et al. 1988; CHO et al. 1988; MARUYAMA et al. 1983; RAITH 1976), an unequivocal statement about the *P-T* change from variation of Al^{3+} and Fe^{3+} in the octahedral M3 site of the epidote structure is problematic as it is influenced by many other factors. The pure aqueous-electrolyte character of E_1 fluid inclusions indicates very low fCO_2 during epidote formation, which is supported by the presence of prehnite together with epidote in a certain part of the veins, because prehnite is stable only at very low fCO_2 conditions (WHEELER et al. 2001). The presence of sulfide ore phases (sphalerite, pyrite) and the lack of other Fe^{3+} containing minerals indicate a low fO_2 level subsequent to the epidote formation.

The various zonation patterns of the epidote crystals can be a powerful indicator of physicochemical evolution of the hydrothermal fluid from which they crystallized. Irregular zoning patterns and patchy inhomogeneity in individual crystals (*Fig. 2.5/f; 9/c, d, e*) can be formed when zoning is modified by retrograde dissolution-precipitation processes, which may reflect the changing *P* and *T* (GRAPES & HOSKINS 2004) and is strongly influenced by the miscibility gaps in the epidote solid solution series (FRANZ & SELVERSTONE 1992). However MENARD & SPEAR (1996) interpreted patchy zoning as the result of locally discontinuous growth and possible resorption and not as the direct result of miscibility gaps. The observed irregular zoning pattern (see *Fig. 2.9/c*) within certain epidote crystals can be observed frequently in low-temperature conditions, where small individual grains of epidote minerals are assembled into one single crystal (FRANZ & LIEBSCHER 2004; GIERÉ & SORENSEN 2004). In the analysed grains the Fe-rich zone generally developed in the inner part of the crystal. Compositional zones that formed earlier appear to have been partially resorbed prior to the growth of later ones, representing a patchy zoning. This suggests that the system was initially under disequilibrium and proceeded further towards an equilibrium state. Similar irregular zoning patterns of epidote can be observed in propylitic alteration zones, suggesting that disequilibrium crystallization and chemical fluctuations occurred during the hydrothermal alteration process (CHOO 2002).

There is a higher An content in pure albite veins, which pre-date the cogenetic alkali-plagioclase feldspar assemblage likely formed during higher *P-T* conditions. However, the difference in An content may be an effect of different host rock chemistry too, because higher

Ca (1–2 An%) albite veins frequently occur in places where amphibolite wall rock is dominant.

The cogenetic occurrence of pure albite and K-feldspar indicates that they grew under low *P-T* conditions. Almost every calculated value in both binary (*T*~296 ± 33 °C) and ternary feldspar systems (*T*~283 ± 53 °C) is in accordance with the textural observation; some textural features of individual crystals draw attention to careful interpretation of these data. Beyond the fact that at low *P–T* conditions coexisting feldspar phases rarely reach equilibrium, the possible effect of subsequently circulating fluids including Na^+ and K^+ may cause a characteristic change in the Na^+/K^+ ratio of cogenetic feldspar compositions (ORVILLE 1963; GIGGENBACH 1988; PARSONS & LEE 2000). In our case, turbidity (a myriad of tiny fluid inclusions) of the feldspars indicates that they were penetrated by fluid following their precipitation (PARSONS & LEE 2000). A possible interpretation of the particular differences between concordant temperatures in some cases using the ternary solvus method is that most feldspar grains could preserve precipitation conditions, while in some cases they were subsequently re-equilibrated via fluid.

The relative succession of chlorites (*chl1*, *chl2*, *chl3, Fig. 2.7.*) in the mineral sequence combined with the calculated formation temperatures reveal a cooling petrographic trend during precipitation of the different chlorite phases (T_{chl1}: 260 ± 32 °C → T_{chl2}: 222 ± 20 °C → T_{chl3}: 154 ± 13 °C). A cooling trend can also be traced in chlorite 1 and chlorite 2 phases deduced from the decreasing value of Al^{IV} from core to rim in single crystals (*Table 2.3*). Nevertheless some important factors should be mentioned that can affect the results. The compositional relationship between the Fe/(Fe + Mg) ratio of chlorites and the host rock composition is confirmed by many studies (e.g. CATHELINEAU & NIEVA 1985; BEVINS et al. 1991). The vermiform green chlorite 1 aggregates with high iron content (Fe/(Fe + Mg) ~ 0.42–0.63) (*Fig. 2.11/b*) occur rather in low epidote content parts of the veins, while, on the contrary, the occurrence of low iron content (Fe/(Fe + Mg) ~ 0.32–0.45) (*Fig. 2.11/b*) chlorites (chlorite 2, chlorite 3) is characteristic in epidote rich domains. These observations indicate that the fluid chemistry and the host rock mineral assemblages had a strong influence on the chemical composition of these phases. Both chlorite 1 and chlorite 2 are arranged around the Al^{VI}/Al^{IV} = 1 line (*Fig. 2.11/c*), suggesting that the charge-balance of Al^{IV}/Si replacement is accomplished by Al^{VI} replacing either Fe or Mg in the octahedral layer. Higher Al^{VI}/Al^{IV} values in the case of chlorite 3 (*Fig. 2.11/c*) may suggest interlayering of a minor amount of corrensite in the chlorite structure (JAHREN & AAGAARD 1992; SHAU et al. 1990).

The careful selection of the representative data of chlorite chemical analyses gives a reliable base for thermometric calculations that imply that these results are applicable for characterizing the temperature change during chlorite formation.

The calcite 1 phase represents a significant change in the evolution of the vein system. This is obvious from the microthermometry data of C_1 FIA (T_h: 75–124 °C; salinity: 22.6–17.5% wCaCl$_2$ eq.) of calcite 1. The stable isotope composition of calcite 1 (7–10.8‰ δ^{18}O V-SMOW; –4.9 to –8.2‰ δ^{13}C V-PDB) is very similar to values measured from fracture filling carbonates in other crystalline basement rocks (KOMOR 1995). The calcite precipitation temperature can be calculated using the carbonate-water fractionation factors after O'NEIL (1969). The calcite δ^{18}O value can be used to calculate a temperature of formation if the δ^{18}O of the water is known or can be constrained. Likewise the δ^{18}O of the water can be determined using the δ^{18}O of the calcite and a precipitation temperature (determined by fluid inclusion analyses). Because the primary fluid inclusions do not show any evidence of post-entrapment modifications, their T_h values can be interpreted as the minimum formation temperature range of calcite 1. These temperature constraints were used together with the fractionation equation of FRIEDMAN & O'NEIL (1977) to calculate the oxygen isotope range of the calcite precipitating fluids.

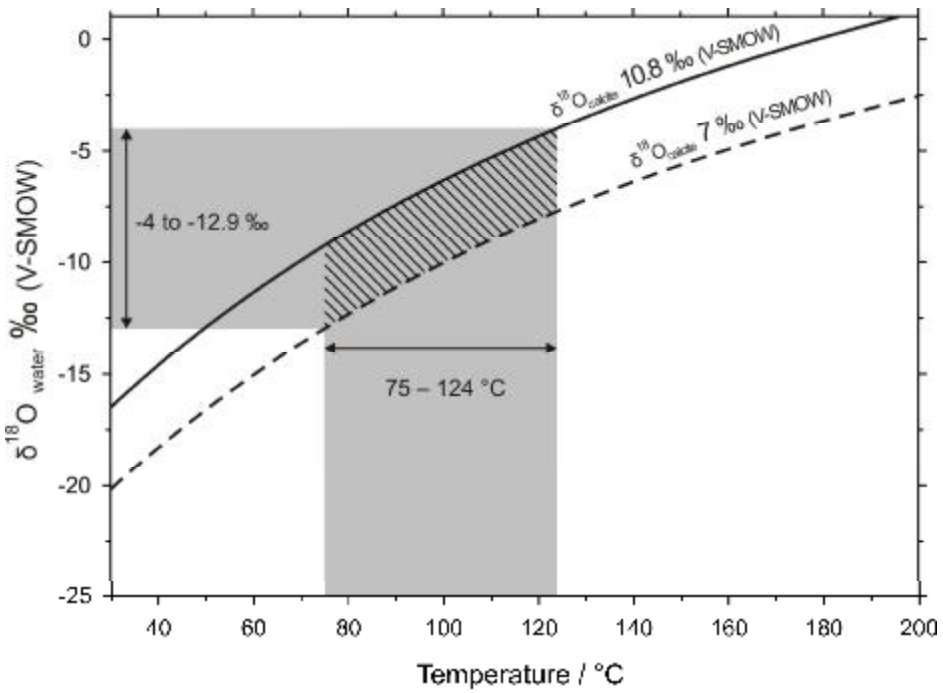

Figure 2.17. *Estimation of δ^{18}O values of pore-water from which calcite 1 phase grew using the δ^{18}O values of calcite 1 and the fractionation equation of FRIEDMAN & O'NEIL (1977)*
Shaded area indicates probable δ^{18}O pore-water composition from which calcite 1 phase precipitated assuming a temperature of formation between 75 and 124 °C

By using T_h values, the calculated $\delta^{18}O$ (V-SMOW) values of the water are in the range –4 to –12.9‰ (*Fig. 2.17*). This ^{18}O signature is well within the ^{18}O signature range of waters that can be found in crystalline rocks (FRAPE et al. 2005), sedimentary basins ('sedimentary brines') (KHARAKA & HANOR 2005), and meteorically originated groundwater (ZHENG & HOEFS 1993). The isotope signature together with the high salinity and low T_h range of the calcite 1 phase indicate that this carbonate phase must have been precipitated from downward-penetrating sedimentary brines or from descending meteoric water that infiltrated through evaporate bodies. The few inclusions containing D_2 fluid in diopside and E_2 epidote crystals also most probably related to fluid from which the calcite 1 phase precipitated. After the precipitation of calcite 1, a significant change occurred in the fluid chemistry that is well marked by microthermometric values of the calcite 2 phase (*Table 2.6; Fig. 2.15/e, f*) that postdate calcite 1. However, relevant conclusions about its origin cannot be deduced from the available data.

2.5.2.2. *P-T* evolution of the mineralizing fluid

No definitive evidence for re-equilibration or other post-entrapment modification of the D_1 fluid inclusions in diopside can be observed; hence the T_h values (276–362 °C) of this FIA can be accepted as a minimum trapping temperature. Because the real trapping conditions must have been at a somewhat higher temperature range, the observed T_h values are in agreement with the temperature of occurrence of clinopyroxenes ($\geq$300 °C) in active geothermal systems (BIRD et al. 1984).

The broad range of T_h data (181–359 °C) of E_1 fluid inclusions of epidote at first appearance is in good accordance with the observation that epidote crystallization shows significant overlap with several other fracture filling minerals (see *Fig. 2.7*). Fluid inclusion assemblages formed by a multistage crystallization process (detailed in a previous section) of epidote cannot be easily distinguished from each other during fluid inclusion petrography. On the contrary, these inclusions can preserve the change of physicochemical circumstances of the hydrothermal fluid during epidote crystallization if significant post-entrapment modifications of the inclusions can be excluded. No unequivocal evidence for post-entrapment modifications of E_1 can be observed, although stretching of the inclusion volume caused by internal overpressure or leakage of inclusions along optically invisible microcracks can never be ruled out entirely. Based on the observed textural patterns of the analysed fluid

inclusions, the obtained T_h values are suitable for determination of the possible trapping conditions of the E_1 fluid inclusions in epidote.

The low T_h values of D_2 (135–200 °C) and E_2 (80–170 °C) fluid inclusions suggest that these inclusions may not be trapped during crystallization of diopside and epidote because their T_h values are out of the stability ranges of both mineral phases (BIRD et al. 1984). However the microthermometry results indicate that D_2 and E_2 inclusions have the same fluid characteristics and their composition can be related to C_1 inclusions of calcite 1. The high salinity can be explained in various ways. Diffusion loss (BAKKER & JANSEN 1990) of a certain amount of water from an originally weakly saline D_1 or E_1 inclusion would lead to a shift of the original T_h values to higher temperatures. A more acceptable situation is that D_1 and E_1 inclusions suffer leakage through optically invisible microcracks (ROEDDER 1984) and the inclusion vacuole is totally or partially refilled by the ambient fluid phase leading to D_2 and E_2 fluid inclusions.

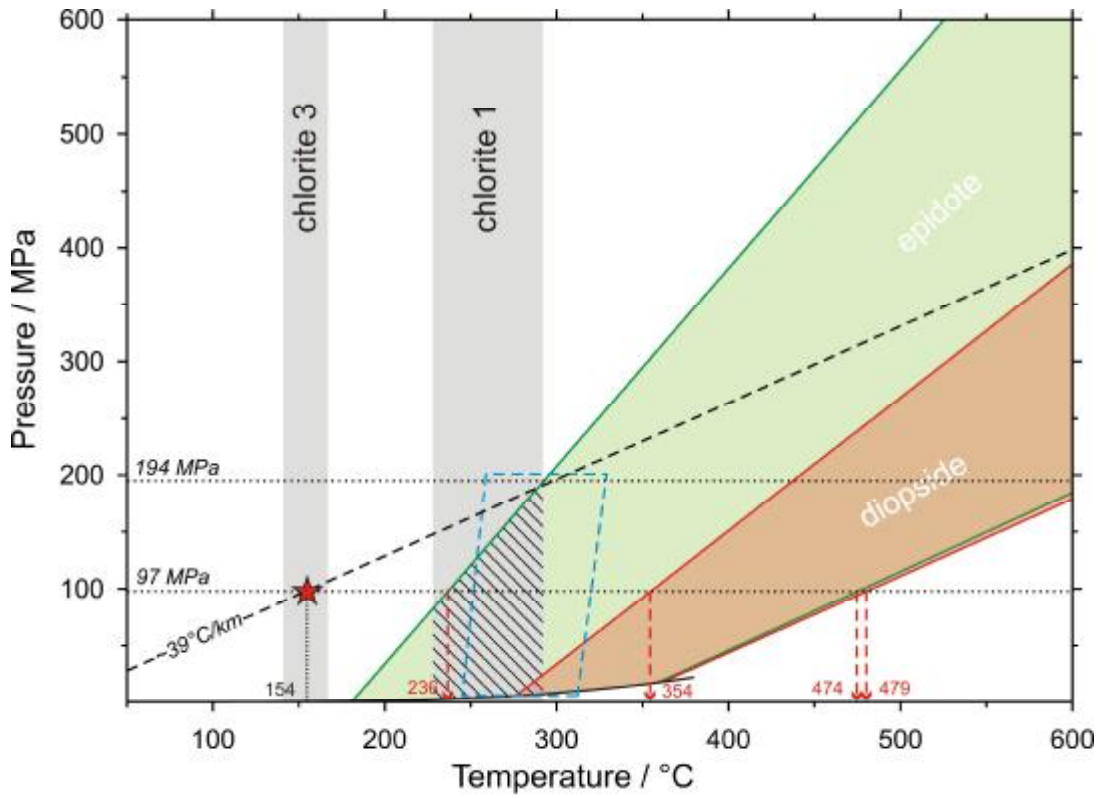

Figure 2.18. *P-T diagram showing calculated isochoric envelopes of the investigated fluid inclusions from D_1 and E_1 inclusions*
Intersection of the mean temperature value of formation of chlorite 3 and the estimated average pressure value is indicated by red pentacle. Black hatched line mark the estimated thermal gradient of the area. Blue hatched rectangle refer to P-T window of feldspar thermometry (WHITNEY & STORMER 1977). Red hatched arrows refer to possible temperature limits of formation of diopside and epidote phases.

In order to outline the possible *P-T* conditions of the vein mineralization history, isochoric envelopes were constructed by using V_m and T_h values of D_1 and E_1 inclusions from diopside and epidote (*Fig. 2.18*). Isochores were constructed by using a 0.6% *w*NaCl model composition in each case. Since fluid inclusions of diopside and epidote captured fluids with almost identical chemical characters, their isochores do not intersect with each other. Hence they cannot be used to originate *P-T* data even if the two minerals show partially coexistent crystallization. The occurrence of the chlorite 1 phase as inclusions in epidote indicates overlapping of crystallization of these two minerals, making it possible to estimate the approximate *P-T* conditions of their formation.

The *P-T* field is constructed by using thermometry data of chlorite 1 (grey shaded area in *Fig. 2.18*) and microthermometry data of E_1 fluid inclusions in epidote (light green area in *Fig. 2.18*). The results indicate that epidote and chlorite 1 formed in a *P-T* window (hatched area on *Fig. 2.18*) characterized by a maximum pressure range of 83–192 MPa. Estimation of the lower pressure limit has high uncertainty in this case and is only delimited by the boiling point curve (*Fig. 2.18*). The calculated pressure–temperature field of the cogenetic albite and K-feldspar assemblage can be characterized by higher temperature values (*Fig. 2.18*). It is in accordance with the overlapping precipitation of the feldspar assemblage with epidote before chlorite 1 was formed. The low *P* values obtained indicate that mineralization occurred due to near surface hydrothermal fluid circulation induced by a shallow magmatic heater. Although the igneous source of the fluid circulation could not be identified with certainty, the magmatic activity that resulted in penetration of the numerous aplite dykes in the drilled rock section can be considered as the potential heat source.

During estimation of the *P-T* evolution of a hydrothermal system, the cooling rate of the hydrothermal fluid may be of high importance. The cooling rate basically depends on the cooling rate of the magmatic heater (igneous body) and the exhumation rate of the area (FU et al. 2009). The relative cooling rate of the igneous body depends on several parameters, namely the size and shape of the body, depth of emplacement, initial emplacement temperature, geothermal gradient, and thermal conductivity of country rocks (FU et al. 2009). Investigations by FU et al. (2009) demonstrated that the cooling rate of a hydrothermal system is most rapid if a thin elongated small volume igneous body intrudes in a shallow, near surface situation where the geothermal gradient is low and the thermal conductivity of the country rocks is high. The cooling rate can be accelerated greatly if igneous bodies generate convective fluid circulation (CATHLES et al. 1997; CATHLES 1981). CATHLES (1981)

constructed a diagram where the time required to cool down a plutonic dyke to 25% of its initial temperature is plotted as a function of the pluton's size and the permeability of the environment into which it is intruded. Based on this model, cooling an 800 °C rectangle magmatic body (2 × 3 km in size) to ~150 °C purely by the conductive mode takes about 100 kyr. This cooling rate would require a rather high uplift velocity of 6 cm/yr by pure exhumation in an average gradient (~35 °C/km) area. Taking into consideration that thin dykes (< 10 m thick) have a very quick cooling rate (FURLONG et al. 1991; DELANEY 1987) even if the cooling mechanism of these dykes is mainly conductive heat transfer (WEBBER et al. 1997), the host rocks do not need any significant vertical movement at the temperature of hydrothermal circulation to cool down to the ambient rock temperature.

Based on this assumption and the fact that none of the aplite dykes reach 10 m thickness in the BC, the regional pressure condition must have been nearly constant during the hydrothermal event. Since significant vertical movement of the crystalline basement can be excluded during an aplite induced hydrothermal event, and the cooling rate of the fluid was influenced mainly by the ambient rock temperature, which was around 154 °C on the basis of thermometry data of the last chlorite phase (chlorite 3). The most conservative estimate of regional pressure conditions of vein formation is obtained if the maximum pressure (~194 MPa) of the possible trapping *P-T* field of E_1 inclusions is used. The regional pressure condition of the area was admittedly lower than ~194 MPa when the temperature of the vein system recovered to ambient rock temperature (~154 °C). A more acceptable approximation would be to choose an average pressure value of around 100 MPa (~97 MPa) (*Fig. 2.18*). This pressure value can be regarded as a nearly constant regional pressure condition during the vein filling process. By using these values (~97 MPa; ~154 °C) a ~39 °C/km thermal gradient can be calculated if 2650 kg/m^3 rock density and lithostatic pressure build-up are assumed (*Fig. 2.18*).

The observed microstructure (euhedral coarse crystals on the vein walls) of the veins indicates that fracture infilling occurred in the fluid filled fracture system which was maintained in an open state during the process. In this case, fluid pressure must be sufficient to keep the crack open for long enough to allow coarse crystal growth (OLIVER & BONS 2001). In the case of these types of veins, significant pressure fluctuation during the vein filling process is not characteristic; the precipitation phase will be influenced only by the magnitude of fluid pressure drops (OLIVER & BONS 2001). As significant pressure fluctuation should be assumed in neither the fluid pressure nor the regional pressure conditions;

approximate formation temperatures of ~354–479 °C for diopside and ~236–474 °C for epidote can be estimated presuming a fairly constant pressure condition (~100 MPa).

2.6. Conclusions

1. The Ca-Al-silicate dominant veins of the BC can be characterized by the *di→ep→sph→ab±kfp→chl1±prh±adu→chl2→chl3→pyr→cal1→cal2→cal3* paragenetic sequence. Fracture filling mineral assemblages similar to this type can be found in rocks that have suffered comprehensive propylitic alteration.
2. The vein filling mineralization formed due to a post-magmatic hydrothermal fluid migration event supported by the Co/Ni ratio (~1–5) of fracture filling pyrite grains. The Co/Ni ratio also supports the proposal that the polymetallic sulfide veins and the Ca-Al-silicate dominant veins of the BC can be related to each other genetically.
3. The vein filling mineralization took place in a cooling hydrothermal system (from ~480 °C down to ~150 °C) at nearly constant pressure conditions (~100 MPa), and the vein filling minerals precipitated from a low salinity (0.2–3% *w*NaCl eq.) aqueous-electrolyte solution.
4. The calculated low $\delta^{18}O$ values (–4 to –12.9‰) of water from which calcite 1 precipitated, together with the microthermometry results (low T_h: 75–124 °C; high salinity: 17.5–22.6% *w*$CaCl_2$ eq.), indicate that precipitation of this carbonate phase occurred from a downward penetrating externally originated fluid.

ACKNOWLEDGEMENTS

The authors would like to thank Ronald J. Bakker and his research group for helping with the fluid inclusion studies. The authors also would like to thank Federica Zaccarrini, Giorgio Garuti, and Helmut Mühlhans for their help during microprobe measurements. Thanks go to Bernadett Bajnóczi for her help during the cathodoluminescence microscopy and to Zoltan Siklosy for the stable isotope measurements. The authors also acknowledge the Stiftung Aktion Österreich-Ungarn (62öu4) and the Hungarian Research Fund (No. K60768) for supporting the project financially.

REFERENCES

AFIFI, M., A., & ESSENE, E. (1988): MINFILE: A microcomputer program for storage and manipulation of chemical data on minerals. *American Mineralogist*, 73, 446-448.

ALFONSO, P., & MELGAREJO, J., C. (2003): Fluid evolution in the beryl-columbite-phosphate pegmatites of Cap de Creus (Catalonia, Spain). *Journal of Geochemical Exploration*, 78-79, 17-21.

ÁRKAI, P. (1985): Polymetamorphic evolution of the South-Hungarian crystalline basement, Pannonian basin: geothermometric and geobarometric data. -*Acta Geologica Hungarica*, 3-4, 23, 165-190.

ÁRKAI, P., HORVÁTH, P., & NAGY, G. (1999): A clockwise P-T path from the Variscan basement of the Tisza Unit, Pannonian basin Hungary. *Geologica Croatica*, 2, 52, 109-117.

BACHINSKY, S., W., & MÜLLER, G. (1971): Experimental determination of the microcline-low albite solvus. *Journal of Petrology*, 12, 329-356.

BAILEY, S., W. (1980): Summary of recommendations of AIPEA Nomenclature Committee. *Clays and Clay Minerals*, 15, 85-93.

BAKER, T., VAN ACHTERBERG, E., RYAN, C., G., & LANG, J., R. (2004): Composition and evolution of ore fluids in a magmatic-hydrothermal skarn deposit. *Geology*, 32, 117-120.

BAKKER, R. J. (2003): Package FLUIDS 1.Computer programs for analysis of fluid inclusion data and for modeling bulk fluid properties. *Chemical Geology*, 194, 3-23.

BAKKER, R. J. E., A., M. (2006): A magmatic-hydrothermal transition in Arkaroola (northern Flinders Ranges, South Australia): from diopside-titanite pegmatites to hematite-quartz growth. *Contribution to Mineralogy and Petrology*, 152, 541-569.

BAKKER, R. J. J., J., B., H. (1990): Preferential water leakage from fluid inclusions by means of mobile dislocations. *Nature*, 345, 58-60.

BEANE, R., E., & TITLEY, S., R. (1981): Porphiry copper deposits, Part II. Hydrothermal alteration and mineralization. *Economic Geology*, 75th Anniversary Volume, 235-269.

BEANE, R., E., & BODNAR, R., J. (1995): Hydrothermal fluids and hydrothermal alteration in porphyry copper deposits. *Porphyry Copper Deposits of the American Cordillera.*, PIERCE, F., W., & BOHM, J., G., Tucson, Arizona Geological Society Digest, 20, 83-93.

BEVINS, R., E., ROBINSON, D., ROWBOTHAM, G. (1991): Compositional variations in mafic phyllosilicates from regional low-grade metabasites and application of the chlorite geothermometer. *Journal of Metamorphic Geology*, 9, 711-721.

BIRD, D., K., SCHIFFMAN, P., ELDERS, W., A., WILLIAMS, A. E., & MCDOWELL, S., D. (1984): Calc-silicate minaralization in active geothermal systems. *Economic Geology*, 79, 671-695.

BIRD, D., K., & SPIELER, A., R. (2004): Epidote in geothermal systems. *Reviews in Mineralogy and geochemistry: Epidotes.*, LIEBSCHER, A., & FRANZ, G., Washington D. C., Mineralogical Society of America., 56, 235-300.

BODNAR, R., J. (2003): Introduction to fluid inclusions. *Fluid Inclusions: Analysis and Interpretation*, SAMSON, I., ANDERSON, A., & MARSHALL, D., Vancouver, Mineralogical Association of Canada, 32, 1-8.

BOIRON, M., . C., CATHELINEAUA, M., BANKS, D., A., FOURCADE, S., & VALLANCE, J. (2003): Mixing of metamorphic and surficial fluids during the uplift of the Hercynian upper crust: consequences for gold deposition. *Chemical Geology*, 194, 119-141.

BRAILA, A., SABATINI, G., & TROJA, F. (1979): A revaluation of the Co/Ni ratio in pyrite as geochemical tool in ore genesis problems. Evidences from Southern Tuscany pyritic deposits. *Mineralium Deposita*, 14, 353-374.

CATHELINEAU, M., & NIEVA, D. (1985): A chlorite solution geothermometer. The Los Azufres (Mexico) geothermal system. *Contribution to Mineralogy and Petrology*, 91, 235-244.

CATHLES, L., M. (1981): Fluid flow and genesis of hydrothermal ore deposits. *Economic Geology*, 75th Anniversary Volume, 442-457.

CATHLES, L., M., ERENDI., A., H., J., & BARRIE, T. (1997): How long can a hydrothermal system be sustained by a single intrusive event? *Economic Geology*, 92, 766-761.

CAVARETTA, G., GIANELLI, G., & PUXEDDU, M. (1982): Formation of authigenic minerals and their use as indicators of the physico-chemical paramters of the fluid in the Larderello-Travale geothermal field. *Economic Geology*, 77, 1071-1084.

CHO, M., LIOU, J., G., & BIRD, D., K. (1988): Prograde phase relations in the State 2-14 well metasandstones, Salton Sea geothermal field, California. *Journal of Geophysical Research*, 93, 13081-13103.

CHOO, C., O. (2002): Complex compositional zoning in epidote from rhyodacitic tuff, Bobae sericite deposit, southeastern Korea. *Neues Jahrbuch für Mineralogie. Abhandlungen*, 177, 2, 181-197.

COX, M., E., & BROWNE, P. (1998): Hydrothermal alteration mineralogy as an indicator of hydrology at the Ngawha geothermal field, New Zealand. *Geothermics*, 27, 3, 259-270.

DEER, W., A., HOWIE, A., R., & ZUSSMANN, J. (2001): An Introduction to the Rock Forming Minerals., London, Longman, 528.

DELANEY, P., T. (1987): Heta-transfer during emplacement and cooling of mafic dykes. *Mafic dyke swarms.*, HALLS, H., C., & FAHRLG, W., F., Geological Association of Canada, 31-46.

DIAMOND, L. W. (2003): Systematics of H_2O inclusions. *Fluid Inclusions: Analisys and interpretation*, IAN SAMSON, A. A., & DAN MARSHALL, Vancouver, Mineralogical Association of Canada, 32, 55-77.

DILLES, J., H., & EINAUDI, M., T. (1992): Wall.Rock Alteration and hydrothermal flow paths about the Ann-Mason porphyry copper deposit, Nevada-A 6 km vertical reconstruction. *Economic Geology*, 87, 1963-2001.

FALL, A., BODNAR, R., J., SZABÓ, CS., & PÁL-MOLNÁR, E. (2007): Fluid evolution in the nepheline syenites of the Ditrau Alkaline Massif, Transylvania, Romania. *Lithos*, 95, 331-345.

FAZEKAS, V., & VINCZE, J. (1991): Hidrotermás ércindikációk a Villány-hegység északi előtere mélyfúrásaiban. *Földtani Közlöny*, 91, 1-4, 23-56.

FEHR, K., T., & HEUSS-AßBICHLER, S. (1997): Intracrystalline equilibria and immiscibility gap along the join cloinozoisite-epidote: An experimental and ^{57}Fe Mössbauer study. *Neues Jahrbuch Mineral Abhandlungen*, 172, 43-67.

FERRY, M., J. (1985): Hydrothermal alteration of Tertiary igneous rocks from the Isle of Skye, northwest Scotland, II. Granites. *Contribution to Mineralogy and Petrology*, 91, 283-304.

FINTOR, K., SCHUBERT, F., & M. TÓTH, T. (2008): Hiperszalin paleofluidum-áramlás nyomai a Baksai Komplexum repedésrendszerében. *Földtani Közlöny*, 138, 3, 257-278.

FOSTER, M., D. (1962): Interpretation of the composition and a classification of the chlorites. *U. S. Geol. Surv. Prof. paper*, 414-A, A1-A33,

FRANZ, G., & SELVERSTONE, J. (1992): An empirical phase diagram for the clinozoisite-zoisite transformation in the system $Ca_2Al_3Si_3O_{12}(OH)$-$Ca_2Al_2FeSi_3O_{12}(OH)$. *American Mineralogist*, 77, 631-642.

FRANZ, G., & LIEBSCHER, A. (2004): Physical and chemical properties of the Epidote minerals-An introduction. *Revies in Mineralogy and Geochemistry: Epidotes.*, LIEBSCHER, A., & FRANZ, G., Washington D. C., Mineralogical Society of America, 56, 1-58.

FRAPE, S. K., & BLYTH, A. (2005): Deep Fluids in the Continents: II. Crystalline Rocks. *Treatise on Geochemistry*, HOLLAND, D. H., AND TUREKIAN, K. K., Oxford, Elsevier Science, 5, 541-580.

FRIEDMAN, I., & O'NEIL, J., R. (1977): Data of Geochemistry, 6th edition. Chapter KK. Compilation of Stable Isotope Fractionation Factors of Geochemical interest. *U. S. Geol. Surv. Prof. paper*, 440-KK.

FU, Q., F., MCINNES, B., I., A., EVANS, N., J., & DAVIES, P., J. (2009): Numerical modeling of magmatic-hydrothermal systems constrained by U-Th-Pb-He time-temperature histories. *Journal of Geochemical Exploration*, In press: doi: 10.1016/j.gexplo.2009.09.001,

FURLONG, K., P., HANSON, R., B., & BOWERS, J., R. (1991): Modelling thermal regimes. *Reviews in Mineralogy: Contact metamorphism.*, KERRICK, D., M., Washington D. C., Mineralogical Society of America., 26, 437-506.

GÉCZY, B. (1973): Plate tectonics and paleogeography in the East- Mediterranean Mesozoic. *Acta Geol. Hung.*, 27, 379-389.

GIANELLI, G., MEKURIA, N., BATTAGLIA, S., CHERSICLA, A., GAROFALO, P., RUGGIERI, G., MAGAELLI, M., & GEBREGZIABHER, Z. (1998): Water-rock interaction and hydrothermal mineral eqilibria in the Tendaho geothermal system. *Journal of Volcaology and Geothermal Research*, 86, 253-276.

GIERÉ, R., & SORENSEN, S., S. (2004): Allanite and other REE-rich epidote-group minerals. *Revies in Mineralogy and Geochemistry: Epidotes.*, LIEBSCHER, A., & FRANZ, G., Washington D. C., Mineralogical Society of America, 56,

GIGGENBACH, W. F. (1988): Geothermal solute equilibria. Derivation of Na-K-Mg-Ca geoindicators. *Geochimica et Cosmochimica Acta*, 52, 2749-265.

GLEESON, S., A., YARDLEY, B., W., D., MUNZ, I., A., & BOYCE, A., J. (2003): Infiltration of basinal fluids into high-grade basement, South Norway: sources and behaviour of waters and brines. *Geofluids*, 3, 33-48.

GOLDSTEIN, R. H., & REYNOLDS, T. J. (1994): Systematics of fluid inclusions in diagenetic minerals., Tulsa, Oklahoma,

GONZAÁLEZ PARTIDA, E., GARCIA GUTIERREZ, A., TORRES RODRIGUEZ, V. (1997): Thermal and petrologic study of the CH-A well from the Chipilapa-Ahuachapan geothermal area, El Salvador. *Geothermics*, 26, 701-713.

GONZALEZ-PARTIDA, E., CARRILLO-CHAVEZ, A., LEVRESSE, G., TELLO-HINOJOSA, E.,, VENEGAS-SALGADO, S., RAMIREZ-SILVA, G., PAL-VERMA, M., and TRITLLA, J., & CAMPRUBI, A. (2005): Hydro-geochemical and isotopic fluid evolution of the Los Azufres geothermal field, Central Mexico. *Applied Geochemistry*, 20, 23-39.

GRAPES, R., H., & HOSKIN, P., W., O. (2004): Epidote group minerals in low-medium pressure metamorphic terranes. *Revies in Mineralogy and Geochemistry: Epidotes.*, LIEBSCHER, A., & FRANZ, G., Washington D. C., Mineralogical Society of America, 56, 301-345.

GRATIER, J. P., & JENATTON, L. (1984): Deformation by solution-deposition, and re-equilibration of fluid inclusions in crystals depending on temperature, internal pressure and stress. *Journal of Structural Geology*, 6, 1/2, 189-200.

HAAS, J., & PÉRÓ, CS. (2004): Mesozoic evolution of the Tisza Mega-unit. -*Int. J. Earth Sci.*, 93, 297-313.

HEY, M., H. (1954): A new review of the chlorites. *Mineraogical Magazine*, 30, 277-292.

HORVÁTH, P., KOVÁCS, G., & SZAKMÁNY, GY. (2003): Eclogite and garnet amphibolite pebbles from niocene conglomerates (Pannonian basin Hungary): implications for the variscab metamorphic evolution of the Tisza Megaunit. *Geologica Catpathica*, 6, 54, 355-366.

HUBER, M., HAŁAS, S., & SIKORSKA, M. (2007): Evolution of prehnite–albite–calcite veins in metamorphic rocks from the Lapland Granulite Belt (Kandalaksha region of Kola Peninsula). *Geologija*, 59, 1-7.

JAHREN, J., S., & AAGAARD, P. (1992): Diagenetic illite-chlorite assemblages in arenites. I. Chemical evolution. *Clays and Clay Minerals*, 40, 540-546.

JUHÁSZ, A., M. TÓTH, T., RAMSEYER, K., & MATTER, A. (2002): Connected fluid evolution in fractured crystalline basement and overlying sediments, Pannonian Basin, SE Hungary. *Chemical Geology*, 182, 91-120.

KASSAI, M. (1972): A Villány-Szalatnaki pleozóos mélytörés . (The Paleozoic Deep Fracture of Villány-Szalatnak .). *MTA X. Oszt. Közl.*, 6, 1, 351-354.

KHARAKA, Y. K., & HANOR, J. S. (2005): Deep Fluids in the Continents: I. Sedimentary Basins. *Treatise on Geochemistry*, H.D. HOLLAND, A. K. K. T., Oxford, Elsevier, 5, 499-540.

KIRÁLY, E. (1996): Adalékok a délkelet-dunántúli polimetamorf aljzat megismeréséhez. *Földtani Közlöny*, 1, 126, 1-23.

KOMOR, C., S. (1995): Chemistry and petrography of calcite in the KTB pilot borehole, Bavarian Oberpfalz, Germany. *Chemical Geology*, 124, 3-4, 199-215.

KOVÁCH, A., SVINGOR, E., & SZEDERKÉNYI, T. (1985): Rb-Sr Dating of basement rocks from the southern foreland of the Mecsek mountains, southeastern transdanubia, Hungary. *Acta Mineralogica-Petrographica, Szeged*, XXVII, 51-57.

KRUMGALZ, B. S., POGORELSKY, R., & PITZER, K. S. (1996): Volumetric properties of single aqueous electrolytes from zero to saturation concentration at 298,15 K Represented by Pitzer's ion-interaction equations. *Journal of Phy sical Chemistry Referential Data*, 25, 639-663.

LEE, R., M., & PARSONS, I. (1997): Dislocation formation and albitization in alkali feldspars from the Shap granite. *American Mineralogist*, 82, 557-570.

LODEMANN, L., FRITZ, P., WOLF, M., IVANOVICH, M., HANSEN, B. T., & NOLTE, E. (1997): On the origin of saline fluids in the KTB (continental deep drilling project of Germany. *Applied Geochemistry*, 12, 831-849.

MAGDE, S., L., DICK, J., B., H., & HART, S., R. (1995): Tectonics, alteration and fractal distribution of hydrothermal veins in the lower ocean crust. *Earth and Planetary Science Letters*, 129, 103-119.

MARTÍNEZ-SERRANO, G., R. (2002): Chemical variations in hydrothermal minerals of the Los Humeros geothermal system, Mexico. *Geothermics*,

MARUYAMA, S., SUZUKI, K.,& LIOU, J., G. (1983): Greenschist-amphibolite transition equilibria at low pressures. *Journal of Petrology*, 24, 583-604.

MCDOWELLL, D., S. (1986): Composition and structural state of coexisting feldspars, Salton Sea geothermal field. *Mineralogical Magazine*, 50, 75-84.

MCLEOD, R., L., & STANDON, R., L. (1984): Phyllosilicates and associated m,inerals in some Paleozoic stratiform sulphide deposits of south eastern Australia. *Economic Geology*, 79, 1-22.

MENARD, T., & SPEAR, F., S. (1996): Interpretation of plagioclase zonation in calcic pelitic schist, south Strafford, Vermont and the effects on thermobarometry. *Canadian Mineralogist*, 34, 133-146.

MEYER, C., & HEMLEY, J., J. (1967): Wall Rock Alteration. *Geochemistry of hydrothermal ors deposits*, BARNES, H., L., University Park, Pennsylvania, Holt, Reinhart & Winston, Inc., 670.

MILLER, A., J., CARTWRIGHT, I., & BARNICOAT, A., C. (1998): The formation of albite veins in high-pressure terrains: examples from Corsica, France and Zermatt-Saas, *9th International Symposium on Water–Rock Interaction*, 789-792

MILLER, J. A., CARTWRIGHT, I., BARNICOAT, A.C., (2001): The formation of albite veins during the exhumation of high-pressure terranes: a case study from the Corsican and Zermatt-Saas Ophiolites, Western European Alps. *Journal of Metamorphic Geology*

NADEN, J. (1996): CalcicBrine 1.5: a Microsoft Excel 5.0 add-in for calculating salinites from microthermometric data in the system NaCl-$CaCl_2$-H_2O., *PACROFI VI*, University of Wisconsin

NAKANO, T. (1989): Fluctuation model for compositional heterogeneity of skarn clynopiroxenes. *Geochemical Journal*, 23, 91-99.

NAKANO, T., YOSHINO, T., SHIMAZAKI, H., SHIMIZU, M. (1994): Pyroxene composition as an indicator in the classification of skarn deposits. *Economic Geology*, 89, 1567-1580.

NEKVASIL, H., & BURNHAM, W., C. (1987): The calculated individual effects of pressure and water content on phase equilibria in the granite system in Mysen, B. O., ed., magmatic processes. *Phisicochemical principles: Geochemical Society, University Park*, 500 pp.

OLIVER, S., H., N., & BONS, P., D. (2001): Mechanisms of flow and fluid-rock interaction in fossil metamorphic hydrothermal systems inferred from vein-wallrock patterns, geometry and microstructure. *Geofluids*, 1, 2, 137-162.

O'NEIL, J., R., CLAYTON, R., N., & MAYEDA, T., K. (1969): Oxygen isotopic fractionation in divalent metal carbonates. *Journal of Chemical Physics*, 51, 5547-5558.

ORVILLE, P., M. (1963): Alkali ion exchange between vapour and feldspar phases. *American Journal of Science*, 261, 201-237.

OXTOBY, N. (2000): Re-equilibration of aquaeous inclusions in carbonate cements by freezing: implications for geologic studies.

PARSONS, I., & LEE, M., R. (2000): Alkali Feldspars as microstructural markers of fluid flow. *Hydrogeology of Crystalline Rocks.*, STOBER, I., & BUCHER, K., Kluwer Academic Publishers, 27-50.

PENNACHIONI, G., DI TORO, G., BRACK, P., MENEGON, L., & VILLA, I., M. (2006): Brittle-ductile-brittle deformation during cooling of tonalite (Adamello, Southern Italian Alps). *Tectonophysics*, 427, 171-197.

PREECE III., R., K., & BEANE, R., E. (1982): Contrasting evolutions of hydrothermal alteration in quartz monzonite and quartz diorite wall rocks at the Sierra porphyry copper deposit, Arizona. *Economic Geology*, 77, 1621-1641.

PRICE, B., G. (1972): Minor elements in pyrites from the Smithers Map area, B. C. and exploration applications of minor elements studies., University of British Columbia, PhD Thesis, 270.

RAITH, M. (1976): The Al-Fe(III) epidote miscibility gap in a metamorphic profile through the Penninc series of the Tauern window, Austria. *Contribution to Mineralogy and Petrology*, 57, 99-117.

RAVASZ BARANYAI, L. (1969): Eclogite from the Mecsek Mountains, Hungary. *Acta Geologica Academiae Scientiarum Hungaricae*, 13, 315-322.

ROEDDER, E. (1984): Fluid Inclusions., Washington, DC., Geological Society of America, 644.

RUGGIERI, G., CATHELINEAU, M., BOIRON, M., & MARIGNAC, C. (1999): Boiling and fluid mixing in the chlorite zone of the Larderello geothermal system. *Chemical Geology*, 154, 1-4, 237-256.

SCIFFMAN, P., ELDERS, W., A., WILLIAMS, A., E., MCDWELL, S. D., & BIRD, D., K. (1984): Activ metasomatism in the Cerro Prieto geothermal syste, Baja California, Mexico: a telescoped low-pressure, low-temperature metamorphic facies series. *Geology*, 12, 12-15.

SECK, H., A. (1971): Koexistierende Alkalifeldspäte und Plagioklase im System $NaAlSi_3O_8$-$KAlSi_3O_8$-$CaAl_2Si_2O_8$-H_2O bei Temperaturen von 650 °C bis 900 °C. *Neues Jahrbuch für Mineralogie Abhandlungen*, 115, 315-345.

SHAU, Y., H., PEACOR, D., R., & ESSENE, E., J. (1990): Corrensite and Mixed-layer chlorite/corrensite in metabasalt from northern Taiwan: TEM/AEM, EMPA, XRD, and optical studies. *Contribution to Mineralogy and Petrology*, 105, 123-142.

SHEPPERD, T. J., RANKIN, A. H., C., & ALDERTON, D. H. M. (1985): A Practical Guide to Fluid Inclusion Studies., Glasgow and London, Blackie,

SHIKAZONO, N. (1984): Compositional variations in epidote from geothermal areas. *Geochemical Journal*, 18, 181-187.

STOBER, I., & BUCHER, K. (2004): Fluid sinks within the earth's crust. *Geofluids*, 4, 143-151.

STOBER, I., & BUCHER, K. (2005): The upper continental crust, an aquifer and its fluid: hydaulic and chemical data from 4 km depth in fractured crystalline basement rocks at the KTB test site. *Geofluids*, 5, 8-19.

SZEDERKÉNYI, T. (1976): Barrow -type metamorphism int he crystalline basement of South-East Transdanubia. *Acta Geol. Ac. Sci. Hung.*, 20, 47-61.

SZEDERKÉNYI, T. (1979): A mecseki ópaleozóos-prekambriumi alapszelvények komplex földtani feldolgozása.,

SZEDERKÉNYI, T. (1981): Character of metamorphism of Görcsöny Hill crystallins (SE Transdanubia, Hungary) based on the Baksa-2 deep drilling. *Acta Geol. Ac. Sci. Hung.*,

SZEDERKÉNYI, T. (1983): Origin of amphibolites and metavolcanics of crystalline complexes of south transdanubia, Hungary. *Acta Geologica Hungarica*, 1-2, 26, 103-136.

SZEDERKÉNYI, T. (1984): Az alföld kristályos aljzata és földtani kapcsolatai (Crystalline basement of the Great Hungarian Plain and its geological connections)., University of Szeged, Department of Mineralogy, Geochemistry and Petrology, PhD, 184.

SZEDERKÉNYI, T. (1996): Metamorphic formations and their correlation in the Hungarian part of Tisia Megaunit (Tisia Composite Terrane). *Acta Mineralogica-Petrographica, Szeged*, XXXVII, 143-160.

TARIELLA, B., R., I., M. (2004): Chemical reaction path modeling of hydrothermal mineralization in the Tongonan geothermal field, Leyte (Philippines). *Geothermics.*, 33, 143–179.

TARNAI, T. (1997): Ore minerals from the key section of the Baksa Complex (W Baranya hills, Hungary). *Acta Mineralogica-Petrographica*, XXXVIII, Supplementum, 119-133.

TARNAI, T. (1998): Mineralogical-petrological study on ore vein penetrated by the key-borehole Baksa No. 2 SE Transdanubia, Hungary. *Acta Mineralogica-Petrographica*, XXXIX, 21-34.

TSUJIMORI, T. (1997): Omphacite-diopside vein in an omphacite block from the Osayama serpentinite melange, Sangun-Renge metamorphic belt, southwestern Japan. *Mineralogical Magazine*, 61, 845-852.

VAN MARCKE DE LUMMEN, G., & VERKAEREN, J. (1986): Physicochemical study of skarn formation in pelitic rock, Costabonne peak area, eastern Pyrenees, France. *Contribution to Mineralogy and Petrology*, 93, 77-88.

WALLIN, B., & PETERMAN, Z. (1999): Calcite fracture fillings as indicators of paleohydrology at Laxemar at the Aspö Hard Rock Laboratory, southern Sweden. *Applied Geochemistry*, 14, 953-962.

WANG, S. W., P., J. (2001): Geochemistry and origin of Proterozoic skarns at the Mount Elliot Cu-Au-(Co-Ni) deposit, Cloncurry district, NW Queensland, Australia. *Mineralium Deposita*, 36, 109-124.

WEBBER, K., . L., FALSTER, A., U., SIMMONS, W., B., & FOORD, E., E. (1997): The role of diffusion-controlled oscillatory nucleation of line rock in pegmatite-aplite dikes. *Journal of Petrology*, 38, 1777-1791.

WEN, S., & NEKVASIL, H. (1994): SOLVCALC: an interactive graphics program package for calculating the ternary feldspar solvus and for two feldspar geothermometry. *Computers and Geosciences*, 20, 6, 1025-1040.

WHEELER, R., S., BROWNE, P., R., L., & RODGERS, K., A. (2001): Iron-rich and iron-poor prehnites from the Way Linggo epithermal Au-Ag deposit, southwest Sumatra, and the Heber geothermal field, California. *Mineralogical Magazine*, 65, 397-406.

WHITNEY, A., J., & STORMER, C., J., JR. (1977): The distribution of $NaAlSi_3O_8$ between coexisting microcline and plagioclase and its effect on geozhermometric calculations. *American Mineralogist*, 62, 687-691.

WILKINSON, J., J., JENKIN, G., R., T., FALLICK, A., E., & FOSTER, R., P. (1995): Oxygen and hydrogen isotopic evolution of Variscan crustal fluids, south Cornwall, U. K. *Chemical Geology*, 123, 239-254.

ZANE, A., & WEISS., Z. (1998): A procedure for classifying rock.forming chlorites based on microprobe data. *Rend. Fiss. Acc. Lincei*, 9, 9, 51-56.

ZHANG, W., & FYFE, W., S. (1995): Chloritization of the hydrothermally altered bedrock at the Igarapé Bahia gold deposit, Carajás, Brazil. *Mineralium Deposita*, 30, 30-38.

ZHANG, Y. G., & FRANTZ, J. D. (1987): Determination of the homogenization temperatures and densities of supercritical fluids in the system NaCl-KCl-$CaCl_2$-H_2O using synthetic fluid inclusions. *Chemical Geology*, 64, 335-350.

ZHARIKOV, V., A., PERTSEV, N., N., RUSINOV, V., L., CALLEGARI, E., & FETTES, D., J. (2007): Metasomatism and metasomatic rocks. *Metamorphic Rocks: A classification and glossary of terms*, FETTES, D., AND DESMONS, J., New York, Cambridge University Press, 58-69.

ZHENG, Y., F., & HOEFS, J. (1993): Carbon and oxygen isotopic covariations in hydrothermal calcites. *Mineralium Deposita*, 28, 79-89.

CHAPTER 3

Near vein metasomatism along propylitic veins in the Baksa Gneiss Complex, Pannonian Basin, Hungary[*]

[*] K. FINTOR, T. M. TÓTH, F. SCHUBERT (2010): Near vein metasomatism along propylitic veins in the Baksa Gneiss Complex, Pannonian Basin, Hungary. Geologia Croatica, 63/1, 75-91.

3. Near vein metasomatism along propylitic veins in the Baksa Gneiss Complex, Pannonian Basin, Hungary

ABSTRACT

In many parts of the metapelitic (gneiss, mica schist) rock section of the Baksa Complex, significant wall-rock alteration is observable along the Ca-Al silicate veins, which show a *di* → *ep* ± *czo* →*sp* → *ab* ± *kfs* → *chl* → *adu* → *prh* → *py* → *cal* mineral sequence (FINTOR et al. 2009). These alterations appear as narrow (few cm thick) bleached margins beside thin veins, and broad alteration bands along thick veins where detailed epidotization and chloritization of the adjacent rock are recognizable. Based on petrographic and mineralogical examination of the altered wall-rocks, metasomatic zones with characteristic mineral paragenesis can be distinguished: Zone 1 (*ab* + *ttn* ± *ep*), Zone 2 (*ep* + *chl*+ *ttn* + *ab* ± *ser*), Zone 3 (*chl* + *ep* + *ser* + *rt* ± *ttn*), Zone 4 (*ser* ± *chl*). Bulk rock chemical analyses were made from the different metasomatic zones. The results show that fluid circulated in the propylitic veins caused metasomatic alteration of the wall-rock, with transport of considerable amount of Ca^{2+} toward the adjacent rocks. The hydrothermal leaching almost totally removed the K, Fe, Mg, and Mn ions from the wall rock. The main alteration processes are the epidotization and chloritization of biotite, and albitization of micas (muscovite + biotite) content of metapelites. Based on mobilization of different cations alteration was due to? to a near neutral fluid (~*pH* 5-7). The pervasive hydrothermal leaching caused significant secondary porosity (cavities) in the altered domains, which were partially filled by epidote. Fluid inclusions of cavity filling epidote indicate a similar character (T_h: 180-360 °C; Salinity: 0.2-1.6% *w*NaCl eq.) to that can be found in Ca-Al silicate veins. The alteration most probably occurred in the 360-480 °C temperature range as products of "near vein metasomatism" and the altered rock can be related to the propylite metasomatic family.

3.1. Introduction

The wall rock alteration activity of hydrothermal fluids that circulate in fractures of crystalline rock bodies of the continental crust has a significant role in different geological processes. Considerable secondary porosity may develop if metasomatic alteration is associated with leaching, and the locally increased porosity can play a pivotal role in the hydrological behaviour of otherwise low permeability crystalline rocks (MAZUREK et al. 2003; JAKOB et al. 2003). Another important aspect is that hydrothermal metasomatism can be frequently associated with formation of mineral deposits. Ore mineral deposition sometimes containing

sulphide minerals (pyrite, chalcopyrite, pyrrhotite, and sphalerite) iron oxides (hematite, magnetite), or in other cases precious metal minerals, can occur during hydrothermal metasomatism that mainly relates to magmatic intrusions (ZHARIKOV et al. 2007; SCHERBAN 1996; GRYAZNOV 1992; RUSINOV 1989). Study of wall rocks where alteration is caused by hydrothermal fluid/rock interaction, may provide important information about the thermodynamic parameters (e. g.: *pH*, *Eh*, *T*, *P*, *X*) of fluids circulated in the rock body (PARSONS & LEE 2000; KULLERUD 2000; GRESENS 1967; MEYER & HEMLEY 1967).

The study area is the Baksa Complex which represents part of the metamorphic crystalline basement of the south-western area of the Pannonian Basin. The Baksa-2 exploratory drillhole penetrated deeply into the Baksa Complex. With almost 100% core recovery, this exposed almost 1200 m of crystalline rocks of the basement. It is the most complete drillcore available from the crystalline basement of the Pannonian Basin.

A lot of evidence for postmetamorphic hydrothermal fluid migration and alteration can be observed in the drillcores of the Baksa-2 well. This alteration can be grouped into two main hydrothermal mineral parageneses. TARNAI (1997, 1998) provided detailed studies of a thick (6-7 cm) sulphide ore vein, cross cutting the metamorphic block. Ore paragenesis (*pyr+po+sp+hem+ccp+gn+pn*) and fluid inclusion studies of the vein filling minerals indicate a postmagmatic hydrothermal origin (TARNAI 1998). The other assemblage suggests that the hydrothermal effect is the occurrence of Ca-Al silicate dominant fracture filling in several Baksa gneiss samples (SZEDERKÉNYI 1979). Comprehensive examination of the latter vein-filling process was made by FINTOR et al. (2009) and they report the presence of sporadic pyrite crystals among the Ca-Al silicate minerals. Detailed mineral chemical analyses of pyrite crystals from both the Ca-Al silicate and the thick sulphide veins (FINTOR et al. 2009) exhibit similar Co/Ni ratios (1-5), which is in the range of pyrites formed in postmagmatic hydrothermal systems (PRICE 1972).

In this study, detailed petrographic, bulk rock chemical, and fluid inclusion analysis of the altered wall rocks along the Ca-Al-silicate veins was undertaken. The aims are to detect the type and physicochemical conditions of metasomatism and element mobilization that occurred along the veins, and to determine the hydrological relationship between the alteration halos and the veins.

3.2. Geological setting

The Baksa Complex (BC) is located in the SW part of the Tisza Mega unit (*Fig. 3.1*), a microplate that forms the basement of South Hungary. The Tisza Mega unit was originally part of the European margin of Neo-Tethys and was separated from the European plate by opening of the Penninic Ocean (Alpine Tethys) (GÉCZY 1973; HAAS & PÉRÓ 2004). SZEDERKÉNYI (1996) divided the pre-Alpine basement complexes of the Tisza Mega unit into three major parts: the Paraautochton, Békés-Codru (BC) and Drava terrains, and related the BC to the Drava Terrain. The metamorphic formations of the complex do not outcrop. They are instead covered by thin (50-100 m) Tertiary and Quaternary sediments in the area of the Görcsöny Ridge. The crystalline schists of the Babócsa Complex border the BC to the west (*Fig. 3.1*). The Villány deep fracture zone (KASSAI 1972), which has a NW-SE strike, separates the Baksa metamorphic block from the Mórágy Granite Complex, and Permo-Triassic sediments to the east. The Mecsekalja Tectonic Zone borders the complex in the north. It separates metamorphic rocks from non-metamorphic Mesozoic sediments of the Mecsek Mountains (*Fig. 3.1*). Further to the south, formations of the complex can be traced over the Slavonian regions, in the Papuk and Krndija Mountains.

Petrology and metamorphic evolution of the BC has been investigated by many researchers (RAVASZ-BARANYAI 1969; SZEDERKÉNYI 1976, 1983; ÁRKAI 1985; ÁRKAI et al. 1999; KIRÁLY 1996; HORVÁTH et al. 2003). The complex consists of polymetamorphic rocks, mainly gneiss, marble bearing mica-schist, dolomite, marble, and amphibolite. Five metamorphic events can be detected in the rocks of the BC. RAVASZ-BARANYAI (1969) detected a high pressure phase that was followed by a significant decompression. The peak conditions of this *P-T* path were around 1300-1500 MPa and 600-650 °C down to approximately 800 MPa and 500 °C (HORVÁTH et al. 2003). Peak conditions of the Barrowian event (SZEDERKÉNYI 1976) occurring after the previous high pressure phase, were around

750±50 MPa, and 660±20 °C according to ÁRKAI et al. (1999), but KIRÁLY (1996) suggests conditions of 500-700 MPa and 540-650 °C. After the Barrowian event, the area underwent secondary albitization and isothermal decompression down to 440±20 MPa and 650±40 °C according to ÁRKAI et al. (1999) or < 200 MPa, 400-560 °C according to KIRÁLY (1996).

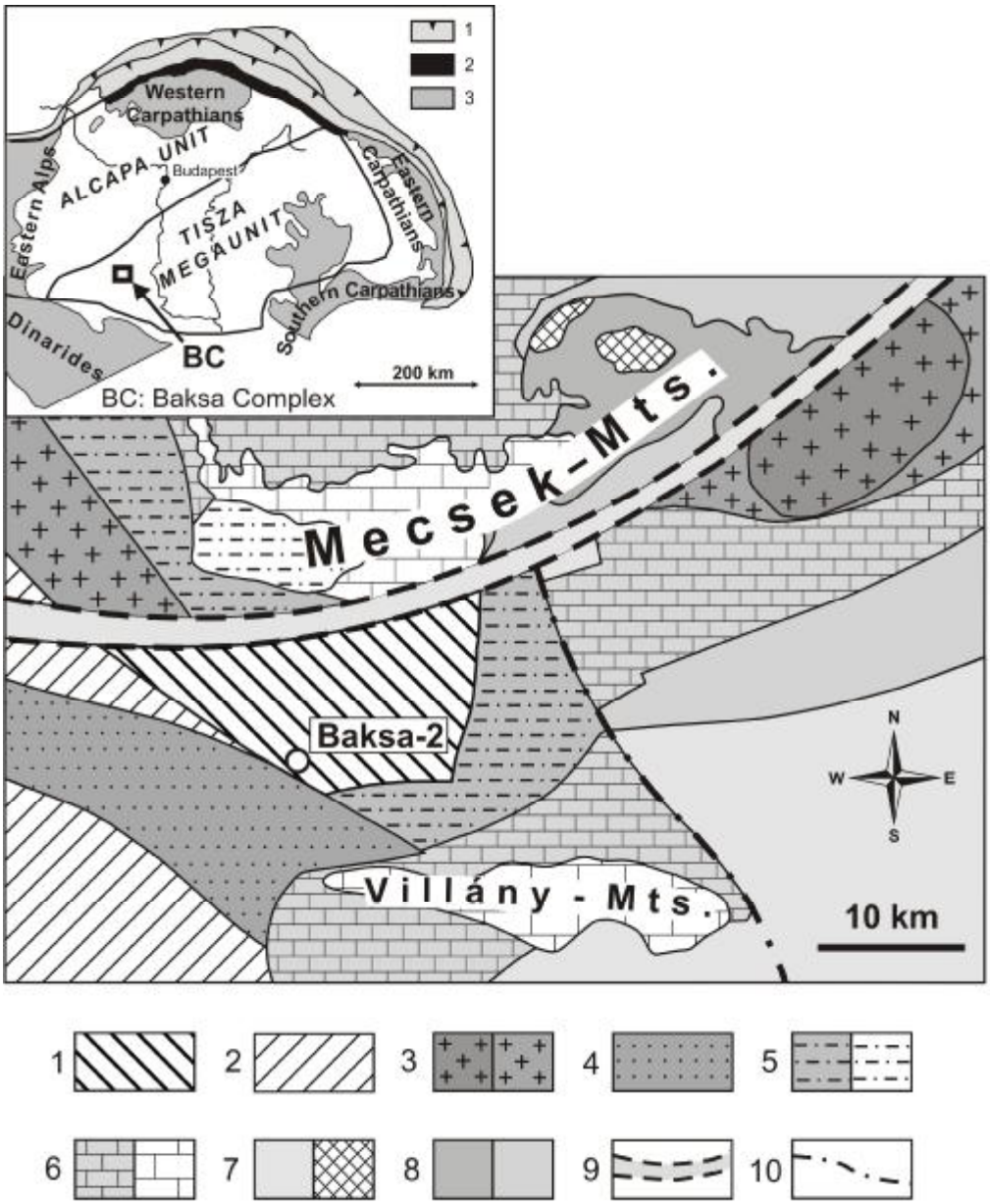

Figure 3.1. *The geological map of the Baksa Complex and its environs is presented without Tertiary and Quaternary sediments*
Legend: 1. Baksa Complex (study area), 2. Babócsa Complex, 3. Mórágy Complex (Carboniferous), 4. Carboniferous sediments, 5. Permian formations, 6. Triassic formations, 7. Jurassic formations, 8. Cretaceous formations, 9. Mecsekalja Tectonic Zone,, 10. Villány-Szalatnak deep fracture zone. Inset: Location of the study area (BC) in the Pannonian Basin (ALCAPA and Tisza mega unit are also represented on the map); Inset legend: 1. Flysch Belt, 2. Pieniny Klippen Belt, 3. Inner Carpathian Mountain Belt.

The isothermal decompression was followed by contact metasomatism related to aplite intrusions. These aplite dykes with unknown origin, caused considerable alteration but only in the carbonate rocks of the complex. Significant alteration products include epidote, diopside, garnet and a wide spectrum of sulphide minerals. There are indications of two phases of

hydrothermal ores in the rock body, an earlier phase with disseminated ores, can be distinguished form a younger formation of veins with massive sulphide infillings.

In the earlier phase, minor amounts of pyrite, and sphalerite grew sporadically in the veins. FINTOR et al. (2009) determined a Ca-Al silicate dominant mineral assemblage with a *di* → *ep* ± *czo* →*sp* → *ab* ± *kfs* → *chl* → *adu* → *prh* → *py* → *cal* mineral sequence (mineral abbreviations after SIIVOLA & SCHMID 2007, except for adularia: adu). A detailed geochemical and fluid inclusion investigation of the vein filling minerals indicates that mineral precipitation occurred during cooling of the hydrothermal system. The *T-X* character of the fluid changed from high temperature (467-370 °C) and low salinity (0.2-1.5% *w*NaCl eq.) down to lower temperature (~150 °C) and low- to moderate salinity (3-6% *w*NaCl eq.) appear in fluid inclusions of diopside, epidote, and calcite phases (FINTOR et al. 2009). Chlorite thermometry data (300 → 140 °C) also supports decreasing temperatures during the vein filling process. Many of these studied veins are surrounded by 0.5-2 cm thick alteration halos.

A detailed investigation of mineralogy and ore genesis of the veins with massive sulphide ore infillings was carried out by TARNAI (1997, 1998). In a study of fluid inclusions of the quartz which was cogenetic with the later ore minerals, he determined a trapping temperature (T_t), of 240 to 300 °C and trapping pressure (P_t), of 15 – 30 MPa (TARNAI 1998). The youngest alteration phase that can be investigated in the rocks is a retrograde greenschist facies event, which caused chloritization and secondary albitization (SZEDERKÉNYI 1979). Its temperature range is assumed to be 200-400 °C by ÁRKAI et al. (1985). The beginning of this event is related to the Alpine orogeny (SZEDERKÉNYI 1984). FINTOR et al. (2008) detected traces of high salinity fluids (~20-25% *w*NaCl eq.) in the postmetamorphic quartz-carbonate veins that penetrate the rock body. Using microthermometry, they obtained conditions of approximately 80-180 °C and 20-100 MPa for the formation parameters of the quartz-carbonate veins.

The Baksa-2 exploratory well (bottom-hole: 1200 m) enables the most detailed investigation of the BC (*Fig. 3.2*). It exposes the crystalline basement formation with a total thickness of over 1100 m and near 100% core recovery. The metamorphic mass was divided (SZEDERKÉNYI 1979) into the following lithostratigraphic units:

1. *Upper marble section (57 – 224 m)*
2. *Chloritic two-mica gneiss (224 – 822 m)*
3. *Lower marble section (822 – 867 m)*
4. *Garnetiferous two-mica gneiss (867 – 922 m)*
5. *Garnetiferous two-mica schist (922 - 1200 m)*

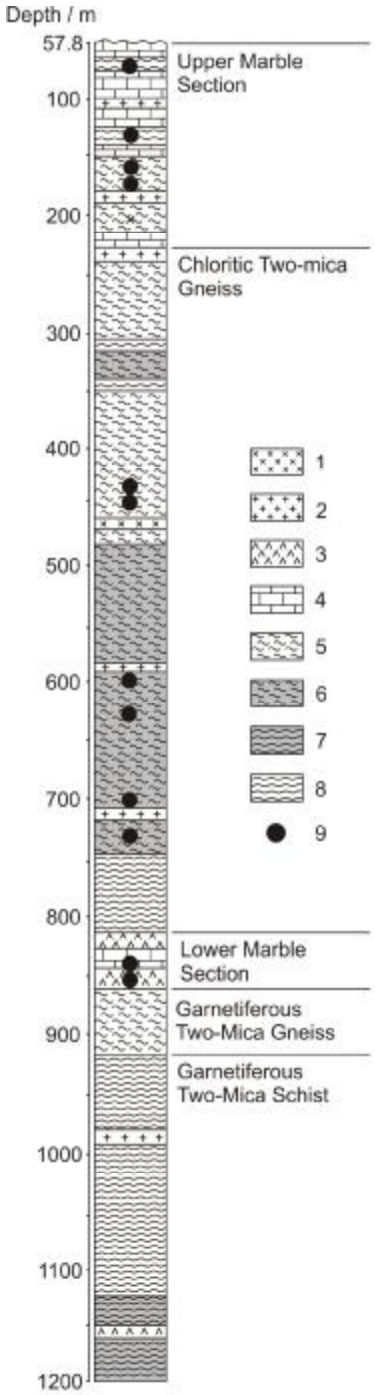

Figure 3.2. *Lithological profile of the Baksa-2 borehole (after Szederkényi 1979) Legend: 1: Biotite-andesite dyke; 2: Aplite dykes; 3: Amphibolite; 4: Marble and Dolomite marble; 5: Two-mica gneiss; 6: Chloritic gneiss; 7: Chloritic schist; 8: Two-mica schist; 9: Samples used for investigations.*

3.2.1. Upper marble section

Marble and dolomite marble are the predominant rock types in this section with gneiss and mica-schist intercalations. Aplite dykes frequently occur in the section and significant alterations in carbonate rocks can be related to them. These alterations are accompanied by the formation of calc-silicate hornfels with epidote and diopside. Ore showings caused by hydrothermal fluids are also common. The most significant ore vein (6-7 cm thick) is found at 186.4 m depth. The formation conditions and ore mineral paragenesis (pyrite, pyrrhotite, sphalerite, chalcopyrite, galena, pentlandite, hematite, covellite, marcasite) of the vein were investigated in detail by TARNAI (1997, 1998); who assumed that these veins were formed in relation to the rhyolitic volcanism that occurred near the northern margin of the Villány Mountains (FAZEKAS & VINCZE 1991).

3.2.2. Chloritic two-mica gneiss

This section is composed of two-mica gneiss and schist with some amphibolite. Significant chloritization (after biotite) is observed in some parts of the rocks (SZEDERKÉNYI 1979). Aplite dykes are rare in this section and a cross-cutting biotite-andesite dyke is observed in a fault zone at approximately 460 m depth.

3.2.3. Lower marble section

This section is comprised of amphibolites, although marble intercalations are the most important rock type of the section. The marble bands are almost pure dolomite. This section is very rich in aplite dykes, which caused alterations similar to those found in the upper marble section.

3.2.4. Garnetiferous two-mica gneiss

This rock section is dominated by gneiss with some mica schist intercalations. Large garnet grains (> 2 cm in diameter) are a common occurrence throughout the section. Aplite dykes do not occur in this section.

3.2.5. Garnetiferous two-mica schist

This section consists predominantly of mica schist, with lesser amounts of gneiss and some amphibolite. Garnets with similar characteristics to those of the garnetiferous two-mica gneiss also occur in considerable amounts. One aplite dyke was discovered in the section, which suffered comprehensive epidotization and tourmalinization.

3.3. Samples and methods

Samples used for analysis were collected throughout the profile of the Baksa-2 drillhole, as detailed locations on Fig. 3.2 show. Mineral abbreviations used in the whole study are after SIIVOLA & SCHMID (2007).

X-ray element maps and bulk rock chemical analyses were made using a Horiba Jobin Yvon XGT 5000 X-ray fluorescence spectrometer. Beam diameter was 100 μm and acceleration voltage was 30 kV in each case. Bulk analyses were made from 5 mm x 5 mm areas of rock surfaces. Analyzed areas were divided into 512 x 512 pixels with 0.01 mm^2 size of each pixel. Natural standards were used for standardization of each measured element. The Surfer 8 surface mapping system was used for the representation of element maps obtained by XRF analyses.

Isocon analysis was made from bulk rock chemical data using the computer program GEOISO (COELHO 2006). This program can calculate and plot (Isocon diagram), the mass and volume changes that can occur in a wide variety of open system geological processes. The Isocon diagram is based on the study of GRANT (1986, 2005) and is a simple solution to GRESENS (1967) equation for metasomatic alteration.

Gresens' basic argument is that some components are likely to have been immobile during the alteration process, and if these can be identified, they can be used to establish any change in volume which has taken place. Gains or losses of other components can then be calculated, assuming that the volume change is a factor common to the behaviour of all components. GRESENS (1967) shows that the transformation of a generic rock A into another generic rock B can be expressed as follows:

$$X_n = \left[f_v \left(g^B / g^A \right) C_n^B - C_n^A \right] a$$

where "X" is the mass change of component "n" relative to "a", "n" the considered component, "g" the densities of each rock, "v" the volume of each rock, "f_v" a volume factor, "a" the mass of the original sample (A) and "C" the concentration.

Even if efficient, the Gresens' method is neither easy nor practical to use. GRANT (1986) proposed a more direct and easier process of using Gresens' equation in the following expression:

$$C_i^f = \left(M^o / M^f \right) \left(C_i^o + \Delta C_i \right)$$

Where "C_i^f" is the resulting concentration of component "*i*", "M^o" is the mass of the original, while "M^f" is the mass of the transformed rock, "C_i^o" is the original concentration of component "*i*" while "ΔC_i" is the change of concentration of component "*i*".

For each component there is an equation of this form, in which (M^o/M^f) is constant. The "perfectly inert" elements must define a line $C_i^f = f\left(C_i^o\right)$, of slope M^o/M^f passing through the graph origin. The line connecting "points with the same concentration", GARY et al. (1974), is defined as an "isocon". Using the computer software GEOISO, the whole rock mass change (M^f-M^o/M^o) and volume change (V^f-V^o/V^o) are also calculable. The program estimates the element mass changes during alteration using two different approaches. In one case the program compares each elements mass change to the original rock mass:

$$\left(M_i^f - M_i^o\right)/M^o = \left(M^f/M^o\right)C_i^f - C_i^o$$

where M_i^f is the mass of component "*i*" in the transformed rock, and M_i^o is the mass of component "*i*" in the original rock. Alternativley, the program compares each elements mass change to its mass in the original sample:

$$\left(M_i^f - M_i^o\right)/M_i^o = \left(M^f/M^o\right)C_i^f / C_i^o - 1$$

Given the better approach, the latter equation was used in this study to estimate element mass changes. In our study we use the nomenclature and abbreviations by GRANT (1986).

Densities of the different metasomatic zones were calculated using the *THERIAK* (HOLLAND & POWELL 1998; DE CAPITANI 1994; DE CAPITANI & BROWN 1987) thermodynamic program package.

Fluid inclusions were studied in 75-150 µm double-polished thick sections prepared from the vein filling minerals. Microthermometric measurements were carried out by means of a Linkam THMSG 600 heating-freezing stage, operating over a temperature range from -190 to 600 °C. Synthetic fluid inclusions were used to calibrate at -56.6, 0.0 and 374.0 °C. The accuracy of the data is ±0.2 °C under freezing and ±0.5 °C under heating conditions. An Olympus LMPlanFI 100X objective was used to analyze the inclusions. The cycling method (GOLDSTEIN & REYNOLDS 1994) was used to determine the last ice melting temperatures, and each melting of ice occurred in the presence of a vapour phase. Estimations of volume fractions of vapour bubbles ($\varphi_{vap}=V_{vap}/V_{liq+vap}$) were obtained from area analysis of a two-dimensional projection of the fluid inclusions. Terms and symbols of DIAMOND (2003) were

used. The computer package *FLUIDS* (BAKKER 2003) was used to calculate fluid properties. The program *AqSo2e* was used to calculate salinities in the NaCl-H_2O systems (NADEN 1996) based on the equivalent *w*% principle. The program *BULK* (BAKKER 2003) allowed us to calculate the bulk fluid properties molar volume (V_m), and bulk composition of individual fluid inclusions. This calculation was accomplished using a purely empirical thermodynamic model, the equation of state for electrolyte-bearing aqueous solutions of KRUMGALZ et al. (1996) and the volume fractions of the liquid phase of the inclusions at room temperature.

A Jobin Yvon LABRAM confocal Raman spectrometer, equipped with a frequency doubled Nd-YAG laser (100 mW, 532.2 nm), with a 100X/0.80 objective lens was used to identify fluid phases in inclusions. The spectrometer was calibrated using a silicon chip. The spectral resolution of the instruments was 4 cm^{-1} and the spatial resolution was a few μm^3. The acquisition time was 100 s with 20 s accumulation periods in each spectrum.

3.4. Results

3.4.1. Petrography and mineralogy

In many parts of the metapelitic (gneiss, mica schist) section of the BC, significant wall-rock alteration is observable along Ca-Al silicate veins (*Fig. 3.3/a, b*). These alterations appear as symmetrical narrow (up to few cm thick) bleached margins beside thin veins and broad alteration bands along thick veins where epidotization and chloritization of the adjacent rock are recognizable.

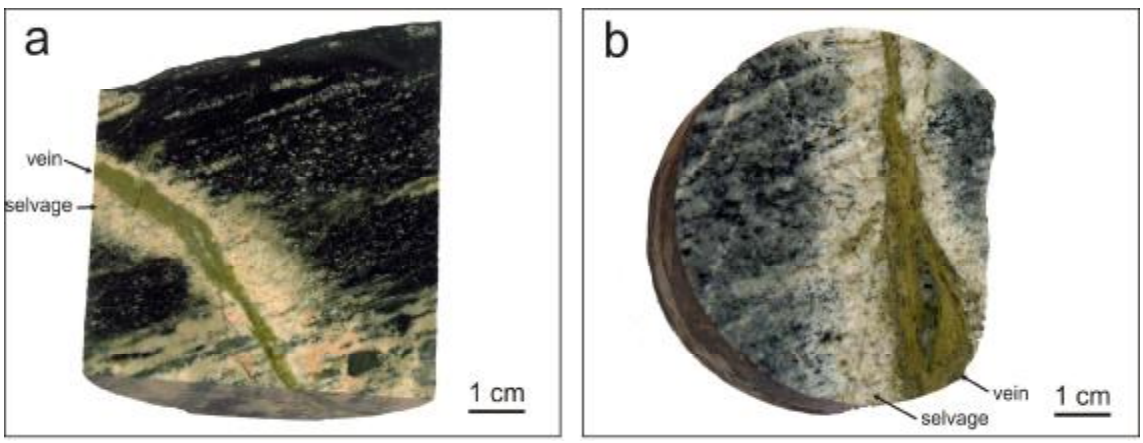

Figure 3.3. *Typical symmetrical wall-rock alteration patterns along propylitic veins*
a) Symmetrical bleached selvage along $V_{cpx\text{-}ep}$ vein (wall-rock: biotite gneiss);
b) symmetrical bleached selvage along $V_{ep\text{-}chl}$ vein (wall-rock: chloritic two-mica gneiss)

The following mineralogical characteristics were observed from the veins toward the unaltered wall rocks.Very close to the vein wall (in a 2-5 mm thick band) the feldspar porphyroblasts (albite) exhibit a turbid appearance because of micro-sized pores (<2 μm fluid inclusions), that fill the entire grain (*Fig. 3.4/a, c*). The micas (muscovite+biotite) of the unaltered wall rock found among feldspar porphyroblasts are totally replaced by albite. These albite pseudomorphs form elongated grains with irregular grain boundaries (*Fig. 3.4/a*) and frequently contain tiny euhedral titanite inclusions (*Fig. 3.4/b*). In both the albite pseudomorphs and in the albite porphyroblasts, small (<0.5 mm) cavities occur in significant amounts. Euhedral albite crystals have frequently grown on the walls of the cavities (*Fig. 3.4/c*). The cavities are filled with epidote that often shows a characteristic zoned growth pattern (*Fig. 3.4/d*). The alteration mineral paragenesis of this domain is: *ab + ttn±ep*

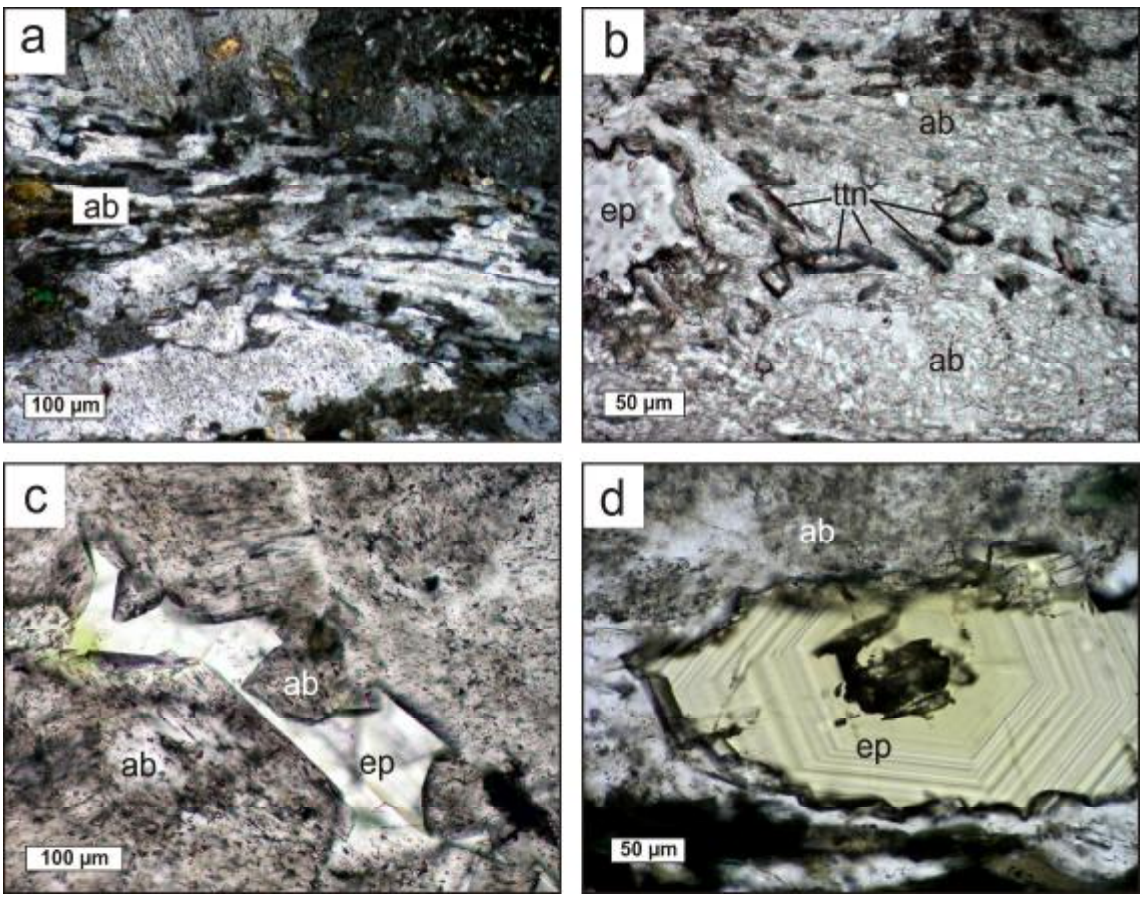

Figure 3.4. *Alteration mineral assemblages in the selvage closest to the veins*
a) Irregularly bordered elongated albite pseudomorph after mica (+N); b) group of euhedral titanite inclusions in albite pseudomorph (1N); c) euhedral albite crystal growth in cavity filled by epidote (note the many micro pores in albite) (1N); d) well developed growing zonation in a cavity filling epidote crystal (1N)

Towards the wall rock the amount of albite pseudomorphs after micas markedly decreases. The amounts of micro-pores observable in the albite porphyroblasts also gradually decreases. Small patches of sericite inclusions appear in the feldspar crystals and their amount progressively increases towards the wall-rock. Epidote and chlorite replacement after biotite become dominant in the altered domains of the wall-rock (*Fig. 3.5/a-f*). Well developed epidote and chlorite pseudomorphs occur in the formerly mica rich bands (*Fig. 3.5/a*). Among the epidote and chlorite pseudomorphs, euhedral titanite crystals frequently occur (*Fig. 3.5/*b). Elongated cavities in the strongly epdotized metapelites, are sometimes filled by very fine grained epidote (*Fig. 3.5/c*). Nevertheless epidote occurs as hypidiomorphic inclusions in chlorite along the cleavage (*Fig. 3.5/d*). In some places, anhedral epidote aggregates "float" in a chlorite rich matrix (*Fig. 3.5/e*) together with anhedral fusiform quartz grains. Here, epidote shows strongly dissolved surfaces and is composed of very fine epidote grains (*Fig. 3.5/f*). Among the little grains, elongated hypidiomorphic, almost clear epidote crystals are observable (*Fig. 3.5/f*). The alteration mineral paragenesis is: *ep* + *chl* + *ttn* + *ab* ± *ser*.

Towards the unaltered wall-rock, the amount of epidote replacing biotite decreases and chloritization of biotite becomes characteristic. Furthermore, increasing numbers of biotite relics can be observed in the chloritized domains (*Fig. 3.6/a, b*). Titanite is almost totally absent from this area, but acicular sagenite rutile inclusions can occasionally be observed in the chlorite pseudomorphs (*Fig. 3.6/c*). Muscovite does not show any alteration except for minor sericitic recrystallization at some places. The alteration mineral paragenesis is: *chl* + *ep* + *ser* + *rt* ± *ttn*.

In the unaltered wall rock part of the alteration zones, sericite is the major alteration mineral. It occurs as tiny lamellar inclusions in feldspars, and frequently forms sericitic rims around the clear cores of feldspar grains (*Fig. 3.6/d*). Micas show a fresh appearance except for partially chloritized biotite flakes. Epidote occurs only as a cavity filling mineral phase, which frequently occurs, even in the unaltered wall-rock far from alteration zones. Alteration mineral paragenesis in this domain is: *ser* ± *chl*.

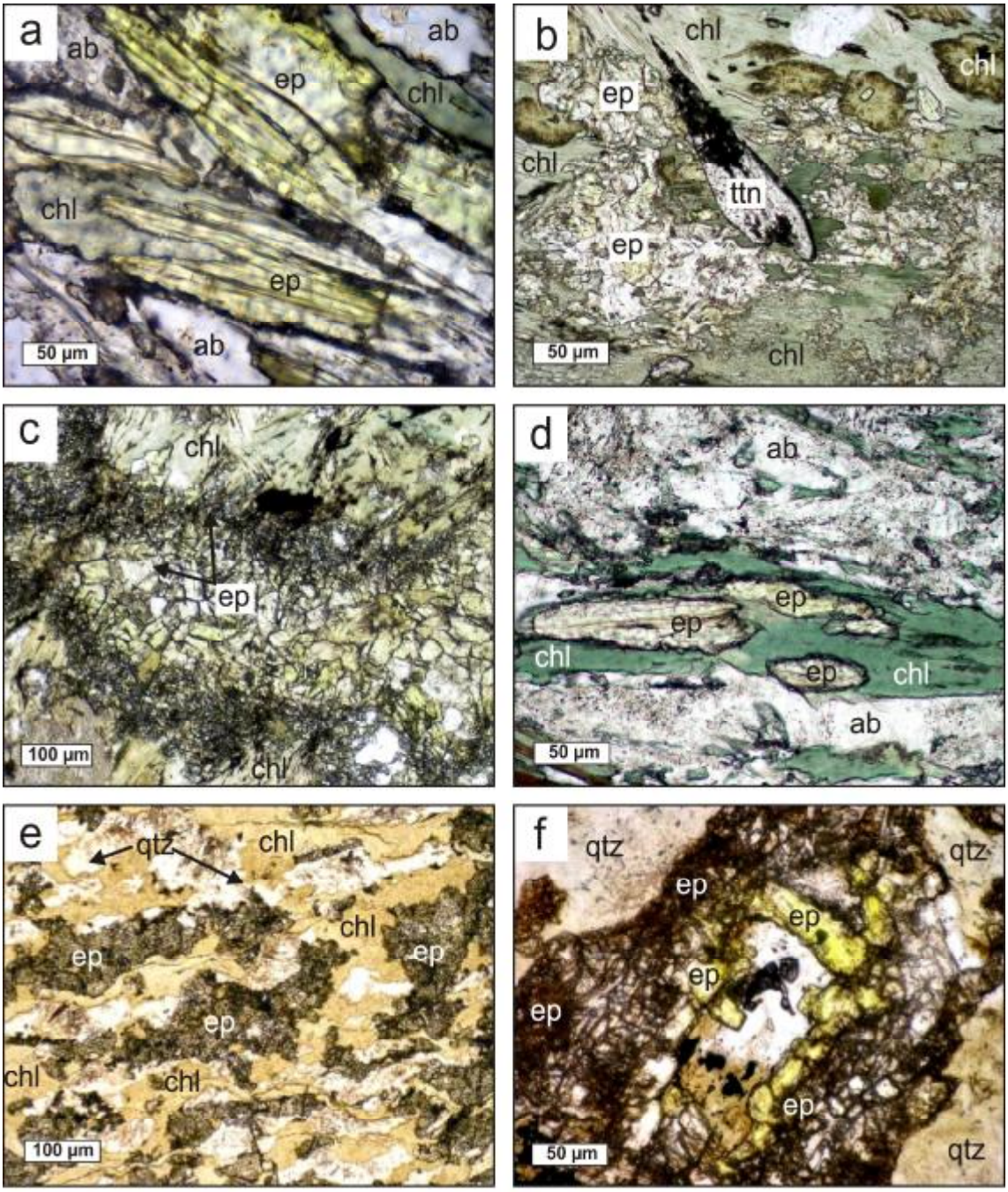

Figure 3.5. *Alteration mineral assemblages from the most epidotized and chloritized parts of the selvage*
a) epidote and chlorite pseudomorphs after biotite (+N); b) euhedral titanite crystal among mass of replacive epidote and chlorite (1N); c) elongated cavities filled by fine grained epidote crystals in chlorite matrix (1N); d) epidote pseudomorphs as inclusions in chlorite replace biotite (1N); e) fine grained anhedral epidote aggregates among chlorite and quartz rich bands along schistosity (1N); f) subhedral elongated epidote crystals among fine grained anhedral epidote (1N)

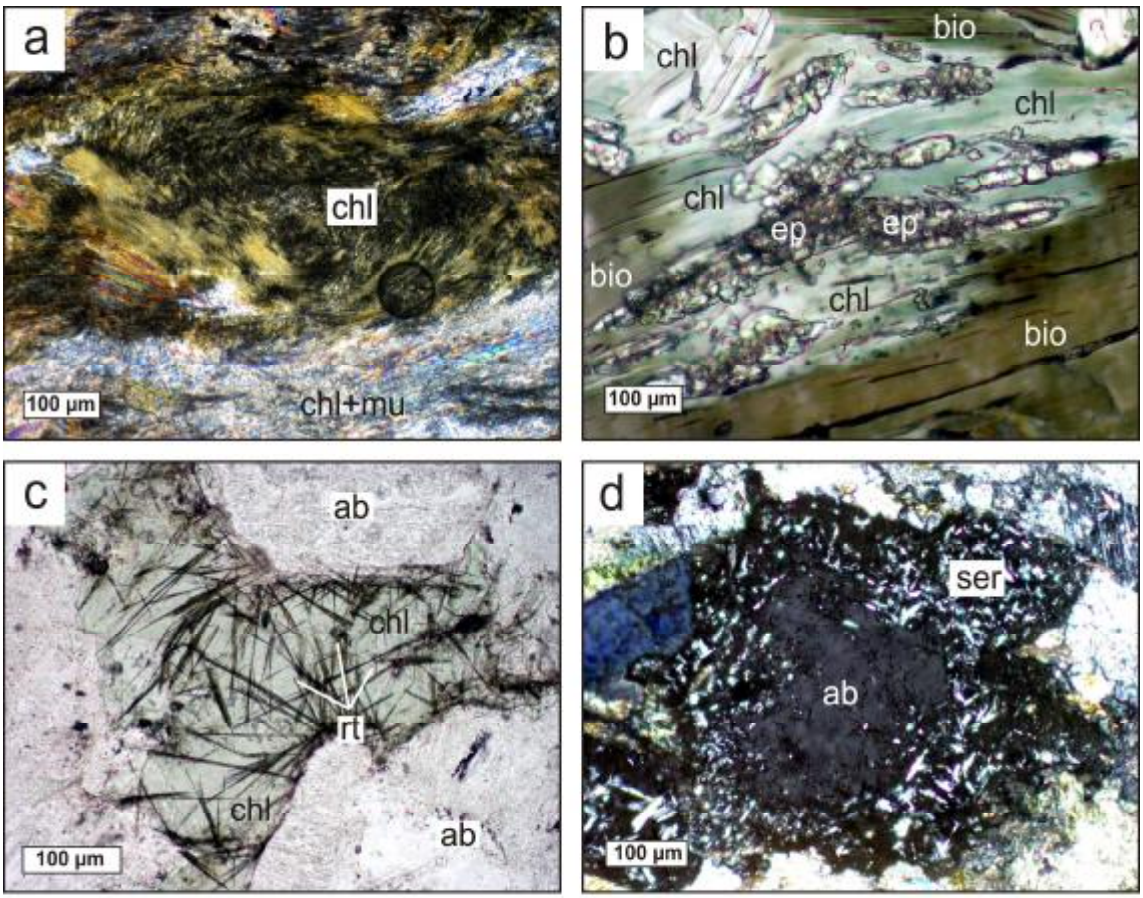

Figure 3.6. *Alteration mineral assemblages in the selvage closest to the unaltered wall-rock a) Chlorite rich band with muscovite in the strongly chloritized domains (+N); b) chloritization and epidotization of biotite (1N); c) acicular rutile inclusions in chlorite pseudomorph after biotite (1N); d) sericitization of feldspar, albite crystal core with a well developed sericite crown (+N).*

3.4.2. Element maps and bulk rock chemistry

Element distribution maps were made from the veins and their adjacent environments including alteration halos and unaltered wall-rocks of gneiss and mica schist (*Fig. 3.7*). The results show that characteristic element distribution patterns can be observed along the studied veins. Based on X-ray maps, the most characteristic distribution patterns can be observed in the case of Si, Fe, Ca, K, and Ti in the veins and their immediate environments (*Fig. 3.7*). Bulk rock analyses made from domains show individual alteration parageneses. Results are summarized in *Table 3.1* where the numbers in brackets (1 to 4) on the head of the columns refer to the different domains (show individual mineral parageneses), from vein to wall rock. The results of bulk rock chemical analyses (*Table 3.1*) support the estimations from element maps. Besides the obvious differences between margins and unaltered wall-rock, with regard to their composition (*wt*%), the rock density data show that the bulk rock density markedly increases from the veins toward the adjacent rocks (*Table 3.1*).

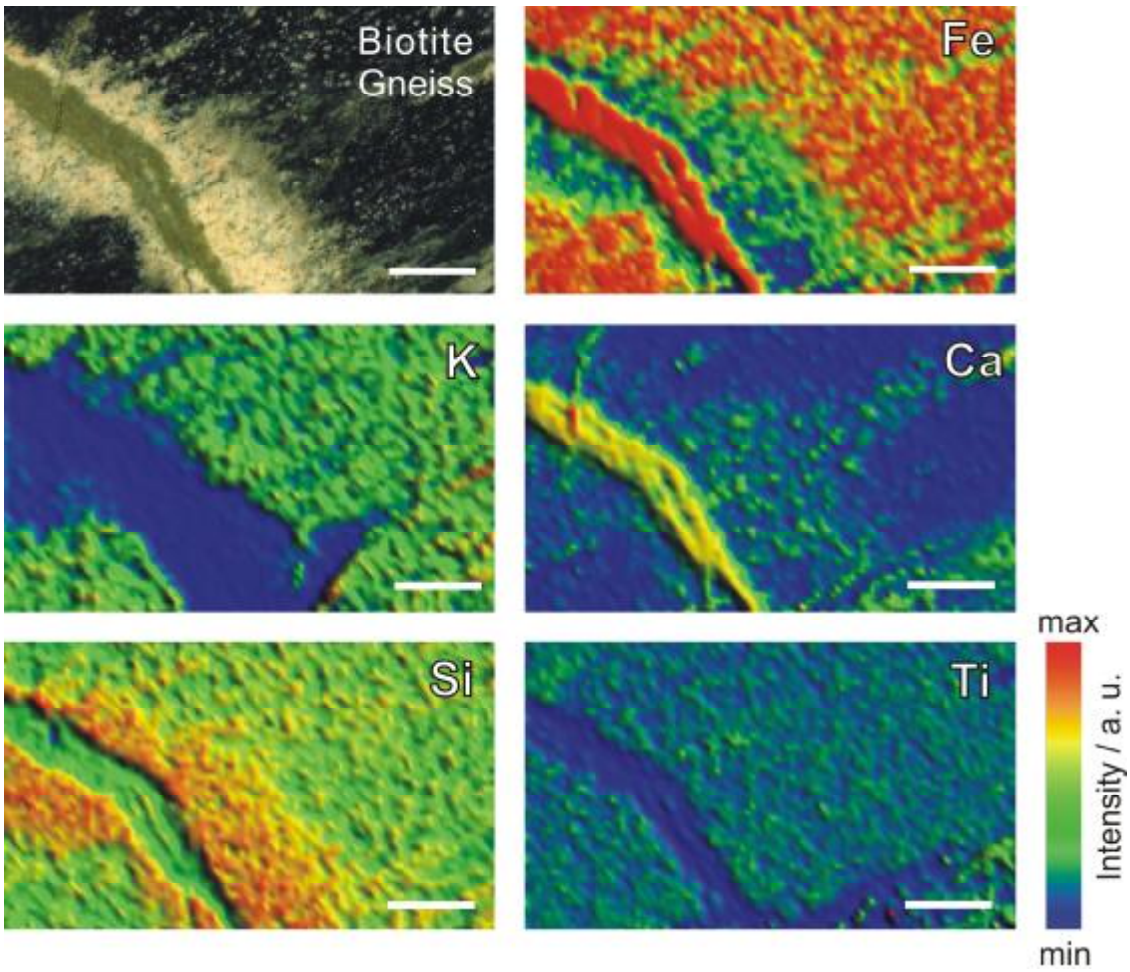

Figure 3.7. *X-ray element maps about a vein with characteristic symmetrical selvage (3D surfaces were constructed by Surfer 8), where relief and color intensity represent the relative concentration of the different elements. Bar scale is 1 cm.*

Table 3.1. *Whole rock chemical data from the selvage and the unaltered wall-rock*
Numbers 1 to 4 in brackets at the head of the columns refer to domains characterized by individual alteration mineral paragenesis. Legend: (1) ab+ttn; (2): ep + chl + ttn + ab ± ser; (3): chl + ep + ser + rt ± ttn; (4): ser ± chl.

Oxides (wt%)	637 (1)	637 (2)	637 (3)	637 (4)	637 UA (average of 4 measurements)
SiO_2	68.11	66.53	64.80	60.59	60.59
TiO_2	0.95	0.88	0.85	0.91	0.88
Al_2O_3	17.65	18.09	19.19	19.05	19.07
Fe_2O_3	1.15	1.48	2.10	5.47	7.21
MnO	0.10	0.12	0.14	0.19	0.30
MgO	0.00	0.26	0.78	1.33	1.09
CaO	4.25	4.09	3.84	4.07	2.10
Na_2O	6.74	5.99	4.63	5.43	5.23
K_2O	0.31	1.72	2.98	2.27	2.70
P_2O_5	0.43	0.57	0.41	0.38	0.56
Total	99.69	99.73	99.72	99.69	99.73
Density (g/cm^3)	2.66	2.66	2.72	2.76	2.77

3.4.3. Fluid inclusion petrography and microthermometry

Analyses were made of fluid inclusions from cavity filling epidote (*Fig. 3.4/d*) and elongated epidote crystals that occur among fine grained epidote aggregates (*Fig. 3.5/f*). The four selected samples originated from 80.6 m, 436.2 m, 730 m, and 858.8 m depths in the drill hole.

In cavity filling epidote grains (*Fig. 3.8/a*), four types of fluid inclusion assemblages (FIA) can be distinguished based on fluid inclusion petrography. A group of fluid inclusions composed of solitary two phase (L+V) liquid dominant fluid inclusions occur randomly, or in small clusters in the host crystals (*Fig. 3.8/b, c*). Their longest dimension is 5-10 µm. They are not related to growth zones of the host mineral and can not be found along cleavage planes or microcracks. Definitive evidence for their primary origin is the occurrence of fluid inclusions along growth zones (GOLDSTEIN & REYNOLDS 1994; BODNAR 2003). Less conclusive is the occurrence of one, or a few inclusions, in the interiors of the minerals (BODNAR 2003) as is the case for the aforementioned group of inclusions. These inclusions are considered to be primary based on their distribution within the crystal (BODNAR 2003). Based on phase volume ratios, two primary FIAs, a P1 with higher (φ_{vap}= 0.3-0.45) and a P2 with lower (φ_{vap}~ 0.15) degree of filling values were distinguished (*Table 3.2*), although their relative ages cannot be determined.

Fluid inclusions of both assemblages contain an aqueous electrolyte solution without any detectable volatile content based on Raman data. Because eutectic melting (T_e) could not be determined in the inclusions, the chemical composition was not ascertainable. Salinity is expressed using the *w*% eq. principle (NADEN 1996). In the P1 assemblage the T_m(Ice) values are very similar; all measured values are between -1 and -0.4 °C (n=10) (*Fig. 3.8/h; Table 3.2*) indicates low salinity (0.4 – 1.6% *w*NaCl eq.). Homogenization temperatures are within the 303 – 364 °C (n=10) range (*Fig. 3.8/g, h; Table 3.2*). In the P2 FIA the T_m(Ice) values vary between -0.8 and -0.3 °C (n=6) (*Fig. 3.8/h; Table 3.2*) indicating low salinity between 0.2 and 1.2% *w*NaCl eq., while T_h values occur in a narrow range between 201 and 214 °C (n=6) (*Fig. 3.8/g, h; Table 3.2*). Fluid inclusions also occur along planes that do not reach the grain boundary of the host crystals (*Fig. 3.8/b*). Their longest dimension is 5-10 µm containing liquid and vapour phases (L+V), and show a liquid dominant (φ_{vap}= 0.4-0.45) character (*Table 3.2*). We regard these inclusions as pseudosecondary (PS) based on criteria after BODNAR (2003).

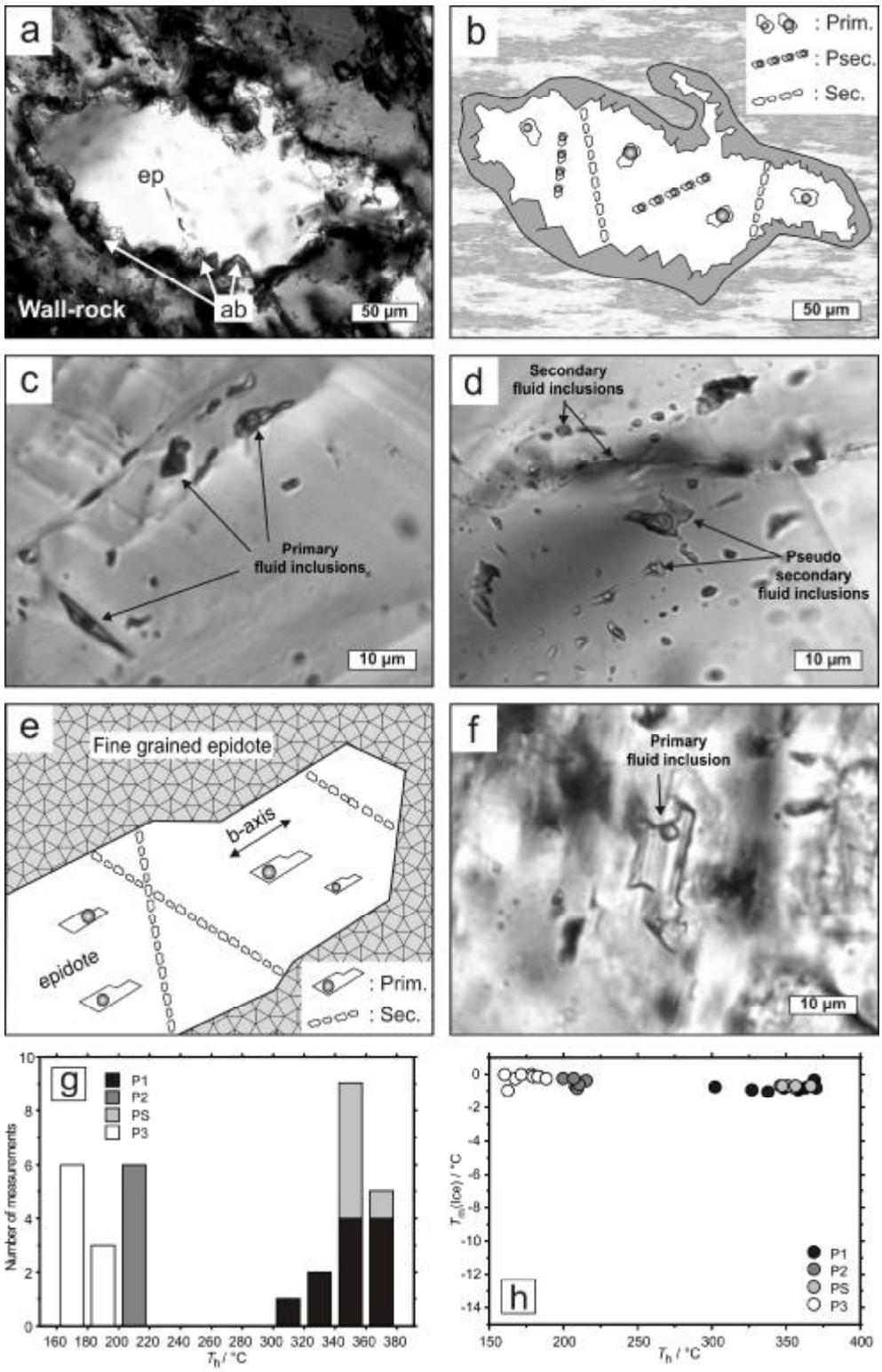

Figure 3.8. *Results of fluid inclusion study*
a) cavity filled by epidote and euhedral albite are deposited to the cavity wall (+N); b) schematic sketch about the distribution of different fluid inclusion assemblages in the cavity filling epidote; c) primary fluid inclusion assemblage in cavity filling epidote (1N); d) pseudo secondary fluid inclusion assemblage in cavity filling epidote (1N); e) schematic sketch about the appearance and distribution of different FIA in the subhedral epidote grains can be found among fine grained epidote; f) primary originated fluid inclusion in subhedral elongated epidote grain (1N); g) histograms of T_h values of each FIA ; h) T_h vs T_m(Ice) plot of each investigated FIA

In the PS assemblage the T_m(Ice) values have a very narrow range around -0.8 °C (n=6; salinity: ~ 1% *w*NaCl eq.; *Fig. 8/h; Table 3.2*), while T_h values are between 344 and 361 °C (n=6) (*Fig. 8/g, h; Table 3.2*).

Table 3.2. *Summarising table of the results of the fluid inclusion study*

Host mineral	Type	Number of Inclusions	Phases (25 °C)	φ_V	T_h (°C) V→L	T_m(Ice) (°C)	Salinity % *w*NaCl eq.
Cavity filling epidote	P1	11	L+V	0.3-0.45	303-364	-0.7±0.3	0.4-1.6
	PS	6	L+V	0.4-0.45	344-361	~-0.8	~1
	P2	6	L+V	~0.15	201-214	-0.55±0.25	0.2-1.2
	S	—	L	—	—	—	—
Elongated epidote crystals	P3	9	L+V	~0.1	163-186	-0.5±0.4	0.2-1.4
	S	—	L	—	—	—	—

Healed microcracks can be found in some parts of the host epidote, and these cracks run through the whole grains (*Fig. 3.8/b*). Fluid inclusions occurring along these healed cracks are very small (less than 3μm), they contain one phase liquid (φ_{vap} ~ 0) (*Table 3.2*) and are definitely secondary in origin. They are not appropriate for microthermometry.

In the elongated epidote crystals that occur in the fine grained epidote matrix (*Fig. 3.5/f.*), two fluid inclusion assemblages can be observed (*Fig. 3.8/e*). Two phase (L+V) liquid dominant (φ_{vap} ~0.1) aqueous inclusions, with elongated shapes (*Fig. 3.8/f; Table 3.2*) can be found in the crystals. Their longest dimensions are in the 5-15 μm range, and although they are not concentrated in a particular growth zone, their elongation in the direction of crystallographic b-axis of epidote (*Fig. 3.8/e*) indicate formation during crystal growth (KLEMD 2004). Based on these considerations, the inclusions are most probably primary in origin and denominated as P3. The measured T_m(Ice) values of fluid inclusions of P3 are between -0.1 and -0.9 °C (n=9) (*Fig. 3.8/h; Table 3.2*) indicating a low salinity fluid (0.2 – 1.4% *w*NaCl eq.; *Table 3.2*). The homogenization temperatures are in the 163 – 186 °C (n=9) interval (*Fig. 3.8/g, h; Table 3.2*).

Small (<3 μm), aqueous one phase (L), irregularly shaped inclusions can be found along trails which crosscut the entire crystals. These inclusions are secondary ones (S) in origin (*Table 3.2*). They occur in subordinate amounts and they are inappropriate for micro-thermometry.

3.5. Discussion

3.5.1. Metasomatism of the wall-rock

The occurrence of the same modification of wall-rock from narrow symmetrical margins along thin veins to wider altered domains is observable. Different types of wall rock alterations along veins have been studied in detail by many researchers (e. g. SCHERBAN 1996; OMEL'YANENKO 1978; SCHERBAN 1975; KORZHINSKII 1946). Occurrence of symmetrical alteration rims around veins is typical feature of so called "near vein metasomatism" (ZHARIKOV et al 2007).

Metasomatic zones (ZHARIKOV et al. 2007) are denominated as zone 1 to zone 4 (zone 1 represents the closest and zone 4 the farthest domain from the vein), and can be assigned on the basis of the individual mineral paragenesis of the altered domains. The metasomatic column (metasomatic facies) (ZHARIKOV et al. 2007) is built up by the following zones:

Zone 1: In this zone albite and titanite are the most characteristic minerals, mineral paragenesis*: ab* + *ttn* ± *ep.*

Zone 2: Here, the appearance of epidote pseudomorphs after biotite flakes is the most characteristic alteration feature. Mineral paragenesis is *ep* + *chl*+ *ttn* + *ab* ± *ser.*

Zone 3: The amount of epidote markedly decreases and the chlorite content increases. Sericite is more common and rutile inclusions in chlorite frequently occur. The mineral paragenesis is *chl* + *ep* + *ser* + *rt* ± *ttn.*

Zone 4: Sericitization is the most characteristic alteration process in this zone; other alteration minerals are in subordinate amounts. The mineral paragenesis consists of *ser* ± *chl.*

Whole rock chemical changes during metasomatic alteration of the wall-rock to alteration halos were evaluated by GRANT'S (1986) method using the whole rock chemical data (*Table 3.1*). Isocon diagrams were constructed to compare the alteration halo with the unaltered wall-rock. Isocon analyses were undertaken using whole rock chemical data of the different metasomatic zones detailed above. This procedure resulted in four isocon diagrams labelled from zone 1 to zone 4 (*Fig. 3.9/a.*). In order to define the best fit isocon, TiO_2 was used as an inert constituent for each isocon diagram. Titanium can be found in the altered domains as titanite and/or rutile in the pseudomorphs after biotite flakes, indicating that the Ti content of the wall rock was not changed during the alteration process (*Fig. 3.7; Table 3.1*).

The most obvious characteristics of each isocon diagram are the significant gain of CaO in the alteration halo relative to the wall-rock. The amount of the gain is almost identical from the vein to the unaltered wall-rock (*Fig. 3.9/b, c, d, e*). The contents of SiO_2, Al_2O_3, Na_2O and P_2O_5 behave very conservatively. They do not show any significant change except for a minor gain of SiO_2 (*Fig. 3.9/b, c, d*) and Na_2O close to the vein (*Fig. 3.9/b*) and a minor loss of Al_2O_3 (*Fig. 3.9/b*). Characteristic losses can be detected in concentrations of Fe_2O_3, MgO, MnO, and K_2O. The Fe_2O_3 and MnO behave similarly; their concentrations decrease gradually from wall-rock towards the vein, except closest to the wall rock where minor differences are observable. (*Fig. 3.9/b, c, d, e*). The MgO content shows an intensive decrease towards the vein and only a little gain closest to the wall-rock. Significant loss of K_2O can be observed in the alteration halo (*Fig. 3.9/b, c, e*), but a minor gain is detectable close to the unaltered wall-rock (*Fig. 3.9/d*).

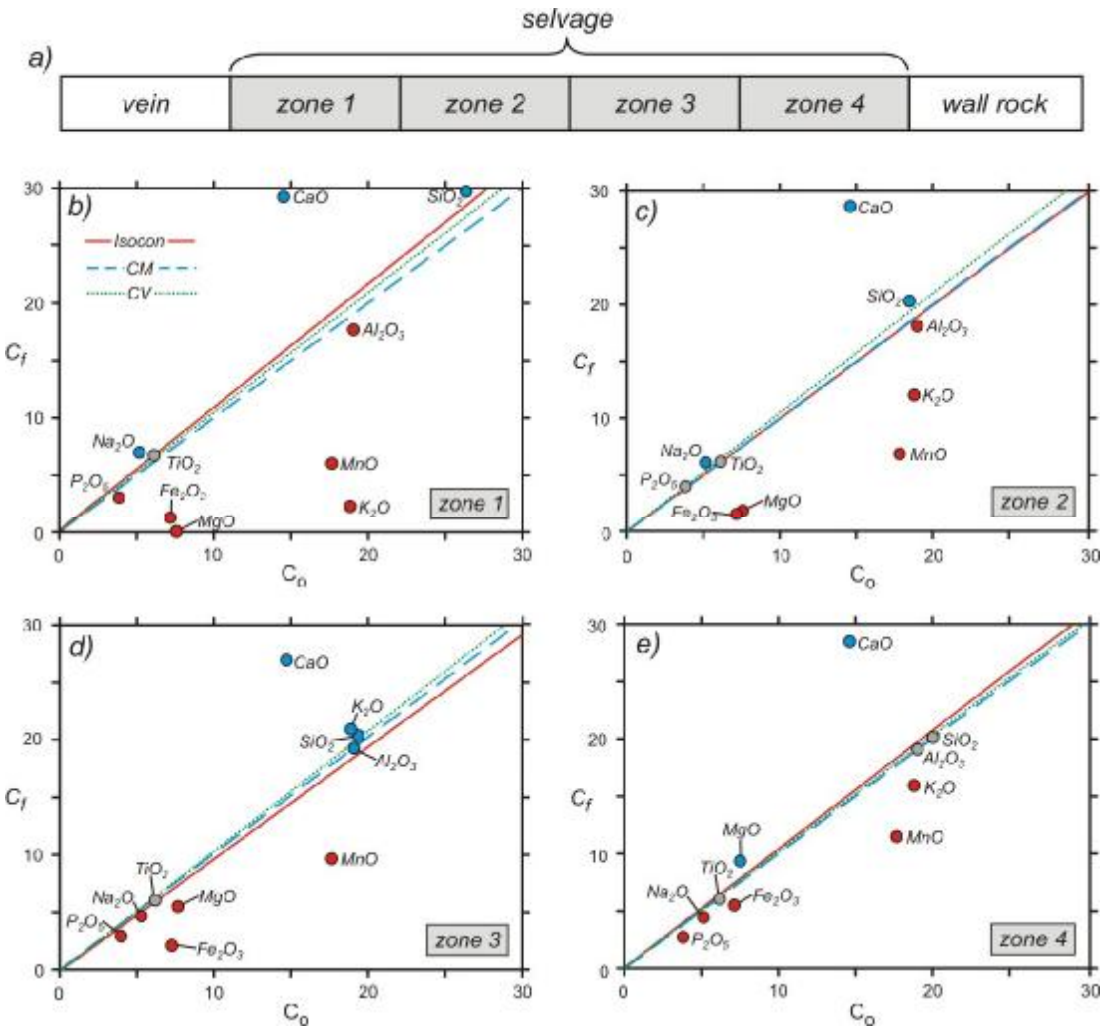

Figure 3.9. *Isocon diagrams of an altered domain occur along propylitic veins*

(where C_o refers to the concentration before, while C_f refers to the concentration after alteration) a) isocon diagram of metasomatic zone 1; b) isocon diagram of metasomatic zone 2; c) isocon diagram of metasomatic zone 3; d) isocon diagram of metasomatic zone 4. CM (dashed line) indicates constant mass-, while CV (dotted line) the constant volume line on the diagrams.

Comparison of the results of the textural observations and isocon analyses may contribute to a better understanding of those processes that induced the characterized alteration patterns in the Baksa gneisses.

The most significant alteration that occurs in great abundance from narrow margins along thin veins to massive alterations of wall-rocks, are epidotization and chloritization of biotite. In some places, albite replacement after micas is also characteristic. In order to better explain the alteration processes, we present the most significant element mass changes as a function of the original mass *(Fig. 3.10)*. Here, the relative mass changes of elements (M_i^f-M_i^o)/M_i^o) are represented as a function of distance from propylitic veins.

In the immediate few mm of the veins (*Fig. 3.10, zone 1*), micas (muscovite+biotite) are totally or partially replaced by albite (*Fig. 3.4/a*). This phenomenon is most probably due to hydrothermal leaching that almost totally removed K, Fe, Mn, and Mg, from these areas (*Fig. 3.9/b, 3.10/zone 1*). Simultaneous to the decomposition of micas, albite crystals of the wall-rock were dissolved by the fluid and were recrystallised in place of the micas. Using known compositions of reagent minerals (ÁRKAI et al. 1999; FINTOR 2005) a relevant reaction equation (1) can be formulated based on constant Al:

$$\underset{\text{muscovite}}{K_{1.7}Na_{0.3}Mg_{0.12}Fe_{0.1}Al_{3.7}(Al_{1.8}Ti_{0.06}Si_{6.2}O_{20})(OH)_4} +$$
$$\underset{\text{biotite}}{K_{0.9}Na_{0.1}(Mg_{2.1}Fe_{2.5}Al_{0.9})Al_{2.7}Ti_{0.2}Si_{5.3}O_{20}(OH)_4} + \underset{\text{quartz}}{12.743SiO_2} + 1.087\,Ca^{2+} + 7.043\,Na^+$$
$$+ 4.052\,H^+ \Rightarrow \underset{\text{albite}}{8.27\,Na_{0.9}Ca_{0.1}Al_{1.1}Si_{2.9}O_8} + \underset{\text{titanite}}{0.26\,CaTiSiO_5} + 2.6\,K^+ + 2.6\,Fe^{2+} + 2.22Mg^{2+}$$
$$+ 6.026\,H_2O \qquad (1)$$

Several researchers (e.g. RUBENACH 2005; HOLNESS 2003; ENGVIK et al. 2008; DOLEJŠ & WAGNER 2008) demonstrated that replacement of micas, (primarily muscovite and biotite) by albite, owing to fluid infiltration can play a significant role in alteration of crystalline rocks. The hydrothermal solution ensured Ca^{2+} transport in the alteration zone (*Fig. 3.10, zone 1*), and Ca^{2+} could be preserved as groups of small titanite crystals in the replacement albite or could be incorporated into albite. The appearance of titanite indicates that the Ti content of biotite was immobile during hydrothermal leaching. Farther away from the veins, epidotiza-

tion of biotite became dominant due to the Ca^{2+}-containing fluid infiltrating the wall-rock. The continuous Ca addition in the whole altered zone is evidenced from *Fig. 3.9*, *and* 3.*10*. Epidotization of biotite releases K^+ and Mg^{2+} ions that were removed by the hydrothermal fluid (*Fig. 3.9/c, 3.10/zone 2*). Significant depletion of Fe (*Fig. 3.10, zones 1-3*) indicates that during epidotization of biotite, a certain amount of iron had been removed by the fluid as Fe^{2+}. The small euhedral titanite grains that occur around and inside replacive epidote indicate that formation of epidote could not consume all of the Ca^{2+} transported by the fluid, hence Ca^{2+} was in excess during metasomatism of the wall-rock (*Fig. 3.10*). In addition, titanite also contains Si, i.e. a certain amount of silica must also have been released from biotite during the alteration.

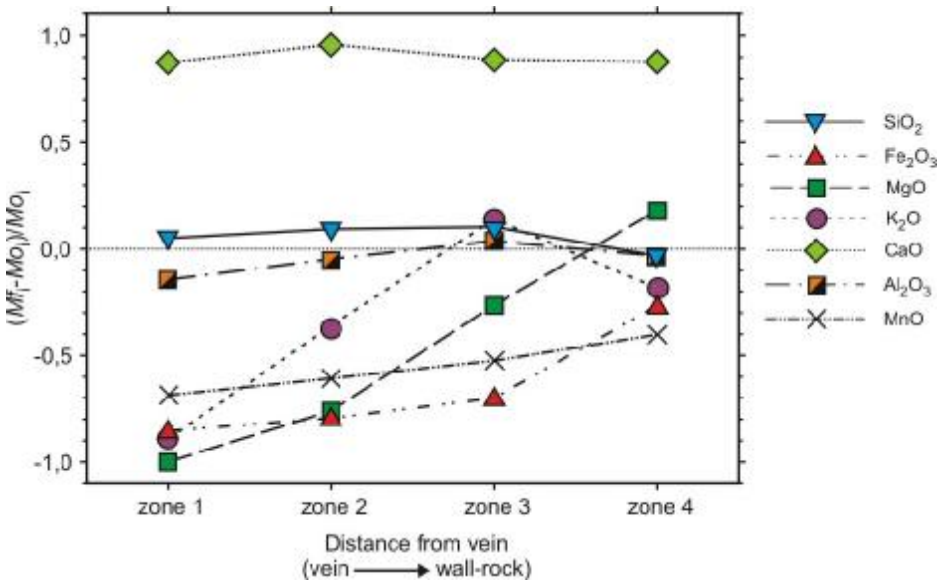

Figure 3.10. *Diagram representing the relative mass changes of element in order to these elements original mass in function of distance from propylitic veins*
Dotted horizontal line at zero value indicate TiO_2 as inert (constant mass) constituent.

Knowing the composition of all initial reactants and final products, the following reaction equation (2) can be constructed (biotite from ÁRKAI et al. 1999; epidote from FINTOR 2005):

$$\underset{\text{biotite}}{K_{1.9}Na_{0.1}Mg_{2.1}Fe_{2.5}Al_{0.9}(Al_{2.7}Ti_{0.2}Si_{5.3}O_{20})(OH)_4} + 3.33Ca^{2+} + 1.2524H^+ \Rightarrow$$

$$1.5652\underset{\text{epidote}}{Ca_2(Al_{2.3}Fe_{0.7})Si_3O_{12}OH} + 0.2\,\underset{\text{titanite}}{CaTiSiO_5} + 1.4044Fe^{2+} + 2.1Mg^{2+} + 1.9K^+$$

$$+ 0.1Na^+ + 0.4044H_4SiO_4(aq) + 1.0348H_2O \qquad (2)$$

Epidotization of biotite is a well-known process especially in metasomatic alterations caused by granitic and granodioritic intrusions (e.g. JACOBSEN & MCCARTHY 1976; SINGLETON 1979; KLEMD & BARTON 1988; ŠARIČ et al. 2009). From comparison of the former equation with *Fig. 3.10* (zone 2), it is obvious that not all of the potassium had been removed from this part of the vein margin. It is likely that this deficit most probably resulted from muscovite that had not suffered epidotic or chloritic alteration and its replacement by albite became weak in the zone 2. However, sericitization became more intensive from zone 2, and a significant amount of potassium that was released during dissociation of biotite could be incorporated into sericite. Towards the unaltered wall-rock, epidotization became less effective and chloritic alteration became predominant. In a few locations of this region chlorite-pseudomorphs contain sagenite rutile inclusions, which support the immobility of titanium in the altered rocks, but indicate that calcium and silica were insufficient to form titanite in these domains.

The Mg content in this zone (*Fig. 3.10/zone 3*) increases most obviously due to the predominance of chlorite and a lesser epidote content. The significant increase in the potassium content (*Fig. 3.10 zone 3*) can be attributed to more factors. Sericitization is the most intensive in this zone; while muscovite is almost unaltered in this part of the alteration zone, except for minor sericitic recrystallization. Although chloritization of biotite is very intensive towards the unaltered wall-rock, more and more unaltered biotite relics occur in the chloritized domains that also conserve potassium.

In zone 4, those components that display the most significant mass depletion elsewhere (*Fig. 3.10, zones 1-3*) reach their mass values characteristic of the unaltered wall-rock (*Fig. 3.10, zone 4*). Here, the major alteration mineral is sericite with a few chlorite filled cavities. The high Ca-content (*Fig. 3.10, zone 4*) of the zone is most probably due to the presence of cavity-filling epidote, which occurs very frequently in the alteration zones, and in the unaltered wall-rock.

3.5.2. Palaeohydrology

The euhedral albite crystals on the cavity walls, and the well-developed growth zonation of the cavity filling epidote (*Fig. 3.4/d*), indicate that these minerals precipitated in an open space system. The secondary porosity was most probably caused by hydrothermal leaching of the circulating fluid, which is one of the most effective processes in the metasomatic regime (PUTNIS 2002). Effective leaching is supported by the significant turbidity of feldspars in the

altered margins, because this texture can develop by fluid infiltration (PARSONS & LEE 2000; WALKER et al. 1995). The primary (P1, P2) and pseudosecondary (PS) fluid inclusions of cavity filling epidote, display a uniform physicochemical character, which is a dilute aqueous-electrolyte solution without any volatile components. Both the composition (0.2-1.6% *w*NaCl eq.) and the range of T_h values (200-360 °C) indicate a fluid identical to that found in the primary fluid inclusions of vein filling diopside (0.7-2.9% *w*NaCl eq., T_h: 308-362 °C), and epidote (0.2-1.2% *wNaCl eq.*, T_h: 206-359 °C), of the Ca-Al-silicate veins (FINTOR et al. 2009) that are bordered by the metasomatised zone. Based on the previous assumptions, it could be stated that an interconnected cavity system existed in the margins that was in connection with the veins. Hence the migrating fluid penetrated the cavity system resulting in epidote precipitation. Although the chemical character of the P3 assemblage (0.2-1.4% *w*NaCl eq.), indicates a similar fluid type to that found in P1 and P2, the lower T_h values (160-200 °C) indicate that trapping of this fluid type occurred later than the main phase of hydrothermal alteration. Taking into consideration that any unambiguous evidence for heterogeneous entrapment, or post-entrapment modifications of inclusions, including leakage/refilling or irreversible change of inclusion volume etc. could not be found, the wide T_h range (200-364 °C) may be explained by subsequent entrapment of primary and pseudosecondary FI in a cooling hydrothermal fluid regime. Such an important drop in temperature (~200 °C) that can be observed between P1 (T_h: 303-364 °C) and P3 (T_h: 160-200 °C) assemblages, can be imagined if the heat effect of an immediate magmatic source caused a short lived fluid flow with a very low fluid/rock ratio and the ambient rock temperature was ~180 °C.

The existence of an interconnected fluid circulation regime between the veins and the metasomatized domains indicates that the same pressure conditions (~100 MPa, FINTOR et al. 2009), which were established in the case of the Ca-Al-silicate veins, can be applied in the case of fluids migrating into the cavities. Based on this approach, the trapping temperature of fluid that entered the rock mass was in the 250-480 °C range similar to that which could have been observed in the Ca-Al-silicate veins (FINTOR et al. 2009). This is in accordance with such a kind of alteration in a hydrothermal metasomatic regime (ROBB 2005).

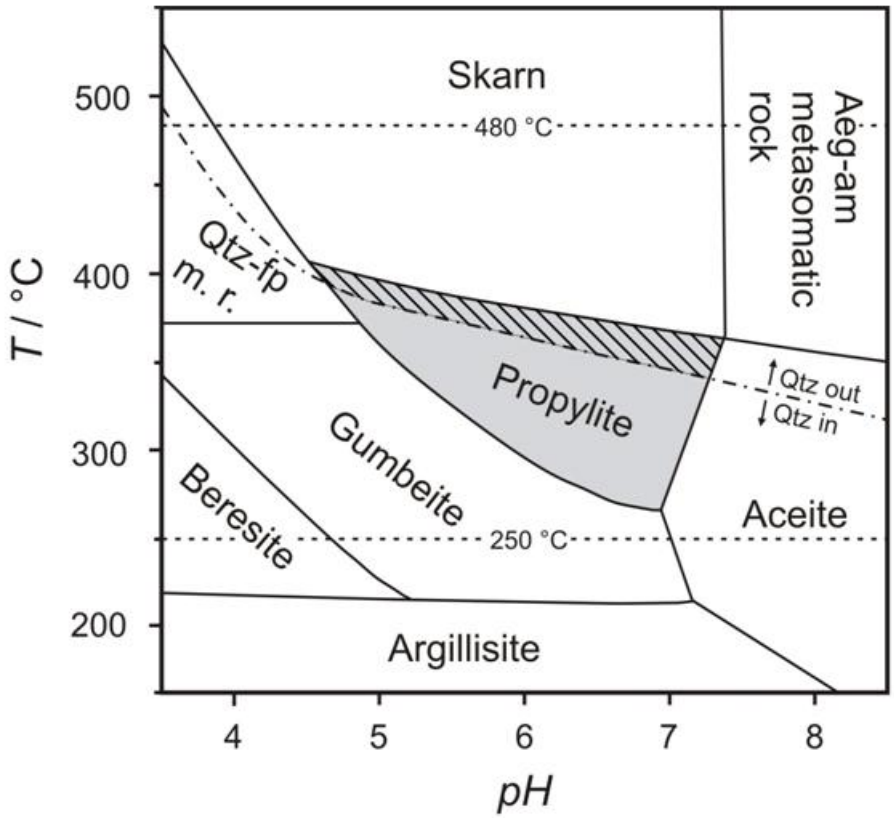

Figure 3.11. *Diagram illustrating a fragment of the general T-qualitative pH fields of the metasomatic families*
(modified after Zharikov et al. 2007) The dot-dash line separates acidic and neutral alkaline-alkaline families (with and without quartz). Dashed lines indicate the possible temperature range of the metasomatic alteration. The grey shaded field represents the possible metasomatic family indicated by mineral paragenesis. The hatched area indicates a metasomatic paragenesis without quartz. (Aeg-am metasomatic rock refers to aegirine-amphibolite metasomatic rock; qtz-fp m. r. refer to quartz-feldspar metasomatic rock).

Based on the observed mineral paragenesis, the estimated temperature range and the type of element mobilization, the studied alteration process belongs to the propylite metasomatic family based on the nomenclature of ZHARIKOV et al. (2007). As chemical compositions of pyrite in both the pure sulphide veins (TARNAI 1998) and the Ca-Al-silicate veins is identical concerning the Co/Ni ratio (FINTOR et al., 2009), both vein types were formed due to postmagmatic hydrothermal processes and the studied veins represent real propylites. According to the "*T*-qualitative *pH* diagram" of metasomatic families (*Fig. 3.11*) (ZHARIKOV et al. 2007), propylite is stable around ~260-410 °C temperature and ~4.5-7 *pH* range, (grey shaded area on *Fig. 3.11*). As the dissociation of water is also temperature dependent, the neutral *pH* value becomes 5 at around 250 °C. Hence the observed mineral assemblage is stable at neutral-weakly alkaline conditions, which is in good agreement with observations in many other fluid-rock interaction systems where albite, epidote, and chlorite are stable (BIRD et al. 1984; GIGGENBACH 1981; BIRD & HELGESON 1980).

The total lack of a quartz phase in the metasomatic column indicates that the peak temperature condition of alteration was above ~340 °C, because quartz free propylite only exists at the 340-400 °C temperature range (ZHARIKOV et al. 2007) (hatched area on *Fig. 3.11*). This estimation is coherent with the fluid inclusion microthermometry data.

We can ascertain from the observed characteristics that the fluid circulated in propylitic veins (FINTOR et al. 2009), and caused significant propylitic alteration in the adjacent rocks. The composition of the metasomatic column can be summarized as *ab+ep+chl+ttn+rt+ser*. The same phases can be found inside the propylitic veins (FINTOR et al 2009). The indications of sulphide ores in the studied well (TARNAI 1997, 1998), and the similarities of the observed propylitic metasomatite with other fields where significant ore mineralization is associated with this type of alteration (KULIKOVA et al. 2007; TASSINARI et al. 2008; ABIA et al. 2003) indicates further investigation of the area.

3.6. Conclusions

1. The fluid circulated in the propylitic veins and caused metasomatism of the wall-rock with transport of considerable amount of Ca^{2+} toward the adjacent rocks. The hydrothermal leaching almost totally removed the K, Fe, Mg, and Mn basic ion content of the wall rock.
2. The characteristic mineral parageneses of individual metasomatic zones of the metasomatic column indicate that the altered wall rock is related to the propylite metasomatic family. The combined mineral assemblage of the metasomatic column is: *ab+ep+chl+ttn+rt+ser*.
3. The pervasive hydrothermal leaching in the wall-rock resulted in significant volume loss and secondary porosity in the altered domains. The fluid migration took place not only in the veins but also in the margins along them, and penetrated a great distance into the adjacent rocks along interconnected cavities.
4. The peak temperature range of the metasomatism was around 360-480 °C, and the alteration occurred as a result of a near neutral, or weakly alkaline hydrothermal solution.
5. The similarities of the studied propylitic mineral assemblages (both in the veins and in the wall-rock) with those that are characteristic in the case of many hydrothermal ore deposits, indicates further research in this topic would be useful.

ACKNOWLEDGEMENTS

The authors would like to thank the Hungarian Research Fund (No. K60768) for providing financial support. The authors also would like to thank to Vesnica Garašić, Ferenc Molnár and an anonymous reviewer for their very useful and detailed reviews which contributed to the improvement of the final draft of the article. Special thanks go to Sándor Kaczur for his help during conversion of the raw element map data and to the American Journal Experts for detailed grammar checking of the manuscript.

REFERENCES

ABIA, E., H., NACHIT, H., MARIGNAC, C., IBHI, A., & SAADI, A., S. (2003): The polymetallic Au –Ag-bearing veins of Bou Madine (Jebel Ougnat,eastern Anti-Atlas,Morocco):tectonic control and evolution of a Neoproterozoic epithermal deposit. *Journal of African Earth Sciences*, 36, 251-271.

ŠARIČ, K., CVETKOVIČ, V., ROMER, R., L., CHRISTOFIDES, G., & KORONEOS, A. (2009): Granitoids associated with East Vardar ophiolites (Serbia, F.Y.R. of Macedonia and northern Greece): Origin, evolution and geodynamic significance inferred from major and trace element data and Sr-Nd-Pb isotopes. *Lithos*, 108, 131-150.

ÁRKAI, P. (1985): Polymetamorphic evolution of the South-Hungarian crystalline basement, Pannonian basin: geothermometric and geobarometric data. *Acta Geologica Hungarica*, 3-4, 23, 165-190.

ÁRKAI, P., HORVÁTH, P., & NAGY, G. (1999): A clockwise P-T path from the Variscan basement of the Tisza Unit, Pannonian basin Hungary. *Geologica Croatica*, 2, 52, 109-117.

BAKKER, R. J. (2003): Package FLUIDS 1.Computer programs for analysis of fluid inclusion data and for modeling bulk fluid properties. *Chemical Geology*, 194, 3-23.

BIRD, D., K., & HELGESON, H., C. (1980): Chemical interaction of aqueous solutions with epidote-feldspar mineral assemblages in geologic systems I. Thermodynamic analysis of phase relations in the system CaO-FeO-Fe_2O_3-Al_2O_3-SiO_2-H_2O-CO_2. *American Journal of Science*, 281, 907-941.

BIRD, D., K., & HELGESON, H., C. (1981): Chemical interaction of aqueous solutions with epidote-feldspar mineral assemblages in geologic systems II.. Equilibrium constraints in metamorphic/geothermal processes. *American Journal of Science*, 281, 576-614.

BIRD, D., K., SCHIFFMAN, W., ELDERS, W., A., WILLIAMS, A., E.., & MCDOWELL, D., S. (1984): Calc-Silicate Mineralization in Active Geothermal Systems. *Economic Geology*, 79, 671-695.

BODNAR, R., J. (2003): Introduction to fluid inclusions. *Fluid Inclusions: Analysis and Interpretation*, SAMSON, I., ANDERSON, A., & MARSHALL, D., Vancouver, Mineralogical Association of Canada, 32, 1-8.

COELHO, J. (2006): GEOISO-A Windows™ program to calculate and plot mass balances and volume changes occurring in a wide variety of geologic processes. *Computers & Geosciences*, 32, 1523-1528.

DE CAPITANI, C., & BROWN, T., H. (1987): The computation of chemical equilibrium in complex systems containing non-ideal solutions. *Geochimica et Cosmochimica Acta*, 51, 2639-2652.

DE CAPITANI, C. (1994): Gleichgewichts-Phasendiagramme: Theorie und Software., *Beihefte zum European Journal of Mineralogy, 72. Jahrestagung der Deutschen Mineralogischen Gesellschaft*, 48

DIAMOND, L. W. (2003): Systematics of H_2O inclusions. *Fluid Inclusions: Analisys and interpretation*, IAN SAMSON, A. A., & DAN MARSHALL, Vancouver, Mineralogical Association of Canada, 32, 55-77.

DOLEJŠ, D., & WAGNER, T. (2008): Thermodynamic modeling of non-ideal mineral-fluid equilibria in the system Si-Al-Fe-Mg-Ca-Na-K-H-O-Cl at elevated temperatures and pressures: Implications for hydrothermal mass transfer in granitic rocks. *Geochimica et Cosmochimica Acta*, 72, 526-553.

ENGVIK, A., K., PUTNIS, A., FITZ GERALD, J., D., & AUSTRHEIM, H. (2008): Albitization of granitic rocks: The mechanism of replacement of oligoclase by albite. *The Canadian Mineralogist*, 46, 6, 1401-1415.

FAZEKAS, V., & VINCZE, J. (1991): Hidrotermás ércindikációk a Villány-hegység északi előtere mélyfúrásaiban. *Földtani Közlöny*, 91, 1-4, 23-56.

FINTOR, K. (2005): Az epidotosodás vizsgálata a Baksai Komplexum képződményeiben. (Analysis of epidotization in the rock body of the Baksa Complex) (In Hungarian)., University of Szeged, Department of Mineralogy, Geochemistry and Petrology, MSc Thesis, 66 p.

FINTOR, K., SCHUBERT, F., & M. TÓTH, T. (2008): Indication of hypersaline paleofluid migration in the fracture system of the Baksa Complex. *Földtani Közlöny*, 138, 3, 257-278.

FINTOR, K., M. TÓTH, T., & SCHUBERT, F., (2009): Indication of hydrothermal paleofluid migration and metasomatism in the fractured rock body of the Baksa Complex, *11th Mining, Metallurgy and Geology Conference.*, Máramarossziget, Romania, 135-138.

GARY, M., MCAFEE, R., & WOLF, C., L. (EDS.) (1974): Glossary of geology., Washington D. C., American Geological Institute, 805.

GÉCZY, B. (1973): Plate tectonics and paleogeography in the East- Mediterranean Mesozoic. *Acta Geol. Hung.*, 27, 379-389.

GIGGENBACH, W., F. (1981): Geothermal mineral equilibria. *Geochimica et Cosmochimica Acta*, 45, 393-410.

GOLDSTEIN, R. H., & REYNOLDS, T. J. (1994): Systematics of fluid inclusions in diagenetic minerals., Tulsa, Oklahoma,

GRANT, J., A. (1986): The Isocon diagram - a simple solution to Gresen's equation for metasomatic alteration. *Economic Geology*, 81, 8, 1976-1982.

GRANT, J., A. (2005): Isocon analysis: A brief review of the method and applications. *Physics and Chemistry of the Earth*, 30, 997-1004.

GRESENS, R., L. (1967): Composition-volume relationships of metasomatism. *Chemical Geology*, 2, 47-65.

GRYAZNOV, O., N. (1992): Ore-bearing metasomatic formations of folded belts., Moscow, Nedra Publishing, 258.

HAAS, J., & PÉRÓ, CS. (2004): Mesozoic evolution of the Tisza Mega-unit. *International Journal of Earth Sciences*, 93, 297-313.

HOLLAND, T., J., B., & POWELL, R. (1998): An internally consistent thermodynamic data set for phases of petrological interest. *Journal of Metamorphic Geology*, 16, 309-343.

HOLNESS, M., B. (2003): Growth and albitization of K-feldspar in crystalline rocks in the shallow crust: a tracer for fluid circulation during exhumation? *Geofluids*, 3, 2, 89-102.

HORVÁTH, P., KOVÁCS, G., & SZAKMÁNY, GY. (2003): Eclogite and garnet amphibolite pebbles from niocene conglomerates (Pannonian basin Hungary): implications for the variscab metamorphic evolution of the Tisza Megaunit. *Geologica Catpathica*, 6, 54, 355-366.

JACOBSEN, J., E., B., & MCCARTHY, T., S. (1976): An unusual hydrothermal copper deposit at Messina, South Africa. *Economic Geology*, 71, 1, 117-130.

JAKOB, A., MAZUREK, M., & HEER, W. (2003): Solute transport in crystalline rocks at Aspo—II: Blind predictions, inverse modelling and lessons learnt from test STT1. *Journal of Contaminant Hydrology*, 61, 175-190.

KASSAI, M. (1972): A Villány-Szalatnaki pleozóos mélytörés . (The Paleozoic Deep Fracture of Villány-Szalatnak .). *MTA X. Oszt. Közl.*, 6, 1, 351-354.

KIRÁLY, E. (1996): Adalékok a délkelet-dunántúli polimetamorf aljzat megismeréséhez. *Földtani Közlöny*, 1, 126, 1-23.

KLEMD, R. (2004): Fluid Inclusions in Epidote Minerals and Fluid Development in Epidote-bearing Rocks. *Reviews in Mineralogy & Geochemistry*, 56, 197-234.

KLEMD, R. B., JR., J., M. (1988): Mineralogy and Geochemistry of the Hydrothermally Altered Archean Granodioritic Rocks of the Vendersdorp Dome Western Transvaal, South Africa. *Mineralogy and Petrology*, 38, 151-160.

KORZHINSKII, D., S. (1946): Metasomatic zonation nearfractures and veins. *Zapiski of All-union Mineralogical Society*, 75, 4, 321-332.

KRUMGALZ, B. S., POGORELSKY, R., & PITZER, K. S. (1996): Volumetric properties of single aqueous electrolytes from zero to saturation concentration at 298,15 K Represented by Pitzer's ion-interaction equations. *Journal of Phy sical Chemistry Referential Data*, 25, 639-663.

KULIKOVA, Z., I., SPIRIDONOV, A., M., & ZORINA, L., D. (2007): Metasomatites of the Kara gold deposit (Eastern Transbaikalia). *Russian Geology and Geophysics*, 48, 901-912.

KULLERUD, K. (2000): Occurrence and origin of Cl-rich amphibole and biotite in the Earth's crust - implications for fluid composition and evolution. *Hydrogeology of crystalline rocks*, STOBER, I., & BUCHER, K., Dordrecht, Kluwer Academic Publishers, 205-226.

MAZUREK, M., JAKOB, A., & BOSSART, P. (2003): Solute transport in crystalline rocks at Aspo— I: Geological basis and model calibration. *Journal of Contaminant Hydrology*, 61, 157-174.

MEYER, C., & HEMLEY, J., J. (1967): Wall rock alteration. *Geochemistry of hydrothermal ore depodits*, BARNES, H., L., Pennsylvania, University park, Holt, Reinhart and Winston, Inc., 166-235.

NADEN, J. (1996): CalcicBrine 1.5: a Microsoft Excel 5.0 add-in for calculating salinites from microthermometric data in the system NaCl-$CaCl_2$-H_2O., *PACROFI VI.*, University of Wisconsin,

OMEL'YANENKO, B., J. (1978): Wall rock hydrothermal alteration., Moscow, Nedra Publishing, 215.

PARSONS, I., & LEE, M., R. (2000): Alkali Feldspars as microstructural markers of fluid flow. *Hydrogeology of Crystalline Rocks.*, STOBER, I., & BUCHER, K., Dordrecht, Kluwer Academic Publishers, 27-50.

PUTNIS, A. (2002): Mineral replacement ractions: from macroscopic observations to microscopic mechanisms. *Mineralogical Magazine*, 66, 5, 689-708.

RAVASZ BARANYAI, L. (1969): Eclogite from the Mecsek Mountains, Hungary. *Acta Geologica Academiae Scientiarum Hungaricae*, 13, 315-322.

ROBB, J., L. (2005): Hydrothermal ore forming processes., Johannesburg, Blackwell Publishing Company, 129-214.

ROEDDER, E. (1984): Fluid Inclusions., Washington, DC., Geological Society of America, 644.

RUBENACH, M., J. (2005): Relative timing of albitization and chlorine enrichment in biotite in proterozoic schists, snake creek anticline, Mount Isa Inlier, Northeastern Australia. *The Canadian Mineralogist*, 43, 349-366.

RUSINOV, V., L. (1989): Metasomatic processes in volcanic rocks., Moscow, Nauka Publishing, 214.

ŠARIČ, K., CVETKOVIČ, V., ROMER, R., L., CHRISTOFIDES, G., & KORONEOS, A. (2009): Granitoids associated with East Vardar ophiolites (Serbia, F.Y.R. of Macedonia and northern Greece): Origin, evolution and geodynamic significance inferred from major and trace element data and Sr-Nd-Pb isotopes. *Lithos*, 108, 131-150.

SCHERBAN', I., P. (1975): Conditions of low temperature wall rock metasomatites formation (on example of Altai-Sayan region)., Novosibirsk, Nauka Publishing, 197.

SCHERBAN', I., P. (1996): Ore-bearing near-vein metasomatites., Kiev, Lebed' Publishing, 350.

SIIVOLA, J., & SCHMID, R. (2007): List of Mineral Abbreviations. *Metamorphic Rocks: A classification and glossary of terms.*, FETTES, D., AND DESMONS, J., New York, Cambridge University Press, 93-110.

SINGLETON, D., G. (1979): Geology of the Seward Mountains, Western Palmer Land. *British Antarctic Survey Bulletin*, 49, 81-89.

SZEDERKÉNYI, T. (1976): Barrow -type metamorphism int he crystalline basement of South-East Transdanubia. *Acta Geol. Ac. Sci. Hung.*, 20, 47-61.

SZEDERKÉNYI, T. (1979): A mecseki ópaleozóos-prekambriumi alapszelvények komplex földtani feldolgozása.,

SZEDERKÉNYI, T. (1983): Origin of amphibolites and metavolcanics of crystalline complexes of south transdanubia, Hungary. *Acta Geologica Hungarica*, 1-2, 26, 103-136.

SZEDERKÉNYI, T. (1984): Az alföld kristályos aljzata és földtani kapcsolatai (Crystalline basement of the Great Hungarian Plain and its geological connections)., University of Szeged, Department of Mineralogy, Geochemistry and Petrology, PhD thesis, 184 p.

SZEDERKÉNYI, T. (1996): Metamorphic formations and their correlation in the Hungarian part of Tisia Megaunit (Tisia Composite Terrane). *Acta Mineralogica-Petrographica, Szeged*, XXXVII, 143-160.

TARNAI, T. (1997): Ore minerals from the key section of the Baksa Complex (W Baranya hills, Hungary). *Acta Mineralogica-Petrographica*, XXXVIII, Supplementum, 119-133.

TARNAI, T. (1998): Mineralogical-petrological study on ore vein penetrated by the key-borehole Baksa No. 2 SE Transdanubia, Hungary. *Acta Mineralogica-Petrographica*, XXXIX, 21-34.

TASSINARI, G., C., C., PINZON, D., F., & VENTURA, B., J. (2008): Age and sources of gold mineralization in the Marmato mining district, NW Colombia: A Miocene-Pliocene epizonal gold deposit. *Ore Geology Reviews*, 33, 505-518.

WALKER, F., D., L., LEE, M., R., & PARSONS, I. (1995): Micropores and micropermeable texture in feldspars: geological and geophysical implications. *Mineralogical Magazine*, 59, 507-536.

ZHARIKOV, V., A., PERTSEV, N., N., RUSINOV, V., L., CALLEGARI, E., & FETTES, D., J. (2007): Metasomatism and metasomatic rocks. *Metamorphic Rocks: A classification and glossary of terms*, FETTES, D., AND DESMONS, J., New York, Cambridge University Press, 58-69.

CHAPTER 4

Indication of hypersaline paleofluid migration in the fracture system of the Baksa Gneiss Complex[*]

[*] FINTOR K., SCHUBERT F., & M. TÓTH T. (2008): Indication of hypersaline paleofluid migration in the fracture system of the Baksa Gneiss Complex. (In Hungarian) *Bulletin of the Hungarian Geological Society*, 138/3, 257-278.

4. Indication of hypersaline paleofluid migration in the fracture system of the Baksa Gneiss Complex

ABSTRACT

The Baksa Complex is a polymetamorphic basement complex in the SW part of the Tisza Megaunit, located in South Hungary. The most important borehole in the area (Baksa-2) is 1200 m depth, and it reveals a variety of polymetamorphic rocks in the Complex. Beyond the metamorphic evolution of the basement rocks, we do not have much information about their postmetamorphic evolution, brittle deformation and cementation processes. In this study, we performed a detailed petrographic and fluid inclusion analysis of the quartz-carbonate fracture infillings in the upper 800 m of the Baksa-2 borehole. A *qtz+dol+cal1+cal2* mineral sequence was observed in the quartz-carbonate veins. The quartz crystals contain several fluid inclusion assemblages (FIAs) aligned along their growth zones. The T_h values of the FIAs in the inner zones vary between 70-130 °C, while in the outermost zone they vary between 50-90 °C. The dissolved salt content is very high in each fluid inclusion, exhibiting a composition that is dominantly NaCl (20.1 – 25.6% *w*NaCl) with a minor amount of $CaCl_2$ (1.5 – 6.0% *w*$CaCl_2$). Significant differences in the concentration or composition of dissolved salts in could not be discerned between the growth zones. CH_4 and N_2 were detected by Raman microspectroscopy in the vapour phases of each FIA. In the *dol* and *cal1* phases, a large number of fluid inclusions exhibited homogenisation temperatures between 130 – 180 °C. The T_m(Ice) data (-25 – -22 °C) indicate a high salt concentration similar to the quartz phase. The Raman spectra suggest that NaCl is the dominant dissolved salt in these fluid inclusions as well. These salt-rich paleofluids probably originated from the Permian and/or Triassic evaporites of the region and imply significant fluid migration between the crystalline basement and the overlying sediments.

4.1. Introduction

The investigation of fractured reservoirs became essential in the last decade in for both applied and basic research. Fractured rock bodies play a significant role in fluid mining (O'REILLY et al. 1998; MUNZ et al. 1998, 2001; KONNERUP-MADSEN 2006), the exploitation of geothermal resources (EVANS et al. 1996; TENZER 2001), and the storage of radioactive waste (BLYTH et al. 2000; WALLIN & PETERMAN 1999). The structural, geometrical and cementation features of the fracture system essentially determine the fluid-retention capacity and fluid conductivity of the container rocks. On the one hand, the fracture-filling minerals cause the

porosity and permeability of rocks to decrease, and on the other hand, they possess essential information about the chemicophysical conditions of cementation processes. From this perspective, fracture-filling mineral grains play a pivotal role by capturing fluid inclusions. These inclusions can preserve the fluid located in the fracture during crystal growth, and permit scientists to determine the original composition and entrapment conditions of the fluid.

Analytical and microthermometric examinations of paleofluids preserved in fluid inclusions can yield fundamental information of paleohydrological history of the investigated area and its geological setting (e.g., WALLIN & PETERMAN 1999; CRESPO et. al. 2002; FOURCADE et. al. 2002; SZABÓ et al. 2003; GONZÁLEZ-PARTIDA et al. 2005). This information, in addition to the fact that it completes our knowledge about recent hydrogeology, can expose earlier events that can be important in future geological planning.

Gaining an understanding of the complex history of Paleozoic basement of the South-Transdanubian region is extremely important, especially from the environmental geology perspective, because of the radioactive waste repository proposed in this region (SZABÓ et al. 2003; KOVÁCS-PÁLFFY & FÖLDVÁRI 2003). The hydrogeological and paleohydrological features of these geologic formations can help determine the long-distance behaviour of the low- and medium-level (Mórágy Granite Formation) and the high-level (Boda Aleurolite Formation) radioactive waste depository sites. For this purpose, recent studies have completed detailed fluid inclusion analyses for rocks of Mórágy Granite Formation (SZABÓ et al. 2003) and the Ófalu Phyllite Zone (DABI et al. 2009).

In this study, we investigate the cementation in the postmetamorphic fracture system and the paleohydrological evolution of the Baksa Gneiss Complex, which is the most important metamorphic mass in the South-Transdanubia region due to the proximity to the mentioned waste depository sites. The Baksa-2 base borehole (depth 1200 m) is critical in the exploration of the area because it reveals the crystalline basement rocks of in the SW part of the Tisza Unit. Although the metamorphic evolution of the Complex is well known (SZEDERKÉNYI 1976, 1983; ÁRKAI 1984, 1985; ÁRKAI et al. 1999), we only have a limited understanding of their postmetamorphic evolution, including their brittle deformation history and the conditions of fracture cementation (TARNAI 1997, 1998).

In this study, we analyse the quartz-carbonate fracture infillings that appear in the crystalline rocks from the Baksa-2 core. Our aim is to attain information about chemicophysical conditions of the fluids circulated in the fractures, their origin and spatial

relationships by detailed petrographical and fluid inclusion analysis. Similar studies facilitate a comparison of the paleohydrological evolution of Baksa Complex to other fractured reservoirs in the region.

4.2. Geological setting

The Baksa Complex (BC) is located in the SW part of the Tisza Megaunit (*Fig. 4.1*), a microplate that forms the basement of South Hungary. The Tisza Megaunit was originally part of the Northern European margin of the Tethys and was separated by predominantly Meso-Alpine horizontal displacements of microplates (GÉCZY 1973; HAAS & PÉRÓ 2004). SZEDERKÉNYI (1996) divided the pre-Alpine basement complexes of the Tisza Megaunit into three major parts: the Kunságia, Békésia and Dravia-Slavonia terranes. According to SZEDERKÉNYI (1996), the BC and the Babócsa Complex belong to the Dravia-Slavonia Terrane. There are no outcrops of the metamorphic basement of the complex; they are instead covered by thin (50-100 m) Tertiary and Quaternary sediments in the area of Görcsöny Ridge. The crystalline schists of the Babócsa Complex form the western border of the BC (*Fig 4.1*). The Villány fracture zone (KASSAI 1972) strikes NW-SE strike and separates the Baksa metamorphic block from the Mórágy Granite Complex and Permo-Triassic sediments to the east. The Mecsekalja Tectonic Zone borders the complex to the north and separates metamorphic rocks and non-metamorphic Mesozoic sediments, which are sandstone, conglomerate, and limestone with evaporite (anhydrite, gypsum) intercalations at the Permian-Triassic boundary (Magyarürög Anhydrite Member of the Hetvehely Dolomite Formation: KONRÁD 1997). The BC is overlain by the Carboniferous Téseny Sandstone Formation and Mesozoic rocks from the Villány Mountains (*Fig. 4.1*).

We have no information about the southern dimensions of the BC because of the thick overlying sediments. SZEDERKÉNYI (1974) observed that the formations within the BC have the same strike and development as the Slavonian Island Hills (Papuk-Krnadija Mts.); however, there is no other evidence of their relationship.

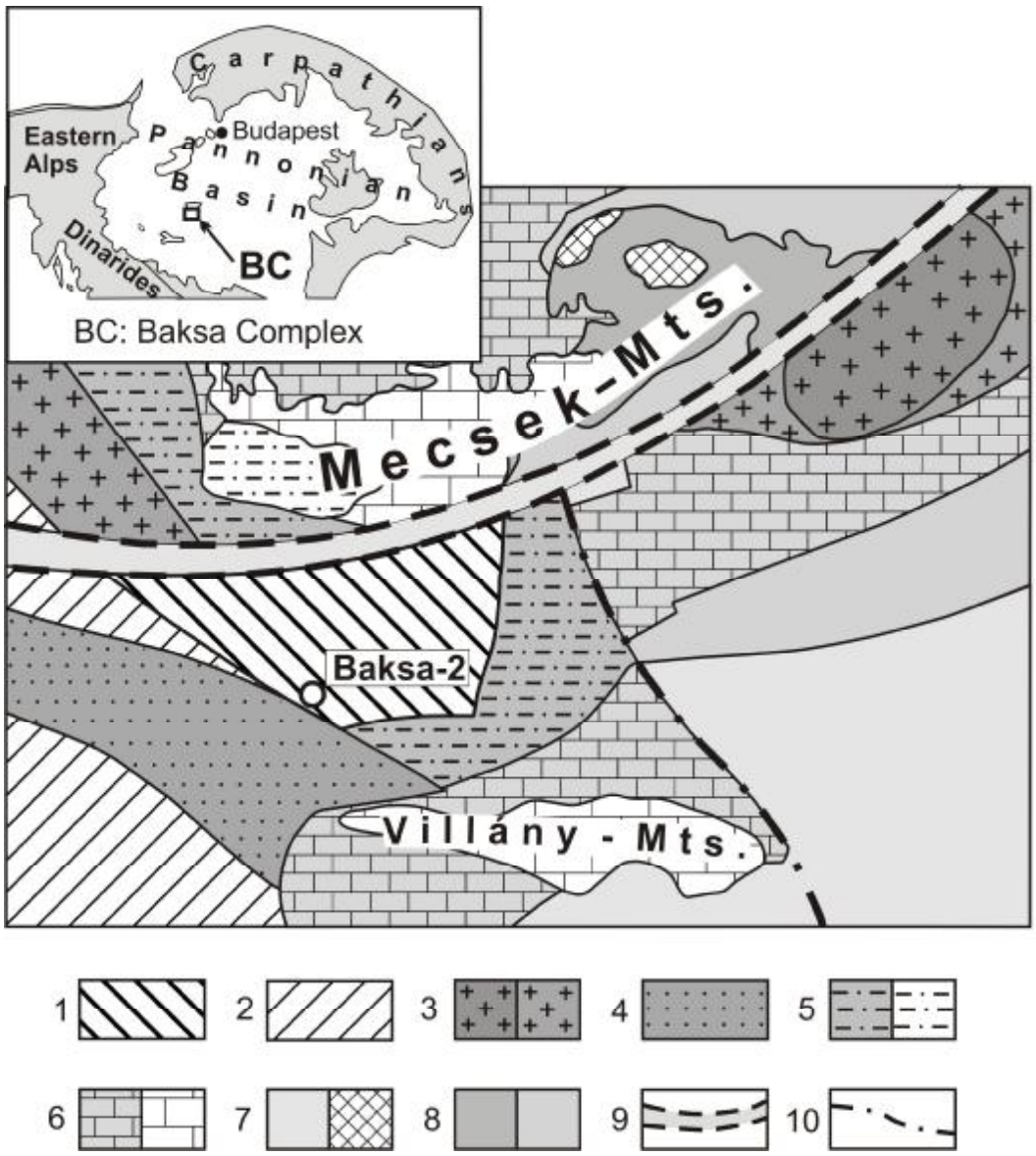

Figure 4.1. *The geologic map of the Baksa Complex and its geological environments is presented without the Tertiary and Quaternary sediments*
Legend: 1. Baksa Complex (study area), 2. Babócsa Complex, 3. Mórágy Complex (Carboniferous), 4. Carboniferous sediments, 5. Permian formations, 6. Triassic formations, 7. Jurassic formations, 8. Cretaceous formations, 9. Ófalu shear zone, 10. Villány-Szalatnak deep fracture zone. Inset: Location of the study area in the Pannonian Basin.

Despite the number of boreholes drilled in the BC, the Baksa-2 is the only one that penetrates these rocks to considerable depth. The borehole was drilled at 1978-79 as part of the Hungarian Paleozoic Research Program as a structural well and facilitates this study of the Complex. Crystalline basement rocks are exposed between 57 and 1200 m depth in the borehole with almost 100% core recovery.

The petrographic development and metamorphic evolution of the BC has been investigated by many researchers (RAVASZ-BARANYAI 1969; SZEDERKÉNYI 1976, 1981, 1983; ÁRKAI 1985; ÁRKAI et al. 1999; KIRÁLY 1996; HORVÁTH et al. 2003). Petrographically, the complex consists of polymetamorphic rocks, mainly gneiss, mica-schist containing marble dolomarble and amphibolite intercalations. SZEDERKÉNYI (1983) determined that the protolith of the amphibolites were volcanic sediments. Subsequent alterations detected in the rocks of the BC are interpreted as the result of individual deformation periods during a single *P-T* path (ÁRKAI et al. 1999; ÁRKAI 1985). Evidence of the earliest detectable metamorphic event is found in the decomposed eclogite of the Görcsöny-1 well. RAVASZ-BARANYAI (1969) concluded there were an earlier progressive and a later retrograde alteration phase, based on the mineral assemblages in the eclogite samples. HORVÁTH et al. (2003) investigated the eclogite and amphibolite pebbles in the Miocene conglomerate, which covers the crystalline basement. They determined pressures of 1300-1500 MPa and temperatures of 600-650 °C for the progressive phase and ~800 MPa pressure and ~500 °C temperature for the retrograde phase. The following progressive, intermediate pressure and temperature alteration resulted in Barrow-type mineral zonation in the crystalline basement formations (SZEDERKÉNYI 1976). This is the oldest metamorphic event that is detectable in almost every location in the Southeast Transdanubia basement rocks (ÁRKAI 1984, ÁRKAI et al. 1985, KIRÁLY 1996, ÁRKAI et al. 1999). For the peak metamorphic conditions were determined to be 750±50 MPa, 660±20 °C by ÁRKAI et al.(1999), and 500-700 MPa, 540-650 °C by KIRÁLY (1996).

The retrograde conditions, which followed the Barrovian phase, caused secondary albitization. After secondary albitization, was approximately isothermal decompression with pressures of 440±20 MPa and temperatures of 650±40 °C, according to ÁRKAI et al. (1999), and <200 MPa and 400-560 °C according to KIRÁLY (1996). ÁRKAI et al. (1999) proposed this event was associated with the Variscan-age, granitoid magmatism that occurred in the BC. KOVÁCH et al. (1985) and BALOGH et al. (1983) place the age of these metamorphic events as well as the Barrovian one, between 307 and 270 Ma with significant uncertainty. The latest research determined an age of 307-312 Ma for these alteration events (LELKES-FELVÁRI & FRANK 2006).

The isothermal decompression was followed by contact metasomatism related to the late orogenic aplite dikes intrusion in the BC. These aplite dikes are distributed throughout the borehole and caused significant alteration in the carbonate rock types. In the rock types formed by contact metasomatism, the most significant minerals in the skarn deposits include

epidote, garnet, diopside, and in lesser amount, sulphide, and epidote hornfels. In addition to the aplite dikes, hydrothermal ore deposits are also observed in these rocks. These deposits can be divided genetically in two groups: one group related to the aplites and the other one independent from aplite dikes (SZEDERKÉNYI 1979). TARNAI (1997, 1998) gave an independent temperature estimate of 240-300 °C for the formation of the ore phase based on the aplite dikes and found that the fluid inclusions in quartz crystals are cogenetic with the ore minerals. The youngest alteration that is detectable in the rocks of the complex is a retrograde greenschist facies event that caused chloritization and secondary albitization (SZEDERKÉNYI 1979). The temperature of this low-grade alteration was established to be approximately 200-400 °C by ÁRKAI et al. (1985), while the age of the alteration is placed around the Alpine orogeny by SZEDERKÉNYI (1984).

The upper section of the borehole is composed of 57.1 m thick sequence of Neogene sediments. The metamorphic rock sequence at 57.1 to 1200 m depth in the borehole was divided into five units (*Fig. 4.2*) based on the dominant and geologically significant rock types determined by SZEDERKÉNYI (1979). In the following section, we will follow the nomenclature of SZEDERKÉNYI (1979) (*Fig. 4.2*):

1. *Upper marble section (57 – 224 m)*
2. *Chloritic two-mica gneiss (224 – 822 m)*
3. *Lower marble section (822 – 867 m)*
4. *Garnetiferous two-mica gneiss (867 – 922 m)*
5. *Garnetiferous two-mica schist (922 – 1200 m)*

4.2.1. Upper marble section

The overlying Neogene sediments were deposited on the upper marble section in an erosional disconformity, thus a portion of the upper marble unit is absent from the borehole data. The upper marble unit is petrographically diverse. In the upper 70 m of this section, marble and dolomite marble are the dominant rock types with intercalations of gneiss and mica schist. In the lower section, these intercalations become the dominant rock type. Here the mineral assemblage is plagioclase + quartz + biotite + muscovite ± garnet and exhibits significant chloritization of biotite and contains the index minerals kyanite, sillimanite, and staurolite.

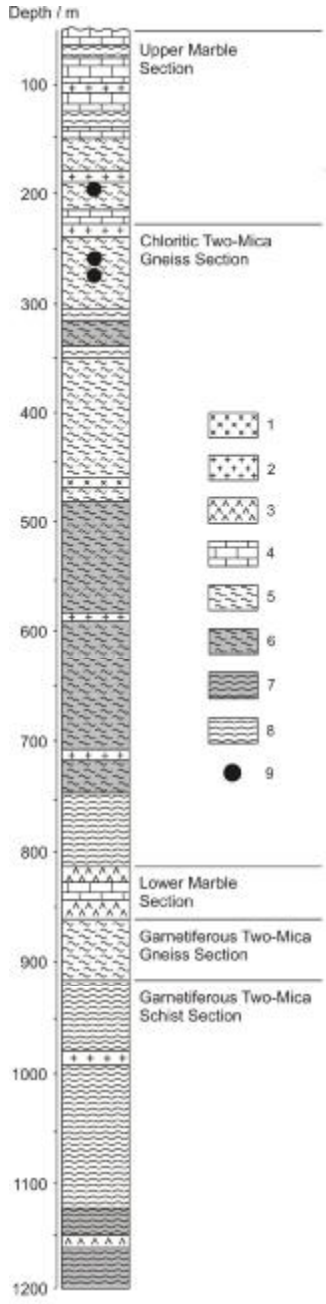

Figure 4.2. *Lithological profile of the Baksa-2 borehole (after SZEDERKÉNYI 1979) Legend: 1. Biotite-andesite dike 2. Aplite dikes 3. Amphibolite 4. Marble and Dolomite marble 5. Two-mica gneiss 6. Chloritic gneiss 7. Chloritic schist 8. Two-mica schist 9. Sampling points*

Aplite dikes are abundant throughout the upper marble section and caused the alteration observed in the carbonates. Epidotisation, the formation of diopside and local calc-silicate hornfels are evidence of this carbonate alternation. The contact zone between the carbonates and dikes are narrow bands (max. 10 cm); however, cavities filled with epidote can be observed at a significant distance from the aplite dikes. Ore deposits are also characteristic of this section, from the hydrothermal alternation produced by the dikes. The most significant

ore deposit is a 6-7 cm thick polymetallic vein that penetrates the borehole at 186.4 m depth. The formation conditions and ore paragenesis (pyrite, pyrrhotite, sphalerite, chalcopyrite, galena, pentlandite, and hematite) of the vein was studied in detail by TARNAI (1998). This vein most probably formed as a result of the rhyolitic volcanism (FAZEKAS & VINCZE 1991) that occurred in the Villány Mountain to the north (TARNAI 1998).

4.2.2. Chloritic two-mica gneiss

The chlorite two-mica gneiss represents the thickest section of the borehole core. The composition of this section is rather homogeneous; it is mainly composed of a two-mica schist and gneiss with minor intercalations of amphibolite. The mineralogy of this unit is similar to that of the gneiss and mica schist found in the upper marble section. Some regions of this unit suffered intensive chloritization and silication caused by retrograde metamorphism (SZEDERKÉNYI 1979). This section is also cross cut by aplite dikes and faults; however, they are much less abundant than in other sections. The aplite dikes occur most frequently between 600-700 m depth and exhibit minor contact metamorphism. The most characteristic fault zones are found around 500 m depth. A young biotite andesite dike is also found in one fault zone.

4.2.3. Lower marble section

This is the thinnest rock section and is dominantly composed of amphibolite. The marble intercalations that appear in the amphibolite are characteristic of this unit and are formed from the dolomite and marble found in the upper marble section. This section contains a greater number of aplite dikes than the underlying and overlying units.

4.2.4. Garnetiferous two-mica gneiss

This section is overall gneiss with a number of mica schist intercalations with abundant garnet. The quantity and size of the garnets increased significantly and reach 2 cm in diameter in some locations.

4.2.5. Garnetiferous two-mica schist

This is the second-thickest section in the core and is two thirds mica schist and by one third gneiss. It also contains abundant garnet and locally contains thin amphibolite intercalations.

4.3. Samples and methods

The samples used for analysis are from the upper marble and chloritic two-mica gneiss sections of the rock column. Optical identification of the vein-filling minerals was made using a Nikon Microphot FXA-type polarisation microscope at the department of Mineralogy, Geochemistry and Petrology at the University of Szeged.

4.3.1. Examination by using SEM

The EDS spectra, element maps and backscattered electron images were obtained for the carbonate phase by using a Hitachi S4700 scanning electron microscope at the electron microscope laboratory in the Institute of Environmental Sciences at the University of Szeged. A 25 keV accelerating voltage and 10 μA beam current were used for these measurements.

4.3.2. Fluid inclusion analyses

Fluid inclusions were studied in 75-150 μm double-polished thick sections prepared from the vein materials. A low-speed sawing machine was used to cut the samples to avoid changes in the volumes of the fluid inclusions. Microthermometric measurements were carried out with a Linkam THMSG 600 heating-freezing stage, operating over a temperature range of -190 to 600 °C. Synthetic fluid inclusions were used to calibrate at -56.6, 0.0 and 374.0 °C. The accuracy of the data is approximately ±0.2 °C at freezing conditions and ±0.5 °C at heating conditions. An LMPlanFI 100X objective lens (Olympus) was used to analyse the inclusions. The first experiments on the quartz inclusions were at freezing conditions, while the heating experiments were carried out first for the carbonate inclusions. In the latter case, inclusions can suffer permanent deformation during the freezing experiment (OXTOBY 2000). The cycling method (GOLDSTEIN & REYNOLDS 1994) was used to determine the last ice melting temperature of fluids trapped in calcite. Determinations of the volume fractions of vapour bubbles (φ_{vap}) were determined using area analysis in a 2D projection of the fluid inclusions. Terms and symbols publicised by DIAMOND (2003) are used in here for analyses.

A thermodynamic model to derive the behaviour of the high-salinity H_2O-salt system with complex compositions does not exist yet (BAKKER 2003). Instead, here we calculate the salinity based on the equivalent *w*% principle, using the H_2O – NaCl binary and H_2O – NaCl – $CaCl_2$ ternary as model systems.

Salinity calculations are based on T_m(Ice) and T_m(Hh) data for fluid inclusions using the *AqSo2e* program from the FLUIDS program package by BAKKER (2003). The *AqSo2e* module

uses formulas from NADEN (1996) for the H_2O – NaCl – $CaCl_2$ ternary system. The program module *BULK* from the FLUIDS program package (BAKKER 2003) was used to determine the main physical parameters (homogenisation pressure (P_h); molar volume (V_m); liquid to vapour ratio (φ_{vap})) of the fluid inclusions. This program uses the equations of state (*EoS*) of ZHANG & FRANTZ (1987) for bulk fluid inclusion and the EoS of KRUMGALZ et al. (1996) for aqueous fluids. To construct *P-T* diagrams, isochores of each fluid inclusion were calculated using the *ISOC* program (BAKKER 2003), based on the EoS of ZHANG & FRANTZ (1987).

4.3.3. Raman microspectroscopy

Raman spectroscopic analyses of the fluid inclusions was carried out at the Department of Mineralogy and Petrology at the Montanuniversität Leoben, using a Jobin Yvon LABRAM confocal Raman microspectroscope, which uses a frequency doubled Nd-YAG 100 mW capacity laser. Each sample was irradiated using a laser light with a 532.2 nm (green) wavelength. This instrument has a spectral resolution of 4 cm^{-1} and a spatial resolution of a few μm^3. Calibration the spectrometer was made by synthetic silicon chip, polyethylene, calcite, and a natural diamond crystal. The recording time was 150 sec for each spectrum, with 30 sec accumulation periods. The Raman spectra of salt hydrates were found between 3000-3700 cm^{-1}, with the most important peaks are around 3400 cm^{-1} (MERNAGH & WILDE 1989; BAKKER 2004).

4.3.4. Combined Raman spectrometry and microthermometry

A Linkam THMSG 600 heating-freezing stage was mounted on the Raman spectrometer for the Raman spectroscopy assisted microthermometry to make the analyses at different temperature conditions. To make an accurate identification of the ice and salt hydrates, spectra were recorded at temperatures lower than -170 °C. This method is very efficient for determining the last melting temperature of salt hydrates and to distinguish the different types of salt hydrates and ice from one another.

4.4. Results

4.4.1. Petrographic description of quartz-carbonate veins

The thickness of the quartz-carbonate veins in the metamorphic rocks of the Baksa Complex are around 2-10 mm thick *(Fig. 4.3/a, b*). The veins are 30-35° from the long axis of drill cores. Quartz is deposited directly on the vein wall as euhedral crystals (*Fig. 4.3/b, c, d*).

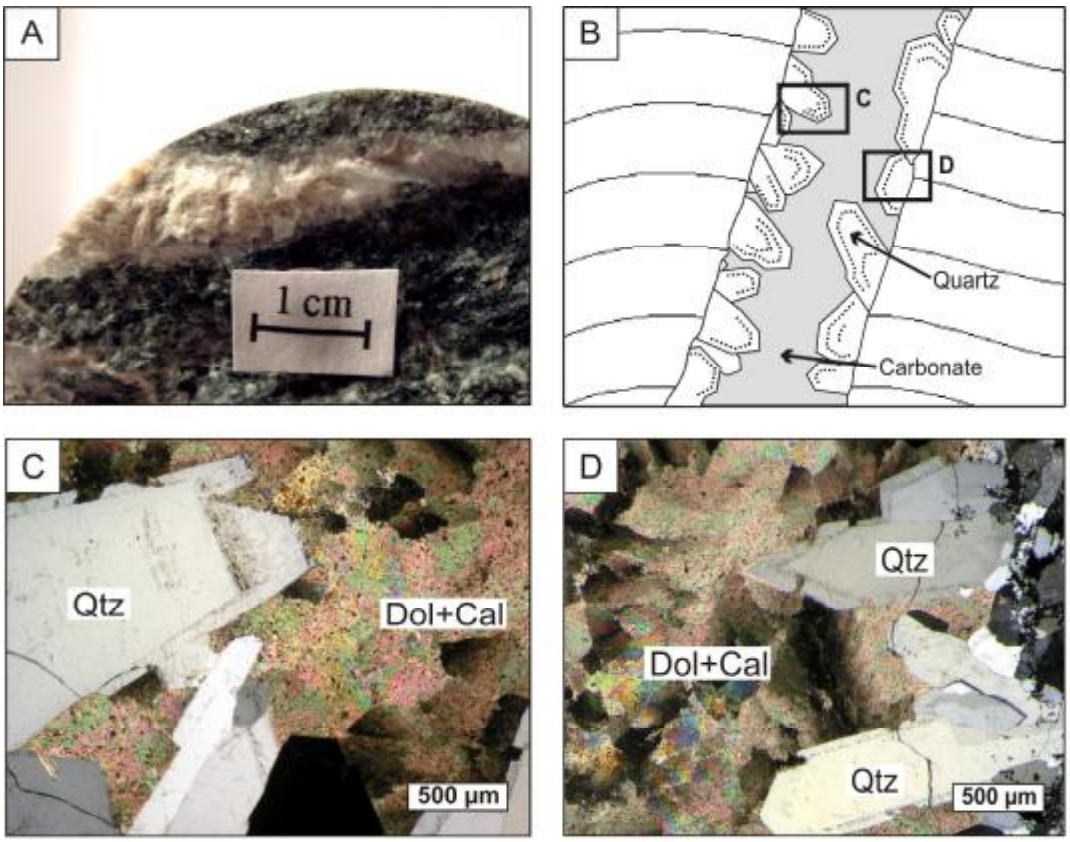

Figure 4.3. *Macroscopic and microscopic images of the quartz carbonate veins*
A) Quartz-carbonate vein in a core sample (adjacent rock: chloritic two-mica gneiss) B) Sketch of the vein infilling C) Euhedral quartz crystals with growth zones D) Euhedral quartz followed by carbonate with undulose extinction

Crystals show growth zoning without evidence of undulose extinction, and these zones are marked by assemblages of fluid inclusions (*Fig. 4.3/b, c, d*). Solid inclusions could not be found in any of the analysed crystals. The pore space between quartz crystals is completely filled by a grey-tinted carbonate phase with a bulky appearance. In this section, the carbonate appears hypidiomorphic, and many of the rhombohedral cross-sections have curved and resorbed crystal boundaries (*Fig. 4.3/c, d; Fig. 4.4/a, b, c*).

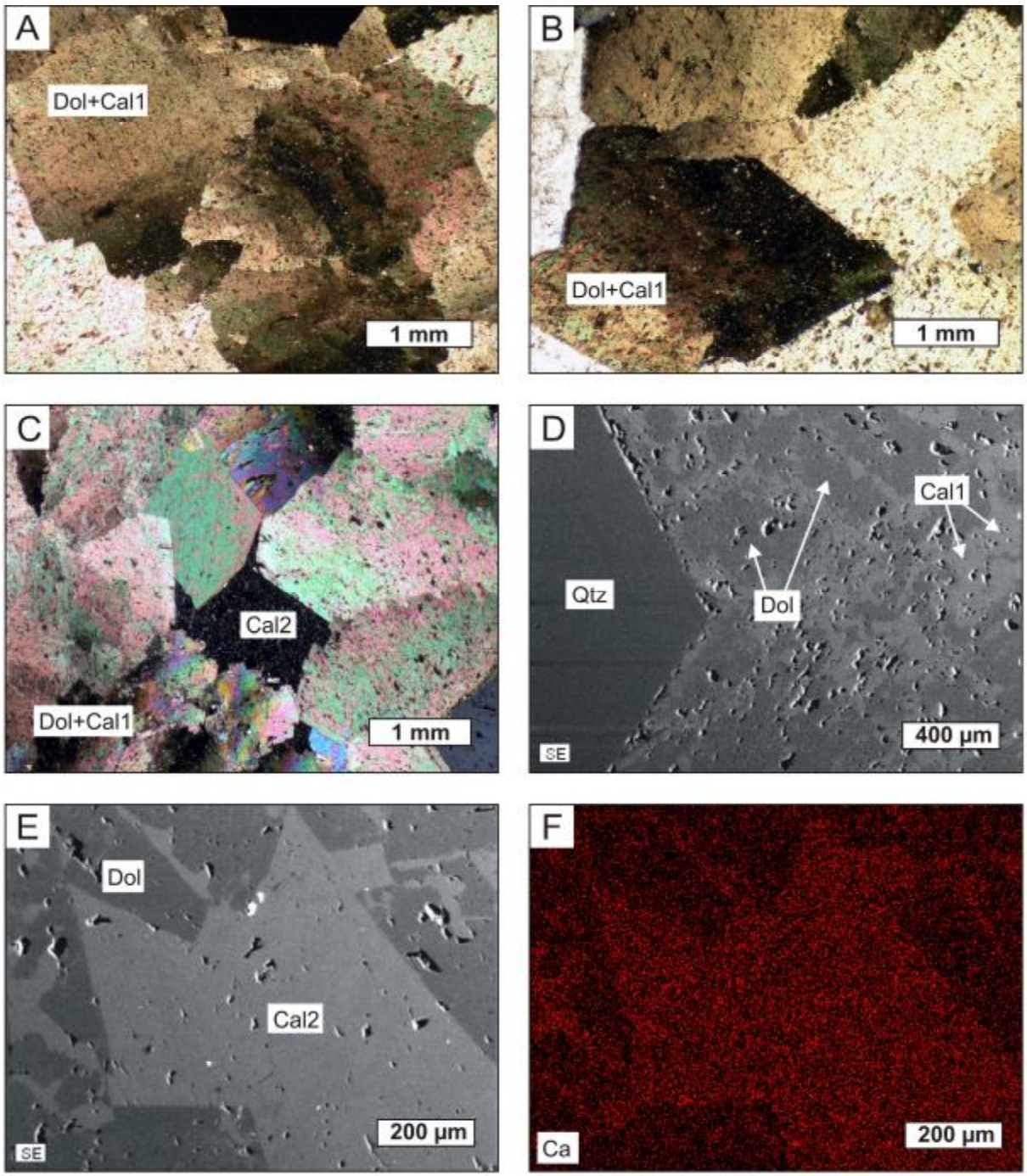

Figure 4.4. *Representative optical microscopic pictures, BSE images, and X-ray element maps of the carbonate phase*
Photo A): Dol+cal1 crystals with undulose extinction and irregular grain boundaries; Photo B): Aggregate of euhedral fracture filling dol+ cal1 crystals; Photo C): The late cal2 phase does not show undulose extinction among dol+ cal1 phases; Photo D): Cal1 phase (light grey) are included into dol phase (dark grey) show irregularly demixing pattern; *Photo E): Secondary electron image (SE) from the cal2 phase are appeared among the dol+ cal1 phases; Photo F): Ca – elementary map from the area are shown on the photo E)*

A majority of carbonate crystals display undulose extinction but do not exhibit deformation lamellae (*Fig. 4.3/c, d; Fig. 4.4/a, b*). Between the crystals that exhibit undulose extinction, small carbonate grains with straight extinction and deformation lamellae are sometimes found (*Fig. 4.4/c, e*). These small grains have a pure calcite composition, based on the EDS analyses *(cal2)*. The carbonate phase with undulose extinction has a uniform appearance in optical microscope but is segregated into two phases in the backscattered electron images. The dominant phase is dolomite with a small iron content ($Ca_{1.07}\,Mg_{0.73}\,Fe_{0.15}\,Mn_{0.05}\,(CO_3)_2$) (*dol*) (*Fig. 4.4./d-f*), and the other phase is pure calcite ($Ca_{1.92}\,Mg_{0.001}\,Fe_{0.03}\,Mn_{0.04}\,(CO_3)_2$) (*cal1*) (*Fig. 4.4/d-f*). The *cal1* occur inside the *dol* phase as irregular patches or show umixing patterns (*Fig. 4.4/d, e*). Based on petrographic markers, the quartz-carbonate veins exhibit a *qtz+(dol+cal1)+cal2* mineral sequence, where the relationship between the *dol* and *cal1* is unclear. However, the *cal2* phase is younger than both the *dol* and *cal1*.

4.4.2. Fluid inclusion petrography and microthermometry

4.4.2.1. Quartz

The euhedral quartz crystals in the analysed samples contain many fluid inclusions. Those FIA found in the crystal zoning were trapped during crystal growth and because no refilling patterns were observed, we conclude they must be primary FIAs (*Fig. 4.5/a, b*). In addition to the primary FIAs, pseudosecondary and secondary inclusions are observed along healed microfractures of crystals (*Fig. 4.5/a, b*). Two-phase liquid-vapour (L+V) and single-phase liquid (L) inclusions can be found in each FIA, no other liquid or solid components were detected in the inclusions. Most of the inclusions are irregularly shaped, and negative crystal-shaped inclusions occur only very rarely. In addition to the five primary assemblages (Q-P1 – Q-P5), three pseudosecondary (Q-PS1 – Q-PS3) and one secondary (Q-S1) FIA can be distinguished (*Fig. 4.5/c*). In the Q-P1 to Q-P4, FIAs the L+V type inclusions are dominant. This is true of the Q-PS1-3 and Q-S1 assemblages as well; however, the single-phase L-type inclusions are predominant in the Q-P5 FIA. The longest dimensions of the two-phase inclusions are between 2-24 μm in length, with a median value of 7-15 μm. In the pseudosecondary and secondary assemblages, the small (<3 μm) inclusions are dominant, and a smaller number of inclusions can be analysed using microthermometry relative to the primary assemblages. The majority of pure liquid single-phase inclusions are very small in size, except in QP5, where single-phase (L) inclusions that are 5-15 μm in size are also observed. The two-phase inclusions are liquid dominant and have φ_{vap} values between 0.02-

0.12 *(Fig. 4.6/d)*. Significant differences in φ_{vap} values are not observed between the FIAs (φ_{vap} Q-P1: 0.1-0.06; Q-P2: 0.12-0.06; Q-P3: 0.1-0.03; Q-P4: 0.08-0.02). During cryoscopic analyses of the inclusions, vapour bubble nucleation occurred in a large number of the single-phase (L) inclusions during cooling.

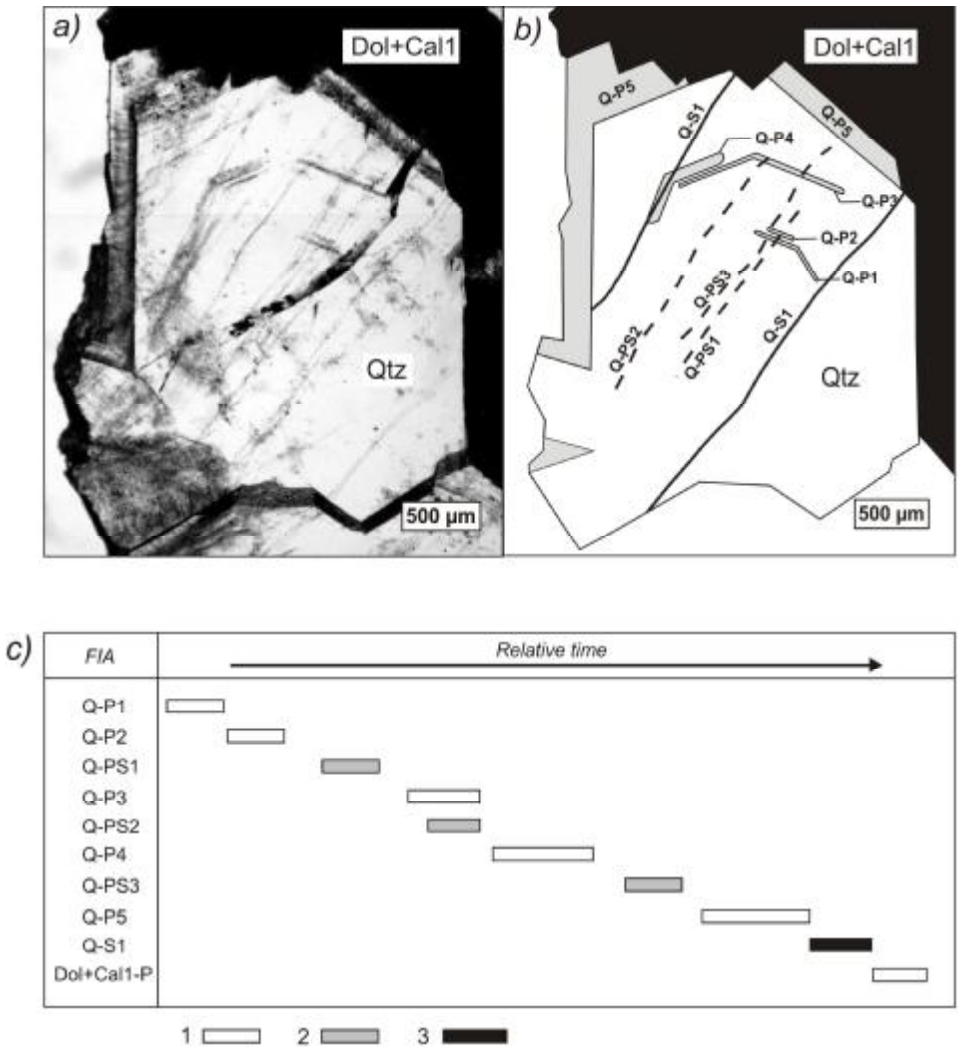

Figure 4.5. *Results of fluid inclusion petrography*
a) Location of the primary, secondary and pseudo-secondary fluid inclusion assemblages in the investigated mineral phases b) relative time-sequence of the FIA-s Legend: 1) primary FIA, 2) pseudo-secondary FIA, 3) secondary FIA

This phenomenon was observed in every FIA. In all of the two-phase inclusions, the last melting temperatures for ice occurred in the presence of the salt hydrate crystal. The melting temperatures of ice are between –27.2 and –18.7ºC in the primary assemblages; however, there are few differences detected between these assemblages (*Fig.* 4.7-*4.8, Table 4.1*). The melting temperatures observed for Q-P1 (T_m(Ice): -25 – -22 °C) are a little lower than those observed for the Q-P2 assemblage (T_m(Ice): -21,7 – -18,7 °C) (*Fig. 4.7/b* and *4.8/a, b; Table*

4.1). The T_m(Ice) values are similar to Q-P1 in both Q-P3 (T_m(Ice): -25.7 – -23.3 °C) and Q-P4 (T_m(Ice): -26.7 – -23.0 °C) (*Fig. 4.7/b,* and *4.8/c, d; Table 4.1*).

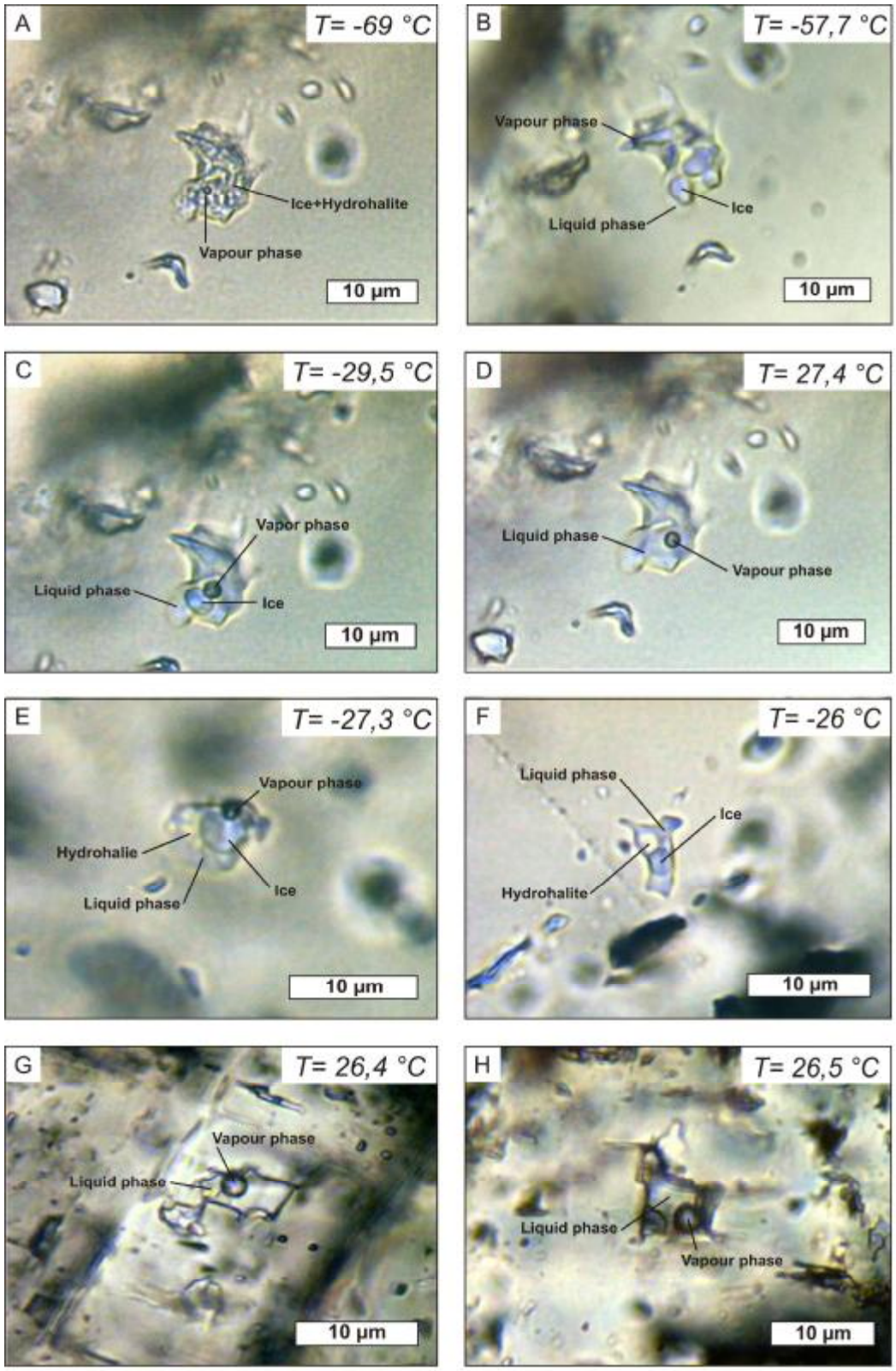

Figure 4.6. *Representative images about fluid inclusions from the quartz and dolomite+calcite 1 host minerals*

Photos A)-D): Phase transitions through heating process in a frozen primary fluid inclusion of quartz (Q-P3); Photo A): Primary two-phase fluid inclusion from the fracture-filling quartz phase (at -69 °C); Photo B): Appearance of liquid phase close to the eutectic temperature of the fluid; Photo C): Melting ice crystal just at -27 °C, before the inclusion reached the final ice melting temperature (-24.8 °C) of the fluid. ; Photo D): Phases of the previous fluid inclusion at room temperature; Photo E): Ice, hydrohalite, liquid, and vapour phases are in equilibrium in a primary fluid inclusion of the quartz (Q-P4); Photo F): Metastable phase equilibria (absent of vapour phase) in a primary fluid inclusion from the quartz phase (Q-P2); Photos G-H): Characteristic fluid inclusion types from the dol+cal1 fracture filling phase; Photo G): Liquid dominant two phase primary fluid inclusion at room temperature conditions from the dol+cal1 phase; Photo H): Liquid dominant approximate negative crystal shaped primary fluid inclusion from the dol+cal1 phase.

In the Q-P5 assemblage, we were unable to measure more than a few melting temperatures because of the absence of a vapour phase in most inclusions, but the data we did collect for this assemblage vary over a wide range (T_m (Ice):-27.2 – -8.7 °C) (*Fig. 4.7/b, and 4.8/e; Table 4.1*). The absence of vapour phase made it difficult to measure the last melting temperature of ice (T_m(Ice): -27 – -20 °C) in the pseudosecondary assemblages, and few differences are observed between the different inclusion generations (*Fig. 4.7/d; Table 4.1*).

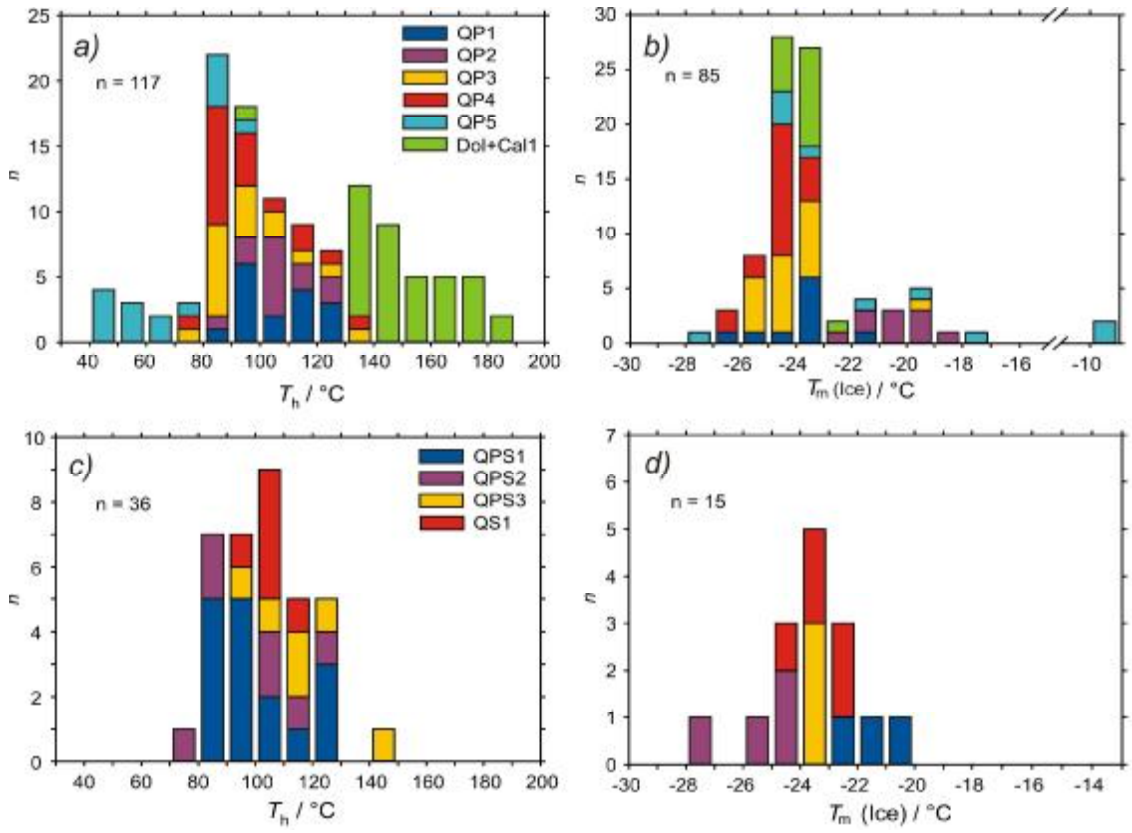

Figure 4.7. *Distribution of homogenisation (T_h) and final ice-melting (T_m(Ice)) temperatures of the inclusions in fracture-filling minerals*
a) and b) (T_h) and T_m(Ice) histograms of the primary fluid inclusions of quartz, dolomite and calcite 1 phases; c) and d) (T_h) and T_m(Ice) histograms of the pseudo-secondary and secondary inclusions of the quartz phase

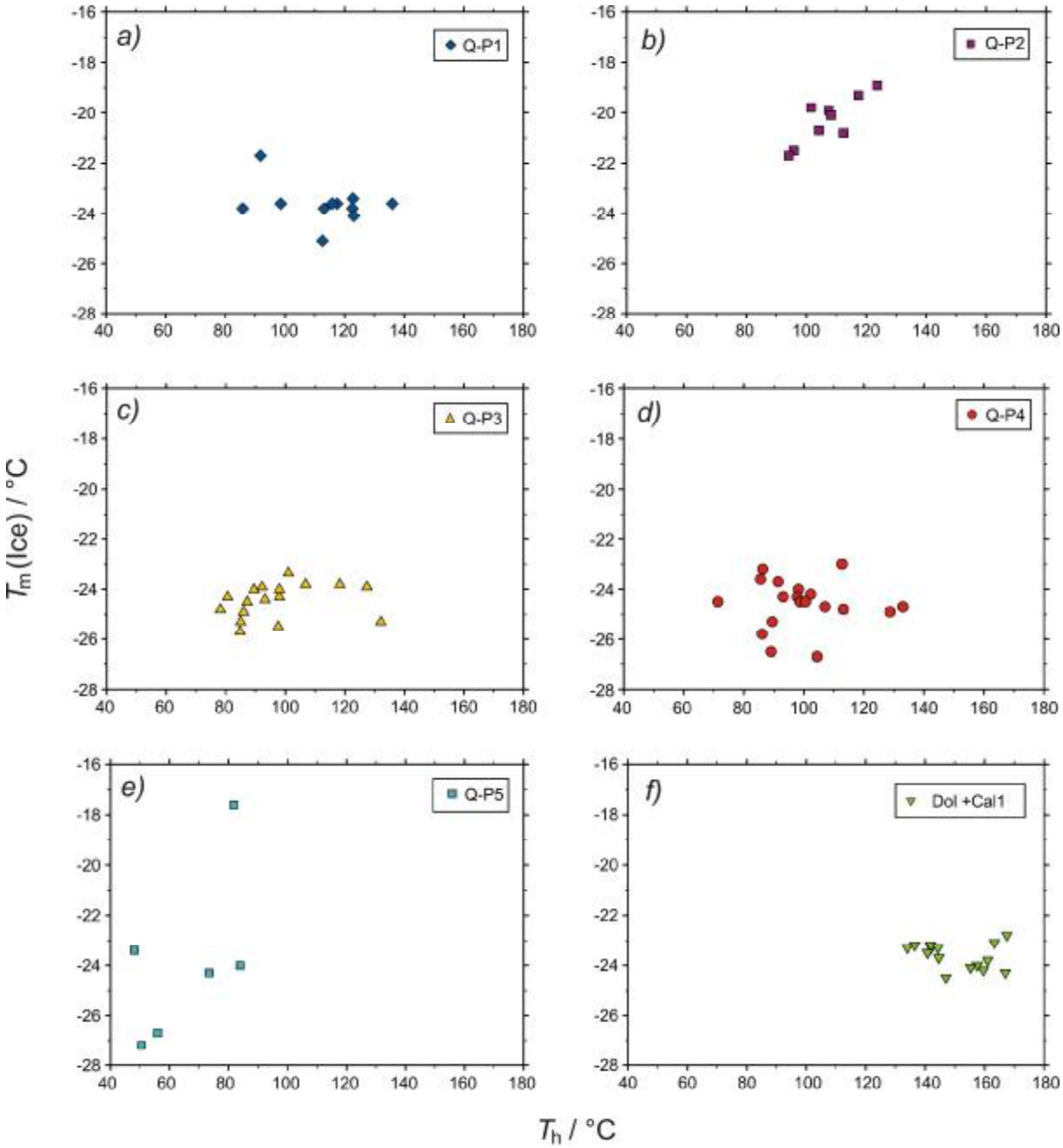

Figure 4.8. *T_m(Ice) vs. T_h data plots of the fluid inclusions from the quartz and dolomite+calcite 1 phases. For details see text.*

The highest T_m(Ice) values are observed in the Q-PS1 assemblage (T_m(Ice): -23 – -20 °C), while the lowest values (T_m(Ice): -27 – -24 °C) occur in the Q-PS2 assemblage, which is located chronologically between the primary generations Q-P3 and Q-P4 (*Fig. 4.7/d; Table 4.1*). In the secondary assemblages, the last ice melting temperatures are also very low, but they fall in a narrow range of -24 – -23 °C (*Fig. 4.7/d; Table 4.1*). The small size of inclusions and the absence of a vapour phase made it difficult to observe the initial melting temperature of ice (T_e). In those cases when it could be analyzed T_e values vary between -60 and -50 °C (*Table 4.1*). The first liquid phase occurred at lower than -40 °C in every measured inclusion

(Fig. 4.6/a, b, c). The Raman spectroscopy identified the characteristic peaks (at 3403.6; 3420.5; 3434; és 3536 cm^{-1}, *Fig. 4.9*) of hydrohalite ($NaCl*2H_2O$) on the salt hydrates spectra in each FIA (*Fig. 4.6/e, f*), which reference the NaCl content of the fluid.

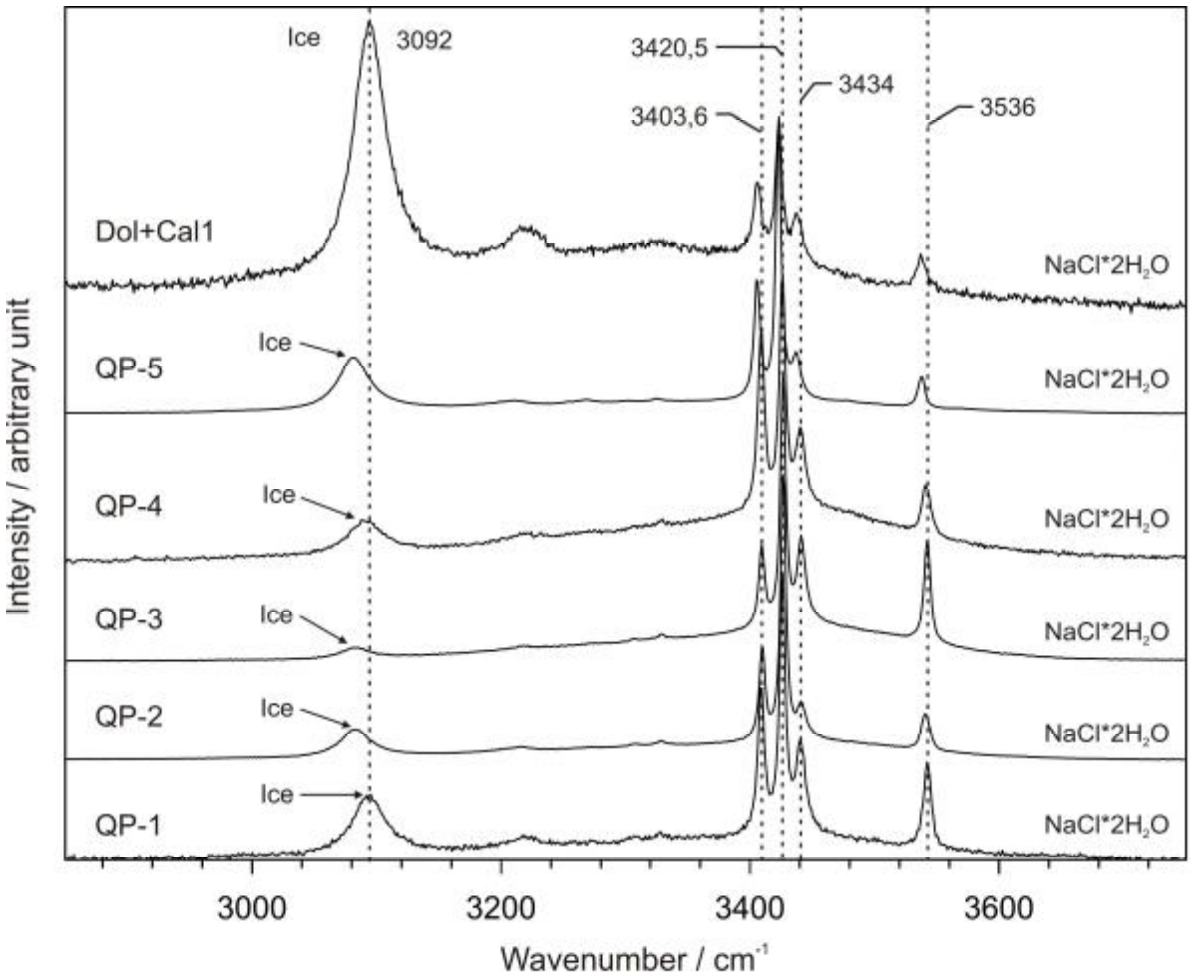

Figure 4.9. *Raman spectra of the O-H stretching region (3000 to 3600 cm^{-1}) of frozen aqueous fluid inclusions in the primary FIA-s of quartz and dol+cal1 phases*

The measured T_e values, the presence of a melt (liquid) phase at lower than -40 °C, and the T_m (Ice) values all indicate that at least one extra component, in addition to NaCl, is required to explain the observed phase transitions. The low T_e values indicate the presence of dissolved $CaCl_2$ in the fluid (YANATIEVA 1946). The last melting temperatures of hydrohalite (T_m(Hh)) were measured in the primary FIAs to determine the accurate concentration of $CaCl_2$ (*Table 4.1*) (BODNAR et al. 1989). No significant differences in the measured T_m(Hh) values were detected between the primary assemblages. Their values show a considerable scattering in Q-P3 and Q-P4, unlike the values observed in Q-P1 (*Table 4.1*). Because of the metastable behaviour (i.e., the absence of nucleation of vapour bubble during freezing process) of the Q-P2 and Q-P5 inclusions, it was not possible to obtain T_m(Hh) values from

these FIA. The formation of a gas-hydrate (clathrate) was not observed in these fluid inclusions during the microthermometric analysis. Raman spectra were recorded for the vapour phase in the primary FIA to clarify whether the fluid inclusions contain a gas phase. N_2 (~2331 cm^{-1}) and CH_4 (~2919 cm^{-1}) were identified by Raman spectra in all the investigated FIA (*Fig. 4.10*).

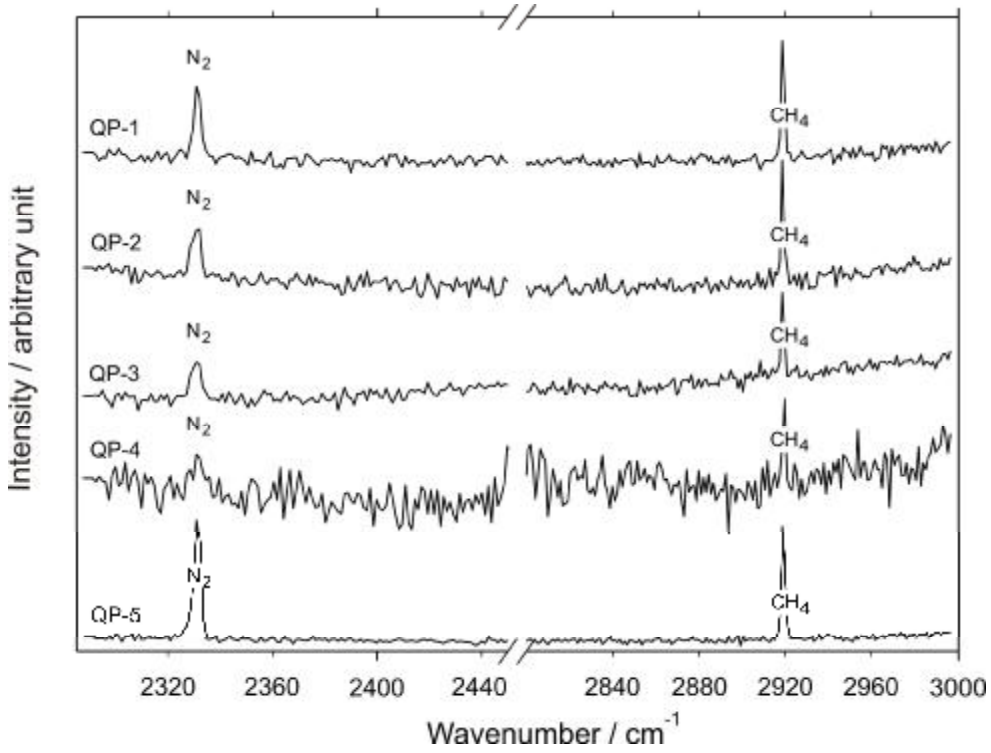

Figure 4.10. *Raman spectra of the vapour phase in primary FIAs in the quartz crystals*

Despite the presence of CH_4 and N_2 in the fluid, CH_4 and N_2 phase transitions were not detected, even at temperatures of -196 °C. Unmixing and homogenisation (partial homogenisation) of the two volatile phases were not detected during the microthermometry. Despite the observed phenomena, small methane content can cause a decrease in T_m (Ice), which will cause a falsely high calculated salinity for the inclusion.

The homogenisation temperatures (T_h) of the inclusions during the heating procedure varied between 90 and 125 °C in the Q-P1 and Q-P2 assemblages (*Fig. 4.7/a* and *4.8/a, b; Table 4.1*). In the Q-P3 and Q-P4 assemblages, there is wider range of temperatures of 80-135 °C, with the majority of the measured values falling between 80 and 100 °C (*Fig. 4.7/a* and *4.8/c, d; Table 4.1*). Data from Q-P5 assemblages differ markedly from the other primary FIA. In these assemblages, T_h values are between 50-90 °C range (*Fig. 4.7/a* and *4.8/e; Table 4.1*). In the secondary assemblages, T_h values are between 90-120 °C (*Fig. 4.7/c; Table 4.1*).

4.4.2.2. Carbonate

Many of the fluid inclusions can be found in the *dol* and *cal1* phases of carbonate that follow the quartz phase. The *cal2* phase is almost free of fluid inclusions, and the rare small inclusions are insufficient for microthermometric analysis. Inclusions of the *dol* and *cal1* phases cannot be distinguished by their petrographical characteristics. Distributions of inclusions along the crystallographic directions could not be detected using crystal morphology, and inclusion trails along healed microfractures can be found very rarely. Instead, the inclusions tend to form a continuous cloud, which fills the entire crystal. The primary origin of the inclusions in the two carbonate phases can be deduced from their observed characteristics. The majority of the inclusions contain two phases: one liquid and one vapour phase (L+V), which can be distinguished in the inclusions at room temperature (*Fig. 4.6/g, h*). The one phase inclusions are filled by liquid (L) and can be found only in subordinate amounts. Two-phase (L+V type) inclusions are liquid dominant, with their φ_{vap} values falling between 0.15-0.2. The irregularly and negative-shaped inclusions can be found in almost equal proportions and both types are between 5-20 μm in size.

Table 4.1. *Measured and calculated data from the fluid inclusion assemblages*

Mineral phases		T_h (°C)	T_e (°C)	T_m (Ice) (°C)	T_m (Hh) (°C)	Salinity			Composition of gaseous phase	
						NaCl-$CaCl_2$-H_2O		NaCl-H_2O		
	Quartz					% *w*NaCl	% *w*$CaCl_2$	% *w*NaCl eq.	CH_4 mol%	N_2 mol%
FIA	QP-1	85.8 – 136	—	-25.0 – -21.6	-19.5 – -11.5	23.1 – 24.7	1.6 – 3.2	23.6 – 24.7	14.0	86,0
	QP-2	89.2 – 139.3	-53.0	-22.4 – -18.8	—	—	—	21.5 – 24.2	12.1	87,9
	QPS-1	81.0 – 127.5	—	-22.6 – -20.5	—	—	—	23.0 – 23.9	—	—
	QP-3	78.2 – 132.1	-57.1	-25.5 – -23.3	-21.1 – -6.5	20.1 – 25.6	1.5 – 4.0	23.4 – 25.8	11.9	88,1
	QPS-2	74.8 – 127	—	-27.4 – -24.2	—	—	—	24.5 – 25.5	—	—
	QP-4	71.3 – 133	-52.6	-26.7 – -23.0	-19.3 – -5.5	21.1 – 24.9	2.1 – 6.1	23.7 – 25.6	27.3	72,7
	QPS3	98.0 – 145.5	—	-24.3 – -23.4	—	—	—	24.2 –24.4	—	—
	QP-5	43.9 – 91.2	—	-27.2 – -8.7	—	—	—	12.6 – 25.4	7.7	92,3
	QS-1	91.1 – 116.7	—	-23.9 – -22.8	—	—	—	24.0 – 25.0	—	—
Dol+Cal1		95,0 – 182	—	-24.2 – -22.8	—	—	—	24.6 – 23.9	—	—

The last ice melting temperatures of inclusions are extremely uniform in appearance. The measured values fall in a narrow temperature interval, -22.5 – -24.5 °C, in both the *dol* and *cal1* phases (*Fig. 4.7/b* and *4.8/f; Table 4.1*). T_e data is not available for interpretation because of the metastable behaviour of the inclusions (i.e., absence of vapour phase); however, a melt phase appeared at lower than -40 °C. Despite the intensive fluorescence of the host mineral, the type of the dominant dissolved salt could be determined using Raman spectroscopy. The Raman spectra indicate the presence of NaCl in the fluid, which is evident in *Fig. 4.9*. The mentioned fluorescence affected our ability to determine the last melting temperature of hydrohalite, therefore the salt concentration of fluid could not be determined in the case of the primary inclusions of do and cc1 phases. The distribution of T_m (Ice) values

and the fact that first melt phase was observed at lower than -40 °C, together indicate that there the fluid contains dissolved $CaCl_2$, in addition to NaCl (YANATIEVA 1946). The dissolved volatile (gas) components in the fluid were not detectable by microthermometry, and their analysis by Raman spectroscopy was interrupted because of the intensive fluorescence of the host mineral.

Inclusions show V→L type homogenisation and their T_h values are between 130 and 180 °C for both the mineral phases (*dol*, and *cal1*) with the majority of values falling between 130-150 °C (*Fig. 4.7/a,* and *4.8/f; Table 4.1*). Fluid inclusions in the *dol* and *cal1* phases cannot be distinguished by their T_h values. An unequivocal relationship/variation or trend between the measured values and the locations of inclusions in the crystals was not detected.

4.5. Discussion

4.5.1. Interpretation of results

The investigated fluid inclusion assemblages, both in the quartz and carbonate phases, are characterised by a narrow range of T_m(Ice) values, in conjunction with a broad range (~70 °C) of homogenisation temperatures. Because the FIAs can be unequivocally discriminated from one other by their textural patterns, the possibility of unintentionally mixing different FIAs can be excluded. The development of extremely different T_h values in one assemblage can be considered to the result of overlapping processes. The possible mechanisms and the related textural/microthermometric patterns for each assemblage are summarised in Table 4.2. (ROEDDER 1984; GRATIER & JENATTON 1984; GOLDSTEIN & REYNOLDS 1994; LOUCKS 2000; BODNAR 2003; DIAMOND 2003). In Table 4.2, many patterns can be attributed to one mechanism but all the patterns cannot be assumed to have formed at the same time. If two fluid phases were stable in the fractures during the formation of the fluid inclusions (e.g., L+V inclusions), then the liquid to vapour ratio would be variable during the entrapment of the fluid (i.e., heterogeneous entrapment, see DIAMOND 2003).

If two fluid phases were stable during the formation of the inclusions, the different T_h values and the different homogenisation types may be related to the extremely different φ_{vap} values in individual assemblages. However both the different φ_{vap} values and V→L homogenisation are not observed in all the investigated samples.

Table 4.2. *Table of the possible reasons for the occurrence of extremely wide T_h interval and the observed textural and microthermometric features in the investigated FIAs (boxes with a grey background show the observed features)*

Oserved textural/ microthermometric features \ Possible causes		Heterogeneous entrapment	Plastic deformation	Recrystallization (necking down)	Leakage/ refilling/ fluid-mixing	Modification
undulate extinction, twin lammellas			+		+	
necking down/negativ crystal shape inclusions				+		
L→V homogeization/vapour dominant inclusions		+		+		
T_m(Ice) values are scattering in broad range					+	
Trend occur on T_m-T_h diagram	similar T_m(Ice) values	+	+			
	T_m(Ice) are changing with T_h				+	
Trend occur on T_h-FI diagram						+
Assymetric T_h histogram		+				

Therefore the petrographic evidence does not support the interpretation of heterogeneous entrapment. Various T_h values can be formed in originally homogeneous fluid inclusion assemblages by natural and/or artificial modifications (GRATIER & JENATTON 1984, SHEPPERD et al. 1985). To eliminate the artificial modifications, our samples were made by using a low speed liquid-cooled sawing, which prevents the formation of scattered T_h values during sample preparation.

Recrystallisation (i.e., local dissolution and reprecipitation) of host mineral can cause changes in density (and on this way T_h) of originally homogeneous FIAs (AUDÉTAT & GÜNTHER 1999; AYLLÓN et al. 2003). In this case, one would expect the T_h values formed by to be scattered over a wide range of values, and heterogeneous entrapment is not required to explain the T_h values. Therefore, the T_h values may not reflect the physical conditions of entrapment of the FIAs (GOLDSTEIN & REYNOLDS 1994).

LOUCKS (2000) examined the liquid-dominant fluid inclusions in FIAs, which show heterogeneous entrapment, and he found that the distribution of T_h values have a typical asymmetric distribution, with a long tail toward the higher temperatures. In the studied samples, we can observe the mentioned asymmetric distribution for the carbonate and the Q-P3 and Q-P4 assemblages. However, other textural patterns of inclusions do not support this heterogeneous entrapment interpretation.

Based on the observations presented here, we interpret the FIAs trapped a homogeneous fluid, and the host mineral subsequently suffered recrystallisation at relatively high

temperatures, just prior to the system reaching the two-phase boundary. This process resulted in the necking of the cavity in individual inclusions. As previously established, the wide range of homogenisation temperatures in the individual fluid inclusion assemblages cannot be explained by either heterogeneous entrapment or necking of the cavity.

A change of in the volume and density in primary FIAs following entrapment is most probable where the host mineral is *dol* and *cal1* and the highest T_h values (130-170 °C) are observed. Cavities of inclusions trapped in relatively soft, sheared minerals theoretically can experience plastic or elastic deformation. The volume of the cavity can increase due to an increase of pressure caused by heating, which can then cause a decrease in density and a higher recorded homogenisation temperature than that of the original undeformed cavity.

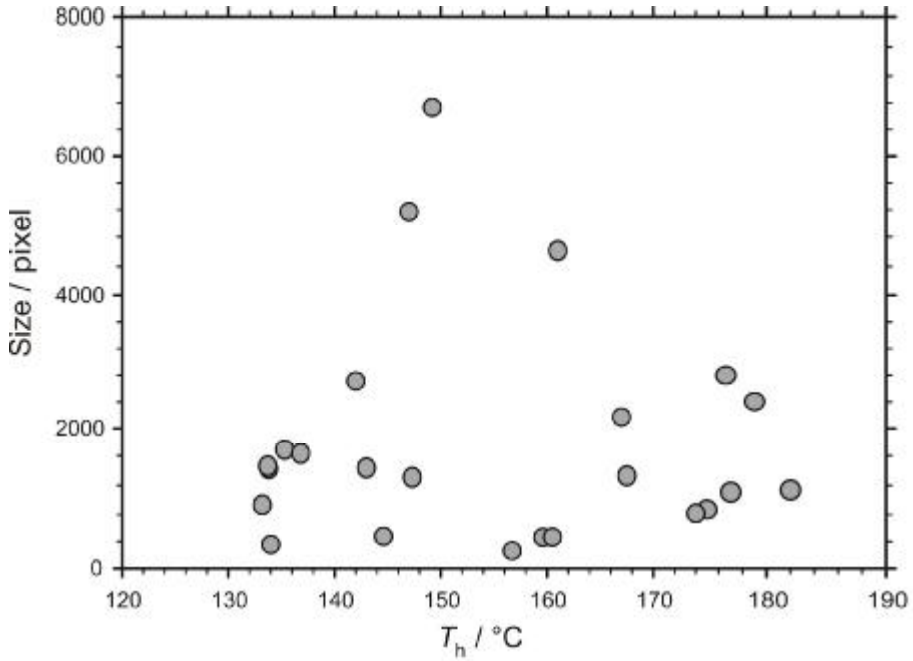

Figure 4.11. *FI size (measured on microphotos) vs. T_h plot of the fluid inclusions of the dol and cal1 phases*

The characteristics that have the greatest control on the probability of post-entrapment alteration of an inclusion are, in addition to the shape of inclusions, the size of an inclusion or the distance of the inclusion from the surface of the sample (LACAZETTE 1990). During the heating of a sample, inclusions found closest to the surface of the section are most likely to experience post-entrapment alteration. T_h versus the maximum size of inclusions in the *dol* and *cal1* phases is represented in *Fig. 4.11*. If internal overpressure has caused the alteration of primary inclusions, the larger inclusions should be associated with the higher T_h values, resulting in a constant positive correlation in *Fig. 4.11*. This kind of relationship is not detected for the *dol* + *cal1* phases. Nevertheless, the possibility of plastic deformation by

other external causes does exist, and it is supported by the undulate extinction observed in the *dol* and *cal1* phases and the twin lamellae that are sometimes found in the *cal2* phase.

The salinity data calculated using the T_m(Ice) and T_m(Hh) values from the NaCl-$CaCl_2$-H_2O system (BAKKER 2003) exhibit a very high concentration of dissolved NaCl of 20-26% *w*NaCl, and a significantly lower $CaCl_2$ content of 1.5-6% *w*$CaCl_2$. The presence of $CaCl_2$ could not be detected because $CaCl_2$*6H_2O (antarcticite) breaks down at the eutectic temperature (-52 °C) of the NaCl-$CaCl_2$-H_2O system (OAKES et al. 1990). Detecting antarcticite in the presence of hydrohalite is very complicated if NaCl/$CaCl_2$>2/1 hence antarcticite could not be identified on the acquired Raman spectra (SAMSON & WALKER 2000).

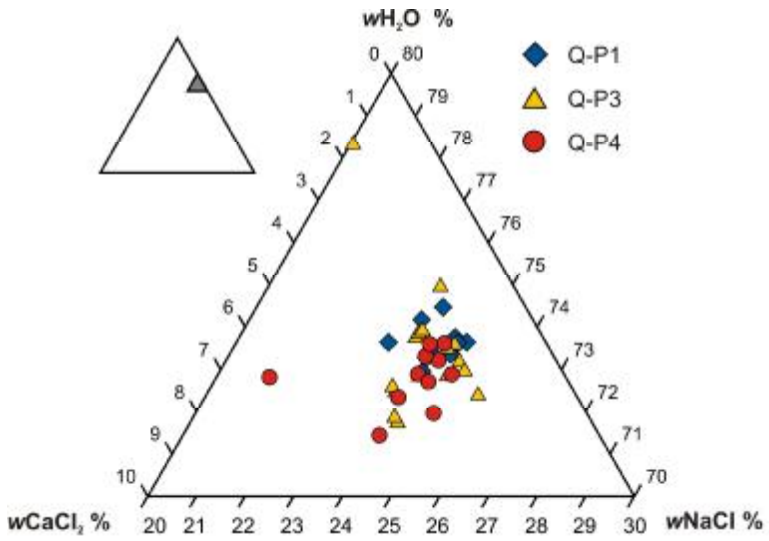

Figure 4.12. *Composition of the primary aqueous fluid inclusions in the quartz FIAs in the NaCl-$CaCl_2$-H_2O system*

The concentration of NaCl does not change significantly or change trend between the different fluid inclusion assemblages. The differences in salinity (20-26 *w*%) observed in the different generations of inclusion do not represent significant fluctuations, in the case of such high dissolved-salt contents (*Fig. 4.12*). The differences of dissolved $CaCl_2$ content are of greater significance, as the amounts of dissolved $CaCl_2$ increases in Q-P3 and Q-P4, which suggests an increase of the $CaCl_2$ concentration of the parent fluid during crystal growth.

Calculation of isochores for the *P-T* diagrams (*Fig. 4.13*), were made in the NaCl-H_2O model system without taking into consideration of the $CaCl_2$ content of fluid. This simplification is based on the study of POTTER & CLYNNE (1978), who demonstrated that the NaCl-H_2O system is valid even in complex electrolyte systems if Ca/Na<0.5. The proportion of CH_4 and N_2 in the aqueous phase could not be estimated because of the absence of

homogenisation temperatures for these components, therefore these gaseous components were not considered in isochores and phase diagrams.

The average geothermal gradient was considered in the calculation of the *P-T* conditions for the trapping of the FIAs. Hydrostatic (35 °C/10 MPa) pressure gradient was used to estimate the minimum trapping parameters while lithostatic (35 °C/22.6 MPa) pressure gradients was used to estimate the maximum trapping parameters of the inclusions (*Fig. 4.13*).

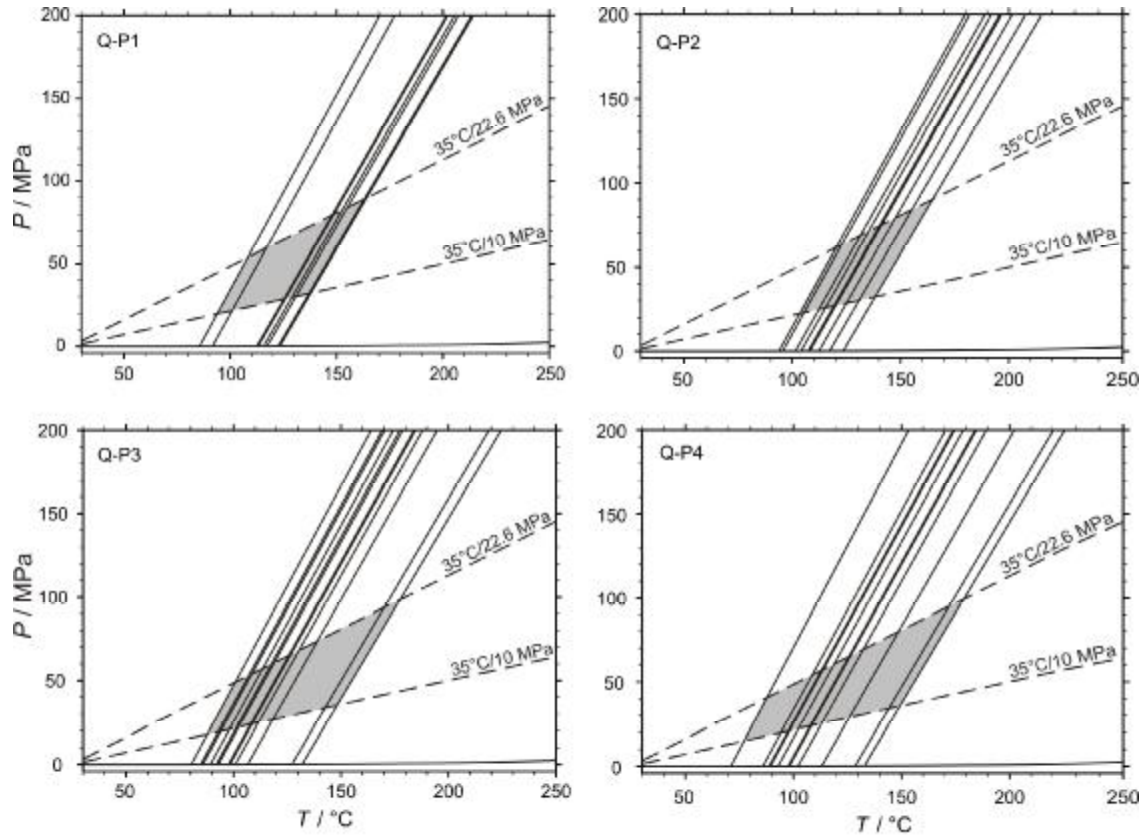

Figure 4.13. *P-T plots of the four primary FIAs of the quartz phase in the NaCl-H_2O system*
The probable P-T conditions of trapping of the fluid inclusions are indicated by the grey shaded regions.

Our results suggest that all the primary FIA in quartz experienced similar *P-T* conditions. Based on the assumptions presented earlier, the trapping of the fluids most likely occurred at T_t of 80-180 °C and P_t of 20-100 MPa (*Fig. 4.13.*).

4.5.2. Hypersaline fluids in crystalline complexes

The Na-Ca-Cl dominant hypersaline fluids or "brine" that contain CH_4, and become Ca-Na-Cl dominant with depth, are characteristic of a constituent of fluid systems in crystalline basement rocks all over the world (e. g. FRITZ & FRAPE 1982; BEHR & GERLER 1987; NORDSTROM et al. 1989a WILKINSON 1990; LODEMANN et al. 1997). A "brine" is defined as

an aqueous solution containing more dissolved salt than seawater ($3.5 \cdot 10^4$ mgL^{-1}) (KHARAKA & HANOR 2005). There are essentially two theories regarding the origin of fluids in crystalline rocks with regard to their high dissolved salt content. One theory explains the origin of the high dissolved-salt content as the result of water-rock interaction with the crystalline rocks (an "internal source"), while the other theory relates the special composition to "externally-derived" fluids.

a) The theory explaining the fluid origin via water-rock interaction attributes the high halogenide concentration, primarily Cl^- and Br^-, by ion exchange between the fluid and the chemical structure of minerals (e. g., apatite, amphiboles, biotite, sodalite) (KAMINENI 1987) – and alkali-halides (KULLERUD 2000; BUCHER & STOBER 2000). Main rock forming minerals, like amphiboles (especially hornblende and actinolite) and biotite can contain ~6-7 *w*% chlorine in the OH position of their crystal structure. The mentioned water-rock interactions can also affect the dissolved cation content (BUCHER & STOBER 2000). FRAPE & BLYTH (2005) suggest the fluid-feldspar interactions as the principal process that occurs in a variety of rock types. During albitization of Ca-rich plagioclase, the Na^+ content of the fluid decreases, while the Ca^{2+} content increase. The interaction of alkali feldspar-fluid, to reach feldspar/fluid equilibrium, can influence the Na^+-K^+ balance of solutions (GIGGENBACH 1988). The chloritization of albite can also increase the Na^+ content of the solution, while decreasing the Mg^{2+} and K^+ content of fluid (FRAPE & BLYTH 2005). The chloritization of biotite, sericitization of feldspars and serpentinization of ultra basic rocks, all can increase the the alkali content of a fluid by consuming of water (ABRAJANO et al. 1990). The formation of zeolites and clay minerals due to the alteration of feldspars, which are common fracture-filling minerals, also can decrease the water content of a fluid. Important source of solutes those liquids that can be found as fluid inclusions in minerals and can reach up to 70 *w*% NaCl (mostly alkali halides) salt content (NORDSTROM et al. 1989b). These entrapped fluids can be then be released from inclusions by brittle deformation processes (NORDSTROM et al. 1989b; IRWIN & REYNOLDS 1995).

Earlier examinations have detected biogenic-bacterial (SHERWOOD LOLLAR et al. 1993a) and abiogenic (SHERWOOD LOLLAR et al. 1993b) origin of CH_4 in crystalline reservoirs. A special H_2-controlled type of bacterial methanogenesis is characteristic of metamorphic complexes (PEDERSEN 1997; KOTELNIKOVA & PEDERSEN 1997). Fischer-Tropsch synthesis is the dominant process during abiogenic methanogenesis (SALVI &

WILLIAMS-JONES 1997); however, the metamorphism of carbonates and the serpentinization of basic and ultra basic rocks also can produce methane if there is a guaranteed source of carbon (SHERWOOD LOLLAR et al. 1993b).

Nitrogen can be found in silicates preferentially as NH^{4+} and can be incorporated into alkali metals (HALL 1999; PAPINEAU et al. 2005). Micas (mainly biotite) and alkali feldspars (mainly k-feldspar) contain the highest nitrogen contents (HONMA & ITIHARA 1981; HALL 1999; MINGRAM & BRÄUER 2001). Nitrogen can be released as NH_3 (HAENDAL et al. 1986) during progressive metamorphism and transform to N_2 by secondary oxidation processes.

b) The geologic formations that can be identified as the sources of high-salinity fluid need to be located in geographic proximity to the crystalline rocks in question. A common source of external fluids is seawater and its derivatives, such as evaporite deposits, or sedimentary brines, but salt lakes and continental evaporite deposits are also play a significant role (FRAPE & BLYTH 2005). Evaporites can be redeposited by wind or can be transported to the depth of migration of meteoric water (FRAPE & BLYTH 2005). The influence of basinal brines in crystalline complexes has been investigated by many researchers (e. g. BEHR & GERLER 1987; BEHR et al. 1987; MULLIS & STALDER 1987; GASCOYNE et al. 1989; MCNUTT et al. 1990; MUNZ et al. 1995; LODEMANN et al. 1997). The composition of this kind of fluid is dominantly NaCl with a significant Ca^{2+} content. They can contain Mg^{2+} and K^{+} in small amounts; however, their HCO_3^- and SO_4^{2-} content can also be high. The composition of fluid can be modified until it reaches the crystalline basement. During the fluid migration, significant water-rock reactions can occur in the sediments, which can increase their Na-Ca-Cl content (KHARAKA & HANOR 2005). One of the most important processes that contribute to the NaCl content of meteoric fluids is the dissolution of halite found in sediments. The amount of Mg^{2+} can be decrease by the formation of chlorite and the dolomitisation of limestone. However, the latter process can increase the Ca^{2+} content of fluid. The albitization that mostly occurs in arkoses sandstones also can increase the Ca^{2+} content of local fluids. The formation of clay minerals with high potassium content can remove significant amount of K^{+} from the fluid. The amount of HCO_3^- in a fluid can decrease due to the precipitation of calcite, while a decrease in SO_4^{2-} can result from the precipitation of anhydrite or gypsum.

In the case of CH_4 originated from external sources, biogenic sources are the most common (SCHOELL 1988), and thermogenetic formation plays a principal role (RICE & CLAYPOOL 1981). In this case, thermo-chemical alteration of accumulated organic matter (primarily II-III. type kerogene, rarely coal strings) can produce methane. This kind of methane deposition is observed in many geologic formations (JENDEN & KAPLAN 1988; JENDEN et al. 1988; RICE et al. 1988).

The other important type of methane formation is by bacterial methanogenesis (SCHOELL 1988; MARTINI et al. 2003). Two processes are significant in this type of methane formation, which are acetate fermentation and CO_2 reduction (WHITICAR et al. 1986; SCHOELL 1988). Fermentation is dominant in younger continental sediments, while CO_2 reduction is common in older basement sediments (WHITICAR et al. 1986; SCHOELL 1988). CO_2 reduction in older basement sediments is of greater importance because methane produced by acetate fermentation can be released to the atmosphere very easily (JENDEN & KAPLAN 1986; COLEMAN et al. 1988).

Nitrogen can also be originated from many external sources (HOLLOWAY & DAHLGREN 2002). Meteoric water can carry high amount of atmospheric nitrogen as a solute below the surface. However most of the subsurface N_2 is produced by the alteration of organic matter (RAMSEYER et al. 1993), or by microbial activity. During the decomposition of organic matter, nitrogen, frequently accompanied by CH_4, can be released as NH_3 and then oxidised to N_2 (ROHRBACK et al. 1983). Nitrogen produced by microbial activity can be attributed to denitrifying bacteria (KOIKE & SORENSEN 1988), and a part of the produced N_2 is carried into subsurface by subsurface fluids.

The effect of fluid migrate into the subsurface depends on many factors. The flow rate of the fluid that migrates into subsurface is of primary importance (GLEESON & YARDLEY 2003). The more time the fluid remains in the same rock type, can better modify the composition of fluid by water-rock reactions (BUCHER & STOBER 2000). Migration of hypersaline fluids into the subsurface is a density-controlled process that requires a corresponding hydraulic gradient. Migration of the high-density fluid into the subsurface is balanced by geothermal buoyancy, which deflects the fluid in the direction of the surface (KHARAKA & HANOR 2005). Fracture systems and fault zones act as channels that can significantly control the pathway of fluids (BEHR & GERLER 1987; BEHR et al. 1987).

4.5.3. Hypersaline fluids in the Baksa Complex

To better understand the origin, composition and physical properties of the fluid that migrated through in the Baksa Complex, many factors need to be clarified. There are high importance of those alterations that are caused by water-rock interactions, because most probable these alteration process are responsible those high salt concentration are observable in the investigated aqueous solutions. The increase in salinity caused by water-rock interaction can be seen in the case of fracture filling carbonate in the Mórágy Granite Formation, which is also found in the vicinity of Baksa Complex (SZABÓ et al. 2003; KOVÁCS-PÁLFFY & FÖLDVÁRI 2003). In this case, the high Na-Ca-Cl composition of the fluid was explained by metasomatic enrichment of hydrothermal fluids, a process characteristically found during the final stage of a magmatic event (SZABÓ et al. 2003). In spite the high salinity fluid can be found in the quartz-carbonate of the BC, SZABÓ et al. (2003) also found middle and low salinity fluid in the primary inclusions in the carbonate veins within the Mórágy Granite.

In the crystalline rocks of the BC, there is also a probability that these processes caused an increase of salinity in the fluid. Chloritization is very characteristic in the rocks of the complex. This phenomenon is found throughout the core, similar to the alteration of biotite. The other important water-consuming alteration, found in smaller abundance than the chloritization, is the sericitization of feldspars, which is most intense in the gneiss and mica schist rocks. However, these two retrograde minerals are generally found in the adjacent rock, not in the quartz-carbonate veins and cannot be found in great abundance near the veins. The temperature estimates of chloritization (200-400 °C) of the adjacent rocks from ÁRKAI (1985) are much higher than can be deduced from the *P-T* diagrams (*Fig. 4.13*) for the formation conditions (80-180ºC) of the quartz-carbonate veins. Zeolites and clay minerals, which are stable at a lower temperature range and can be attributed to intensive water-rock interactions, are not observed in the wall rocks. From this it can be deduced that the high salinity cannot be the result of water-rock interactions in the crystalline rocks of the BC and instead the result of an exotic high-salinity fluid. The sources of CH_4 and N_2 in the fluid are most likely the thick local sedimentary formations that contain carbonised organic matter. One of the most probable sources is the Téseny Sandstone Formation, which overlies a significant portion of the rocks of BC.

The high dissolved ion content likely originated from sedimentary brines, or fluids that percolated through evaporite formations. This type of formation also can be found in proximity to the BC. For this reason, the Permo-Triassic arkosic (Kővágószőlős Sandstone

Formation, FAZEKAS 1987) and evaporitic (Hetvehely Dolomite Formation, Magyarürög Anhydrite Member, KONRÁD 1997) formations are of primary importance. The fluids that migrate through the fractured basement owe their Na-Ca-Cl composition to the water-rock interactions that occur in the overlying sediments, and they can preserve these characteristics even in the fracture system of the BC. The effect of external fluids is exploited by fault zones and deep fracture systems produced by tectonism, and their influence has been detected in many situation other crystalline complexes. BEHR & GERLER (1987) and BEHR et al. (1987) attributed the rhythmic fluctuation in fluid chemistry between the growth zones of fracture-filling quartz crystals in basement complexes to the tectonic activation of fault zones. In their opinion, periods of increased tectonic activity could cause migration of a large amount of sedimentary basin fluids into the crystalline basement.

Even though we could not detect a fluctuation in fluid chemistry between growth zones of the quartz crystals we investigated, and T_h values do not show any significant petrographical trend, there is a high probability that external fluids influenced the rocks of the BC after the last period of structural deformation. Based on the parameters we determined for the formation of vein-filling mineral phases from our fluid inclusion study, the cementation of the fractures most probably occurred at a few km depth (2-5 km), given an average geothermal gradient. At this depth range, circulation of the surface-derived and sedimentary basin-derived fluids is general phenomena. Many studies can confirm the universal occurrence of these types of fluids in the deeper part of crystalline basements. In the case of metamorphic complexes, their presence and influence can be detected even at ~8 km depth (MORRISON 1994; NESBITT & MUEHLENBACHS 1989; READ & CARTWRIGHT 2000).

ACKNOWLEDGEMENTS

Thank goes to the Stiftung Aktion Österreich-Ungarn (project No. 62öu4) who supported the measurements critical to my work. I would like to thank for Ronald J. Bakker and his research group for the helping in the fluid inclusion studies and Raman spectroscopy and the Hungarian Research Found (No. K60768) for supporting the project financially.

REFERENCES

ABRAJANO, T. A., STURCHIO, N. C., KENNEDY, B. M., LYON, G. L. (1990). Geochemistry of reduced gas related to serpentinization of the Zambales ophiolite, Philippines. *Applied Geochemistry* 5, 625-630.

ÁRKAI, P. (1984): Polymetahmorphism of the crystalline basement of the Somogy-Dráva basin southwestwern transdanubia, Hungary. *Acta Mineralogica-Petrographica, Szeged* 2/XXVI, 129-153.

ÁRKAI, P. (1985): Polymetamorphic evolution of the South-Hungarian crystalline basement, Pannonian basin, geothermometric and geobarometric data. *Acta Geologica Hungarica* 3-4/23, 165-190.

ÁRKAI, P., HORVÁTH, P., NAGY, G. (1999): A clockwise P-T path from the Variscan basement of the Tisza Unit, Pannonian basin Hungary. *Geologica Croatica* 2/52, 109-117.

AUDETAT, A., & GÜNTHER, D. (1999): Mobility and H_2O loss from fluid inclusions in natural quartz crystals. *Contribution Mineralogy and Petrology* 137, 1-14.

AYLLÓN, F., BAKKER, R. J., & WARR, L. N. (2003): Re-equilibration of fluid inclusions in diagenetic-anchizonal rocks of the Cinera-Matallana coal basin NW Spain. *Geofluids* 3, 49-68.

BAKKER, R. J. (2003): Package FLUIDS 1. Computer programs for analysis of fluid inclusion data and for modeling bulk fluid properties. *Chemical Geology,* 194, 3-23.

BAKKER, R. J. (2004): Raman spectra of fluid and crystal mixtures in the systems H_2O, H_2O–NaCl and H_2O–$MgCl_2$ at low temperatures: applications to fluid-inclusion research. *The Canadian Mineralogist* 42, 1283-1314.

BALOGH, K., ÁRVA-SÓS, E., BUDA, GY. (1983): Chronology of granitoid and metamorphic rocks of Transdanubia Hungary. *Anuarul Institului de Geologie şi Geofizică* 61, 359-364.

BEHR, H. J., & GERLER, J. (1987): Inclusions of Sedimentary Brines in Post-Variscan Mineralizations in the Federal republic of Germany - A Study by Neutron Activation Analysis. *Chemical Geology,* 61, 65-77.

BEHR, H. J., HORN, E. E., FRENTZEL-BEYME, K., & REUTEL, C. (1987): Fluid unclusion characteristics of the Variscan and Post-Variscan mineralizing fluids in the Federal Republic of Germany. *Chemical Geology,* 61, 273-285.

BLYTH, A., FRAPE, S., BLOMQVIST, R., NISSINEN, P. (2000): Assessing the past thermal and chemical history of fluids in crystalline rock by combining fluid inclusion and isotopic investigations of fracture calcite. *Applied Geochemistry,* 15, 1417-1437.

BODNAR, R. J., STERNER, S. M., & HALL, D. L. (1989): SALTY: a FORTRAN program to calculate compositions of fluid inclusions in the system NaCl-KCl- H_2O. *Computers & Geosciences,* 15, 19-41.

BODNAR, R. J. (2003): Re-equilibration of fluid inclusions. In: SAMSON, I., & MARSHALL, D. (eds.) Fluid Inclusions: Analisys and interpretation. *Mineralogical Association of Canada., Short Course Ser*. 32, 213-230.

BUCHER, K., & STOBER, I. (2000): The composition of groundwater in the continental crystalline crust. In: BUCHER, K., & STOBER, I. (eds.) Hydrogeology of Crystalline Rocks. Dordrecht, *Kluwer Academic Publishers*, 34, 141-176.

COLEMAN, D. D., LIU, C. L., & RILEY, K. M. (1988): Microbial methane in the shallow Paleozoic sediments and glacial drift deposits of Ilinois, U. S. A. *Chemical Geology* 71, Origins of methane in the Earth, 23-40.

CRESPO, M. T., DELGADO, A., CATENA, E. V., GARCÍA, L. A. J., FABRE, C. (2002): The latest Post-Variscan fluids in the SpanishCentral System: evidence from fluid inclusion and stable isotope data. *Marine and Petroleum Geology,* 19, 323-337.

DABI, G., M. TÓTH T., SCHUBERT F. (2008): Eltérő genetikájú többgenerációs érkitöltő karbonát cementáció a Mecsekalja zónában (Ófalu Aranyosvölgy). *Földtani közlöny bírálat alatt*.

DIAMOND, L. W. (2003): Systematics of H_2O inclusions. In: IAN SAMSON, & DAN MARSHALL (eds.) Fluid Inclusions: Analisys and interpretation, Vancouver, *Mineralogical Association of Canada*, 32, 55-77.

EVANS, K. F., KOHL, T., HOPKIRK, R. J., & RYBACH, L. (1996): Studies the nature of non linear impedance to flow within the fractured granitic reservoir at the European Hot Dry Rock Project site at Soutz-sous-Forets, France. Zürich, Eidgenössische Technische Hochschule, 152.

FAZEKAS, V. (1987): A mecseki perm és alsótriász korú törmelékes formációk ásványos összetétele. *Földtani Közlöny,* 117, 11-30.

FAZEKAS, V., & VINCZE, J. (1991): Hidrotermás ércindikációk a Villány-hegység északi előtere mélyfúrásaiban. *Földtani Közlöny,* 91/1-4, 23-56.

FOURCADE, S., MICHELOT, J. L., BUSCHAERT, S., CATHELINEAU, M., FREIBERGER, R., COULIBALY, Y., & J. ARANYOSSY, F. (2002): Fluid transfers at the basment/cover interface: Part I. Subsurface recycling of the carbonate from gtranitoid basement rocks France. *Chemical Geology,* 192, 1-2, 99-119.

FRAPE, S. K., & BLYTH, A. (2005): Deep Fluids in the Continents: II. Crystalline Rocks. In: HOLLAND, D. H., & TUREKIAN, K. K (eds.) Treatise on Geochemistry, Oxford, *Elsevier Science*, 5, 541-580.

FRITZ, P., & FRAPE, S. K. (1982): Saline groundwaters in the Canadian Shield - a first overview. *Chemical Geology* 36, 179-190.

GASCOYNE, M., PURDY, A., FRITZ, P., ROSS, J. D., FRAPE, S. K., DRIMMIE, R. J., & BETCHER, R. N. (1989): Evidence for penetration of sedimentary basin brines into an Archean granite of the Canadian shield. Proc. *6th int. Symp. Water-Rock Interaction*, Malvern, UK, Balkema, Rotterdam The Netherlands, 243-24

GÉCZY, B. (1973): Plate tectonics and palaeogeography int he East-Mediterranean Mesozoic. –*Acta Geol. Hung.,* 27, 379-389

GIGGENBACH, W. F. (1988): Geothermal solute equilibria. Derivation of Na-K-Mg-Ca geoindicators. *Geochimica et Cosmochimica Acta,* 52, 2749-265.

GLEESON, S. A., & YARDLEY, B. W. D. (2003): Surface-derived fluids in basement rocks: inferences from palaeo-hydrothermal systems. *Journal of Geochemical Exploration,* 78-79, 61-65.

GOLDSTEIN, R. H., & REYNOLDS, T. J. (1994): Systematics of fluid inclusions in diagenetic minerals. SEPM Short Course, Society for Sedimentary Geology, 31, 199p.

GONZALEZ-PARTIDA, E., CARRILLO-CHAVEZ, A., LEVRESSE, G., TELLO-HINOJOSA, E., VENEGAS-SALGADO, S., RAMIREZ-SILVA, G., PAL-VERMA, M., TRITLLA, J., CAMPRUBI, A. (2005): Hydro-geochemical and isotopic fuid evolution of the Los Azufres geothermal feld, Central Mexico. *Applied Geochemistry,* 20, 23-39.

GRATIER, J. P., & JENATTON, L. (1984): Deformation by solution-deposition, and re-equilibration of fluid inclusions in crystals depending on temperature, internal pressure and stress. *Journal of Structural Geology,* 61/2, 189-200.

HAAS, J., & PÉRÓ, CS. (2004): Mesozoic evolution of the Tisza Mega-unit. *Int. J. Earth Sci.,* 93, 297-313.

HAENDAL, D., MUHLE, K., NITZSCHE, H. M., STEIHL, G., & WAND, U. (1986): Isotopic variation of the fixed nitrogen in metamorphic rocks. *Geochimica et Cosmochimica Acta,* 50, 749-758.

HALL, A. (1999): Ammonium in granites and its petrogenetic significance. *Earth-Science Reviews,* 45, 145-165.

HOLLOWAY, J. M., & DAHLGREN, R. A. (2002): Nitrogen in Rock: Occurences and biogeochemical implications. *Global Biogeochemical Cycles,* 16/4, 1118.

HOLLOWAY, J. R. (1984): Graphite-CH_4-H_2O-CO_2 equlibria at low-grade metamorphic conditions. *Geology* 12, 455-458.

HONMA, H., & ITIHARA, Y. (1981): Distribution of ammonium in minerals of metamorphic and granitic rocks. *Geochimica et Cosmochimica Acta,* 45, 983-988.

HORVÁTH, P., KOVÁCS, G., SZAKMÁNY, GY. (2003): Eclogite and garnet amphibolite pebbles from niocene conglomerates Pannonian basin Hungary: implications for the variscab metamorphic evolution of the Tisza Megaunit. *Geologica Catpathica,* 6/54, 355-366.

IRWIN, J. J., & REYNOLDS, J. H. (1995): Multiple stages of fluid trapping in the Stripa granite indicated by laser microprobe analysis of Cl, Be, I, U, and nucleogenic Ar, Kr, and Xe in fluid inclusions. *Geochimica et Cosmochimica Acta,* 59, 355-369.

JENDEN, P. D., & KAPLAN, I. R. (1988): Origin of natural gas in the Sacramento Basin. *Am. Assoc. Pet. Geol. Bull,* 72.

JENDEN, P. D., NEWELL, K. D., KAPLAN, I. R., & WATNEY, W. L. (1988): Composition and stable-isotope geochemistry of natural gases from Kansas, midcontinent, U.S.A. *Chemical Geology* 71 Origins of methane in the Earth, 117-147.

KAMINENI, C. D. (1987): Halogen bearing minerals in plutonic rocks: a possible source of chlorine in salne groundwater in the Canadian shoeld. In: FRAPE, S. K. & FRITZ. P (eds.) Saline Water and Gases in Crystalline Rocks. Special Paper 33, 69-79.

KASSAI, M. (1972): A Villány-Szalatnaki pleozóos mélytörés. The Paleozoic Deep Fracture of Villány-Szalatnak *MTA X. Oszt. Közl.* 61, 351-354.

KHARAKA, Y. K., & HANOR, J. S. (2005): Deep Fluids in the Continents: I. Sedimentary Basins. In: HOLLAND, D. H., & TUREKIAN, K. K (eds.) Treatise on Geochemistry, Oxford, *Elsevier Science*, 5, 499-540.

KIRÁLY, E. (1996): Adalékok a délkelet-dunántúli polimetamorf aljzat megismeréséhez. *Földtani Közlöny,* 1/126, 1-23.

KOIKE, I., & SORENSEN, J. (1988): Nitrate reduction and Denitrification in Marine Sediments. In: BLACKBURN, H. T., & SORENSEN, J., (eds.) Nitrogen Cycling in Coastal Marine Environments. *John Wiley & Sons Ltd.*, 251-273.

KONNERUP-MADSEN, J. (2006): A reconaissance study of fluid inclusions in fracture-filing quartz and calcite from the Lopra-1/1A well, Faroe Islands. In: CHALMERS, A. J., & WAAGSTEIN, R., (eds.) *Scyentific results from the deepened Lopra-1 borehole, Faroe Islands*., Copenhagen. 9, 118-122.

KONRÁD, GY. (1997): A DK-dunántúli alsó - és középső triász képződmények szedimentológiai vizsgálatának eredményei. *Kandidátusi értekezés*. Budapest.

KOTELNIKOVA, S., & PEDERSEN, K. (1997): Evidence for methanogenic *Archaea* and honoacetogenic *Bacteria* in deep granitic rock aqufers. *FEMS Microbiology Reviews,* 20, 339-349.

KOVÁCH, A., SVINGOR, E., & SZEDERKÉNYI, T. (1985): Rb-Sr Dating of basement rocks from the southern foreland of the Mecsek mountains, southeastern transdanubia, Hungary. *Acta Mineralogica-Petrographica, Szeged* XXVII, 51-57.

KOVÁCS-PÁLFFY, P., & FÖLDVÁRI, M. (2003): Hidrotermális képződmények és jelenségek a Mórágyi Gránit Formációban. Budapest, *Magyar Állami Földtani Intézet évi jelentése 2003 (2004) MÁFI*, 327-331.

KRUMGALZ, B. S., POGORELSKY, R., & PITZER, K. S. (1996): Volumetric properties of single aqueous electrolytes from zero to saturation concentration at 298,15 K Represented by Pitzer's ion-interaction equations. *Journal of Phy sical Chemistry Referential Data,* 25, 639-663.

KULLERUD, K. (2000): Occurence and origin of Cl-rich amphibole and biotite in the Earth's crust-implications for fluid composition and evolution. In: BUCHER, K., & STOBER, I. (eds.) Hydrogeology of Crystalline Rocks. Dordrecht Kluwer Academic Publishers, 34, 205-225.

LACAZETTE, A. (1990): Application of linear elastic fracture mechanics to the quantitative evaluation of fluid-inclusion decrepitation. *Geology,* 18, 782-785.

LELKES-FELVÁRI, GY. & FRANK, W. (1997): Geochronology of the metamorphic basement, Transdanubian part of the Tisza Mega-Unit. *Acta Geologica Hungarica,* 49/3, 189-206.

LODEMANN, L., FRITZ, P., WOLF, M., IVANOVICH, M., HANSEN, B. T., & NOLTE, E. (1997): On the origin of saline fluids in the KTB continental deep drilling project of Germany. *Applied Geochemistry,* 12, 831-849.

LOUCKS, R. R. (2000): Precise geothermometry on fluid inclusion populations that trapped mixtures of immiscible fluids. *American Journal of Science,* 300, 23-59.

MARTINI, A. M., WALTER, L. M., KU, T. C. W., BUDAI, J. M., KAISER C. J., MCINTOSH, J. C., & SCHOELL, M. (2003): Microbial production ad modification of gases in sedimentary basins: A geochemical case study from a Devonian shale gas play, Michigan basin. *AAPG Bulletin,* 87/8, 1355-1375.

MCNUTT, R. H., FRAPE, S. K., FRITZ, P., JONES, M. G., & MACDONALD, I. M. (1990): The $^{87}Sr/^{86}Sr$ values of Canadian Shield brines andfracture minerals with applications to groundwater mixing, fracture history, and geochronology. *Geochimica et Cosmochimica Acta* 54, 205-215.

MERNAGH, T. P., & WILDE, A. R. (1989): The use of laser Raman microprobe for the determination of salinity in fluid inclusions. *Geochimica et Cosmochimica Acta,* 53, 765-771.

MINGRAM, B., & BRÄUER, K. (2001): Ammonium concentracion and nitrogen isotope composition in metasedimentary rocksfrom different tectonometamorphic units of the European Variscan Belts. *Geochimica et Cosmochimica Acta,* 65, 273-287.

MORRISON, J. (1994): Meteoric water-rock interaction in the lower plate of the Whipple Mountain metamorphic core complex, California. *Journal of Metamorphic Geology* 12, 827-840.

MULLIS, J., & STALDER, H. A. (1987). Salt-poor and salt-rich fluid inclusions in quartz from two boreholes in northern Switzerland. *Chemical Geology* 61, 263-272.

MUNZ, I. A., YARDLEY, B. W. D., BANKS, D. A., & WAYNE, D. (1995): Deep penetration of sedimentary fluids in basement rocks from southern Norway: Evidence from hydrocarbon and brine inclusion in quartz veins. *Geochimica et Cosmochimica Acta,* 59/2, 239-254.

MUNZ, I. A., IDEN, K., JOHANSEN, H., VAGLE, K. (1998): The fluid regime during fracturing of the Embla field, Central Trough, North Sea. *Marine and Petroleum Geology,* 15, 751-768.

MUNZ, I. A. (2001): Petroleum inclusions in sedimentary basins: systematics analytical methods and application. *Lithos,* 55, 195-212

NADEN, J. (1996): CalcicBrine 1.5: a Microsoft Excel 5.0 add-in for calculating salinites from microthermometric data in the system NaCl-$CaCl_2$-H_2O. *PACROFI VI*, University of Wisconsin.

NESBITT, E. B., & MUEHLENBACHS, K. (1989): Origins and Movement of Fluids during Deformation and Metamorphism in the Canadian Cordillera. *Science,* 245/4919, 733-736.

NORDSTROM, D. K., BALL, J. B., DONAHOE, R. J., & WHITTEMORE, D. (1989a): Groundwater chemistry and wate-rock interactions at Stripa. *Geochimica et Cosmochimica Acta,* 53, 1727-1740.

NORDSTROM, D. K., LINDBLOM, S., DONAHOE, R. J., & BARTON, C.C. (1989b): Fluid Inclusion in the Stripa granite and their possible influence on the groundwater chemistry. *Geochimica et Cosmochimica Acta,* 53, 1741-1755.

OAKES, C., BODNAR, R. J., SIMONSON, J. M. (1990): The System NaCl-$CaCl_2$-H_2O: I. The ice liquidus at 1 atm total pressure. *Geochimica et Cosmochimica Acta,* 54, 603-610.

O'REILLY, C., SHANNON, P. M., FEELY, M. (1998): A fluid inclusion study of cement and vein minerals from the Celtic Sea Basins, offshore Ireland. *Marine and Petroleum Geology,* 15, 519-533.

OXTOBY, N. (2000). Re-equilibration of aquaeous inclusions in carbonate cements by freezing: implications for geologic studies. http://www.gl.rhul.ac.uk/poros/fia/Unpublished.htm

PAPINEAU, D., MOJZSIS, S. J., KARHU, J. A., & MARTY, B. (2005): Nitrogen isotopic composition of ammoniated phyllosilicates, case studies from Precambrian metamorphosed sedimentary rocks. *Chemical Geology,* 216, 37-58.

PEDERSEN, K. (1997): Microbial life in deep granitic rock. *FEMS Microbiology Reviews,* 20, 399-414.

POTTER, R. W. I., & CLYNNE, M. A. (1978): Pressure correction for fluid inclusion homogenization temperatures *Abstract.* International Association on the genesis of ore deposits, 5th Symposium, *Program and Abstracts*, Alta, ÚT, 146 p.

RAMSEYER, K., DIAMOND, L. W., & BOLES, J. R. (1993): Authigenic K-NH_4 - feldspar in sandstones? a fingerprint of the diagenesis of organic matter. *Journal of Sedimentary Research,* 63/6, 1092-1099.

RAVASZ-BARANYAI, L. (1969): Eclogite from the Mecsek Mountains, Hungary. *Acta Geologica Academiae Scientiarum Hungaricae,* 13, 315-322.

READ, C. M., & CARTWRIGHT, I. (2000): Meteoric fluid infiltration in the middle crust during shearing: examples from the Arunta Inlier, central Australia. *Journal of Geochemical Exploration,* 69-70, 333-337.

RICE, D. D., & CLAYPOOL, G. E. (1981): Generation, accumulation and resource potential of biogenic gas. *Am. Assoc. Pet. Geol. Bull.,* 65, 5-25.

RICE, D. D., THRELKELD, C. N., & VULETICH, A. K. (1988): Character, Origin and Occurence of Natural Gases in the Andarko Basin, Southwestern Kansas, Western Oklahoma and Texas Panhandle U.S.A. *Chemical Geology,* 71 Origins of methane in the Earth, 149-157.

ROEDDER, E. (1984): Fluid Inclusions. *Reviews in Mineralogy, Mineralogical Society of America*, 12, 644 p..

ROHRBACK, G. B., PETERS, E. K., SWEENEY, E. R., & KAPLAN, R. I. (1983): Ammonia formation in laboratory simulated thermal maturaion: Implications related to the origin of nitrogen in natural gas. In: BJOROY, M. (eds.) Advances in Organic Geochemistry. New York, *John Wiley & Sons*, 819-823.

SALVI, S., & WILLIAMS-JONES, A. E. (1997): Fischer -Tropsch synthesis of hydrocarbons during sub-solidus alteration of the Strange Lakeperalkaline granite, Quebec/Labrador, Canada. *Geochimica et Cosmochimica Acta,* 61/1, 83-99.

SAMSON, I. M., & WALKER, R. T. (2000): Cryogenic Raman Spectroscopic Studies in the System NaCl-$CaCl_2$-H_2O and Implications for Low-Temperature Phase Behavior in Aquaeous Fluid Inclusions. *The Canadian Mineralogist,* 38, 35-43.

SCHOELL, M. (1988): Multiple origins of methane in the Earth. *Chemical Geology* 71, 1-10.

SCHUBERT, F., KÓTHAY, K., DÉGI, J., M. TÓTH, T., BALI, E., SZABÓ, CS., BENKÓ, ZS., ZAJACZ, Z. (2007): A szakirodalomban használt fluidum- és olvadékzárványokkal kapcsolatos kifejezések és szimbólumok szótára. *Földtani Közlöny,* 137/1, 83-102.

SHEPPERD, T. J., & RANKIN, A. H., C ALDERTON, D. H. M. (1985): A Practical Guide to Fluid Inclusion Studies: Glasgow, Blackie and Son, 239 p.

SHERWOOD LOLLAR, S. K. F., P. FRITZ, S. A. MACKO, J. A. WELHAN, R. BLOMQVIST, & P. W. LAHERMO (1993a): Evidence for bacterially generated hydrocarbon gas in canadian Shield and Fennoscandian Shield rocks. *Geochimica et Cosmochimica Acta,* 57, 5073-5085.

SHERWOOD LOLLAR, B., FRAPE, K. S., WEISE, M. S., FRITZ, P., MACKO, A. S., & WELHAN, A. J. (1993b): Abiogenic methanogenesis in crystalline rocks. *Geochimica et Cosmochimica Acta,* 57, 5087-5097.

SZABÓ, CS., GÁLNÉ SÓLYMOS, K., & FALL, A. (2003): Karbonátos repedéskitöltés-vizsgálatok Üveghuta környékén mélyített fúrások granitoid kőzetein. *Kis és közepes radioaktivitású erőművi hulladékok végleges elhelyezése. Telephelykutatás Üveghuta körzetében*. Budapest, 110 p.

SZEDERKÉNYI, T. (1974): A DK-Dunántúli ópaleozóos képződmények ritkaelem kutatása. *Manuscript. Kandidátusi értekezés MTAK*, 184 p.

SZEDERKÉNYI, T. (1976): Barrow -type metamorphism int he crystalline basement of South-East Transdanubia. *Acta Geol. Ac. Sci. Hung.,* 20, 47-61.

SZEDERKÉNYI, T. (1979): A mecseki ópaleozóos-prekambriumi alapszelvények komplex földtani feldolgozása. *Manuscript*., JATE, Szeged

SZEDERKÉNYI, T. (1983): Origin of amphibolites and metavolcanics of crystalline complexes of south transdanubia, Hungary. *Acta Geologica Hungarica,* 1-2/26, 103-136.

TARNAI, T. (1997): Ore minerals from the key section of the Baksa Complex W Baranya hills, Hungary. *Acta Mineralogica-Petrographica,* XXXVIII, Supplementum, 119-133.

TARNAI, T. (1998): Mineralogical-petrological study on ore vein penetrated by the key-borehole Baksa No. 2 SE Transdanubia, Hungary. *Acta Mineralogica-Petrographica,* XXXIX, 21-34.

TENZER, H. (2001): Development of Hot Dry Rock Technology. *Geo-Heat Center Quarterly Bulletin,* 22/4, 16-22.

WALLIN, B., PETERMAN, Z. (1999): Calcite fracture fillings as indicators of paleohydrology at Laxemar at the Aspö Hard Rock Laboratory, southern Sweden. *Applied Geochemistry,* 14, 953-962.

WHITICAR, M. J., FABER, E., & SCHOELL, M. (1986): Biogenic methane formation in marine and freshwater environments: CO_2 reduction vs. acetate fermentation - Isotope evidence. *Geochimica et Cosmochimica Acta,* 50, 693-709.

WILKINSON, J. J. (1990): The role of metamorphic fluids in the evolution of the Cornubian orefield: Fluid inclusion evidence from south Cornwall. *Mineralogical Magazine,* 54, 219-230.

YANATIEVA, O. K. (1946): Polythermal solubilituies in the systems $CaCl_2$-$MgCl_2$-H_2O and $CaCl_2$-NaCl-H_2O. *Zhur. Priklad. Khim*., 19, 709-722.

ZHANG, Y. G., & FRANTZ, J. D. (1987): Determination of the homogenization temperatures and densities of supercritical fluids in the system NaCl-KCl-$CaCl_2$-H_2O using synthetic fluid inclusions. *Chemical Geology,* 64, 335-350.

CHAPTER 5

Postmetamorphic palaeofluid evolution of the Baksa Complex

Summary

A Baksai Komplexum posztmetamorf paleofluidum evolúciója

Összegzés

5.1. Postmetamorphic palaeofluid evolution of the Baksa Complex

Summary

Postmetamorphic palaeohydrological evolution of the Baksa Complex (BC) can be outlined from the penetration of the aplite dykes up to the youngest detected fluid circulation event based on the results detailed in the previous chapters. Since radiometric ages of the subsequent stages are not yet available, the fluid evolution model will be sketched based on the relative ages (from the oldest to the youngest stage) of the distinct events.

5.1.1. Post magmatic hydrothermal evolutionary stage

5.1.1.1. Propylitic veins

The oldest observed fracture filling minerals form Ca-Al silicate dominant veins, which are the most frequent vein type in BC. Three subtypes can be distinguished based on petrographic examinations: clinopyroxene dominant veins (V_{cpx}) with the mineral sequence *cpx→ep→sph→ab→cal1*; feldspar dominant veins (V_{fp}) with the mineral sequence *ab±kfp→chl1→adu→chl2→cal1*; and epidote dominant veins (V_{ep}) with the mineral sequence *chl1→ep→czo→prh±adu→chl2→chl3→pyr→cal1→cal2→cal3*. Almost every fracture filling mineral can be found in each distinguished subtype, and the subsequent minerals frequently show overlap in the veins. Similar fluid compositions (0.2–3.0% *w*NaCl eq.) can be measured in the primary fluid inclusions of the diopside and epidote phases in every depth level of the drilled rock body. These observed characteristics indicate that the different subtypes (V_{cpx}, V_{fp}, V_{ep}) of Ca-Al silicate dominant veins can be considered to be the product of continuous fluid evolution and that they formed in an interconnected fracture system. Accordingly, the fracture filling mineralization can be characterized by a single ideal paragenetic sequence:

di→ep→sph→ab+kfp→chl1→prh±adu→chl2→chl3→pyr→cal1→cal2→cal3.

This fracture filling mineral paragenetic sequence is very similar to those that can be found in propylitic wall-rock alterations along hydrothermal veins (MEYER & HEMLEY 1967).

The T_h (di: 297–365 °C; ep: 180–359 °C) values were obtained from primary fluid inclusions of diopside and epidote crystals. Compared to their relative position in the paragenetic sequence, these data indicate a temperature decrease during mineral precipitation

in the fracture system (T_h: 365→180 °C). This tendency and the low *P-T* formation conditions of the vein system are also supported by the mineral chemistry and thermometry data. Syngenetic alkali and plagioclase feldspars with such a pure end member composition (albite: ~$Or_{1.0}Ab_{99}$ $An_{0.0}$; K-feldspar: ~$Or_{99}Ab_{1.0}An_{0.0}$) are typical in < 300 °C conditions, and are supported by the data of two-feldspar thermometry (220–300 °C).

The temperature decrease during fracture cementation is most characteristically indicated by the calculated formation temperature values of the different chlorite phases (T_{chl1}: 260 ± 32 °C → T_{chl2}: 222 ± 20 °C → T_{chl3}: 156 ± 10 °C). This tendency is supported by the decreasing value of Al^{IV} from core to rim in single chlorite crystals of *chl1* and *chl2* phases, and this phenomenon is also in accordance with the temperature decrease The pyrite crystals contain trace elements (Co, Ni, Cu, As, Mn, and Zn) in considerable amounts. The Co/Ni ratio varies between 1 and 5 in pyrite characteristic for pyrites from post-magmatic hydrothermal veins (Co/Ni: 1–10).

The fracture cementation occurred owing to a post-magmatic hydrothermal fluid that circulated in the fracture system of the BC eventuating propylitic mineral paragenetic succession in the veins. SZEDERKÉNYI (1979) related the propylitic vein filling mineralization of the BC to the aplite dykes that can be found very frequently in the drilled rock section of the complex. With respect to the rapid cooling rate of thin (< 10 m thickness) dykes intruded into shallow environments (FURLONG et al. 1991), the vertical movement of the crystalline block was not significant during the cooling of the igneous body to the temperature of the adjacent rock. Hence, the regional *P-T* condition had to be nearly constant during the hydrothermal vein formation. In this case, cooling of the hydrothermal fluid was driven by the temperature of the adjacent rocks, which was ~154 °C on the basis of the crystallization temperature of the very last observed phase, *chl3*.

The intersection of isochoric slopes of primary fluid inclusions of epidote with thermometric values of *chl1* indicate that these cogenetic minerals formed in a temperature range of ~230–290 °C at a pressure range of ~83–194 MPa. The regional pressure condition of the area was admittedly lower than ~194 MPa when the temperature of the vein system recovered to the ambient rock temperature (~154 °C). A more acceptable approximation would be, rather around the average of the above pressure range, at ~97 MPa. This pressure value can be considered as a nearly constant regional pressure condition during the vein filling process. By using these values (~97 MPa; ~154 °C) a ~39 °C/km thermal gradient can

be calculated if a 2650 kg/m^3 rock density and lithostatic pressure field were assumed. As significant pressure fluctuation should be assumed in neither the fluid pressure nor the regional pressure conditions, approximate formation temperatures of ~354–479 °C for diopside and ~236–474 °C for epidote can be estimated presuming fairly constant pressure (~100 MPa).

5.1.1.2. Metasomatism along the veins

The fluid that migrated in the propylitic veins infiltrated the adjacent rock resulting in characteristic wall-rock alteration patterns. The alterations can be divided into four alteration zones based on their specific alteration paragenesis:

Zone 1: In this zone albite and titanite are the most characteristic minerals; the mineral paragenesis is *ab* + *ttn* ± *ep*.

Zone 2: Here, the appearance of epidote pseudomorphs after biotite flakes is the most characteristic alteration feature. The mineral paragenesis is *ep* + *chl*+ *ttn* + *ab* ± *ser*.

Zone 3: The amount of epidote decreases markedly and the chlorite content increases. Sericite is more common and rutile inclusions occur frequently in chlorite. The mineral paragenesis is *chl* + *ep* + *ser* + *rt* ± *ttn*.

Zone 4: Sericitization is the most characteristic alteration process in this zone; other alteration minerals are present in subordinate amounts. The mineral paragenesis consists of *ser* ± *chl*.

These alteration mineral assemblages are typical in propylitic wall-rock alterations due to near vein metasomatism (ZHARIKOV et al. 2007), and the altered rock is related to the propylite metasomatic family. The hydrothermal leaching caused secondary porosity in the altered wall-rock, where epidote filled the dissolution cavities subsequently. The similar characters of the fluid inclusions of the cavity filling epidote as well as fracture filling epidote and diopside indicate that wall-rock alteration occurred in similar conditions as proposed in the case of propylitic veins. The metasomatic alteration occurred at <200 MPa and ~360–480 °C conditions in a near neutral weakly alkaline medium. Element mobilization occurred between the wall-rock and the hydrothermal fluid, which caused Ca transport to the wall-rock while significant amount of Fe, Mn, K, and Mg basic cations were removed from the adjacent rock.

5.1.1.3. Relationship between propylitic and polymetallic veins

The presence of polymetallic (”stockwork”-like) sulfide veins has been emphasized by SZEDERKÉNYI (1979), who presumed that these veins were the result of a hydrothermal event. This hydrothermal activity was considered to be younger than those that led to propylitic fracture filling mineralization (SZEDERKÉNYI 1979). TARNAI (1997, 1998) made a detailed mineralogical and ore genetic examination of a polymetallic vein of 6–7 cm thickness. He distinguished an early and a late ore mineralization phase in this vein. Studying fluid inclusions in quartz cogenetic with the later ore minerals, he obtained T_t: 240–300 °C and P_t: 15–30 MPa as a trapping condition (TARNAI 1998). These formation *P-T* values of the sulfide veins are similarly low as in the case of propylitic veins.

The Co/Ni ratio of the pyrite phase, ~0.8–4.6, is well within the range of disseminated pyrite grains from the propylitic veins, which supports the post-magmatic hydrothermal origin of both vein types. This kind of low pressure ore mineralization is typical in cases where an igneous heat source has intruded at near surface conditions (CLINE & BODNAR 1991). CLINE & BODNAR (1991) also found that at low pressure conditions the early igneous fluids usually represent low salinity (chloride) composition leading to the formation of veins filled essentially by gangue minerals with only a minor amount of ore phases (CLINE & BODNAR 1991). In the last stage, fluids are significantly higher in chloride, causing higher sulfidation of ore veins, where the majority of ore deposition occurs in the 250–350 °C range (CLINE & BODNAR 1991; BARNES 1979). Whether or not a significant amount of ore minerals formed in relation to the igneous derived fluid activity in the case of the BC should be studied in detail later. Nevertheless, based on the above detailed similarities between the propylitic and polymetallic sulfide veins, a significant analogy between the genetics and formation conditions of these veins is presumable.

5.1.2. Externally derived fluid in the crystalline basement

Mineralization of the quartz-carbonate veins in the studied crystalline complex was a result of a significant change in fluid characteristics following the post-magmatic hydrothermal fluid circulation. The quartz-carbonate veins are characterized by a *qtz→dol+cal1→cal2* fracture filling mineral sequence. The new fluid type (T_h: 60–200 °C, and T_m(Ice): –28 to –17 °C) can be found in primary, pseudosecondary, and secondary fluid inclusions of the *qtz* phase and in primary inclusions in the subsequent *dol* + *cal1* phases of the quartz-carbonate veins. Moreover, this fluid type can be traced in D_1, E_1, and C_1 inclusions of *di*, *ep*, and *cal1* phases

of the propylitic veins too. The $\delta^{18}O$ isotopic signature of water ($\delta^{18}O$: –4 to –12.9‰ V–SMOW) from which the *cal1* phase had precipitated, together with the high salinity (22.6–17.5% *w*$CaCl_2$) and low T_h range (75–124 °C) of the *cal1* phase, indicate that this carbonate phase probably precipitated from downward-penetrating sedimentary brines or from descending meteoric water that infiltrated through evaporite interbeddings in sediments. The occurrence of this externally derived fluid in the propylitic veins indicates the existence of open pore space in this vein generation when the new fluid type penetrated the fracture system of the BC.

The mineralizing fluid can be characterized by the H_2O-NaCl-$CaCl_2$ model system with a minor amount of CH_4 and N_2 detected in the primary fluid inclusion assemblages of quartz of the quartz-carbonate veins. Salinity varies in the ranges 20–26% *w*NaCl and 1–6% *w*$CaCl_2$, while T_h shows decreasing values (130 → 60 °C) from the inner to outer growth zones of quartz single crystals. The real *P-T* parameters of quartz precipitation were most probably governed by the real value of the local geothermal gradient. By using an average thermal gradient (35 °C/km) and lithostatic (~22.6 MPa/km) and hydrostatic (~10 MPa/km) pressure gradients, T_t: 80–180 °C and P_t: 20–100 MPa *P-T* values can be computed as approximate formation conditions of the quartz phase. The subsequent *dol* + *cal1* phases contain primary fluid inclusions with rather similar chemical compositions (T_m(Ice): –22.5 to –24.5 °C) to quartz but with slightly higher homogenization temperatures (130–180 °C).

FINTOR et al. (2009) detected quartz-carbonate veins with the paragenetic sequence $qtz \rightarrow dol_C \rightarrow dol_{Mn} \rightarrow dol_{Fe}$ and pure quartz veins in the overlying sedimentary cover (Téseny Sandstone Formation) of the BC. Beyond the petrographical similarities between quartz-carbonate veins of the BC and Téseny Sandstone, primary fluid inclusions in both *qtz* and dol_C phases show similar physicochemical characteristics (*qtz:*T_h*:* 45–135 °C, 0.5–6% *w*$CaCl_2$, 22–25% *w*NaCl; dol_C: T_h:130–180 °C, T_m(Ice): –28 to –25 °C) to inclusions detailed above in quartz-carbonate veins of the BC.

The many similarities indicate that the two quartz-carbonate vein types most probably originated due to the same fracture cementation process during the same fluid migration period. Therefore a significant hydrodynamic connection had to exist between the fluid systems of the crystalline basement (BC) and the overlying clastic sedimentary rocks (Téseny Sandstone Formation).

The specific physicochemical character of the fluids including the high dissolved ion content and ion ratio likely originated from sedimentary brines or surface derived fluids that percolated through evaporite formations. Several potential source formations can be found in proximity to the BC. The Permo-Triassic arkosic Kővágószőlős Sandstone Formation (FAZEKAS 1987) or rocks with evaporitic interbeddings like the Magyarürög Anhydrite Member of the Hetvehely Dolomite Formation (KONRÁD 1997) may have been of primary importance. The fluids that migrated through the fractured basement probably owe their high Na-Ca-Cl composition to the water–rock interactions that occurred in the overlying sediments, and they could preserve this chemical character even in the fracture system of the Baksa Gneiss Complex.

5.2. A Baksai Komplexum posztmetamorf paleofluidum evolúciója

Összegzés

Az eredmények alapján a Baksai Komplexum kőzeteiben az aplit telérek benyomulásától a legfiatalabb kimutatott fluidum áramlási eseményig végbement posztmetamorf paleohidrológiai fejlődéstörténet főbb vonalaiban vázolható. Mivel az egyes fluidumáramlási események abszolút kora eredményeink alapján pontosan nem állapítható meg, a fejlődési modellt az egyes események relatív kora alapján (a legidősebbtől a legfiatalabbig) szakaszokra bontva mutatom be.

5.2.1. Posztmagmás hidrotermális fejlődési szakasz

5.2.1.1. Propilites erek

A legkorábbi repedéskitöltő ásványok a Ca-Al-szilikát domináns erekben találhatók, melyek a Baksai Komplexum leggyakoribb értípusát képezik. Ásvány-kőzettani megfigyelések alapján három altípus különíthető el: klinopiroxén domináns erek (V_{cpx}) *cpx→ep→sph→ab→cal1* ásvány szekvenciával; földpát domináns erek (V_{fp}) *ab±kfp→chl1→adu→chl2→cal1* ásványszekvenciával; valamint epidot domináns erek (V_{ep}) melyek *chl1→ep→czo→prh±adu→chl2→chl3→pyr→cal1→cal2→cal3* ásvány szekvenciát mutatnak. Majdnem minden érkitöltő ásványfaj megjelenik valamennyi altípusban és az egys ásványok képződési időrendjében jelentős átfedések mutatkoznak. Az átfúrt kőzetoszlop valamennyi mélységszintjében hasonló fluidum összetételek (0,2–3% *w*NaCl eq.) mutathatók ki a diopszid és epidot fázisok fluidumzárványaiban. Ezek a jellegzetességek arra utalnak, hogy a Ca-Al-szlikát domináns erek egymással összefüggő töréshálózatban végbement folyamatos fluidum fejlődési sorozat termékeiként értelmezhetők. Ezek alapján a repedéskitöltő ásványosodás egyetlen idealizált ásványszekvenciával jellemezhető:

di→ep→sph→ab+kfp→chl1→prh±adu→chl2→chl3→pyr→cal1→cal2→cal3.

Ehhez hasonló ásványegyüttesek gyakran figyelhetők meg hidrotermális erek mentén megjelenő propilites mellékkőzet átalakulásoknál (MEYER & HEMLEY 1967).

A diopszid és epidot kristályok elsődleges fluidum zárványainak T_h értékei (di: 297–365 °C; ep: 180–359 °C) összevetve ezen ásványok érkitöltő szekvenciában elfoglalt helyével hőmérséklet csökkenésről árulkodnak az érképződés során (T_h: 365→180 °C). Ezt a tendenciát, valamint az alacsony *P-T* viszonyok közötti képződést alátámasztják az ásványkémiai

és termometriai adatok is. A nagyon tiszta szélsőtag összetételeket mutató kogenetikus alkáli- és plagioklász földpátok (albit: $\sim Or_{1.0} Ab_{99}\ An_{0.0}$; káliföldpát: $\sim Or_{99} Ab_{1.0} An_{0.0}$) tipikusak <300 °C körülmények között, amit a földpát-földpát termométer adatok (220–300 °C) is megerősítenek. A törés cementáció során bekövetkező hőmérséklet csökkenést, leginkább a klorit fázisok számított kristályosodási hőmérsékletei jelzik (T_{chl1}: 260 ± 32 °C → T_{chl2}: 222 ± 20 °C → T_{chl3}: 156 ± 10 °C). Ezt a trendet a *chl1* és *chl2* fázisokban a kristálymagoktól a kristályperemek felé csökkenő Al^{IV} koncentráció is alátámasztja. A szórványosan megjelenő pirit kristályok jelentős nyomelem tartalmat mutatnak (Co, Ni, Cu, As, Mn, és Zn). A piritek Co/Ni mért arányának 1 és 5 közötti értékei posztmagmás hidrotermális erek piritjeihez hasonlóak (Co/Ni: 1–10). Mindezek alapján a törés cementáció a Baksai Komplexum repedésrendszerében áramlott posztmagmás hidrotermális fluidum termékének tekinthető, ami propilites érkitöltő paragenetikus szekvenciát hozott létre az erekben. SZEDERKÉNYI (1979) ezt a propilites érkitöltő ásványosodást a Baksai Komplexum kőzeteiben nagy gyakorisággal fellelhető aplit dájkok jelenlétével hozta kapcsolatba. Figyelembe véve a keskeny (<10 m vastagságú) sekély mélységbe nyomult dájkok gyors hűlési rátáját (FURLONG ET AL. 1991), a magmás testek környezetük hőmérsékletére való lehűlése során a kristályos blokk jelentős vertikális mozgásával nem számolhatunk. Ebből kifolyólag közel állandó regionális *P-T* viszonyokat feltételezhetünk a hidrotermális erek képződése során. Ebben az esetben a hidrotermális fluidum hűlését a mellékkőzet hőmérséklete szabályozta, ami ~154 °C-nak tekinthető a *chl3* számított képződési hőmérséklete alapján. Az epidot elsődleges fluidum zárványainak izokorjai, és a *chl1* fázis termometriai értékeinek metszése arról árulkodik, hogy ezek a kogenetikus kristályosodást mutató fázisok ~230–290 °C hőmérséklet és <~194 MPa nyomás tartományban képződtek. A terület regionális nyomásviszonyai nagy valószínűséggel ~194 MPa-nál alacsonyabbak voltak, amikor az érrendszer hőmérséklete beállt a mellékkőzet hőmérsékletére (~154 °C). A legelfogadhatóbb közelítés, ha a fenti nyomás érték felével (~97 MPa) számolunk. Ez a nyomás közel állandó regionális értéknek tekinthető az érképződés során. Felhasználva a ~97 MPa nyomás és ~154 °C hőmérséklet értékeket ~39 °C/km hőmérsékleti gradiens becsülhető a területre, ha 2650 kg/m^3 kőzetsűrűséget és litosztatikus nyomás gradienst feltételezünk. Mivel lényeges nyomás fluktuáció sem a regionális, sem pedig a fluidum nyomás esetében nem feltételezhető, a diopszid esetében ~354–479 °C, míg az epidot esetében ~236–474 °C képződési hőmérséklet intervallum valószínűsíthető közel állandó nyomásviszonyok között (~100 MPa).

5.2.1.2. Erek menti metaszomatózis

A propilites erekben áramlott fluidum átjárta a mellékkőzeteket jellegzetes mellékkőzet átalakulásokat okozva. Az átalakult mellékkőzetekben a jellegzetes átalakulási ásványparagenezisek alapján négy átalakulási zóna különböztethető meg:

1-es zóna: Ebben a zónában albit és titanit a legjellegzetesebb ásványok, ásványparagenezis: *ab* + *ttn* ± *ep.*

2-es zóna: A biotit utáni epidot pszeudomorfózák a legjellegzetesebb átalakulási jellemzők. Ásványparagenezis: *ep* + *chl*+ *ttn* + *ab* ± *ser.*

3-as zóna: Az epidot mennyisége csökken, míg a klorité megnövekszik. A szericit jóval gyakoribb, és rutil zárványok gyakran jelennek meg a kloritban. Ásványparagenezis: *chl* + *ep* + *ser* + *rt* ± *ttn.*

4-es zóna: A szericitesedés a legjellemzőbb átalakulási folyamat, más átalakulási termékek csak alárendelt mennyiségben jelennek meg. Ásványparagenezis: *ser* ± *chl.*

Ezek az átalakulási ásványegyüttesek tipikusak érmenti metaszomatózishoz köthető propilites mellékkőzet átalakulások esetében (ZHARIKOV ET AL. 2007), az átalakult kőzet pedig a propilit metaszomatikus családba sorolható. A hidrotermális oldás másodlagos porozitást hozott létre az átalakult mellékkőzetben, ahol az oldási üregekben másodlagosan epidot vált ki. Az üregkitöltő epidot, valamint az érkitöltő epidot és diopszid kristályok fluidum zárványainak hasonló kémiai karakterű fluidumai arra utalnak, hogy a mellékkőzet átalakulása hasonló körülmények között ment végbe, mint amik a propilites erek képződése során fennálltak. A metaszomatikus átalakulás <200 MPa nyomáson és ~360–480 °C hőmérséklet viszonyok között közel semleges-gyengén lúgos közegben ment végbe. A hidrotermális fluidum és a mellékkőzet közötti elem mobilizáció Ca transzportot biztosított a mellékkőzet irányába, miközben jelentős mennyiségű Fe, Mn, K, és Mg báziskationt oldott ki a mellékkőzetből.

5.2.1.3. A propilites és polimetallikus erek kapcsolata

Polimetallikus (stockwerk-szerű) szulfid erek jelenlétét a képződményben már SZEDERKÉNYI (1979) is kimutatta és eredetüket hidrotermális tevékenységgel hozta kapcsolatba. Ezt a hidrotermális eseményt fiatalabbnak találta a propilites ereket létrehozónál. TARNAI (1997, 1998) részletes ásványtani és ércgenetikai vizsgálatokat végzett a képződményben fellelhető 6-7 cm

vastag polimetallikus ércteléren, és egy korai, valamint egy késői érc ásványosodási fázist különített el benne. A késői ércfázissal kogenetikus kvarckristályok fluidum zárványaiból T_t: 240–300 °C és P_t: 15–30 MPa bezáródási paramétereket határozott meg, amik a propilites erek képződési paramétereihez nagyon hasonlóak. A piritek Co/Ni aránya ~0,8–4,6, ami jól összeegyeztethető a propilites erek piritjeiben megfigyelhető értékekkel, és mindkét értípus eredetét posztmagmás hidrotermális eseményhez kapcsolja. Az ilyen alacsony nyomású ércesedés tipikusan felszínközeli mélységbe nyomult magmás intrúziók esetében jellemző (CLINE & BODNAR 1991). CLINE & BODNAR (1991) kimutatta, hogy alacsony nyomásviszonyokon a korai magmás fluidum általában alacsony sótartalmat (kloridos) mutat és többnyire meddő ásványok által kitöltött erek képződésében játszik szerepet, igen alárendelt mennyiségű ércesedéssel. A végső szakaszban a fluidumok jelentősen nagyobb klorid tartalmat mutatnak, nagyobb szulfid ércesedési potenciállal, ahol az ércek fő képződési tartománya 250–350 °C intervallumban mozog (CLINE & BODNAR 1991; BARNES 1979). További kutatásokat igényel, annak megállíptása, hogy a magmás eredetű fluidum áramlás okozott-e jelentősebb ércfelhalmozódást a Baksa Komplexum kőzeteiben. Mindazonáltal a fenti hasonlóságok alapján a propilites és a polimetallikus szulfid erek eredete és képződése között párhuzam feltételezhető.

5.2.2. Kristályos aljzaton kívüli eredetű fluidumok a Baksai Komplexumban

A komplexum kvarc-karbonát ereinek képződése a posztmagmás hidrotermális fluidumoktól gyökeresen eltérő jellegű fluidumok hatására vezethető vissza. A kvarc-karbonát erek *qtz*→ *dol*+*cal1*→*cal2* ásványszekvenciával jellemezhetők. Az új fluidum típus (T_h: 60–200 °C, és T_m(Ice): –28 to –17 °C) a kvarc elsődleges, álmásodlagos, és másodlagos fluidum zárványaiban, valamint az azt követő *dol*+*cal1* fázisok elsődleges fluidum zárványaiban jelenik meg. Ezen kívül ez a fluidum megjelenik a propilites erek diopszid, epidot, és kalcit 1 ásványainak D_2, E_2, és C_1 zárványaiban is. A kalcit 1 fázissal egyensúlyban levő víz számított $\delta^{18}O$ összetétele ($\delta^{18}O$: –4 to –12,9‰ V–SMOW) a magas sótartalommal (22,6–17,5% *w*$CaCl_2$) és alacsony homogenizációs hőmérsékletekkel (T_h: 75–124 °C) együtt arra utal hogy ez az ásványfázis nagy valószínűséggel mélybe szivárgó mélymedence eredetű, vagy evaporitos rétegeken átszivárgó meteorikus vizekből képződött. A fluidum megjelenése a propilites érrendszerben arra utal, hogy az nyitott pórustérrel rendelkezett, amikor az új fluidum megjelent a komplexum törésrendszerében.

Az ásványosító fluidum H_2O-NaCl-$CaCl_2$ modell összetételt mutat minimális menynyiségű CH_4 és N_2 tartalommal a kvarc elsődleges fluidum zárványaiban. A sótartalom 20–

26% *w*NaCl és 1–6% *w*$CaCl_2$ értékeket mutat, míg a T_h értékek a kristálymagoktól a peremek irányába csökkenést jeleznek (130 → 60 °C). Ez esetben nagy valószínűséggel a geotermikus gradiens értéke szabta meg a bezáródás körülményeit. Átlagos (35 °C/km) geotermikus gradiens és litosztatikus (22,6 MPa) valamint hidrosztatikus (10 MPa) nyomásgradiens mellett T_t: 80-180 °C és P_t: 20-100 MPa értékeknek vehetők a kvarc bezáródási *P-T* paraméterei. A kvarcot követő *dol+cal1* fázisok a kvarc zárványaihoz hasonló kémiai karakterű fluidumot csapdáztak (T_m(Ice): –22,5-től –24,5 °C-ig), azonban T_h értékeik némileg magasabb hőmérséklet tartományban (130–180 °C) vannak.

FINTOR ET AL. (2009) a Baksai Komplexum fedő üledékes képződményeiben (Tésenyi Homokkő Formáció) $qtz \rightarrow dol_C \rightarrow dol_{Mn} \rightarrow dol_{Fe}$ ásvány szekvenciát mutató kvarc-karbonát ereket és tisztán kvarc kitöltésű ereket vizsgáltak. A Tésenyi homokkő kvarc-karbonát erei petrográfiailag is hasonlóságokat mutatnak, a Baksai Komplexum kvarc-karbonát ereivel, amit a *qtz* és dol_C fázisok elsődleges fluidum zárványainak fizikokémiai karaktere (*qtz:* T_h*:* 45–135 °C, 0,5–6% *w*CaCl2, 22–25% *w*NaCl; dol_C: T_h:130–180 °C, T_m(Ice): –28-tól –25 °C-ig) még jobban megerősít.

Az említett hasonlóságok arra utalnak, hogy a Baksai Komplexum repedezett kristályos kőzetei és a fedő törmelékes üledékek (Tésenyi Homokkő Formáció) paleohidrológiai rendszere összekapcsolódott a kvarc-karbonát erek egyes cementációs szakaszai során.

A fluidum magas sótartalmának eredete az üledékes mélymedencebeli vizekhez, vagy felszíni eredetű evaporit betelepüléseket tartalmazó fedőképződményeken átszivárgó fluidumokhoz kapcsolódhat. FINTOR et al. (2008) a Perm-Triász képződményekben lezajló vízkőzet kölcsönhatásokkal (Kővágószőlősi Homokkő Formáció; FAZEKAS 1987) – különösen az evaporitos betelepülések (Hetvehelyi Dolomit Formáció, Magyarürögi Anhidrit Tagozata; KONRÁD 1997) fluidumok általi infiltrációjával – hozzák kapcsolatba eredetüket. A repedezett aljzat irányába vándorló fluidumok a fedő üledékes képződményekben lejátszódó fluidum-kőzet reakcióknak köszönhetik Na-Ca-Cl domináns jellegüket, és a BK repedésrendszereiben áramolva is számottevően megőrizhették ezt a karakterüket.

REFERENCES

BARNES, H., L. (1979): Solubilities of ore minerals. *Geochemistry of Hydrothermal Ore Deposits, 2nd ed*., Barnes, H., L., New York, Wiley Interscience: 404-460.

CLINE J., S., & BODNAR, R., J. (1991): Can economic porphyry copper mineralization be generated by a typical calc-alkaline melt? *Journal of Geophysical Research*, 96/B5, 8113-8126.

FAZEKAS, V. (1987): A mecseki perm és alsótriász korú törmelékes formációk ásványos összetétele. – *Földtani Közlöny,* 117, 11-30.

FINTOR, K., SCHUBERT, F., M. TÓTH, T. (2008). Hiperszalin paleofluidum-áramlás nyomai a Baksai Komplexum repedésrendszerében. *Földtani Közlöny* 138(3), 257-278.

FINTOR, K., M. TÓTH, T., SCHUBERT, F. (2009): A Baksai Komplexum posztmetamorf fluidum evolúciója. In: M. Tóth, T. ed.: Magmás és metamorf képződmények a Tiszai Egységben. GeoLitera, p. 245-258.

FURLONG, K., P., HANSON, R., B., & BOWERS, J., R. (1991): Modelling thermal regimes. *Reviews in Mineralogy: Contact metamorphism.*, KERRICK, D., M., Washington D. C., Mineralogical Society of America., 26, 437-506.

KONRÁD, GY. (1997): A DK-dunántúli alsó - és középső triász képződmények szedimentológiai vizsgálatának eredményei. – *Kandidátusi értekezés*. Budapest.

MEYER, C., HEMLEY, J., J. (1967). Wall Rock Alteration. *Geochemistry of hydrothermal ore deposits*. H. BARNES, L. University Park, Pennsylvania, Holt, Reinhart & Winston, Inc.: 670.

SZEDERKÉNYI, T. (1979): A mecseki ópaleozóos-prekambriumi alapszelvények komplex földtani feldolgozása. *Manuscript*, JATE, Szeged

TARNAI, T. (1997): Ore minerals from the key section of the Baksa Complex W Baranya hills, Hungary. *Acta Mineralogica-Petrographica,* XXXVIII, Supplementum, 119-133.

TARNAI, T. (1998): Mineralogical-petrological study on ore vein penetrated by the key-borehole Baksa No. 2 SE Transdanubia, Hungary. *Acta Mineralogica-Petrographica,* XXXIX, 21-34.

ZHARIKOV, V., A., PERTSEV, N., N., RUSINOV, V., L., CALLEGARI, E., & FETTES, D., J. (2007): Metasomatism and metasomatic rocks. *Metamorphic Rocks: A classification and glossary of terms*, FETTES, D., AND DESMONS, J., New York, Cambridge University Press, 58-69.

Acknowledgements

In the first instance I would like to express thanks to those people who helped in any kind of form to let this work allowed to be ready. Hereafter I would like to say thank namely for those contributions that were essential in the last years, although I would like to apologize to them who I do not enumerate here but they contributed to my work got ready. First of all I would like to express my thanks to my parents who believed in me always, and supported me even in the most difficult moments. I am particularly indebted to my supervisors Tivadar M. Tóth and Félix Schubert for his indespensible professional advises, patient and helpful attitude during my work without this paper could not have come into existence. Thank goes to Prof. Dr. Magdolna Hetényi for her supporting my work after my scholarship finished. I would like to say thank to Ronald J. Bakker and his fluid inclusion research group (especially to Miriam Baumgartner, and Yvan Coquinot) for their unselfish help during fluid inclusion microthermometry and Raman spectroscopic investigations. Special thanks goes to Ronald J. Bakker for the the important vocational consultations. For the help during mineral chemistry analyses and the constructive consultations special thanks go to Federica Zaccarrini, Helmut Mühlhans, and Giorgio Garuti. Special thanks go to Federica Zaccarrini for her useful advices in ore petrological questions. Thanks go to Zoltán Siklósy for the stable isotope measurements, and for Bernadett Bajnóczy for her help in cathodoluminescence microscopy investigations. For his help in X-ray fluorescence analyses thank goes to Gábor Bozsó. Thank goes to Sándor Kaczur for his help during conversion of the raw element map data. Special thank goes to Pápayné Zsóka for the refreshments coffes and the gaiety workdays and because she believed in me unbrokenly even in the most difficult moments. Eventually I would like to express my thanks to all of the employees of the department of Mineralogy, Geochemistry and Petrology for all provided help during my work.

APPENDIX

Appendix

APPENDIX I. - SOURCES OF SAMPLES

Sample Number	Depth / m	Adjacent rock	Vein type	Textural features	Examinations and Applied methods
AGK-284	80.6	Epidotic hornfels	Vep	euhedral epidote	Petrography. CL.[1] Mineral Chemistry. FI.[2] Raman
AGK-303	107.4	Marble with pink and greenish grey bands	Vep	euhedral epidote	Petrography
AGK-304	108.6	Marble-amphiboite contact	Vep	euhedral epidote	Petrography
AGK-367	199	pale grey sericitous mica schist	Qtz-Carb	euhadral quartz	Petrography
AGK-372	208.4	grey-colored two-mica gneiss	Vfp	cogenetic alkali and plagioclase feldspars	Petrography. CL. Mineral Chemistry. FI. Raman. SI.[3]
AGK-378	238.7	grey two-mica gneiss	Vfp	—	Petrography
AGK-383	231.8	Greenish grey (retrograde) gneiss	Vfp	cogenetic alkali and plagioclase feldspars	Petrography. CL
AGK-387	253.5	strongly foliated ortogneiss	Qtz-Carb	euhadral quartz	Petrography. CL. Mineral Chemistry. FI. Raman
AGK-391	258.7	grey-colored two-mica gneiss	Qtz-Carb	euhadral quartz	Petrography. CL. Mineral Chemistry. FI. Raman
AGK-519	436.2	pale grey -colored muscovite gneiss	Vep	euhedral epidote, alteration margin	Petrography. CL. Mineral Chemistry. FI. Raman
AGK-523	442.8	Epidotic quartzite	Vep	euhedral epidote, alteration margin	Petrography
AGK-525	446.7	chloritic two-mica gneiss	Vep	euhedral epidote	Petrography
AGK-550	517.1	chloritic gneiss	Vfp	—	Petrography
AGK-557	535.5	Middle grained chloritic gneiss	Vfp	euhedral epidote and kfeldspar	Petrography
AGK-574	591.2	Two-mica gneiss	Vfp	—	Petrography
AGK-581	599.8	Chlorite schist	Vfp	—	Petrography. CL.
AGK-591	624.8	Two-mica gneiss	Vfp	—	Petrography
AGK-610	679.7	Chlorite schist	Vfp	—	Petrography. CL. SI.
AGK-628	712.6	Epidotic aplite	Vep	euhedral epidote	Petrography
AGK-637	730	Two-mica gneiss	Vcpx	euhedral epidote, alteration margin	Petrography. CL. Mineral Chemistry. FI. Raman
AGK-638	733.1	Epidotic aplite	Vfp	cogenetic alkali and plagioclase feldspars	Petrography. CL. FI. Raman. SI.
AGK-653	769.3	Middle crystallized two-mica gneiss	Vfp	—	Petrography
AGK-670	812.5	Pale grey chloritic gneiss	Vfp	—	Petrography
AGK-676	824.7	Epidotic hornfels	Vep	euhedral epidote	Petrography
AGK-677	825	Amphibolite	Vep	euhedral epidote	Petrography
AGK-680	826.7	Amphibolite	Vep	euhedral epidote	Petrography
AGK-681	829	Amphibolite	Vep	euhedral epidote	Petrography
AGK-699	846.5	Amphibolite	Vcpx	euhedral epidote	Petrography. CL. Mineral Chemistry. FI. Raman
AGK-701	850.1	Grey amphibolite	Vcpx	euhedral epidote	Petrography
AGK-702	852.7	Middle crystallized amphibolite	Vep	euhedral epidote	Petrography. CL. Mineral Chemistry. FI. Raman
AGK-707	858.8	Fine grained amphibolite	Vcpx	euhedral epidote, alteration margin	Petrography
AGK-870	1108	Chloritic tectonic breccia	Vfp	cogenetic alkali and plagioclase feldspars	Petrography. CL. Mineral Chemistry. FI. Raman

[1]CL: Cathodoluminescence microscopy; [2]FI: Fluid inclusion analysis; [3]SI: Stable isotope analysis

APPENDIX II. - MINERAL CHEMISTRY / 1

DIOPSIDE

Oxides	637Di1	637Di2	637Di3	637Di4	637Di5	637Di6	699Di1	699Di2	699Di3	699Di4	699Di5	699Di6
SiO_2	51.93	52.25	51.07	53.34	53.03	53.54	53.61	53.28	54.16	53.81	53.04	54.48
TiO_2	0.03	0.00	0.00	0.03	0.08	0.03	0.00	0.01	0.01	0.02	0.05	0.01
Al_2O_3	0.24	0.77	0.24	0.44	0.16	0.17	0.23	0.16	0.16	0.16	0.21	0.12
Cr_2O_3	0.02	0.00	0.00	0.04	0.02	0.00	0.00	0.00	0.06	0.00	0.06	0.01
FeO	13.29	14.85	14.47	13.33	12.97	12.82	9.71	10.04	7.21	6.20	10.14	6.75
MnO	0.83	0.54	0.73	0.70	0.52	0.71	0.42	0.32	0.33	0.53	0.35	0.57
MgO	9.83	7.95	9.20	8.90	9.37	9.47	12.00	11.45	13.08	13.84	11.60	13.24
CaO	23.64	23.28	23.74	22.53	23.08	22.95	23.95	24.62	24.98	25.56	24.67	25.39
Na_2O	0.00	0.08	0.08	0.07	0.00	0.00	0.51	0.06	0.09	0.12	0.06	0.10
K2O	0.01	0.00	0.00	0.02	0.01	0.00	0.00	0.00	0.00	0.00	0.00	0.00
Total	99.82	99.72	99.53	99.40	99.24	99.69	100.43	99.94	100.08	100.24	100.18	100.67
Chemical formula on a basis of 6 oxygen pfu												
Si	1.995	2.015	1.983	2.041	2.033	2.040	2.006	2.016	2.022	1.995	2.002	2.020
Al^{IV}	0.005	0.000	0.011	0.000	0.000	0.000	0.000	0.000	0.000	0.000	0.000	0.000
T-site	2.000	2.015	1.994	2.041	2.033	2.040	2.006	2.016	2.022	1.995	2.002	2.020
Ti	0.006	0.035	0.000	0.020	0.007	0.008	0.000	0.000	0.000	0.001	0.001	0.000
Al^{VI}	0.001	0.000	0.000	0.001	0.002	0.001	0.010	0.007	0.007	0.007	0.009	0.005
Fe^{+3}	0.001	0.000	0.000	0.001	0.001	0.000	0.015	0.000	0.000	0.011	0.000	0.000
Cr^{+3}	0.000	0.000	0.000	0.000	0.000	0.000	0.000	0.000	0.002	0.000	0.002	0.000
Fe^{+2}	0.427	0.479	0.470	0.427	0.416	0.409	0.289	0.318	0.225	0.181	0.320	0.209
Mn	0.027	0.018	0.024	0.023	0.017	0.023	0.013	0.010	0.010	0.017	0.011	0.018
Mg	0.563	0.457	0.533	0.508	0.536	0.538	0.669	0.646	0.728	0.765	0.653	0.732
Ca	0.973	0.962	0.988	0.924	0.948	0.937	0.960	0.998	0.999	1.015	0.998	1.008
Na	0.000	0.006	0.006	0.005	0.000	0.000	0.037	0.004	0.007	0.009	0.004	0.007
K	0.000	0.000	0.000	0.001	0.000	0.000	0.000	0.000	0.000	0.000	0.000	0.000
M-site	1.998	1.956	2.020	1.909	1.927	1.915	1.994	1.984	1.978	2.005	1.998	1.980
Total Oxygen	6.000	6.000	6.000	6.000	6.000	6.000	6.000	6.000	6.000	6.000	6.000	6.000
X_{Mg}	0.553	0.479	0.519	0.530	0.553	0.555	0.679	0.663	0.756	0.786	0.664	0.763
Sodic and calcic end members												
X_{Aeg}	0.01	0.00	0.00	0.00	0.00	0.00	0.00	0.00	0.00	0.00	0.00	0.00
X_{Jd}	0.02	0.00	0.01	0.01	0.00	0.01	0.00	0.01	0.01	0.02	0.02	0.03
X_{Di}	0.96	1.00	0.99	0.99	1.00	0.99	1.00	0.99	0.99	0.98	0.98	0.97
Ortho and calcic end members												
X_{Wo}	0.50	0.51	0.51	0.52	0.51	0.52	0.48	0.51	0.47	0.50	0.50	0.50
X_{En}	0.35	0.33	0.37	0.39	0.33	0.38	0.29	0.24	0.28	0.27	0.28	0.29
X_{Fs}	0.15	0.16	0.12	0.09	0.16	0.11	0.22	0.25	0.25	0.23	0.22	0.22

APPENDIX II. - MINERAL CHEMISTRY / 2

EPIDOTE

Oxides	702 Ep1	702 Ep2	702 Ep3	702 Ep4	702 Ep5	702 Ep6	702 Ep7	702 Ep8	702 Ep9	702 Ep10	702 Ep11	702 Ep12
SiO_2	38.72	38.83	38.36	40.34	38.74	37.64	39.79	37.79	39.25	38.42	39.06	40.19
TiO_2	0.02	0.02	0.02	0.00	0.02	0.00	0.10	0.00	0.05	0.26	0.00	0.07
Al_2O_3	25.76	26.32	21.12	25.42	21.48	20.67	27.96	22.19	27.99	23.39	22.20	26.86
Fe_2O_3	10.2	9.92	17.80	9.89	16.10	17.51	6.53	16.80	7.43	12.62	14.78	7.57
MnO	0.19	0.11	0.18	0.07	0.00	0.15	0.18	0.15	0.25	0.11	0.07	0.15
CaO	23.23	22.90	20.26	22.70	21.57	22.20	23.76	21.97	23.47	23.02	22.12	23.21
Na_2O	0	0.00	0.00	0.00	0.00	0.00	0.00	0.00	0.07	0.00	0.00	0.00
Total	98.12	98.10	97.73	98.41	97.91	98.17	98.31	98.90	98.51	97.82	98.22	98.05
Chemical formula on a basis of 12.5 oxygen pfu												
Si^{IV}	3.009	3.009	3.030	3.105	3.050	2.984	3.052	2.961	3.014	3.017	3.058	3.092
Al^{IV}	0.000	0.000	0.000	0.000	0.000	0.016	0.000	0.039	0.000	0.000	0.000	0.000
T-site	3.009	3.009	3.030	3.105	3.050	3.000	3.052	3.000	3.014	3.017	3.058	3.092
Al^{VI}	2.359	2.404	1.966	2.306	1.993	1.915	2.528	2.010	2.533	2.165	2.048	2.436
Fe^{3+}	0.661	0.641	1.173	0.637	1.057	1.158	0.419	1.098	0.474	0.827	0.966	0.487
Mn^{3+}	0.000	0.000	0.000	0.000	0.000	0.000	0.000	0.000	0.000	0.000	0.000	0.000
Ti	0.001	0.001	0.001	0.000	0.001	0.000	0.006	0.000	0.003	0.015	0.000	0.004
Fe^{2+}	0.001	0.001	0.002	0.000	0.002	0.001	0.000	0.001	0.002	0.001	0.001	0.000
Mn^{2+}	0.007	0.003	0.006	0.004	0.000	0.005	0.011	0.005	0.008	0.003	0.003	0.009
M-site	3.029	3.050	3.148	2.946	3.053	3.079	2.963	3.114	3.020	3.011	3.018	2.936
Mn^{3+}	0.000	0.000	0.000	0.000	0.000	0.000	0.000	0.000	0.000	0.000	0.000	0.000
Mn^{2+}	0.006	0.004	0.006	0.001	0.000	0.005	0.001	0.005	0.008	0.004	0.002	0.001
Fe^{2+}	0.001	0.001	0.001	0.000	0.001	0.001	0.000	0.001	0.001	0.001	0.001	0.000
Ca	1.934	1.901	1.714	1.872	1.819	1.885	1.953	1.844	1.931	1.937	1.855	1.913
Na	0.000	0.000	0.000	0.000	0.000	0.000	0.000	0.000	0.010	0.000	0.000	0.000
A-site	1.941	1.906	1.721	1.873	1.820	1.891	1.954	1.850	1.950	1.942	1.858	1.914
O	12.000	12.000	12.000	12.000	12.000	12.000	12.000	12.000	12.000	12.000	12.000	12.000
OH	0.998	0.998	0.997	1.000	0.997	0.998	1.000	0.998	0.997	0.998	0.998	1.000
Total	20.977	20.964	20.896	20.924	20.920	20.968	20.969	20.962	20.981	20.968	20.932	20.942
X_{Fe}	0.22	0.21	0.37	0.22	0.35	0.38	0.14	0.35	0.16	0.27	0.32	0.17
X_{Ep}	0.66	0.64	1.17	0.64	1.06	1.16	0.42	1.10	0.47	0.83	0.97	0.49
X_{Al}	0.78	0.79	0.62	0.78	0.65	0.62	0.85	0.65	0.84	0.72	0.68	0.83

APPENDIX II. - MINERAL CHEMISTRY / 3

EPIDOTE

Oxides	699-ep1	699-ep2	699-ep3	699-ep4	699-ep5	699-ep6	699-ep7	699-ep8	699-ep9	699-ep10	699-ep11	699-ep12	699-ep13	699-ep14	699-ep15	699-ep16	699-ep17
SiO_2	38.53	38.35	38.10	40.89	40.20	39.00	39.46	37.07	39.44	37.51	37.79	38.51	37.66	36.60	37.29	36.97	37.66
TiO_2	0.02	0.02	0.02	0.00	0.02	0.00	0.10	0.00	0.05	0.26	0.00	0.07	0.00	0.07	0.00	0.00	0.00
Al_2O_3	25.76	26.32	21.12	25.42	21.48	20.67	27.96	22.19	27.99	23.39	22.20	26.86	27.69	22.83	26.12	21.77	27.41
Fe_2O_3	10.2	9.92	17.80	9.89	16.10	17.51	6.53	16.80	7.43	12.62	14.78	7.57	10.31	15.90	11.97	17.32	9.65
MnO	0.19	0.11	0.18	0.07	0.00	0.15	0.18	0.15	0.25	0.11	0.07	0.15	0.01	0.07	0.20	0.05	0.10
CaO	23.23	22.90	20.26	22.70	21.57	22.20	23.76	21.97	23.47	23.02	22.12	23.21	22.85	22.42	22.55	22.83	23.02
Na_2O	0	0.00	0.00	0.00	0.00	0.00	0.00	0.00	0.07	0.00	0.00	0.00	0.00	0.00	0.01	0.00	0.10
Total	97.93	97.62	97.47	98.96	99.37	99.52	97.98	98.17	98.70	96.90	96.95	96.37	98.52	97.89	98.13	98.94	97.94
Chemical formula on a basis of 12.5 oxygen pfu.																	
Si^{IV}	3.009	3.009	3.030	3.105	3.050	2.984	3.052	2.961	3.014	3.017	3.058	3.092	2.911	2.901	2.911	2.913	2.928
Al^{IV}	0.000	0.000	0.000	0.000	0.000	0.016	0.000	0.039	0.000	0.000	0.000	0.000	0.089	0.099	0.089	0.087	0.072
T-site	3.009	3.009	3.030	3.105	3.050	3.000	3.052	3.000	3.014	3.017	3.058	3.092	3.000	3.000	3.000	3.000	3.000
Al^{VI}	2.359	2.404	1.966	2.306	1.993	1.915	2.528	2.010	2.533	2.165	2.048	2.436	2.434	2.034	2.315	1.934	2.441
Fe^{3+}	0.661	0.641	1.173	0.637	1.057	1.158	0.419	1.098	0.474	0.827	0.966	0.487	0.664	1.052	0.779	1.139	0.625
Mn^{3+}	0.000	0.000	0.000	0.000	0.000	0.000	0.000	0.000	0.000	0.000	0.000	0.000	0.000	0.000	0.000	0.000	0.000
Ti	0.001	0.001	0.001	0.000	0.001	0.000	0.006	0.000	0.003	0.015	0.000	0.004	0.000	0.004	0.000	0.000	0.000
Fe^{2+}	0.001	0.001	0.002	0.000	0.002	0.001	0.000	0.001	0.002	0.001	0.001	0.000	0.002	0.001	0.001	0.001	0.002
Mn^{2+}	0.007	0.003	0.006	0.004	0.000	0.005	0.011	0.005	0.008	0.003	0.003	0.009	0.001	0.003	0.006	0.001	0.003
M-site	3.029	3.050	3.148	2.946	3.053	3.079	2.963	3.114	3.020	3.011	3.018	2.936	3.100	3.094	3.101	3.076	3.071
Mn^{3+}	0.000	0.000	0.000	0.000	0.000	0.000	0.000	0.000	0.000	0.000	0.000	0.000	0.000	0.000	0.000	0.000	0.000
Mn^{2+}	0.006	0.004	0.006	0.001	0.000	0.005	0.001	0.005	0.008	0.004	0.002	0.001	0.000	0.002	0.007	0.002	0.004
Fe^{2+}	0.001	0.001	0.001	0.000	0.001	0.001	0.000	0.001	0.001	0.001	0.001	0.000	0.001	0.001	0.001	0.001	0.001
Ca	1.934	1.901	1.714	1.872	1.819	1.885	1.953	1.844	1.931	1.937	1.855	1.913	1.893	1.904	1.886	1.927	1.918
Na	0.000	0.000	0.000	0.000	0.000	0.000	0.000	0.000	0.010	0.000	0.000	0.000	0.000	0.000	0.002	0.000	0.015
A-site	1.941	1.906	1.721	1.873	1.820	1.891	1.954	1.850	1.950	1.942	1.858	1.914	1.894	1.907	1.896	1.930	1.938
O	12.000	12.000	12.000	12.000	12.000	12.000	12.000	12.000	12.000	12.000	12.000	12.000	12.000	12.000	12.000	12.000	12.000
OH	0.998	0.998	0.997	1.000	0.997	0.998	1.000	0.998	0.997	0.998	0.998	1.000	0.997	0.998	0.998	0.998	0.997
Total	20.977	20.964	20.896	20.924	20.920	20.968	20.969	20.962	20.981	20.968	20.932	20.942	20.991	20.999	20.995	21.004	21.006
X_{Fe}	0.22	0.21	0.37	0.22	0.35	0.38	0.14	0.35	0.16	0.27	0.32	0.17	0.21	0.34	0.25	0.37	0.20
X_{Ep}	0.66	0.64	1.17	0.64	1.06	1.16	0.42	1.10	0.47	0.83	0.97	0.49	0.60	0.96	0.71	1.06	0.58
X_{Al}	0.78	0.79	0.62	0.78	0.65	0.62	0.85	0.65	0.84	0.72	0.68	0.83	0.79	0.66	0.75	0.63	0.79

APPENDIX II. - MINERAL CHEMISTRY / 4

EPIDOTE

Oxides	637ep1	637ep2	637ep3	637ep4	637ep5	637ep6	637ep7	637ep8	637ep9	637ep10	637ep11	637ep12	637ep13	637ep14	637ep15
SiO_2	38.26	39.55	38.52	38.03	39.25	38.38	38.47	38.79	39.49	38.59	38.78	38.74	39.34	39.10	39.00
TiO_2	0.24	0.06	0.03	0.03	0.08	0.05	0.26	0.14	0.03	0.08	0.17	0.22	0.05	0.38	0.12
Al_2O_3	26.56	26.13	25.02	21.68	26.31	22.54	25.07	22.10	26.46	21.08	26.11	24.39	21.47	25.43	27.10
Fe_2O_3	8.39	8.09	10.51	15.04	8.17	14.58	10.40	14.69	9.53	16.26	10.39	11.49	15.27	9.32	9.83
MnO	0.08	0.08	0.21	0.00	0.13	0.00	0.00	0.00	0.04	0.11	0.08	0.11	0.03	0.03	0.05
CaO	24.87	24.56	23.81	23.30	23.32	23.11	24.10	22.82	22.96	22.26	22.43	23.29	22.19	23.77	22.64
Na_2O	0.00	0.00	0.00	0.08	0.00	0.00	0.00	0.00	0.00	0.00	0.00	0.00	0.19	0.86	0.00
Total	98.40	98.53	98.09	98.17	98.15	98.66	98.30	98.55	98.54	98.39	98.06	98.25	98.53	98.96	98.91
Chemical formula on a basis of 12.5 oxygen pfu.															
Si^{IV}	3.035	3.053	3.006	3.004	3.057	3.003	2.996	3.035	3.040	3.036	3.009	2.997	3.076	3.096	2.996
Al^{IV}	0.000	0.000	0.000	0.000	0.000	0.000	0.004	0.000	0.000	0.000	0.000	0.003	0.000	0.000	0.004
T-site	3.035	3.053	3.006	3.004	3.057	3.003	3.000	3.035	3.040	3.036	3.009	3.000	3.076	3.096	3.000
Al^{VI}	2.483	2.377	2.301	2.018	2.415	2.079	2.297	2.038	2.400	1.954	2.388	2.221	1.979	2.373	2.450
Fe^{3+}	0.502	0.522	0.686	0.991	0.532	0.951	0.677	0.959	0.611	1.067	0.672	0.743	0.999	0.604	0.629
Mn^{3+}	0.000	0.000	0.000	0.000	0.000	0.000	0.000	0.000	0.000	0.000	0.000	0.000	0.000	0.000	0.000
Ti	0.014	0.003	0.002	0.002	0.005	0.003	0.015	0.008	0.002	0.005	0.010	0.013	0.003	0.023	0.007
Fe^{2+}	0.054	0.000	0.000	0.001	0.000	0.002	0.000	0.002	0.002	0.002	0.002	0.000	0.000	0.013	0.002
Mn^{2+}	0.004	0.004	0.011	0.000	0.008	0.000	0.000	0.000	0.002	0.003	0.002	0.006	0.001	0.001	0.001
M-site	3.059	2.908	3.000	3.012	2.960	3.035	2.989	3.007	3.016	3.031	3.073	2.984	2.981	3.014	3.088
Mn^{3+}	0.000	0.000	0.000	0.000	0.000	0.000	0.000	0.000	0.000	0.000	0.000	0.000	0.000	0.000	0.000
Mn^{2+}	0.001	0.001	0.003	0.000	0.001	0.000	0.000	0.000	0.001	0.004	0.003	0.001	0.001	0.001	0.002
Fe^{2+}	0.000	0.000	0.000	0.001	0.000	0.001	0.000	0.001	0.001	0.001	0.001	0.000	0.000	0.000	0.001
Ca	2.114	2.031	1.991	1.972	1.946	1.938	2.011	1.913	1.894	1.876	1.865	2.022	1.859	2.017	1.863
Na	0.000	0.000	0.000	0.000	0.000	0.000	0.000	0.000	0.000	0.000	0.000	0.000	0.029	0.132	0.000
A-site	2.115	2.032	1.994	1.973	1.947	1.939	2.011	1.914	1.896	1.881	1.869	2.023	1.889	2.150	1.866
O	12.000	12.000	12.000	12.000	12.000	12.000	12.000	12.000	12.000	12.000	12.000	12.000	12.000	12.000	12.000
OH	1.502	1.000	1.000	0.998	1.000	0.997	1.000	0.997	0.997	0.997	0.997	1.000	1.000	1.604	0.997
Total	21.711	20.993	20.999	20.986	20.964	20.974	21.000	20.954	20.949	20.945	20.948	21.006	20.947	21.864	20.952
X_{Fe}	0.16	0.18	0.23	0.33	0.18	0.31	0.23	0.32	0.20	0.35	0.22	0.25	0.33	0.20	0.20
X_{Ep}	0.50	0.52	0.69	0.99	0.53	0.95	0.68	0.96	0.61	1.07	0.67	0.74	1.00	0.60	0.63
X_{Al}	0.81	0.82	0.77	0.67	0.82	0.68	0.77	0.68	0.80	0.64	0.78	0.74	0.66	0.79	0.79

APPENDIX II. - MINERAL CHEMISTRY / 5

EPIDOTE

Oxides	519ep1	519ep2	519ep3	519ep4	519ep5	519ep6	519ep7	519ep8	519ep9	519ep10	519ep11	519ep12	519line1	519line2	519line3	519line4
SiO_2	39.48	38.98	38.25	38.55	38.22	37.57	36.88	38.18	39.58	39.32	40.17	38.56	39.39	39.16	39.17	39.51
TiO_2	0.04	0.00	0.04	0.00	0.00	0.11	0.02	0.04	0.00	0.19	0.12	0.23	0.08	0.12	0.14	0.18
Al_2O_3	26.62	21.30	22.35	27.47	26.23	22.63	20.11	24.40	25.58	26.60	28.85	20.64	26.38	26.30	25.87	25.80
Fe_2O_3	9.58	16.95	15.89	9.33	9.40	14.89	18.26	13.17	8.54	7.20	4.60	14.93	8.15	8.01	9.02	8.81
MnO	0.16	0.25	0.20	0.05	0.05	0.03	0.04	0.04	0.00	0.04	0.21	0.33	0.39	0.23	0.25	0.05
CaO	21.79	19.92	21.35	22.60	23.09	22.77	21.97	22.47	23.89	24.60	24.20	23.52	23.91	23.77	24.07	24.06
Na_2O	0.00	0.00	0.01	0.00	0.00	0.00	0.00	0.00	0.01	0.00	0.00	0.05	0.00	0.01	0.06	0.04
Total	97.67	97.39	98.10	98.00	96.98	98.00	97.28	98.30	97.60	97.96	98.18	98.37	98.31	97.59	98.58	98.45
Chemical formula on a basis of 12.5 oxygen pfu.																
Si^{IV}	3.054	3.076	3.006	2.981	2.998	2.961	2.960	2.977	3.079	3.046	3.073	2.952	3.045	3.046	3.029	3.052
Al^{IV}	0.000	0.000	0.000	0.190	0.002	0.039	0.040	0.023	0.000	0.000	0.000	0.048	0.000	0.000	0.000	0.000
T-site	3.054	3.076	3.006	3.000	3.000	3.000	3.000	3.000	3.079	3.046	3.073	3.000	3.045	3.046	3.029	3.052
Al^{VI}	2.427	1.981	2.070	2.485	2.423	2.064	1.862	2.220	2.345	2.429	2.601	2.073	2.403	2.411	2.358	2.349
Fe^{3+}	0.618	1.116	1.042	0.601	0.614	0.979	1.193	0.857	0.556	0.467	0.294	0.953	0.527	0.521	0.583	0.569
Mn^{3+}	0.000	0.000	0.000	0.000	0.000	0.000	0.000	0.000	0.000	0.000	0.000	0.000	0.000	0.000	0.000	0.000
Ti	0.002	0.000	0.002	0.000	0.000	0.006	0.001	0.002	0.000	0.011	0.007	0.013	0.005	0.007	0.008	0.010
Fe^{2+}	0.001	0.001	0.001	0.002	0.001	0.002	0.002	0.001	0.000	0.000	0.000	0.001	0.000	0.000	0.000	0.000
Mn^{2+}	0.005	0.008	0.007	0.001	0.001	0.007	0.021	0.005	0.000	0.000	0.013	0.010	0.025	0.014	0.015	0.002
M-site	3.054	3.107	3.122	3.089	3.039	3.058	3.079	3.086	2.901	2.906	2.915	3.052	2.959	2.953	2.964	2.931
Mn^{3+}	0.000	0.000	0.000	0.000	0.000	0.000	0.000	0.000	0.000	0.000	0.000	0.000	0.000	0.000	0.000	0.000
Mn^{2+}	0.005	0.008	0.007	0.002	0.001	0.008	0.021	0.005	0.000	0.000	0.001	0.011	0.001	0.001	0.001	0.001
Fe^{2+}	0.001	0.001	0.001	0.001	0.001	0.001	0.001	0.001	0.000	0.000	0.000	0.001	0.000	0.000	0.000	0.000
Ca	1.806	1.684	1.798	1.873	1.940	1.923	1.889	1.878	1.991	2.042	1.983	1.929	1.980	1.981	1.994	1.991
Na	0.000	0.000	0.000	0.000	0.000	0.000	0.000	0.000	0.000	0.000	0.000	0.007	0.000	0.002	0.009	0.006
A-site	1.812	1.693	1.806	1.876	1.942	1.932	1.911	1.884	1.991	2.042	1.984	1.948	1.981	1.983	2.004	1.998
O	12.000	12.000	12.000	12.000	12.000	12.000	12.000	12.000	12.000	12.000	12.000	12.000	12.000	12.000	12.000	12.000
OH	0.998	0.998	0.998	0.997	0.998	0.997	0.997	0.998	1.000	1.000	1.000	0.998	1.000	1.000	1.000	1.000
Total	20.918	20.873	20.932	20.962	20.979	20.987	20.987	20.967	20.971	20.995	20.972	20.998	20.985	20.982	20.997	20.981
X_{Fe}	0.20	0.36	0.33	0.19	0.20	0.32	0.39	0.28	0.19	0.16	0.10	0.31	0.18	0.18	0.20	0.19
X_{Ep}	0.79	0.64	0.66	0.80	0.80	0.67	0.60	0.72	0.62	0.51	0.32	0.91	0.55	0.55	0.60	0.61
X_{Al}	0.59	1.02	0.94	0.55	0.59	0.94	1.13	0.80	0.81	0.84	0.89	0.68	0.81	0.82	0.80	0.80

APPENDIX II. - MINERAL CHEMISTRY / 6

EPIDOTE

Oxides	519line5	519line6	519line7	519line8	519line9	519line10	519line11	519line12	519line13	519line14	519line15	519line16	519line17	519line18	519line19	519line20
SiO_2	39.10	39.48	39.39	38.84	39.41	39.45	40.05	39.67	39.52	39.16	39.34	37.94	38.36	38.66	38.57	38.42
TiO_2	0.16	0.04	0.02	0.14	0.09	0.14	0.14	0.02	0.12	0.23	0.17	0.21	0.24	0.22	0.05	0.25
Al_2O_3	26.05	25.84	25.79	25.97	26.62	26.80	28.36	28.16	27.88	26.51	24.78	20.60	20.02	19.94	20.42	21.30
Fe_2O_3	8.91	8.92	8.76	8.56	7.88	7.66	5.44	5.67	6.14	7.83	9.65	14.95	15.90	16.83	16.06	14.33
MnO	0.19	0.10	0.04	0.08	0.03	0.03	0.01	0.04	0.09	0.21	0.21	0.27	0.00	0.16	0.15	0.05
CaO	23.81	24.25	23.86	24.01	24.10	24.24	24.35	24.25	24.70	23.93	23.71	23.56	23.66	23.22	23.48	23.65
Na_2O	0.05	0.01	0.00	0.01	0.00	0.00	0.03	0.00	0.00	0.01	0.04	0.00	0.00	0.02	0.00	0.02
Total	98.27	98.64	97.87	97.61	98.14	98.32	98.39	97.81	98.45	97.88	97.91	97.53	98.19	99.03	98.73	98.03
Chemical formula on a basis of 12.5 oxygen pfu.																
Si^{IV}	3.028	3.047	3.058	3.028	3.046	3.042	3.064	3.056	3.035	3.037	3.064	3.024	3.039	3.038	3.037	3.035
Al^{IV}	0.000	0.000	0.000	0.000	0.000	0.000	0.000	0.000	0.000	0.000	0.000	0.000	0.000	0.000	0.000	0.000
T-site	3.028	3.047	3.058	3.028	3.046	3.042	3.064	3.056	3.035	3.037	3.064	3.024	3.039	3.038	3.037	3.035
Al^{VI}	2.378	2.350	2.360	2.386	2.425	2.436	2.557	2.556	2.524	2.423	2.275	1.935	1.869	1.847	1.895	1.983
Fe^{3+}	0.577	0.576	0.569	0.558	0.509	0.494	0.348	0.365	0.394	0.508	0.629	0.996	1.054	1.106	1.058	0.947
Mn^{3+}	0.000	0.000	0.000	0.000	0.000	0.000	0.000	0.000	0.000	0.000	0.000	0.000	0.000	0.000	0.000	0.000
Ti	0.009	0.002	0.001	0.008	0.005	0.008	0.008	0.001	0.007	0.013	0.010	0.013	0.014	0.013	0.003	0.015
Fe^{2+}	0.000	0.000	0.000	0.000	0.000	0.000	0.000	0.000	0.000	0.000	0.000	0.000	0.000	0.000	0.000	0.000
Mn^{2+}	0.011	0.006	0.002	0.004	0.001	0.001	0.001	0.002	0.005	0.013	0.013	0.017	0.000	0.010	0.009	0.002
M-site	2.976	2.934	2.932	2.957	2.940	2.939	2.914	2.924	2.930	2.957	2.926	2.961	2.937	2.976	2.965	2.947
Mn^{3+}	0.000	0.000	0.000	0.000	0.000	0.000	0.000	0.000	0.000	0.000	0.000	0.000	0.000	0.000	0.000	0.000
Mn^{2+}	0.001	0.001	0.001	0.001	0.001	0.001	0.000	0.001	0.001	0.001	0.001	0.001	0.000	0.001	0.001	0.001
Fe^{2+}	0.000	0.000	0.000	0.000	0.000	0.000	0.000	0.000	0.000	0.000	0.000	0.000	0.000	0.000	0.000	0.000
Ca	1.976	2.005	1.985	2.005	1.995	2.003	1.996	2.001	2.033	1.988	1.979	2.012	2.008	1.955	1.981	2.002
Na	0.008	0.001	0.000	0.002	0.000	0.000	0.004	0.000	0.000	0.002	0.006	0.000	0.000	0.003	0.000	0.003
A-site	1.984	2.008	1.986	2.008	1.996	2.004	2.000	2.002	2.034	1.991	1.986	2.013	2.008	1.959	1.982	2.006
O	12.000	12.000	12.000	12.000	12.000	12.000	12.000	12.000	12.000	12.000	12.000	12.000	12.000	12.000	12.000	12.000
OH	1.000	1.000	1.000	1.000	1.000	1.000	1.000	1.000	1.000	1.000	1.000	1.000	1.000	1.000	1.000	1.000
Total	20.989	20.988	20.976	20.993	20.982	20.985	20.978	20.982	20.999	20.985	20.977	20.998	20.985	20.974	20.984	20.987
X_{Fe}	0.19	0.20	0.19	0.19	0.17	0.17	0.12	0.12	0.13	0.17	0.21	0.34	0.36	0.37	0.36	0.32
X_{Ep}	0.59	0.62	0.61	0.58	0.54	0.53	0.38	0.40	0.42	0.53	0.68	1.04	1.12	1.13	1.10	1.00
X_{Al}	0.80	0.80	0.81	0.81	0.82	0.83	0.88	0.87	0.86	0.82	0.78	0.65	0.64	0.62	0.64	0.67

EPIDOTE

Oxides	284ep1	284ep2	284ep3	284ep4	284ep5	284ep6	284ep7	284ep8	284ep9	284ep10	284ep11	284ep12	284ep13	284ep14	284ep15	284ep16
SiO_2	39.59	38.71	39.57	38.89	38.46	42.07	38.89	38.57	39.08	39.01	38.57	38.57	39.02	38.22	38.78	39.53
TiO_2	0.21	0.00	0.00	0.04	0.23	0.16	0.09	0.03	0.09	0.05	0.00	0.00	0.08	0.22	0.06	0.05
Al_2O_3	26.51	23.25	26.50	24.47	21.73	25.57	26.09	21.85	26.15	25.80	22.52	22.06	23.06	21.01	25.67	26.17
Fe_2O_3	10.17	15.36	10.58	13.66	16.42	7.46	8.52	14.08	8.30	9.01	13.33	13.47	12.74	15.00	9.37	8.39
MnO	0.08	0.25	0.16	0.13	0.04	0.00	0.08	0.42	0.14	0.21	0.23	0.17	0.08	0.04	0.12	0.04
CaO	20.30	19.94	20.38	20.02	20.57	22.44	24.53	23.61	24.10	24.06	23.71	23.56	23.80	23.91	24.20	24.23
Na_2O	0.18	0.00	0.00	0.36	0.00	0.00	0.00	0.01	0.01	0.04	0.00	0.01	0.01	0.00	0.02	0.02
Total	97.20	97.59	97.27	97.64	97.48	97.89	98.31	98.60	97.90	98.21	98.37	97.87	98.82	98.48	98.31	98.50
Chemical formula on a basis of 12.5 oxygen pfu.																
Si^{IV}	3.071	3.037	3.068	3.036	3.036	3.090	3.018	3.030	3.036	3.029	3.027	3.043	3.046	3.016	3.014	3.051
Al^{IV}	0.000	0.000	0.000	0.000	0.000	0.000	0.000	0.000	0.000	0.000	0.000	0.000	0.000	0.000	0.000	0.000
T-site	3.071	3.037	3.068	3.036	3.036	3.090	3.018	3.030	3.036	3.029	3.027	3.043	3.046	3.016	3.014	3.051
Al^{VI}	2.424	2.149	2.421	2.251	2.022	2.620	2.386	2.023	2.395	2.361	2.083	2.051	2.121	1.954	2.351	2.381
Fe^{3+}	0.658	1.005	0.684	0.889	1.081	0.400	0.553	0.925	0.539	0.585	0.875	0.889	0.814	0.990	0.609	0.542
Mn^{3+}	0.000	0.000	0.000	0.000	0.000	0.000	0.000	0.000	0.000	0.000	0.000	0.000	0.000	0.000	0.000	0.000
Ti	0.013	0.000	0.000	0.002	0.013	0.010	0.006	0.002	0.005	0.003	0.000	0.000	0.005	0.013	0.004	0.003
Fe^{2+}	0.001	0.001	0.002	0.001	0.002	0.000	0.000	0.000	0.000	0.000	0.000	0.000	0.000	0.000	0.000	0.000
Mn^{2+}	0.003	0.009	0.005	0.004	0.001	0.000	0.004	0.027	0.008	0.013	0.014	0.010	0.004	0.002	0.007	0.002
M-site	3.098	3.164	3.112	3.148	3.119	3.030	2.949	2.976	2.947	2.961	2.972	2.950	2.944	2.959	2.971	2.927
Mn^{3+}	0.000	0.000	0.000	0.000	0.000	0.000	0.000	0.000	0.000	0.000	0.000	0.000	0.000	0.000	0.000	0.000
Mn^{2+}	0.003	0.008	0.005	0.004	0.002	0.000	0.001	0.001	0.001	0.001	0.001	0.001	0.001	0.001	0.001	0.001
Fe^{2+}	0.001	0.001	0.001	0.001	0.001	0.000	0.000	0.000	0.000	0.000	0.000	0.000	0.000	0.000	0.000	0.000
Ca	1.688	1.675	1.692	1.674	1.740	1.750	2.039	1.987	2.006	2.001	1.994	1.992	1.990	2.022	2.015	2.004
Na	0.027	0.000	0.000	0.055	0.000	0.010	0.000	0.002	0.002	0.006	0.000	0.002	0.002	0.000	0.003	0.003
A-site	1.718	1.684	1.698	1.734	1.743	1.770	2.040	1.990	2.009	2.008	1.995	1.994	1.993	2.023	2.019	2.008
O	12.000	12.000	12.000	12.000	12.000	12.000	12.000	12.000	12.000	12.000	12.000	12.000	12.000	12.000	12.000	12.000
OH	0.998	0.998	0.997	0.998	0.997	1.000	1.000	1.000	1.000	1.000	1.000	1.000	1.000	1.000	1.000	1.000
Total	20.885	20.883	20.876	20.916	20.895	20.890	21.007	20.996	20.992	20.999	20.994	20.988	20.983	20.998	21.004	20.986
X_{Fe}	0.21	0.32	0.22	0.28	0.35	0.13	0.19	0.31	0.18	0.20	0.29	0.30	0.28	0.33	0.21	0.19
X_{Ep}	0.78	0.68	0.78	0.72	0.65	0.86	0.58	0.95	0.57	0.61	0.90	0.94	0.86	1.03	0.63	0.58
X_{Al}	0.61	0.87	0.62	0.78	0.98	0.39	0.81	0.68	0.81	0.80	0.70	0.70	0.72	0.66	0.79	0.81

APPENDIX II. - MINERAL CHEMISTRY / 8

FELDSPAR

Oxides	372ab1	372ab2	372ab3	372ab4	372ab5	870ab1	870ab2	870ab3	870ab4	870ab5	870ab7	870ab8	870ab9	870ab10	870ab11
SiO_2	67.13	66.88	65.59	65.66	65.53	68.98	69.34	68.76	68.83	69.26	69.37	68.73	68.74	68.17	68.28
TiO_2	0.04	0.00	0.00	0.00	0.04	0.00	0.00	0.00	0.00	0.00	0.03	0.02	0.03	0.01	0.01
Al_2O_3	20.41	20.73	21.45	21.62	21.13	19.78	19.22	19.54	19.57	18.94	19.94	18.94	19.06	18.82	18.79
FeO	0.12	0.07	0.07	0.05	0.00	0.04	0.08	0.00	0.00	0.04	0.08	0.01	0.02	0.04	0.00
MnO	0.00	0.05	0.05	0.05	0.00	0.00	0.03	0.00	0.03	0.00	0.00	0.00	0.00	0.00	0.00
MgO	0.00	0.00	0.05	0.00	0.00	0.00	0.00	0.00	0.00	0.06	0.00	0.01	0.00	0.01	0.02
CaO	0.08	0.12	0.18	0.19	0.37	0.02	0.02	0.18	0.19	0.10	0.01	0.00	0.02	0.04	0.02
Na_2O	11.15	11.11	11.13	11.17	11.38	11.08	10.86	10.93	11.08	10.96	10.60	11.55	11.56	11.51	11.60
K_2O	0.11	0.19	0.11	0.13	0.12	0.05	0.07	0.10	0.09	0.12	0.07	0.03	0.22	0.08	0.05
BaO	0.00	0.00	0.00	0.00	0.00	0.00	0.12	0.00	0.00	0.00	0.02	0.00	0.00	0.00	0.00
Total	99.04	99.15	98.63	98.87	98.57	99.96	99.74	99.51	99.79	99.48	100.12	99.29	99.69	98.74	98.77
Structural formula on a basis of 8 oxygen pfu.															
Si	2.959	2.947	2.910	2.906	2.913	2.938	2.960	2.942	2.939	2.965	2.944	3.017	3.011	3.013	3.016
Ti	0.001	0.000	0.000	0.000	0.001	0.000	0.000	0.000	0.000	0.000	0.001	0.980	0.984	0.981	0.978
Al	1.061	1.077	1.122	1.128	1.107	1.081	1.053	1.073	1.073	1.041	1.086	0.001	0.001	0.000	0.000
Fe	0.004	0.003	0.003	0.002	0.000	0.002	0.003	0.000	0.000	0.002	0.003	0.000	0.001	0.002	0.000
Mn	0.000	0.002	0.002	0.002	0.000	0.000	0.001	0.000	0.001	0.000	0.000	0.000	0.000	0.000	0.000
Mg	0.000	0.000	0.003	0.000	0.000	0.000	0.000	0.000	0.000	0.004	0.000	0.001	0.000	0.001	0.001
Ca	0.004	0.006	0.009	0.009	0.018	0.001	0.001	0.009	0.009	0.005	0.000	0.000	0.001	0.002	0.001
Na	0.953	0.949	0.957	0.959	0.981	0.997	0.979	0.988	0.999	0.991	0.950	0.983	0.981	0.986	0.993
K	0.006	0.011	0.006	0.007	0.007	0.003	0.004	0.006	0.006	0.007	0.004	0.001	0.012	0.005	0.003
Ba	0.000	0.000	0.000	0.000	0.000	0.000	0.002	0.000	0.000	0.000	0.000	0.000	0.000	0.000	0.000
Total	4.989	4.984	5.011	5.013	5.026	5.022	5.005	5.018	5.027	5.014	4.989	4.984	4.992	4.991	4.993
Endmember composition															
X_{Ab}	0.990	0.982	0.985	0.984	0.975	0.996	0.994	0.985	0.985	0.988	0.995	0.999	0.987	0.993	0.996
X_{Or}	0.006	0.011	0.006	0.007	0.007	0.003	0.004	0.006	0.005	0.007	0.004	0.001	0.012	0.005	0.003
X_{An}	0.004	0.006	0.009	0.009	0.018	0.001	0.001	0.009	0.009	0.005	0.001	0.000	0.001	0.002	0.001

APPENDIX II. - MINERAL CHEMISTRY / 9

FELDSPAR

Oxides	870ab12	870ab13	870ab14	870ab15	637ab1	637ab2	637ab3	699ab1	699ab2	699ab3	699ab4	699ab5	702ab1	702ab2
SiO_2	67.98	68.24	67.23	68.27	68.59	69.74	69.75	69.65	69.00	68.82	67.66	67.53	69.72	69.34
TiO_2	0.00	0.00	0.00	0.00	0.03	0.00	0.08	0.03	0.00	0.03	0.00	0.03	0.09	0.00
Al_2O_3	19.11	18.91	18.21	18.77	18.68	18.31	18.93	18.90	18.67	19.11	19.01	20.55	19.03	18.99
FeO	0.02	0.01	0.01	0.00	0.26	0.41	0.26	0.07	0.22	0.11	0.01	0.03	0.03	0.03
MnO	0.00	0.00	0.02	0.01	0.00	0.00	0.03	0.03	0.00	0.00	0.06	0.11	0.08	0.05
MgO	0.03	0.00	0.01	0.01	0.05	0.00	0.00	0.00	0.00	0.08	0.01	0.00	0.02	0.02
CaO	0.05	0.31	0.09	0.02	0.65	0.34	0.43	0.10	0.12	0.14	0.32	0.32	0.33	0.27
Na_2O	11.41	11.43	11.43	11.61	11.03	10.44	10.58	10.96	11.05	10.92	11.37	11.78	10.45	10.84
K_2O	0.12	0.10	0.12	0.07	0.09	0.12	0.07	0.06	0.05	0.05	0.09	0.09	0.06	0.03
BaO	0.00	0.00	0.00	0.00	0.00	0.00	0.00	0.00	0.00	0.00	0.00	0.00	0.00	0.00
Total	98.70	99.05	97.10	98.76	99.38	99.36	100.13	99.80	99.11	99.26	98.53	100.44	99.81	99.57
Structural formula on a basis of 8 oxygen pfu.														
Si	3.005	3.009	3.023	3.016	2.950	2.990	2.967	2.971	2.968	2.953	3.00	2.95	2.970	2.964
Ti	0.996	0.983	0.965	0.977	0.001	0.000	0.003	0.001	0.000	0.001	0.00	0.00	0.003	0.000
Al	0.000	0.000	0.000	0.000	1.032	1.008	1.034	1.035	1.031	1.053	0.99	1.06	1.041	1.042
Fe	0.001	0.001	0.000	0.000	0.010	0.016	0.010	0.003	0.009	0.004	0.00	0.00	0.001	0.001
Mn	0.000	0.000	0.001	0.000	0.000	0.000	0.001	0.001	0.000	0.000	0.00	0.00	0.003	0.002
Mg	0.002	0.000	0.001	0.001	0.003	0.000	0.000	0.000	0.000	0.006	0.00	0.00	0.001	0.001
Ca	0.002	0.015	0.004	0.001	0.033	0.017	0.021	0.005	0.006	0.007	0.02	0.01	0.016	0.014
Na	0.978	0.977	0.997	0.995	1.002	0.945	0.950	0.987	1.004	0.990	0.98	1.00	0.940	0.979
K	0.007	0.006	0.007	0.004	0.005	0.007	0.004	0.004	0.003	0.003	0.01	0.00	0.003	0.002
Ba	0.000	0.000	0.000	0.000	0.000	0.000	0.000	0.000	0.000	0.000	0.00	0.00	0.000	0.000
Total	4.990	4.991	4.996	4.995	5.036	4.983	4.991	5.006	5.020	5.016	4.99	5.02	4.979	5.005
Endmember composition														
X_{Ab}	0.991	0.979	0.989	0.995	0.964	0.975	0.974	0.991	0.991	0.990	0.980	0.980	0.979	0.985
X_{Or}	0.007	0.006	0.007	0.004	0.005	0.007	0.004	0.004	0.003	0.003	0.005	0.006	0.003	0.002
X_{An}	0.002	0.015	0.004	0.001	0.031	0.018	0.022	0.005	0.006	0.007	0.015	0.014	0.017	0.014

APPENDIX II. - MINERAL CHEMISTRY / 10

FELDSPAR

Oxides	372kfp1	372kfp2	372kfp3	372kfp4	372kfp5	870kfp1	870kfp2	870kfp3	870kfp4	870kfp5	870kfp6	870kfp7	870kfp10	870kfp9	870kfp8
SiO_2	63.30	63.25	62.17	62.22	62.25	65.23	64.80	65.63	65.02	65.98	65.97	64.74	64.19	64.69	64.30
TiO_2	0.04	0.04	0.00	0.00	0.00	0.00	0.00	0.00	0.00	0.00	0.03	0.04	0.03	0.00	0.00
Al_2O_3	19.32	19.67	21.13	20.44	20.55	17.92	18.53	18.60	18.69	18.11	18.60	17.57	17.68	17.78	17.99
FeO	0.12	0.02	0.07	0.12	0.07	0.00	0.04	0.04	0.00	0.04	0.04	0.05	0.04	0.00	0.00
MnO	0.00	0.00	0.03	0.00	0.00	0.00	0.00	0.00	0.05	0.05	0.00	0.00	0.08	0.00	0.10
MgO	0.00	0.00	0.00	0.02	0.00	0.00	0.00	0.03	0.03	0.05	0.03	0.01	0.00	0.00	0.01
CaO	0.00	0.00	0.00	0.00	0.00	0.00	0.00	0.00	0.00	0.00	0.00	0.01	0.02	0.00	0.00
Na_2O	0.33	0.22	0.19	0.17	0.32	0.26	0.30	0.29	0.18	0.17	0.16	0.17	0.25	0.13	0.18
K_2O	15.96	16.07	15.98	15.97	16.01	15.53	15.80	15.57	15.69	15.53	15.34	16.54	16.42	16.79	16.76
BaO	0.00	0.00	0.00	0.00	0.00	0.21	0.12	0.05	0.09	0.23	0.15	0.00	0.00	0.00	0.00
Total	99.07	99.27	99.58	98.94	99.20	99.15	99.60	100.21	99.75	100.16	100.32	99.14	98.71	99.40	99.34
Structural formula on a basis of 8 oxygen pfu.															
Si	2.954	2.945	2.888	2.910	2.905	2.963	2.934	2.945	2.935	2.964	2.952	3.022	3.011	3.014	2.999
Ti	0.001	0.001	0.000	0.000	0.000	0.000	0.000	0.000	0.000	0.000	0.001	0.967	0.978	0.977	0.989
Al	1.063	1.080	1.157	1.127	1.130	1.045	1.077	1.071	1.083	1.045	1.069	0.002	0.001	0.000	0.000
Fe	0.005	0.001	0.003	0.005	0.003	0.000	0.002	0.002	0.000	0.002	0.002	0.002	0.002	0.000	0.000
Mn	0.000	0.000	0.001	0.000	0.000	0.000	0.000	0.000	0.002	0.002	0.000	0.000	0.003	0.000	0.004
Mg	0.000	0.000	0.000	0.001	0.001	0.000	0.000	0.002	0.002	0.004	0.002	0.000	0.000	0.000	0.000
Ca	0.000	0.000	0.000	0.000	0.000	0.000	0.000	0.000	0.000	0.000	0.000	0.001	0.001	0.000	0.000
Na	0.030	0.020	0.021	0.015	0.029	0.025	0.029	0.027	0.017	0.016	0.015	0.016	0.022	0.012	0.016
K	0.950	0.955	0.947	0.953	0.953	0.980	0.994	0.971	0.984	0.970	0.954	0.985	0.983	0.998	0.997
Ba	0.000	0.000	0.000	0.000	0.000	0.004	0.002	0.001	0.002	0.004	0.003	0.000	0.000	0.000	0.000
Total	5.003	5.001	5.017	5.011	5.021	5.017	5.039	5.019	5.025	5.006	4.997	4.994	5.001	5.000	5.006
Endmember composition															
X_{Ab}	0.031	0.021	0.022	0.016	0.030	0.025	0.028	0.028	0.017	0.017	0.016	0.016	0.022	0.012	0.016
X_{Or}	0.969	0.979	0.978	0.984	0.970	0.975	0.972	0.972	0.983	0.983	0.984	0.984	0.977	0.988	0.984
X_{An}	0.000	0.000	0.000	0.000	0.000	0.000	0.000	0.000	0.000	0.000	0.000	0.001	0.001	0.000	0.000

APPENDIX II. - MINERAL CHEMISTRY / 11

FELDSPAR

Oxides	870kfp11	870kfp12	870adu1	870adu2	870adu3	870adu4	870adu5	870adu6	870adu7	870adu8	870adu9	870adu10	870adu11	870adu12
SiO_2	64.56	63.53	65.33	65.31	65.38	64.95	64.90	64.64	64.59	64.73	64.29	63.63	63.55	64.40
TiO_2	0.00	0.01	0.04	0.00	0.02	0.00	0.01	0.06	0.04	0.00	0.00	0.00	0.00	0.02
Al_2O_3	17.65	17.71	17.09	17.24	17.23	17.16	17.24	17.33	17.65	17.65	17.76	17.77	17.88	17.62
FeO	0.02	0.01	0.03	0.04	0.04	0.00	0.05	0.04	0.06	0.00	0.00	0.09	0.10	0.05
MnO	0.00	0.00	0.05	0.00	0.04	0.00	0.02	0.05	0.02	0.00	0.00	0.00	0.00	0.16
MgO	0.01	0.00	0.01	0.00	0.02	0.01	0.00	0.01	0.00	0.01	0.00	0.00	0.01	0.00
CaO	0.00	0.00	0.09	0.07	0.00	0.00	0.09	0.04	0.00	0.00	0.00	0.00	0.02	0.03
Na_2O	0.18	0.21	0.19	0.24	0.18	0.17	0.17	0.17	0.13	0.13	0.14	0.14	0.18	0.17
K_2O	16.59	16.44	16.75	16.64	16.66	16.68	16.60	16.69	16.63	16.48	16.42	16.43	16.38	16.49
BaO	0.00	0.00	0.00	0.00	0.00	0.00	0.00	0.00	0.00	0.00	0.00	0.00	0.00	0.00
Total	99.00	97.91	99.58	99.54	99.57	98.97	99.08	99.03	99.11	99.01	98.61	98.06	98.12	98.93
Structural formula on a basis of 8 oxygen pfu.														
Si	3.018	3.005	3.039	3.037	3.038	3.037	3.033	3.025	3.017	3.023	3.015	3.005	3.000	3.015
Ti	0.973	0.987	0.001	0.000	0.001	0.000	0.000	0.002	0.001	0.000	0.000	0.000	0.000	0.001
Al	0.000	0.000	0.937	0.945	0.944	0.946	0.950	0.956	0.972	0.971	0.982	0.990	0.995	0.972
Fe	0.001	0.001	0.001	0.002	0.002	0.000	0.002	0.002	0.002	0.000	0.000	0.004	0.004	0.002
Mn	0.000	0.000	0.002	0.000	0.002	0.000	0.001	0.002	0.001	0.001	0.000	0.000	0.000	0.006
Mg	0.001	0.000	0.001	0.000	0.001	0.001	0.000	0.001	0.000	0.000	0.000	0.000	0.001	0.000
Ca	0.000	0.000	0.004	0.003	0.000	0.000	0.005	0.002	0.000	0.000	0.000	0.000	0.001	0.001
Na	0.016	0.019	0.017	0.022	0.016	0.015	0.015	0.015	0.012	0.012	0.013	0.013	0.016	0.015
K	0.989	0.992	0.994	0.987	0.988	0.995	0.990	0.996	0.991	0.982	0.982	0.990	0.986	0.985
Ba	0.000	0.000	0.000	0.000	0.000	0.000	0.000	0.000	0.000	0.000	0.000	0.000	0.000	0.000
Total	4.998	5.005	4.997	4.995	4.991	4.995	4.995	5.001	4.997	4.988	4.992	5.001	5.004	4.998
Endmember composition														
X_{Ab}	0.016	0.019	0.017	0.021	0.016	0.015	0.015	0.015	0.012	0.012	0.013	0.013	0.016	0.015
X_{Or}	0.984	0.981	0.979	0.975	0.984	0.985	0.980	0.983	0.988	0.988	0.987	0.987	0.982	0.984
X_{An}	0.000	0.000	0.004	0.003	0.000	0.000	0.004	0.002	0.000	0.000	0.000	0.000	0.001	0.001

APPENDIX II. - MINERAL CHEMISTRY / 12

CHLORITE

Oxides	372chl1	372chl2	372chl3	372chl4	372chl5	372chl6	372chl7	870chl1	870chl2	870chl3	870chl4	870chl5	870chl6	870chl7	870chl8
SiO_2	26.74	28.04	26.11	27.80	26.63	25.63	25.41	26.13	27.17	26.26	27.14	26.43	24.95	27.09	24.84
TiO_2	0.02	0.00	0.02	0.04	0.02	0.04	0.04	0.02	0.07	0.00	0.00	0.05	0.05	0.00	0.05
Al_2O_3	16.30	14.43	17.07	16.94	17.66	18.98	18.35	20.54	19.81	19.88	21.60	20.45	21.33	20.31	21.37
FeO	30.38	31.52	30.37	28.53	30.23	29.27	29.80	29.58	27.48	29.98	29.45	30.14	31.95	28.80	29.69
MnO	0.54	0.72	0.53	0.45	0.49	0.46	0.51	0.31	0.10	0.31	0.17	0.10	0.10	0.23	0.15
MgO	13.83	13.93	13.54	13.75	13.56	14.28	13.89	12.62	11.84	11.99	9.56	11.11	10.47	12.21	12.73
CaO	0.59	0.57	0.28	0.77	0.29	0.40	0.50	0.02	0.00	0.05	0.33	0.06	0.04	0.05	0.00
Na_2O	0.00	0.00	0.20	0.00	0.00	0.00	0.21	0.00	0.00	0.00	0.00	0.00	0.00	0.00	0.00
K_2O	0.04	0.04	0.01	0.07	0.01	0.00	0.00	0.17	1.98	0.14	0.15	0.13	0.12	0.15	0.10
Total	88.44	89.25	88.12	88.36	88.90	89.05	88.72	89.39	88.44	88.61	88.41	88.46	89.00	88.83	88.93
Structural formula on a basis of 28 oxygen pfu.															
Si	5.753	6.011	5.622	5.924	5.689	5.429	5.412	5.520	5.600	5.620	5.760	5.640	5.360	5.720	5.280
Al^{IV}	2.247	1.989	2.378	2.076	2.311	2.571	2.588	2.480	2.400	2.380	2.240	2.360	2.640	2.280	2.720
T-site	8.000	8.000	8.000	8.000	8.000	8.000	8.000	8.000	8.000	8.000	8.000	8.000	8.000	8.000	8.000
Al^{VI}	1.908	1.676	1.991	2.184	2.147	2.194	2.067	2.640	2.420	2.620	3.160	2.800	2.780	2.760	2.640
Ti	0.003	0.000	0.003	0.006	0.003	0.006	0.006	0.000	0.020	0.000	0.000	0.000	0.000	0.000	0.000
Fe^{+3}	0.000	0.000	0.000	0.059	0.000	0.000	0.000	0.000	0.420	0.000	0.000	0.000	0.000	0.040	0.040
Fe^{+2}	5.607	5.783	5.655	5.025	5.467	5.337	5.549	5.220	4.320	5.360	5.220	5.380	5.740	5.040	5.260
Mn	0.098	0.131	0.097	0.081	0.089	0.083	0.092	0.060	0.020	0.060	0.040	0.020	0.020	0.040	0.020
Mg	4.435	4.452	4.346	4.368	4.319	4.509	4.410	3.980	4.560	3.820	3.020	3.540	3.360	3.840	4.040
Ca	0.136	0.131	0.065	0.176	0.066	0.091	0.114	0.000	0.000	0.020	0.080	0.020	0.000	0.020	0.000
Na	0.000	0.000	0.167	0.000	0.000	0.000	0.173	0.000	0.000	0.000	0.000	0.000	0.000	0.000	0.000
K	0.022	0.022	0.005	0.038	0.005	0.000	0.000	0.040	0.420	0.040	0.040	0.040	0.040	0.040	0.020
O-site	12.210	12.194	12.329	11.938	12.097	12.220	12.412	11.940	12.180	11.900	11.560	11.800	11.940	11.780	12.040
OH	16.000	16.000	16.000	16.000	16.000	16.000	16.000	16.000	16.000	16.000	16.000	16.000	16.000	16.000	16.000
Total	36.210	36.194	36.329	35.938	36.097	36.220	36.412	35.940	36.180	35.900	35.560	35.800	35.940	35.780	36.040
X_{Al}	0.156	0.137	0.161	0.183	0.178	0.180	0.167	0.221	0.199	0.220	0.273	0.237	0.233	0.234	0.220
X_{Fe}	0.459	0.474	0.459	0.426	0.452	0.437	0.447	0.437	0.389	0.450	0.452	0.456	0.481	0.431	0.440
X_{Mg}	0.363	0.365	0.353	0.366	0.357	0.369	0.355	0.333	0.374	0.321	0.261	0.300	0.281	0.326	0.336
Fe/(Fe+Mg)	0.558	0.565	0.565	0.538	0.559	0.542	0.557	0.567	0.510	0.584	0.633	0.603	0.631	0.570	0.567
Al^{VI}/Al^{IV}	0.849	0.843	0.837	1.052	0.929	0.854	0.799	1.065	1.008	1.101	1.411	1.186	1.053	1.211	0.971
Thermometry / Zhang & Fyfe 1995															
T / °C	–	–	249	–	242	272	–	260	–	247	228	244	271	238	285

APPENDIX II. - MINERAL CHEMISTRY / 13

CHLORITE

Oxides	870chl9	870chl10	870chl11	870chl12	870chl13	870chl14	870chl15	870chl16	870chl17	870chl18	870chl19	870chl20	870chl21	870chl22	870chl23
SiO_2	26.57	26.24	25.96	25.57	26.20	26.12	26.51	26.24	25.84	25.71	25.72	26.12	26.46	25.77	25.84
TiO_2	0.02	0.06	0.05	0.00	0.08	0.00	0.02	0.04	0.04	0.02	0.00	0.04	0.02	0.11	0.00
Al_2O_3	19.21	18.99	19.01	20.24	20.04	19.91	19.69	19.05	19.96	19.78	20.04	19.21	18.77	19.54	19.81
FeO	31.17	29.60	29.45	29.38	29.48	29.21	29.92	29.16	28.65	28.53	27.82	29.85	29.69	28.79	29.33
MnO	0.25	0.15	0.19	0.03	0.00	0.03	0.05	0.16	0.10	0.16	0.03	0.24	0.31	0.12	0.05
MgO	11.08	12.11	12.60	10.97	11.61	11.53	10.51	12.76	12.49	11.93	11.27	11.85	12.62	12.08	11.82
CaO	0.08	0.00	0.02	0.02	0.00	0.00	0.17	0.02	0.05	0.05	0.09	0.04	0.06	0.09	0.01
Na_2O	0.01	0.11	0.00	0.01	0.05	0.01	0.02	0.09	0.00	0.00	0.04	0.01	0.00	0.04	0.00
K_2O	0.01	0.05	0.11	0.10	0.10	0.06	0.09	0.05	0.11	0.14	0.13	0.07	0.09	0.11	0.11
Total	88.40	87.31	87.39	86.32	87.56	86.87	86.98	87.57	87.24	86.32	85.14	87.43	88.02	86.65	86.97
Structural formula on a basis of 28 oxygen pfu.															
Si	5.701	5.671	5.616	5.568	5.616	5.642	5.723	5.643	5.558	5.591	5.629	5.648	5.681	5.590	5.594
Al^{IV}	2.299	2.329	2.384	2.432	2.384	2.358	2.277	2.357	2.442	2.409	2.371	2.352	2.319	2.410	2.406
T-site	8.000	8.000	8.000	8.000	8.000	8.000	8.000	8.000	8.000	8.000	8.000	8.000	8.000	8.000	8.000
Al^{VI}	2.574	2.521	2.469	2.783	2.700	2.730	2.760	2.482	2.630	2.678	2.825	2.555	2.439	2.600	2.663
Ti	0.003	0.010	0.008	0.000	0.013	0.000	0.003	0.006	0.006	0.003	0.000	0.007	0.003	0.018	0.000
Fe^{+3}	0.159	0.090	0.042	0.189	0.174	0.196	0.269	0.057	0.102	0.136	0.236	0.109	0.063	0.110	0.129
Fe^{+2}	5.434	5.260	5.286	5.161	5.111	5.080	5.133	5.188	5.051	5.054	4.856	5.289	5.269	5.113	5.181
Mn	0.045	0.027	0.035	0.006	0.000	0.005	0.009	0.029	0.018	0.029	0.006	0.044	0.056	0.022	0.009
Mg	3.544	3.901	4.063	3.561	3.710	3.712	3.382	4.091	4.004	3.868	3.677	3.819	4.039	3.906	3.814
Ca	0.018	0.000	0.005	0.005	0.000	0.000	0.039	0.005	0.012	0.012	0.021	0.009	0.014	0.021	0.002
Na	0.008	0.092	0.000	0.008	0.042	0.008	0.017	0.075	0.000	0.000	0.034	0.008	0.000	0.034	0.000
K	0.005	0.029	0.061	0.056	0.055	0.034	0.050	0.027	0.060	0.078	0.073	0.039	0.049	0.061	0.061
O-site	11.793	11.930	11.968	11.767	11.805	11.767	11.662	11.960	11.884	11.857	11.726	11.879	11.933	11.885	11.859
OH	16.000	16.000	16.000	16.000	16.000	16.000	16.000	16.000	16.000	16.000	16.000	16.000	16.000	16.000	16.000
Total	35.793	35.930	35.968	35.767	35.805	35.767	35.662	35.960	35.884	35.857	35.726	35.879	35.933	35.885	35.859
X_{Al}	0.218	0.211	0.206	0.236	0.229	0.232	0.237	0.208	0.221	0.226	0.241	0.215	0.204	0.219	0.225
X_{Fe}	0.474	0.448	0.445	0.455	0.448	0.448	0.463	0.439	0.434	0.438	0.434	0.454	0.447	0.439	0.448
X_{Mg}	0.301	0.327	0.339	0.303	0.314	0.315	0.290	0.342	0.337	0.326	0.314	0.322	0.339	0.329	0.322
Fe/(Fe+Mg)	0.612	0.578	0.567	0.600	0.588	0.587	0.615	0.562	0.563	0.573	0.581	0.586	0.569	0.572	0.582
Al^{VI}/Al^{IV}	1.120	1.082	1.036	1.144	1.133	1.158	1.212	1.053	1.077	1.112	1.191	1.086	1.052	1.079	0.430
Thermometry / Zhang & Fyfe 1995															
T / °C	236	243	249	251	247	245	234	247	256	251	247	244	242	252	250

APPENDIX II. - MINERAL CHEMISTRY / 14

CHLORITE

Oxides	702chl1	702chl2	702chl3	702chl4	702chl5	702chl6	702chl7	519chl1	519chl2	519chl3	519chl4	519chl5	519chl6	519chl7	519chl8
SiO_2	25.62	25.62	26.11	26.45	26.58	26.80	27.18	29.29	29.14	29.23	29.89	28.88	29.91	30.68	30.00
TiO_2	0.00	0.02	0.02	0.00	0.00	0.05	0.05	0.11	0.00	0.00	0.04	0.00	0.01	0.00	0.00
Al_2O_3	20.15	19.41	18.98	17.35	17.07	17.30	16.60	17.04	17.53	17.21	17.52	18.31	17.64	16.65	17.38
FeO	23.87	25.30	26.29	29.82	29.66	29.04	29.77	18.85	21.07	21.01	19.28	20.86	22.12	21.45	20.22
MnO	0.38	0.44	0.44	0.33	0.33	0.31	0.44	0.47	0.57	0.84	0.67	0.50	0.66	0.71	0.79
MgO	17.85	17.00	16.67	14.48	14.84	15.60	15.14	22.35	20.63	20.12	19.17	18.88	18.07	18.83	19.04
CaO	0.32	0.25	0.40	0.64	0.45	0.59	0.64	0.67	0.31	0.35	0.75	0.41	0.09	0.02	0.13
Na_2O	0.00	0.00	0.00	0.00	0.00	0.00	0.00	0.00	0.18	0.18	0.14	0.02	0.04	0.00	0.09
K_2O	0.03	0.03	0.00	0.02	0.00	0.02	0.00	0.03	0.00	0.02	0.05	0.03	0.03	0.01	0.03
Total	88.22	88.06	88.92	89.09	88.94	89.70	89.82	88.81	89.43	88.96	87.50	87.88	88.56	88.36	87.69
Structural formula on a basis of 28 oxygen pfu.															
Si	5.340	5.400	5.480	5.660	5.680	5.660	5.760	5.881	5.865	5.927	6.079	5.904	6.079	6.223	6.106
Al^{IV}	2.660	2.600	2.520	2.340	2.320	2.340	2.240	2.119	2.135	2.073	1.921	2.096	1.921	1.777	1.894
T-site	8.000	8.000	8.000	8.000	8.000	8.000	8.000	8.000	8.000	8.000	8.000	8.000	8.000	8.000	8.000
Al^{VI}	2.300	2.220	2.180	2.020	1.980	1.960	1.900	1.924	2.038	2.051	2.298	2.328	2.324	2.222	2.296
Ti	0.000	0.000	0.000	0.000	0.000	0.000	0.000	0.017	0.000	0.000	0.006	0.000	0.002	0.000	0.000
Fe^{+3}	0.000	0.000	0.060	0.000	0.000	0.000	0.180	0.000	0.000	0.000	0.187	0.123	0.217	0.247	0.206
Fe^{+2}	4.160	4.460	4.560	5.320	5.300	5.120	5.080	3.234	3.610	3.596	3.092	3.443	3.544	3.390	3.236
Mn	0.060	0.080	0.080	0.060	0.060	0.060	0.080	0.080	0.097	0.144	0.115	0.086	0.113	0.121	0.137
Mg	5.560	5.340	5.220	4.620	4.720	4.900	4.780	6.690	6.189	6.082	5.812	5.754	5.475	5.692	5.778
Ca	0.080	0.060	0.080	0.140	0.100	0.140	0.140	0.144	0.067	0.076	0.163	0.090	0.019	0.004	0.028
Na	0.000	0.000	0.000	0.000	0.000	0.000	0.000	0.000	0.140	0.142	0.112	0.013	0.031	0.000	0.072
K	0.000	0.000	0.000	0.000	0.000	0.000	0.000	0.015	0.000	0.010	0.025	0.015	0.014	0.007	0.015
O-site	12.160	12.160	12.180	12.160	12.160	12.180	12.160	12.104	12.141	12.102	11.810	11.853	11.738	11.684	11.767
OH	16.000	16.000	16.000	16.000	16.000	16.000	16.000	16.000	16.000	16.000	16.000	16.000	16.000	16.000	16.000
Total	36.160	36.160	36.180	36.160	36.160	36.180	36.160	36.104	36.141	36.102	35.810	35.853	35.738	35.684	35.767
X_{Al}	0.189	0.183	0.179	0.166	0.163	0.161	0.156	0.159	0.168	0.169	0.195	0.196	0.198	0.190	0.195
X_{Fe}	0.342	0.367	0.379	0.438	0.436	0.420	0.433	0.267	0.297	0.297	0.278	0.301	0.320	0.311	0.292
X_{Mg}	0.457	0.439	0.429	0.380	0.388	0.402	0.393	0.553	0.510	0.503	0.492	0.485	0.466	0.487	0.491
Fe/(Fe+Mg)	0.428	0.455	0.470	0.535	0.529	0.511	0.524	0.326	0.368	0.372	0.361	0.383	0.407	0.390	0.373
Al^{VI}/Al^{IV}	0.865	0.854	0.865	0.863	0.853	0.838	0.848	0.908	0.954	0.990	1.196	1.111	1.210	1.250	1.212
Thermometry / Zhang & Fyfe 1995															
T / °C	292	283	273	–	246	–	–	–	242	–	–	236	215	202	215

CHLORITE

Oxides	519chl9	519chl10	284chl1	284chl2	284chl3	284chl4	284chl5	284chl6	284chl7	284chl8	284chl9	284chl10	284chl11	284chl12	284chl13
SiO_2	30.47	29.80	33.50	33.31	33.78	34.54	33.72	35.39	34.19	33.43	33.33	29.08	29.25	32.86	33.22
TiO_2	0.04	0.02	0.02	0.00	0.00	0.00	0.00	0.00	0.00	0.00	0.03	0.02	0.03	0.04	0.05
Al_2O_3	17.32	17.62	15.47	15.14	13.86	14.83	14.36	14.23	14.16	14.01	14.36	15.78	15.79	13.85	14.37
FeO	20.73	20.90	20.63	19.98	21.35	19.64	20.25	19.48	19.63	19.52	20.00	23.95	24.04	20.94	21.08
MnO	0.99	0.89	0.18	0.19	0.24	0.15	0.10	0.18	0.18	0.17	0.21	0.64	0.68	0.22	0.13
MgO	19.21	18.73	19.16	20.16	19.50	20.13	21.63	20.16	18.95	18.42	18.37	16.91	16.68	17.51	17.45
CaO	0.26	0.17	0.27	0.27	0.40	0.33	0.26	1.07	0.48	0.37	0.30	0.06	0.14	0.57	0.53
Na_2O	0.00	0.04	0.00	0.00	0.00	0.00	0.16	0.19	0.03	0.07	0.00	0.00	0.00	0.04	0.00
K_2O	0.02	0.00	0.09	0.03	0.03	0.08	0.04	0.02	0.02	0.03	0.04	0.00	0.01	0.02	0.08
Total	89.03	88.16	89.32	89.08	89.16	89.70	90.52	90.72	87.64	86.02	86.64	86.44	86.62	86.05	86.91
Structural formula on a basis of 28 oxygen pfu.															
Si	6.126	6.061	6.608	6.584	6.724	6.734	6.585	6.823	6.826	6.808	6.757	6.155	6.178	6.764	6.754
Al^{IV}	1.874	1.939	1.392	1.416	1.276	1.266	1.415	1.177	1.174	1.192	1.243	1.845	1.822	1.236	1.246
T-site	8.000	8.000	8.000	8.000	8.000	8.000	8.000	8.000	8.000	8.000	8.000	8.000	8.000	8.000	8.000
Al^{VI}	2.246	2.301	2.237	2.137	1.999	2.175	1.910	2.090	2.193	2.207	2.223	2.103	2.121	2.156	2.234
Ti	0.006	0.003	0.003	0.000	0.000	0.000	0.000	0.000	0.000	0.000	0.005	0.003	0.005	0.006	0.008
Fe^{+3}	0.213	0.200	0.469	0.403	0.404	0.503	0.249	0.482	0.567	0.556	0.552	0.148	0.171	0.516	0.556
Fe^{+2}	3.272	3.354	2.935	2.900	3.150	2.699	3.059	2.659	2.711	2.768	2.838	4.092	4.075	3.089	3.029
Mn	0.169	0.153	0.030	0.032	0.040	0.025	0.017	0.029	0.030	0.029	0.036	0.115	0.122	0.038	0.022
Mg	5.759	5.679	5.634	5.940	5.786	5.851	6.297	5.794	5.640	5.592	5.551	5.336	5.251	5.373	5.289
Ca	0.056	0.036	0.057	0.057	0.085	0.069	0.054	0.221	0.103	0.081	0.065	0.014	0.032	0.126	0.115
Na	0.000	0.028	0.000	0.000	0.000	0.000	0.121	0.142	0.023	0.055	0.000	0.000	0.000	0.032	0.000
K	0.010	0.000	0.045	0.015	0.015	0.040	0.020	0.010	0.010	0.016	0.021	0.000	0.005	0.011	0.041
O-site	11.730	11.754	11.410	11.485	11.480	11.362	11.726	11.427	11.277	11.304	11.291	11.809	11.782	11.346	11.295
OH	16.000	16.000	16.000	16.000	16.000	16.000	16.000	16.000	16.000	16.000	16.000	16.000	16.000	16.000	16.000
Total	35.730	35.754	35.410	35.485	35.480	35.362	35.726	35.427	35.277	35.304	35.291	35.809	35.782	35.346	35.295
X_{Al}	0.192	0.196	0.196	0.186	0.174	0.191	0.163	0.183	0.194	0.195	0.197	0.178	0.180	0.190	0.198
X_{Fe}	0.297	0.302	0.298	0.288	0.310	0.282	0.282	0.275	0.291	0.294	0.300	0.359	0.360	0.318	0.317
X_{Mg}	0.491	0.483	0.494	0.517	0.504	0.515	0.537	0.507	0.500	0.495	0.492	0.452	0.446	0.474	0.468
Fe/(Fe+Mg)	0.377	0.385	0.377	0.357	0.381	0.354	0.344	0.352	0.368	0.373	0.379	0.443	0.447	0.402	0.404
Al^{VI}/Al^{IV}	1.199	1.187	1.608	1.510	1.566	1.719	1.350	1.776	1.868	1.851	1.788	1.140	1.164	1.744	1.794
Thermometry / Zhang & Fyfe 1995															
T / °C	213	219	162	166	149	151	167	–	–	141	146	204	201	–	–

APPENDIX II. - MINERAL CHEMISTRY / 16

PREHNITE

Oxides	702Prh1	702Prh2	702Prh3	702Prh4	702Prh5	702Prh6	702Prh7	702Prh8	702Prh9	702Prh10
SiO_2	44.00	43.15	43.20	43.58	43.65	43.88	43.24	43.06	45.56	43.50
TiO_2	0.37	0.05	0.00	0.00	0.07	0.00	0.00	0.00	0.03	0.03
Al_2O_3	23.42	24.18	23.26	24.45	22.15	22.01	23.01	23.44	22.68	23.10
Fe2O3	0.16	0.28	0.71	0.32	3.13	2.19	2.13	0.40	1.43	1.59
MnO	0.26	0.00	0.59	0.00	0.13	0.00	0.26	0.00	0.00	0.00
CaO	27.56	26.79	27.41	27.16	26.96	27.11	27.23	28.65	23.63	26.43
Na_2O	0.07	0.14	0.07	0.00	0.00	0.00	0.00	0.00	0.00	0.13
Total	95.84	94.59	95.24	95.51	96.09	95.19	95.87	95.55	93.33	94.78
Structural formula on a basis of 12 oxygen pfu										
Si IV	3.025	2.998	3.001	2.998	3.011	3.046	2.987	2.984	3.176	3.022
Al IV	0.000	0.002	0.000	0.002	0.000	0.000	0.013	0.016	0.000	0.000
T site	3.025	3.000	3.001	3.000	3.011	3.046	3.000	3.000	3.176	3.022
Al VI	1.898	1.978	1.904	1.981	1.801	1.801	1.861	1.898	1.864	1.892
Ti	0.019	0.003	0.000	0.000	0.004	0.000	0.000	0.000	0.002	0.002
Fe^{+3}	0.009	0.016	0.041	0.018	0.181	0.127	0.123	0.023	0.000	0.092
Fe^{+2}	0.000	0.000	0.000	0.000	0.000	0.000	0.000	0.000	0.083	0.000
Mn	0.015	0.000	0.035	0.000	0.008	0.000	0.015	0.000	0.000	0.000
O site	1.941	1.997	1.980	1.999	1.992	1.928	1.999	1.921	1.949	1.986
Ca	2.030	1.994	2.040	2.002	1.992	2.016	2.016	2.127	1.765	1.967
Na	0.009	0.019	0.009	0.000	0.000	0.000	0.000	0.000	0.000	0.018
A site	2.040	2.013	2.050	2.002	1.992	2.016	2.016	2.127	1.765	1.985
O	10.000	10.000	10.000	10.000	10.000	10.000	10.000	10.000	10.000	10.000
OH	2.000	2.000	2.000	2.000	2.000	2.000	2.000	2.000	2.000	2.000
Total	19.007	19.010	19.031	19.001	18.995	18.990	19.015	19.048	18.890	18.993
X_{Fe}	0.00	0.01	0.02	0.01	0.09	0.07	0.06	0.01	0.04	0.05

PYRITE

	284pyr1	284pyr2	284pyr3	284pyr4	284pyr5	284pyr6	284pyr7	284pyr8	284pyr9	284pyr10	284pyr11	284pyr12	284pyr13
Fe	46.78	44.92	46.84	46.75	47.12	47.22	47.04	46.97	46.65	46.30	46.59	46.19	47.00
S	52.23	52.56	52.19	52.29	52.42	52.42	52.50	52.62	52.49	52.16	52.55	52.02	52.50
Trace elements in ppm													
Co	1470	3610	1670	1270	2310	1130	850	850	1310	660	930	1270	1010
Ni	920	730	390	250	250	250	260	850	810	390	240	810	320
As	1580	1310	0	1670	2380	0	1210	0	1740	2830	3550	4440	670
Cu	200	1750	3380	1430	0	1320	1390	680	680	0	0	320	0
Zn	940	0	10	110	650	0	1560	0	610	1170	0	700	0
Cd	0	0	0	0	0	0	0	0	0	0	0	0	0
Mn	0	0	640	0	1080	410	480	690	0	900	150	570	210
Total	99.52	98.22	99.64	99.52	100.21	99.94	100.11	99.89	99.65	99.05	99.62	99.02	99.71
S:(Fe+Co+Ni)	0.02	0.01	0.02	0.03	0.02	0.04	0.05	0.03	0.02	0.05	0.04	0.02	0.04
Co/Ni	1.6	4.9	4.3	5.1	9.2	4.5	3.3	1.0	1.6	1.7	3.9	1.6	3.2

	362pyr1	362pyr2	362pyr3	362pyr4	362pyr5	362pyr6	362pyr7	362pyr8	362pyr9	362pyr10	362pyr11	362pyr12	362pyr13
Fe	47.55	47.79	47.59	46.89	47.14	47.71	47.54	47.38	47.37	47.18	47.12	47.36	47.25
S	52.50	52.39	52.05	52.20	52.67	52.76	52.93	52.97	53.07	52.63	52.54	52.50	52.30
Trace elements in ppm													
Co	400	630	1380	2420	710	980	1480	760	1580	460	940	670	730
Ni	480	360	670	530	270	440	760	300	250	320	210	740	550
As	330	0	730	1050	3270	0	720	0	0	2650	0	0	0
Cu	910	910	0	40	890	0	0	0	50	50	480	0	0
Zn	1680	550	0	410	410	0	0	2680	0	0	150	0	250
Cd	0	0	0	0	0	0	0	0	0	0	0	0	0
Mn	0	370	920	10	0	0	470	810	0	0	750	610	0
Total	100.43	100.47	100.01	99.53	100.37	100.61	100.80	100.81	100.63	100.16	99.91	100.06	99.70
S:(Fe+Co+Ni)	0.06	0.05	0.02	0.02	0.05	0.04	0.02	0.05	0.03	0.06	0.04	0.04	0.04
Co/Ni	0.8	1.8	2.1	4.6	2.6	2.2	1.9	2.5	6.3	1.4	4.5	0.9	1.3

APPENDIX III. - FELDSPAR THERMOMETRY / 1									
BINARY SOLVUS METHOD / Whitney & Stormer (1977)									
Pressure (MPa)		FELDSPAR PAIRS							
		372ab1–kfp1	372ab2–kfp2	372ab3–kfp3	372ab4–kfp4	372ab5–kfp5	870ab1-kfp1	870ab2-kfp2	870ab3-kfp3
5		312	282	285	263	309	296	305	305
50		317	287	290	267	314	300	308	309
100		320	289	293	270	317	303	312	313
150		325	295	298	275	322	307	316	317
200		329	298	302	279	326	313	321	320
Pressure (MPa)	Concordant temperatures	TERNARY SOLVUS METHOD / Nekvasil & Burnham (1987)							
5	T_{Ab}	322	272	259	261	289	305	314	280
	T_{Or}	276	272	259	261	289	256	249	280
	T_{An}	312	272	259	261	289	281	281	280
	$T_{(AV.)}$	304	272	259	261	289	281	281	280
50	T_{Ab}	326	296	267	251	296	308	242	279
	T_{Or}	281	296	267	251	296	261	242	279
	T_{An}	307	296	267	251	296	272	242	279
	$T_{(AV.)}$	305	296	267	251	296	280	242	279
100	T_{Ab}	329	299	270	253	328	312	321	285
	T_{Or}	287	299	270	253	304	265	271	285
	T_{An}	325	299	270	253	328	305	282	285
	$T_{(AV.)}$	314	299	270	253	320	294	291	285
150	T_{Ab}	333	303	250	257	331	315	271	288
	T_{Or}	292	303	250	257	310	260	271	288
	T_{An}	293	303	250	257	310	312	271	288
	$T_{(AV.)}$	307	303	250	257	317	296	271	288
200	T_{Ab}	336	306	252	230	304	319	278	328
	T_{Or}	298	306	252	230	304	277	278	303
	T_{An}	304	306	252	230	304	278	278	328
	$T_{(AV.)}$	313	306	252	230	304	291	278	320

APPENDIX III. - FELDSPAR THERMOMETRY / 2									
BINARY SOLVUS METHOD / Whitney & Stormer (1977)									
Pressure (MPa)		FELDSPAR PAIRS							
		870ab4-kfp4	870ab5-kfp5	870ab6-kfp6	870ab8-kfp8	870ab9-kfp9	870ab10-kfp10	870ab11-kfp11	870ab12-kfp12
5		268	268	264	286	245	264	264	276
50		271	271	267	290	248	267	267	279
100		275	275	271	294	252	271	271	283
150		279	279	275	298	255	275	275	287
200		283	283	278	302	259	278	278	291
Pressure (MPa)	Concordant temperatures	TERNARY SOLVUS METHOD / Nekvasil & Burnham (1987)							
5	T_{Ab}	215	277	257	180	239	252	272	237
	T_{Or}	215	277	257	180	239	252	272	237
	T_{An}	215	277	257	180	239	252	272	237
	$T_{(AV.)}$	215	277	257	180	239	252	272	237
50	T_{Ab}	203	280	275	204	230	173	275	255
	T_{Or}	203	280	265	190	230	173	275	255
	T_{An}	203	280	266	210	230	173	275	255
	$T_{(AV.)}$	203	280	268	211	230	173	275	255
100	T_{Ab}	203	236	278	191	231	264	279	249
	T_{Or}	203	236	270	191	231	264	279	249
	T_{An}	203	236	273	191	231	264	279	249
	$T_{(AV.)}$	203	236	273	191	231	264	279	249
150	T_{Ab}	262	276	268	188	261	261	282	232
	T_{Or}	262	276	268	281	261	261	282	232
	T_{An}	262	276	268	281	261	261	282	232
	$T_{(AV.)}$	262	276	268	250	261	261	282	232
200	T_{Ab}	250	278	278	194	264	273	285	262
	T_{Or}	250	278	278	194	264	273	285	262
	T_{An}	250	278	278	194	264	273	285	262
	$T_{(AV.)}$	250	278	278	194	264	273	285	262

APPENDIX IV-WHOLE ROCK CHEMISTRY								
Oxides	637 (1)	637 (2)	637 (3)	637 (4)	637 UA (1)	637 UA (2)	637 UA (3)	637 UA (4)
SiO2	68.106	66.529	64.804	60.592	60.606	59.583	61.515	60.642
TiO2	0.952	0.876	0.853	0.909	0.937	0.919	0.777	0.886
Al2O3	17.651	18.091	19.191	19.052	19.398	19.261	18.809	18.796
Fe2O3	1.149	1.479	2.104	5.474	6.969	7.615	6.654	7.596
MnO	0.1	0.125	0.142	0.187	0.312	0.322	0.283	0.284
MgO	0	0.261	0.778	1.332	1.013	0.873	1.606	0.872
CaO	4.253	4.09	3.839	4.067	2.563	1.998	1.863	1.963
Na2O	6.735	5.988	4.628	5.433	4.555	5.487	5.676	5.187
K2O	0.314	1.717	2.979	2.274	2.747	3.322	1.997	2.724
P2O5	0.428	0.568	0.413	0.381	0.612	0.394	0.541	0.684
Total	99.688	99.724	99.731	99.701	99.712	99.774	99.721	99.634

APPENDIX V. – MICROTHERMOMETRY / 1

FI type	Origin	Number of phases	φ_V	T_h (°C)	P_h (MPa)	T_n(Ice) (°C)	T_e (°C)	T_m(Ice) (°C)	T_m(HH) (°C)	Salinity eq. *w*%		V_m (cm3/mol)	Bulk Composition					
										NaCl	$CaCl_2$		XH_2O	XNa	XCa	XCl	XCH_4	XN_2
DIOPSIDE																		
D1/1	P	L+V	0.38	334	12.9	—	—	-0.7	—	1.2	—	29	0.992	0.004	—	0.004	—	—
D1/2	P	L+V	0.38	335	13.1	-35	—	-0.9	—	1.6	—	28.88	0.99	0.005	—	0.005	—	—
D1/3	P	L+V	0.32	308	9.2	—	—	-0.6	—	1.1	—	26.44	0.993	0.003	—	0.003	—	—
D1/4	P	L+V	0.36	327	11.8	—	—	-0.7	—	1.2	—	28.2	0.992	0.004	—	0.004	—	—
D1/5	P	L+V	0.37	330	12.3	—	—	-0.7	—	1.2	—	28.53	0.992	0.004	—	0.004	—	—
D1/6	P	L+V	0.37	332	12.6	-34.2	—	-0.8	—	1.4	—	28.65	0.991	0.004	—	0.004	—	—
D1/7	P	L+V	0.39	338	13.6	—	—	-0.6	—	1.1	—	29.61	0.993	0.003	—	0.003	—	—
D1/8	P	L+V	0.39	337	13.5	—	—	-0.6	—	1.1	—	29.48	0.993	0.003	—	0.003	—	—
D1/9	P	L+V	0.36	333	12.8	-36	—	-1.7	—	2.9	—	27.84	0.982	0.009	—	0.009	—	—
D1/10	P	L+V	0.39	336	13.3	—	—	-0.5	—	0.9	—	29.48	0.994	0.003	—	0.003	—	—
D1/11	P	L+V	0.39	—	—	—	—	-1	—	1.7	—	28.94	0.989	0.005	—	0.005	—	—
D1/12	P	L+V	0.38	335.6	13.2	—	—	-0.9	—	1.6	—	28.95	0.99	0.005	—	0.005	—	—
D1/13	P	L+V	0.39	—	—	-34.2	—	-0.6	—	1.1	—	29.49	0.993	0.003	—	0.003	—	—
D1/14	P	L+V	0.36	326	11.7	—	—	-0.9	—	1.6	—	27.89	0.99	0.005	—	0.005	—	—
D1/15	P	L+V	0.46	362	18.1	—	—	-0.6	—	1.1	—	33.2	0.993	0.003	—	0.003	—	—
D1/16	P	L+V	0.25	276	5.6	—	—	-0.6	—	1.1	—	24.07	0.993	0.003	—	0.003	—	—
D1/17	P	L+V	0.41	346	15	—	—	-0.6	—	1.1	—	30.67	0.993	0.003	—	0.003	—	—
D1/18	P	L+V	0.45	360	17.7	—	—	-0.5	—	0.9	—	33.04	0.994	0.003	—	0.003	—	—
D1/19	P	L+V	0.32	309	9.3	—	—	-0.8	—	1.4	—	26.37	0.991	0.004	—	0.004	—	—
D1/20	P	L+V	0.33	310.7	9.5	—	—	-0.6	—	1.1	—	26.68	0.993	0.003	—	0.003	—	—
D1/21	P	L+V	0.27	285	6.5	—	—	-0.6	—	1.1	—	24.65	0.993	0.003	—	0.003	—	—
D1/22	P	L+V	0.37	332	12.6	—	—	-0.9	—	1.6	—	28.54	0.99	0.005	—	0.005	—	—
D1/23	P	L+V	0.44	353	16.3	—	—	-0.4	—	0.7	—	32.04	0.995	0.002	—	0.002	—	—
D1/24	P	L+V	0.41	342	14.3	—	—	-0.4	—	0.7	—	30.4	0.995	0.002	—	0.002	—	—
D2/1	P	L+V	0.14	135	0.5	-80.6	—	-25.2	—	—	22.9	19.58	0.874	—	0.042	0.084	—	—
D2/2	P	L+V	0.09	162.8	0.6	—	—	-23.5	—	—	22.2	19.91	0.878	—	0.041	0.081	—	—
D1/25	P	L+V	0.35	325	11.5	—	—	-0.9	—	1.6	—	27.79	0.99	0.005	—	0.005	—	—
D1/26	P	L+V	0.39	336.5	13.4	—	—	-0.7	—	1.2	—	29.36	0.993	0.004	—	0.004	—	—
D1/27	P	L+V	0.35	322	—	—	—	—	—	—	—	—	—	—	—	—	—	—
D2/3	P	L+V	0.17	192.6	1.1	—	—	-24.6	—	—	22.7	20.37	0.875	—	0.042	0.083	—	—
D2/4	P	L+V	0.17	200.7	—	—	—	-22.2	—	—	21.6	20.49	0.882	—	0.039	0.079	—	—
D1/28	P	L+V	0.37	330	—	-34	—	-0.9	—	1.6	—	28.32	0.99	0.005	—	0.005	—	—
D1/29	P	L+V	0.37	—	—	—	—	-0.8	—	1.4	—	28.31	0.99	0.005	—	0.005	—	—

APPENDIX V. – MICROTHERMOMETRY / 2

FI type	Origin	Number of phases	φ_V	T_h (°C)	P_h (MPa)	T_n(Ice) (°C)	T_e (°C)	T_m(Ice) (°C)	T_m(HH) (°C)	Salinity eq. *w*%		V_m (cm3/mol)	Bulk Composition					
										NaCl	$CaCl_2$		XH_2O	XNa	XCa	XCl	XCH_4	XN_2
D1/30	P	L+V	0.39	—	—	—	—	-0.8	—	1.4	—	29.36	0.991	0.004	—	0.004	—	—
D1/31	P	L+V	0.34	—	—	—	—	-1	—	1.7	—	27.3	0.989	0.005	—	0.005	—	—
D1/32	P	L+V	0.39	336	—	—	—	—	—	—	—	—	—	—	—	—	—	—
D1/33	P	L+V	0.35	321	—	—	—	—	—	—	—	—	—	—	—	—	—	—
D1/34	P	L+V	0.37	331	—	—	—	—	—	—	—	—	—	—	—	—	—	—
D1/35	P	L+V	0.4	342	—	—	—	—	—	—	—	—	—	—	—	—	—	—
D1/36	P	L+V	0.4	341	—	—	—	—	—	—	—	—	—	—	—	—	—	—
D1/37	P	L+V	0.36	320	—	—	—	—	—	—	—	—	—	—	—	—	—	—
D1/38	P	L+V	0.38	335	—	—	—	—	—	—	—	—	—	—	—	—	—	—
D1/39	P	L+V	0.38	336	—	—	—	—	—	—	—	—	—	—	—	—	—	—
D1/40	P	L+V	0.34	318	—	—	—	—	—	—	—	—	—	—	—	—	—	—
EPIDOTE																		
E1/1	P	L+V	0.23	264.8	4.7	—	—	-0.5	—	0.9	—	23.45	0.995	0.003	—	0.003	—	—
E2/1	P	L+V	0.16	174.1	0.7	-78	-58.5	-23.2	-24.3	2.3	22.2	20.14	0.842	0.074	0.003	0.081	—	—
E2/2	P	L+V	0.15	172.2	0.7	—	—	-20	—	—	20.6	20	0.888	—	0.037	0.075	—	—
E1/2	P	L+V	0.28	287.8	6.8	—	—	-0.6	—	1.1	—	24.85	0.993	0.003	—	0.003	—	—
E1/3	P	L+V	0.41	345	14.9	-41	—	-0.6	—	1.1	—	30.54	0.993	0.003	—	0.003	—	—
E1/4	P	L+V	0.14	207	1.5	—	—	-0.3	—	0.5	—	21	0.997	0.002	—	0.002	—	—
E1/5	P	L+V	0.3	301	8.3	—	—	-0.6	—	1.1	—	25.84	0.993	0.003	—	0.003	—	—
E1/6	P	L+V	0.22	259	4.2	—	—	-0.5	—	0.9	—	23.14	0.994	0.003	—	0.003	—	—
E1/7	P	L+V	0.16	220	2	-43.2	—	-0.6	—	1.1	—	21.4	0.993	0.003	—	0.003	—	—
E1/8	P	L+V	0.12	—	—	-49.2	—	-4.4	—	7	—	20.07	0.956	0.022	—	0.022	—	—
E1/9	P	L+V	0.14	206	1.4	—	—	-0.6	—	1.1	—	20.93	0.993	0.003	—	0.003	—	—
E1/10	P	L+V	0.17	225	2.2	—	—	-0.6	—	1.1	—	21.59	0.993	0.003	—	0.003	—	—
E1/11	P	L+V	0.15	212.4	1.7	—	—	-0.6	—	1.1	—	21.14	0.993	0.003	—	0.003	—	—
E1/12	P	L+V	0.18	227.8	—	—	—	—	—	—	—	—	—	—	—	—	—	—
E2/3	P	L+V	0.13	130.5	0.4	—	—	-25.3	—	—	22.9	19.52	0.873	—	0.042	0.084	—	—
E2/4	P	L+V	0.14	151.3	0.5	—	—	-25.3	—	—	22.9	19.78	0.873	—	0.042	0.084	—	—
E1/13	P	L+V	0.17	225	2.2	—	—	-0.6	—	1.1	—	21.59	0.993	0.003	—	0.003	—	—
E1/14	P	L+V	0.17	226.5	2.2	—	—	-0.6	—	1.1	—	21.64	0.993	0.003	—	0.003	—	—
E1/15	P	L+V	0.14	206	1.4	—	—	-0.8	—	1.4	—	20.91	0.991	0.004	—	0.004	—	—
E1/16	P	L+V	0.3	300.5	8.2	—	—	-0.4	—	0.7	—	25.95	0.996	0.002	—	0.002	—	—
E1/17	P	L+V	0.24	269	5	—	—	-0.5	—	0.9	—	23.7	0.994	0.003	—	0.003	—	—
E1/18	P	L+V	0.16	219.3	1.9	—	—	-0.6	—	1.1	—	21.38	0.994	0.003	—	0.003	—	—

APPENDIX V. – MICROTHERMOMETRY / 3

FI type	Origin	Number of phases	φ_V	T_h (°C)	P_h (MPa)	T_n(Ice) (°C)	T_e (°C)	T_m(Ice) (°C)	T_m(HH) (°C)	Salinity eq. *w*%		V_m (cm3/mol)	Bulk Composition					
										NaCl	$CaCl_2$		XH_2O	XNa	XCa	XCl	XCH_4	XN_2
E1/19	P	L+V	0.41	347	15.2	—	—	-0.8	—	1.4	—	30.53	0.992	0.004	—	0.004	—	—
E1/20	P	L+V	0.44	355	16.7	—	—	-0.4	—	0.7	—	32.37	0.995	0.002	—	0.002	—	—
E1/21	P	L+V	0.45	358	17.3	-40.1	—	-0.6	—	1.1	—	32.51	0.993	0.003	—	0.003	—	—
E1/22	P	L+V	0.45	359	17.5	—	—	-0.4	—	0.7	—	33.06	0.996	0.002	—	0.002	—	—
E1/23	P	L+V	0.42	350	15.8	—	—	-0.6	—	1.1	—	31.26	0.993	0.003	—	0.003	—	—
E1/24	P	L+V	0.43	352	16.1	-40.5	—	-0.6	—	1.1	—	31.56	0.993	0.003	—	0.003	—	—
E1/25	P	L+V	0.42	347	15.2	—	—	-0.6	—	1.1	—	30.82	0.993	0.003	—	0.003	—	—
E1/26	P	L+V	0.4	343.5	—	—	—	—	—	—	—	—	—	—	—	—	—	—
E1/27	P	L+V	0.15	218	1.9	-41	—	-0.7	—	—	—	21.34	—	—	—	—	—	—
E1/28	P	L+V	0.12	193	—	—	—	—	—	—	—	—	—	—	—	—	—	—
E1/29	P	L+V	0.13	200	—	—	—	—	—	—	—	—	—	—	—	—	—	—
E1/30	P	L+V	0.14	205.1	1.4	—	—	-0.1	—	0.2	—	20.97	0.999	0.0005	—	0.0005	—	—
E1/31	P	L+V	0.36	322.3	11.1	-31.5	—	-0.1	—	0.2	—	28.33	0.999	0.0005	—	0.0005	—	—
E1/32	P	L+V	0.25	274	5.4	-35.7	—	-0.1	—	0.2	—	24.19	0.999	0.0005	—	0.0005	—	—
E1/33	P	L+V	0.23	259.8	—	—	—	—	—	—	—	—	—	—	—	—	—	—
E1/34	P	L+V	0.2	—	—	-34.3	—	-0.3	—	0.5	—	22.52	0.997	0.0015—	—	0.00015—	—	—
E1/35	P	L+V	0.11	181	0.8	-34.8	—	-0.1	—	0.2	—	20.25	0.999	0.0005	—	0.0005	—	—
E1/36	P	L+V	0.2	—	—	-37.6	—	-0.1	—	0.2	—	—	0.999	0.0005	—	0.0005	—	—
E1/37	P	L+V	0.25	—	—	-38.7	—	-0.1	—	0.2	—	—	0.999	0.0005	—	0.0005	—	—
E1/38	P	L+V	0.23	—	—	-32.3	—	-0.1	—	0.2	—	—	0.999	0.0005	—	0.0005	—	—
E1/39	P	L+V	0.18	238	—	—	—	—	—	—	—	—	—	—	—	—	—	—
E1/40	P	L+V	0.12	192	—	—	—	—	—	—	—	—	—	—	—	—	—	—
E1/41	P	L+V	0.2	247.7	3.4	—	—	-0.2	—	0.4	—	22.66	0.998	0.001	—	0.001	—	—
E1/42	P	L+V	0.17	234	2.6	-38.4	—	-0.1	—	0.2	—	21.82	0.999	0.0005	—	0.0005	—	—
E1/43	P	L+V	0.11	181	0.8	-38.7	—	-0.1	—	0.2	—	20.25	0.999	0.0005	—	0.0005	—	—
E1/44	P	L+V	0.13	199.3	—	—	—	—	—	—	—	—	—	—	—	—	—	—
E1/45	P	L+V	0.12	193	1.1	-32.2	—	-0.1	—	0.2	—	20.59	0.999	0.0005	—	0.0005	—	—
E1/46	P	L+V	0.12	192.8	1.1	-37.2	—	-0.1	—	0.2	—	20.58	0.999	0.0005	—	0.0005	—	—
E1/47	P	L+V	0.12	316.9	10.4	-39.8	—	-0.1	—	0.2	—	27.74	0.999	0.0005	—	0.0005	—	—
E1/48	P	L+V	0.35	327.8	12	-40.5	—	-0.1	—	0.2	—	29	0.999	0.0005	—	0.0005	—	—
E1/49	P	L+V	0.38	186.5	0.9	—	—	-0.2	—	0.4	—	20.39	0.998	0.001	—	0.001	—	—
E1/50	P	L+V	0.12	302.7	8.5	-39.5	—	-0.1	—	0.2	—	26.37	0.999	0.0005	—	0.0005	—	—
E1/51	P	L+V	0.32	203.4	1.4	-39.2	—	-0.1	—	0.2	—	20.91	0.999	0.0005	—	0.0005	—	—

APPENDIX V. – MICROTHERMOMETRY / 4

FI type	Origin	Number of phases	φ_V	T_h (°C)	P_h (MPa)	T_n(Ice) (°C)	T_e (°C)	T_m(Ice) (°C)	T_m(HH) (°C)	Salinity eq. *w*%		V_m (cm3/mol)	Bulk Composition					
										NaCl	$CaCl_2$		XH_2O	XNa	XCa	XCl	XCH_4	XN_2
E1/52	P	L+V	0.14	278.3	—	—	—	—	—	—	—	—	—	—	—	—	—	—
E1/53	P	L+V	0.25	292.5	—	—	—	—	—	—	—	—	—	—	—	—	—	—
E1/54	P	L+V	0.28	237.2	2.8	-31.8	—	-0.1	—	0.2	—	22.2	0.999	0.0005	—	0.0005	—	—
E1/55	P	L+V	0.19	192.9	1.1	-36.8	—	-0.2	—	0.4	—	20.58	0.998	0.001	—	0.001	—	—
E1/56	P	L+V	0.15	207	1.5	-36.7	—	-0.3	—	0.5	—	21.03	0.997	0.0015	—	0.0015	—	—
E2/11	P	L+V	0.09	—	—	-84.8	-53.8	-23.8	—	—	22.1	19.52	0.879	—	0.04	0.081	—	—
E2/12	P	L+V	0.13	133	0.4	—	—	-23.2	—	—	22.1	19.52	0.879	—	0.04	0.081	—	—
E2/13	P	L+V	0.13	138	0.4	-75.5	—	-20.3	—	—	20.7	19.54	0.887	—	0.037	0.075	—	—
E2/14	P	L+V	0.12	93	0.5	-86.5	—	-26	—	—	23.2	19.13	0.872	—	0.043	0.086	—	—
E2/15	P	L+V	0.12	90	0.6	-85	-52.7	-26	—	—	23.2	19.1	0.872	—	0.043	0.086	—	—
E2/16	P	L+V	0.11	87	0.6	-86.1	—	-25.6	—	—	23.1	19.06	0.873	—	0.042	0.085	—	—
E2/17	P	L+V	0.12	113	0.5	-86.4	-56.6	-24.5	—	—	—	19.31	0.875	—	0.042	0.083	—	—
CALCITE 1																		
C1/1	P	L+V	0.07	106.5	0.5	-57.8	—	-18	—	21	—	19.03	0.859	0.07	0.07	—	—	—
C1/2	P	L+V	0.05	75.5	—	—	—	—	—	—	—	—	—	—	—	—	—	—
C1/3	P	L+V	0.05	77.5	0.6	—	—	-21.7	—	—	21.4	18.91	0.883	—	0.039	0.078	—	—
C1/4	P	L+V	0.05	80.5	—	—	—	—	—	—	—	—	—	—	—	—	—	—
C1/5	P	L+V	0.05	76.5	—	—	—	—	—	—	—	—	—	—	—	—	—	—
C1/6	P	L+V	0.06	94.5	—	—	—	—	—	—	—	—	—	—	—	—	—	—
C1/7	P	L+V	0.06	98.3	0.5	—	—	-16.7	—	20	—	18.95	0.867	0.067	—	0.067	—	—
C1/8	P	L+V	0.07	110.5	0.5	—	—	-20.3	—	—	20.7	19.21	0.887	—	0.038	0.075	—	—
C1/9	P	L+V	0.06	101.5		—	—	-20.5*	—	—	—	—	—	—	—	—	—	—
C1/10	P	L+V	0.07	107.5	0.5	—	—	-20.5	—	—	20.8	19.18	0.886	—	0.038	0.076	—	—
C1/11	P	L+V	0.06	105	0.5	—	—	-21	—	—	21	19.17	0.885	—	0.038	0.077	—	—
C1/12	P	L+V	0.07	108.3	0.5	—	—	-20.7	—	—	20.9	19.2	0.886	—	0.038	0.076	—	—
C1/13	P	L+V	0.08	118.5	—	—	—	—	—	—	—	—	—	—	—	—	—	—
C1/14	P	L+V	0.08	115	0.5	-56.1	—	-16.3	—	—	18.6	19.19	0.9	—	0.33	0.67	—	—
C1/15	P	L+V	0.05	82	0.6	—	—	-20.4	—	—	20.8	18.93	0.887	—	0.038	0.075	—	—
C1/16	P	L+V	0.08	123.6	0.5	—	—	-16.4	—	—	18.7	19.29	0.899	—	0.034	0.067	—	—
C1/17	P	L+V	0.06	90	0.6	—	—	-24.5	—	—	22.6	19.08	0.875	—	0.042	0.083	—	—
C1/18	P	L+V	0.06	91	—	—	—	—	—	—	—	—	—	—	—	—	—	—
C1/19	P	L+V	0.04	75	0.6	—	—	-23.9	—	—	22.4	18.92	0.877	—	0.041	0.082	—	—
C1/20	P	L+V	0.07	101.5	—	—	—	—	—	—	—	—	—	—	—	—	—	—

FI type	Origin	Number of phases	φ_V	T_h (°C)	P_h (MPa)	T_n(Ice) (°C)	T_e (°C)	T_m(Ice) (°C)	T_m(HH) (°C)	Salinity eq. *w*%		V_m (cm^3/mol)	Bulk Composition					
										NaCl	$CaCl_2$		XH_2O	XNa	XCa	XCl	XCH_4	XN_2
C1/21	P	L+V	0.08	89.4	0.6	—	—	-17.2	—	—	19.1	18.93	0.897	—	0.034	0.069	—	—
C1/22	P	L+V	0.05	75	—	—	—	—	—	—	—	—	—	—	—	—	—	—
C1/23	P	L+V	0.06	101.5	0.5	-52.2	—	-14.5	—	—	17.5	19	0.906	—	0.31	0.062	—	—
C1/24	P	L+V	0.07	107.8	0.5	-73.2	—	-24.8	—	—	22.7	19.26	0.875	—	0.042	0.084	—	—
C1/25	P	L+V	0.07	99.7	0.5	—	—	-24.4	—	—	22.6	19.17	0.876	—	0.041	0.083	—	—
C1/26	P	L+V	0.07	99.5	0.5	-69.3	—	-24.7	—	—	22.7	19.17	0.875	—	0.042	0.083	—	—
C1/27	P	L+V	0.07	102	—	—	—	—	—	—	—	—	—	—	—	—	—	—
C1/28	P	L+V	0.07	111.1	0.5	-80.2	—	-25.3	—	—	22.9	19.31	0.873	—	0.042	0.084	—	—
C1/29	P	L+V	0.07	99.5	0.5	—	—	-24.5	—	—	22.6	19.17	0.875	—	0.042	0.083	—	—
C1/30	P	L+V	0.08	119.5	0.5	-61.4	—	-16.8	—	—	18.9	19.25	0.898	—	0.034	0.068	—	—
C1/31	P	L+V	0.06	97.7	0.5	-78.9	—	-24	—	—	22.4	19.14	0.877	—	0.041	0.082	—	—
C1/32	P	L+V	0.08	118.3	0.5	-80.1	—	-24.7	—	—	22.7	19.37	0.875	—	0.042	0.083	—	—
C1/33	P	L+V	0.08	119	0.5	—	—	-18.1	—	—	19.6	19.27	0.894	—	0.035	0.071	—	—
C1/34	P	L+V	0.06	95	—	—	—	—	—	—	—	—	—	—	—	—	—	—
C1/35	P	L+V	0.06	97.5	—	-76.2	—	—	—	—	—	—	—	—	—	—	—	—
C1/36	P	L+V	0.07	100	—	-62.2	—	—	—	—	—	—	—	—	—	—	—	—
C1/37	P	L+V	0.07	108	—	—	—	—	—	—	—	—	—	—	—	—	—	—
C1/38	P	L+V	0.1	118	—	-70.8	—	—	—	—	—	—	—	—	—	—	—	—
C1/39	P	L+V	0.09	116.7	—	—	—	—	—	—	—	—	—	—	—	—	—	—
C1/40	P	L+V	0.09	111	0.5	-61.2	—	-25.5	—	—	23	19.31	0.873	—	0.042	0.085	—	—
C1/41	P	L+V	0.08	117	—	—	—	—	—	—	—	—	—	—	—	—	—	—
C1/42	P	L+V	0.07	107.4	—	—	—	—	—	—	—	—	—	—	—	—	—	—
C1/43	P	L+V	0.11	123	—	—	—	—	—	—	—	—	—	—	—	—	—	—
C1/44	P	L+V	0.07	110.4	0.5	—	—	-24.4	—	—	22.6	19.28	0.876	—	0.041	0.083	—	—
C1/45	P	L+V	0.07	113.8	0.5	-76.5	—	-26.7	—	—	23.5	19.36	0.87	—	0.043	0.087	—	—
C1/46	P	L+V	0.07	105.7	0.5	—	—	-24.8	—	—	22.7	19.24	0.875	—	0.042	0.084	—	—
C1/47	P	L+V	0.07	112	—	—	—	—	—	—	—	—	—	—	—	—	—	—
C1/48	P	L+V	0.07	105.2	0.5	—	—	-24.7	—	—	22.7	19.23	0.875	—	0.042	0.083	—	—
C1/49	P	L+V	0.08	108	0.5	—	—	-24.3	—	—	22.5	19.26	0.876	—	0.041	0.083	—	—
C1/50	P	L+V	0.08	110	—	—	—	—	—	—	—	—	—	—	—	—	—	—
C1/51	P	L+V	0.09	118.7	0.5	-78.6	—	-24.2	—	—	22.5	19.37	0.876	—	0.041	0.082	—	—
C1/52	P	L+V	0.04	72	—	—	—	—	—	—	—	—	—	—	—	—	—	—
C1/53	P	L+V	0.07	102	0.5	-84.1	—	-25	—	—	22.8	19.2	0.874	—	0.042	0.084	—	—

APPENDIX V. – MICROTHERMOMETRY / 6

FI type	Origin	Number of phases	φ_V	T_h (°C)	P_h (MPa)	T_n(Ice) (°C)	T_e (°C)	T_m(Ice) (°C)	T_m(HH) (°C)	Salinity eq. *w*%		V_m (cm^3/mol)	Bulk Composition					
										NaCl	$CaCl_2$		XH_2O	XNa	XCa	XCl	XCH_4	XN_2
C1/54	P	L+V	0.06	90	0.6	-84.1	—	-24.5	—	—	22.6	19.08	0.875	—	0.042	0.083	—	—
C1/55	P	L+V	0.03	58	0.6	-81	—	-24	—	—	22.4	18.78	0.877	—	0.041	0.082	—	—
C1/56	P	L+V	0.06	95	—	—	—	—	—	—	—	—	—	—	—	—	—	—
C1/57	P	L+V	0.09	117	0.5	-69.5	-56.7	-25.7	—	—	23.1	19.38	0.872	—	0.043	0.085	—	—
C1/58	P	L+V	0.07	107	—	—	—	—	—	—	—	—	—	—	—	—	—	—
C1/59	P	L+V	0.06	87	—	—	—	—	—	—	—	—	—	—	—	—	—	—
C1/60	P	L+V	0.06	88	—	—	—	—	—	—	—	—	—	—	—	—	—	—
C1/61	P	L+V	0.04	73	—	—	—	—	—	—	—	—	—	—	—	—	—	—
C1/62	P	L+V	0.06	88	—	—	—	—	—	—	—	—	—	—	—	—	—	—
C1/63	P	L+V	0.09	96	—	—	—	—	—	—	—	—	—	—	—	—	—	—
C1/64	P	L+V	0.07	110	—	—	—	—	—	—	—	—	—	—	—	—	—	—
C1/65	P	L+V	0.06	95	—	—	—	—	—	—	—	—	—	—	—	—	—	—
C1/66	P	L+V	0.06	88	0.6	-82.5	-54.5	-26.5	—	—	23.4	19.09	0.87	—	0.043	0.086	—	—
C1/67	P	L+V	0.07	101	0.5	-70.6	-54.7	-24.1	—	—	22.4	19.18	0.877	—	0.041	0.082	—	—
C1/68	P	L+V	0.06	87	0.6	-74	—	-24.5	—	—	22.6	19.05	0.875	—	0.042	0.083	—	—
C1/69	P	L+V	0.07	103	0.5	-85.3	—	-24.7	—	—	22.7	19.21	0.875	—	0.042	0.083	—	—
C1/70	P	L+V	0.08	116	0.5	-84.1	—	-25.2	—	—	22.9	19.36	0.874	—	0.042	0.084	—	—
C1/71	P	L+V	0.08	105	—	—	—	—	—	—	—	—	—	—	—	—	—	—
C1/72	P	L+V	0.05	80	0.6	-87.8	—	-25.5	—	—	23	18.98	0.873	—	0.042	0.085	—	—
C1/73	P	L+V	0.06	98	0.5	-86.6	—	-25	—	—	22.8	19.16	0.874	—	0.042	0.084	—	—
C1/74	P	L+V	0.07	106	0.5	-80.2	—	-27.5	—	—	23.8	19.29	0.868	—	0.044	0.088	—	—
C1/75	P	L+V	0.06	98	—	—	—	—	—	—	—	—	—	—	—	—	—	—
C1/76	P	L+V	0.08	118	—	—	—	—	—	—	—	—	—	—	—	—	—	—
C1/77	P	L+V	0.09	120	0.5	-59.7	—	-16.8	—	—	18.9	19.26	0.898	—	0.034	0.068	—	—
C1/78	P	L+V	0.07	107	—	—	—	—	—	—	—	—	—	—	—	—	—	—
C1/79	P	L+V	0.06	87.5	—	—	—	—	—	—	—	—	—	—	—	—	—	—
C1/80	P	L+V	0.08	115	—	—	—	—	—	—	—	—	—	—	—	—	—	—
C1/81	P	L+V	0.06	93	0.5	-86.1	—	-24.5	—	—	22.6	19.1	0.875	—	0.042	0.083	—	—
C1/82	P	L+V	0.06	94	—	—	—	—	—	—	—	—	—	—	—	—	—	—
C1/83	P	L+V	0.08	114	—	—	—	—	—	—	—	—	—	—	—	—	—	—
C1/84	P	L+V	0.08	119	—	—	—	—	—	—	—	—	—	—	—	—	—	—
C1/85	P	L+V	0.07	108	—	—	—	—	—	—	—	—	—	—	—	—	—	—
C1/86	P	L+V	0.06	95	—	—	—	—	—	—	—	—	—	—	—	—	—	—

FI type	Origin	Number of phases	φ_V	T_h (°C)	P_h (MPa)	T_n(Ice) (°C)	T_e (°C)	T_m(Ice) (°C)	T_m(HH) (°C)	Salinity eq. *w*%		V_m (cm3/mol)	Bulk Composition					
										NaCl	$CaCl_2$		XH_2O	XNa	XCa	XCl	XCH_4	XN_2
CALCITE-2																		
C2/1	P	L+V	0.09	141.7	0.5	-34	—	-2.7	—	4.5	—	19.46	0.972	0.014	—	0.014	—	—
C2/2	P	L+V	0.08	123.5	—	—	—	—	—	—	—	—	—	—	—	—	—	—
C2/3	P	L+V	0.08	123	—	-34	—	—	—	—	—	—	—	—	—	—	—	—
C2/4	P	L+V	0.13	180	—	-41	—	—	—	—	—	—	—	—	—	—	—	—
C2/5	P	L+V	0.14	197	1.2	—	—	-3.9	—	6.3	—	20.48	0.96	0.02	—	0.02	—	—
C2/6	P	L+V	0.13	186.5	0.9	—	—	-3.7	—	6	—	20.26	0.962	0.019	—	0.019	—	—
C2/7	P	L+V	0.1	155.7	0.5	-45	—	-3.5	—	5.7	—	19.7	0.964	0.018	—	0.018	—	—
C2/8	P	L+V	0.08	126.5	—	—	—	—	—	—	—	—	—	—	—	—	—	—
C2/9	P	L+V	0.13	181.5	0.9	—	—	-3.5	—	5.7	—	20.16	0.964	0.018	—	0.018	—	—
C2/10	P	L+V	0.12	164	—	—	—	—	—	—	—	—	—	—	—	—	—	—
C2/11	P	L+V	0.12	153.5	—	—	—	—	—	—	—	—	—	—	—	—	—	—
C2/12	P	L+V	0.12	181	0.8	—	—	-3.7	—	6	—	20.15	0.962	0.019	—	0.019	—	—
C2/13	P	L+V	0.12	163	0.6	—	—	-3.8	—	6.2	—	19.82	0.961	0.019	—	0.019	—	—
C2/14	P	L+V	0.06	105.3	—	—	—	—	—	—	—	—	—	—	—	—	—	—
C2/15	P	L+V	0.08	123.3	—	—	—	—	—	—	—	—	—	—	—	—	—	—
C2/16	P	L+V	0.09	142.6	0.5	-43.7	—	-3.5	—	5.7	—	19.5	0.964	0.018	—	0.018	—	—
C2/17	P	L+V	0.08	127.5	0.4	-47.4	—	-3.3	—	5.4	—	19.28	0.966	0.017	—	0.017	—	—
C2/18	P	L+V	0.08	128.5	—	—	—	—	—	—	—	—	—	—	—	—	—	—
C2/19	P	L+V	0.09	139.2	—	—	—	—	—	—	—	—	—	—	—	—	—	—
C2/20	P	L+V	0.08	131.5	—	—	—	—	—	—	—	—	—	—	—	—	—	—
C2/21	P	L+V	0.08	135.5	—	—	—	—	—	—	—	—	—	—	—	—	—	—
C2/22	P	L+V	0.08	129	—	—	—	—	—	—	—	—	—	—	—	—	—	—
C2/23	P	L+V	0.08	122.7	—	-45.2	—	—	—	—	—	—	—	—	—	—	—	—
C2/24	P	L+V	0.08	117.7	—	—	—	—	—	—	—	—	—	—	—	—	—	—
C2/25	P	L+V	0.09	137.5	0.5	—	—	-3.7	—	6	—	19.43	0.962	0.019	—	0.019	—	—
C2/26	P	L+V	0.07	—	—	-40.5	—	—	—	—	—	—	—	—	—	—	—	—
C2/27	P	L+V	0.09	132.6	—	—	—	—	—	—	—	—	—	—	—	—	—	—
C2/28	P	L+V	0.12	160	0.6	—	—	-1.8	—	3.1	—	19.75	0.981	0.019	—	0.019	—	—
C2/29	P	L+V	0.12	167	0.6	—	—	-2.7	—	4.5	—	19.88	0.972	0.014	—	0.014	—	—
C2/30	P	L+V	0.08	125.5	0.5	-39	—	-3.5	—	5.7	—	19.26	0.964	0.018	—	0.018	—	—
C2/31	P	L+V	0.09	138.5	0.5	-35	—	-2.5	—	4.2	—	19.4	0.974	0.013	—	0.013	—	—
C2/32	P	L+V	0.12	157.5	0.5	—	—	-2.7	—	4.5	—	19.71	0.972—	0.014	—	0.014	—	—

APPENDIX V. – MICROTHERMOMETRY / 8

FI type	Origin	Number of phases	φ_V	T_h (°C)	P_h (MPa)	T_n(Ice) (°C)	T_e (°C)	T_m(Ice) (°C)	T_m(HH) (°C)	Salinity eq. *w*%		V_m (cm3/mol)	Bulk Composition					
										NaCl	$CaCl_2$		XH_2O	XNa	XCa	XCl	XCH_4	XN_2
C2/33	P	L+V	0.1	142	—	-38	—	—	—	—	—	—	—	—	—	—	—	—
C2/34	P	L+V	0.08	129.5	—	—	—	—	—	—	—	—	—	—	—	—	—	—
C2/35	P	L+V	0.1	148	—	-37.3	—	—	—	—	—	—	—	—	—	—	—	—
C2/36	P	L+V	0.09	135.5	—	-43.2	—	—	—	—	—	—	—	—	—	—	—	—
C2/37	P	L+V	0.09	140.5	—	—	—	—	—	—	—	—	—	—	—	—	—	—
C2/38	P	L+V	0.08	120	0.5	—	—	-1.7	—	2.9	—	19.11	0.982	0.009	—	0.009	—	—
C2/39	P	L+V	0.07	106.3	0.5	—	—	-2	—	3.4	—	18.95	0.979	0.011	—	0.011	—	—
C2/40	P	L+V	0.07	105.8	—	—	—	—	—	—	—	—	—	—	—	—	—	—
C2/41	P	L+V	0.08	129	—	-31.6	—	—	—	—	—	—	—	—	—	—	—	—
C2/42	P	L+V	0.12	126.7	—	-32.8	—	—	—	—	—	—	—	—	—	—	—	—
C2/43	P	L+V	0.1	129	—	—	—	—	—	—	—	—	—	—	—	—	—	—
C2/44	P	L+V	0.12	136	0.5	-46.8	—	-2.9	—	4.8	—	19.38	0.97	0.015	—	0.015	—	—
C2/45	P	L+V	0.07	115	0.5	—	—	-3.4	—	5.6	—	19.13	0.965	0.018	—	0.018	—	—
EPIDOTES - Wall-rock																		
P1/1	P	L+V	0.45	360.6	17.8	-42.3	—	-0.7	—	1.2	—	32.77	0.992	0.004	—	0.004	—	—
P1/2	P	L+V	0.46	363	18.3	—	—	-0.4	—	0.7	—	33.78	0.996	0.002	—	0.002	—	—
P1/3	P	L+V	0.42	354	16.5	-43.5	—	-0.9	—	1.6	—	31.38	0.99	0.005	—	0.005	—	—
P1/4	P	L+V	0.4	346	15	—	—	-0.8	—	1.4	—	30.39	0.991	0.004	—	0.004	—	—
P1/5	P	L+V	0.38	337	13.5	-41.6	—	-1	—	1.7	—	29	0.989	0.005	—	0.005	—	—
P1/6	P	L+V	0.36	328	12	-42	—	-0.9	—	1.6	—	28.1	0.99	0.005	—	0.005	—	—
P1/7	P	L+V	0.3	303	8.5	—	—	-0.7	—	1.2	—	25.94	0.992	0.004	—	0.004	—	—
P1/8	P	L+V	0.44	358	17.3	—	—	-0.8	—	1.4	—	32.16	0.991	0.004	—	0.004	—	—
P1/9	P	L+V	0.46	364	18.5	—	—	-0.8	—	1.4	—	33.17	0.991	0.004	—	0.004	—	—
P1/10	P	L+V	0.43	354	16.5	—	—	-0.8	—	1.4	—	31.54	0.991	0.004	—	0.004	—	—
P1/11	P	L+V	0.45	361	17.9	—	—	-0.8	—	1.4	—	32.88	0.991	0.004	—	0.004	—	—
PS/1	PS	L+V	0.42	352	16.1	—	—	-0.8	—	1.4	—	31.24	0.991	0.004	—	0.004	—	—
PS/2	PS	L+V	0.41	344	14.7	—	—	-0.7	—	1.2	—	30.26	0.992	0.004	—	0.004	—	—
PS/3	PS	L+V	0.45	361	18	—	—	-0.7	—	1.2	—	32.84	0.992	0.004	—	0.004	—	—
PS/4	PS	L+V	0.42	348	15.4	—	—	-0.7	—	1.2	—	30.81	0.992	0.004	—	0.004	—	—
PS/5	PS	L+V	0.41	345	14.9	—	—	-0.7	—	1.2	—	30.39	0.992	0.004	—	0.004	—	—
PS/6	PS	L+V	0.43	352.5	16.2	—	—	-0.7	—	1.2	—	31.47	0.992	0.004	—	0.004	—	—
P2/1	P	L+V	0.14	208	1.5	-41	—	-0.7	—	1.2	—	20.98	0.992	0.004	—	0.004	—	—
P2/2	P	L+V	0.15	214	1.7	-39.7	—	-0.4	—	0.7	—	21.22	0.996	0.002	—	0.002	—	—

FI type	Origin	Number of phases	φ_V	T_h (°C)	P_h (MPa)	T_n(Ice) (°C)	T_e (°C)	T_m(Ice) (°C)	T_m(HH) (°C)	Salinity eq. *w*%		V_m (cm3/mol)	Bulk Composition					
										NaCl	$CaCl_2$		XH_2O	XNa	XCa	XCl	XCH_4	XN_2
P2/3	P	L+V	0.13	201	1.3	-38.7	—	-0.3	—	0.5	—	20.81	0.997	0.002	—	0.002	—	—
P2/4	P	L+V	0.14	209	1.5	-41.4	—	-0.8	—	1.4	—	21	0.991	0.004	—	0.004	—	—
P2/5	P	L+V	0.14	210	1.6	—	—	-0.6	—	1.1	—	21.06	0.993	0.003	—	0.003	—	—
P2/6	P	L+V	0.14	207	1.5	—	—	-0.7	—	1.2	—	20.97	0.992	0.004	—	0.004	—	—
P3/1	P	L+V	0.12	164.5	0.6	—	—	-0.9	—	1.6	—	19.84	0.99	0.005	—	0.005	—	—
P3/2	P	L+V	0.12	168.7	0.6	—	—	-0.3	—	0.5	—	19.94	0.997	0.0015	—	0.0015	—	—
P3/3	P	L+V	0.15	181.8	0.8	-39.8	—	-0.2	—	0.4	—	20.27	0.998	0.001	—	0.001	—	—
P3/4	P	L+V	0.15	177.6	0.8	—	—	-0.1	—	0.2	—	20.17	0.999	0.0005	—	0.0005	—	—
P3/5	P	L+V	0.12	162.7	0.6	—	—	-0.1	—	0.2	—	19.81	0.999	0.0005	—	0.0005	—	—
P3/6	P	L+V	0.14	178.6	0.8	-40.7	—	-0.2	—	0.4	—	20.19	0.998	0.001	—	0.001	—	—
P3/7	P	L+V	0.15	181.4	0.8	—	—	-0.2	—	0.4	—	20.26	0.998	0.001	—	0.001	—	—
P3/8	P	L+V	0.15	186	0.9	—	—	-0.3	—	0.5	—	20.37	0.997	0.0015	—	0.0015	—	—
P3/9	P	L+V	0.13	172	0.7	—	—	-0.1	—	0.2	—	20.03	0.999	0.0005	—	0.0005	—	—
QUARTZ - Quartz-carbonate veins																		
QP1/1	P	L+V	0.08	122.6	—	-75.9	—	-23.7	-14.5	24.4	1.8	18.17	0.827	0.082	0.0024	0.087	0.0002	0.0015
QP1/2	P	L+V	0.07	117.5	—	-75.1	—	-23.5	-11.5	24.8	1.6	17.96	0.824	0.084	0.0022	0.088	0.0002	0.0013
QP1/3	P	L+V	0.07	115.8	—	-74.9	—	23.5	-19.5	23.7	1.6	18.01	0.832	0.08	0.0022	0.084	0.0002	0.0013
QP1/4	P	L+V	0.08	113.1	—	-75.6	—	-23.7	-13.5	24.4	1.8	18.16	0.826	0.082	0.0024	0.087	0.0002	0.0015
QP1/5	P	L+V	0.06	85.8	—	—	—	-23.7	-12.5	24.6	1.8	18.12	0.827	0.083	0.0024	0.088	—	—
QP1/6	P	L+V	0.06	91.8	—	-65.3	—	-23.6	-18.5	23.2	1.7	18.47	0.837	0.078	0.0023	0.083	—	—
QP1/7	P	L+V	0.06	98.4	—	—	—	—	—	—	—	—	—	—	—	—	—	—
QP1/8	P	L+V	0.08	112.6	—	—	—	-25	-19.5	23.1	3.2	18.19	0.831	0.077	0.0045	0.086	0.0003	0.0015
QP1/9	P	L+V	0.08	122.8	—	—	—	-23.3	-12.5	24.6	1.4	18.16	0.826	0.083	0.002	0.087	0.0002	0.0015
QP1/10	P	L+V	0.08	123.1	—	—	—	-24	-12	24.5	2.1	18.15	0.824	0.083	0.0029	0.088	0.0002	0.0015
QP1/11	P	L+V	0.06	99.8	—	—	—	—	—	—	—	—	—	—	—	—	—	—
QP1/12	P	L+V	0.06	98.6	—	—	—	—	—	—	—	—	—	—	—	—	—	—
QP1/13	P	L+V	0.06	98.6	—	-79.8	—	-23.6	-18.5	23.8	1.7	17.82	0.831	0.08	0.0023	0.084	0.0002	0.0012
QP1/14	P	L+V	0.06	93.6	—	—	—	—	—	—	—	—	—	—	—	—	—	—
QP1/15	P	L+V	0.09	136	—	—	—	-23.6	—	—	22.2	18.77	0.876	—	0.041	0.081	0.0003	0.0018
QP1/16	P	L+V	0.06	101.8	—	—	—	-23.8	—	—	22.3	19.18	0.877	—	0.041	0.082	—	—
QP1/17	P	L+V	0.06	94	—	—	—	—	—	—	—	—	—	—	—	—	—	—
QP1/18	P	L+V	0.06	105	—	—	—	—	—	—	—	—	—	—	—	—	—	—
QP2/1	P	L+V	0.07	108.2	—	-63.6	—	-20	—	—	20.6	18.26	0.887	—	0.037	0.074	0.0002	0.0014

APPENDIX V. – MICROTHERMOMETRY / 10

FI type	Origin	Number of phases	φ_V	T_h (°C)	P_h (MPa)	T_n(Ice) (°C)	T_e (°C)	T_m(Ice) (°C)	T_m(HH) (°C)	Salinity eq. *w*%		V_m (cm3/mol)	Bulk Composition					
										NaCl	$CaCl_2$		XH_2O	XNa	XCa	XCl	XCH_4	XN_2
QP2/2	P	L+V	0.06	101.6	—	-62.2	—	-19.7	—	—	20.4	18.07	0.888	—	0.037	0.074	0.0002	0.0012
QP2/3	P	L+V	0.08	117.4	—	-69.9	—	-19.2	—	—	20.2	18.47	0.89	—	0.037	0.073	0.0002	0.0016
QP2/4	P	L+V	0.09	123.6	—	67.1	—	-18.8	—	—	20	18.68	0.892	—	0.036	0.072	0.0002	0.0017
QP2/5	P	L+V	0.07	107.4	—	—	—	-19.8	—	—	20.5	18.26	0.889	—	0.037	0.074	0.0002	0.0014
QP2/6	P	L+V	0.08	—	—	-73.5	—	-22.4	—	—	21.7	18.4	0.881	—	0.04	0.079	0.0002	0.0015
QP2/7	P	L+V	0.06	94.1	0.5	-75.3	—	-21.6	—	—	21.3	19.06	0.883	—	0.039	0.078	—	—
QP2/8	P	L+V	0.06	89.2	—	—	—	—	—	—	—	—	—	—	—	—	—	—
QP2/9	P	L+V	0.06	95.8	0.5	-74.3	—	-21.4	—	—	21.2	19.08	0.884	—	0.039	0.077	—	—
QP2/10	P	L+V	0.07	104.2	1.1	-68.5	—	-20.6	—	—	20.9	19.15	0.886	—	0.038	0.076	—	—
QP2/11	P	L+V	0.06	102.7	—	—	—	—	—	—	—	—	—	—	—	—	—	—
QP2/12	P	L+V	0.07	109.3	—	—	—	—	—	—	—	—	—	—	—	—	—	—
QP2/13	P	L+V	0.11	139.3	—	—	—	—	—	—	—	—	—	—	—	—	—	—
QP2/14	P	L+V	0.09	121.3	—	—	—	—	—	—	—	—	—	—	—	—	—	—
QPS1/1	PS	L+V	0.09	127	—	—	—	—	—	—	—	—	—	—	—	—	—	—
QPS1/2	PS	L+V	0.06	97.8	0.5	—	—	-22.6	—	—	21.8	19.12	0.88	—	0.04	0.08	—	—
QPS1/3	PS	L+V	0.06	101	—	—	—	—	—	—	—	—	—	—	—	—		
QPS1/4	PS	L+V	0.06	94.6	—	—	—	—	—	—	—	—	—	—	—	—	—	—
QPS15	PS	L+V	0.06	90	—	—	—	—	—	—	—	—	—	—	—	—	—	—
QPS1/6	PS	L+V	0.08	113	—	—	—	-18.8*	—	—	—	—	—	—	—	—	—	—
QPS1/7	PS	L+V	0.09	125	—	—	—	-20.5	—	—	20.8	19.38	0.886	—	0.038	0.076	—	—
QPS1/8	PS	L+V	0.09	127.5	—	—	—	-21	—	—	21.1	19.42	0.885	—	0.038	0.077	—	—
QPS1/9	PS	L+V	0.06	85.5	—	—	—	-14*	—	—	—	—	—	—	—	—	—	—
QPS1/10	PS	L+V	0.07	85	—	—	—	-18.2*	—	—	—	—	—	—	—	—	—	—
QPS1/11	PS	L+V	0.06	99	—	—	—	-18.2*	—	—	—	—	—	—	—	—	—	—
QPS1/12	PS	L+V	0.08	86.8	—	—	—	-18.5*	—	—	—	—	—	—	—	—	—	—
QPS1/13	PS	L+V	0.09	81	—	—	—	—	—	—	—	—	—	—	—	—	—	—
QPS1/14	PS	L+V	0.07	86.5	—	—	—	—	—	—	—	—	—	—	—	—	—	—
QPS1/15	PS	L+V	0.08	105	—	—	—	—	—	—	—	—	—	—	—	—	—	—
QPS1/16	PS	L+V	0.06	96	—	—	—	—	—	—	—	—	—	—	—	—	—	—
QP3/1	P	L+V	0.09	118.3	—	—	—	-23.8	-12.7	24.5	1.9	18.35	0.825	0.083	0.003	0.088	0.0003	0.0017
QP3/2	P	L+V	0.06	84.8	—	—	—	-25.5	-6.5	24.3	4	17.73	0.82	0.081	0.006	0.092	0.0002	0.0012
QP3/3	P	L+V	0.07	78.2	—	-78.5	—	-24.5	-17.7	23.6	2.6	17.99	0.829	0.079	0.004	0.086	0.0002	0.0013
QP3/4	P	L+V	0.06	80.6	—	—	—	-24.3	-9.5	24.7	2.4	17.96	0.823	0.083	0.003	0.09	—	—

FI type	Origin	Number of phases	φ_V	T_h (°C)	P_h (MPa)	T_n(Ice) (°C)	T_e (°C)	T_m(Ice) (°C)	T_m(HH) (°C)	Salinity eq. *w*%		V_m (cm3/mol)	Bulk Composition					
										NaCl	$CaCl_2$		XH_2O	XNa	XCa	XCl	XCH_4	XN_2
QP3/5	P	L+V	0.07	87.2	—	—	—	-25.4	-17.7	.23.9	3.7	17.95	0.824	0.08	0.005	0.09	0.0002	0.0013
QP3/6	P	L+V	0.11	85	—	—	—	-25.3	-11.5	23.9	3.7	17.95	0.824	0.08	0.005	0.09	0.0002	0.0014
QP3/7	P	L+V	0.09	101	—	—	—	-26.3	-21.1	23.3	1.5	18.82	0.835	0.077	0.003	0.083	0.0002	0.0015
QP3/8	P	L+V	0.09	127.4	—	-69.3	—	-23.9	-8.3	23.1	2	18.42	0.835	0.077	0.003	0.083	0.0003	0.0021
QP3/9	P	L+V	0.43	83.6	—	—	—	—	—	—	—	—	—	—	—	—	—	—
QP3/10	P	L+V	0.06	92.2	0.5	-69.4	—	-23.9	-3.8	25.6	2	18.1	0.818	0.087	0.0027	0.092	—	—
QP3/11	P	L+V	0.08	106.8	—	-75.5	—	-23.8	-19.2	20.1	1.6	18.39	0.859	0.066	0.0023	0.071	0.0002	0.0015
QP3/12	P	L+V	0.1	132.1	—	-67.4	—	-25.3	-12.5	23.7	3.7	18.54	0.824	0.079	0.0051	0.089	0.0003	0.0019
QP3/13	P	L+V	0.06	97.6	—	-68.6	—	-25.5	-7.5	24.1	4	17.73	0.821	0.081	0.0056	0.092	0.0002	0.0012
QP3/14	P	L+V	0.06	93.2	0.5	-76	—	-24.4	-18	23.6	2.5	18.43	0.831	0.079	0.035	0.086	—	—
QP3/15	P	L+V	0.06	98	—	-73.1	—	-24.3	-14.5	24.1	2.4	17.78	0.827	0.081	0.033	0.088	0.0002	0.0012
QP3/16	P	L+V	0.06	86	—	-72.6	—	-24.8	-12	24.2	3	17.76	0.824	0.081	0.0041	0.089	0.0002	0.0012
QP3/17	P	L+V	0.06	89.5	—	-79.6	—	-23.9	-10	24.8	2	17.76	0.823	0.084	0.0027	0.089	0.0002	0.0012
QP31/18	P	L+V	0.06	98	—	—	—	-24	-13	24.4	2.1	17.77	0.826	0.082	0.0028	0.088	0.0002	0.0012
QP31/19	P	L+V	0.08	113.2	—	—	—	—	—	—	—	—	—	—	—	—	—	—
QP31/20	P	L+V	0.09	—	—	—	—	-23.9	-8.3	25	2	18.37	0.823	0.085	0.0027	0.09	—	—
QP31/21	P	L+V	0.09	126.5	—	—	—	-24.3	-18	23.7	2.4	18.38	0.829	0.079	0.0033	0.086	0.0003	0.0016
QP31/22	P	L+V	0.08	100.5	—	—	—	-22.5	—	—	21.7	18.4	0.879	—	0.04	0.079	0.0002	0.0016
QP31/23	P	L+V	0.06	—	—	—	—	-25.5	-7.5	24.1	4	17.77	0.822	0.081	0.0055	0.092	—	—
QPS2/1	PS	L+V	0.08	112.6	0.5	—	—	-24.3	—	—	22.5	19.3	0.876	—	0.041	0.083	—	—
QPS2/2	PS	L+V	0.05	74.8	—	—	—	-18.6*	—	—	—	—	—	—	—	—	—	—
QPS2/3	PS	L+V	0.07	87	—	—	—	—	—	—	—	—	—	—	—	—	—	—
QPS2/4	PS	L+V	0.06	—	—	—	—	-24.2	—	—	22.5	18.02	0.876	—	0.041	0.082	—	—
QPS2/5	PS	L+V	0.09	127	0.5	—	—	-25	—	—	22.8	19.48	0.874	—	0.042	0.084	—	—
QPS2/6	PS	L+V	0.06	82.4	—	—	—	-19.8*	—	—	—	—	—	—	—	—	—	—
QPS2/7	PS	L+V	0.09	102	0.5	—	—	-27.4	—	—	23.8	19.24	0.868	—	0.044	0.088	—	—
QPS2/8	PS	L+V	0.09	—	—	—	—	-17.5*	—	—	—	—	—	—	—	—	—	—
QPS2/9	PS	L+V	0.07	—	—	—	—	-19.2*	—	—	—	—	—	—	—	—	—	—
QPS2/10	PS	L+V	0.08	103.4	—	—	—	—	—	—	—	—	—	—	—	—	—	—
QP4/1	P	L+V	0.08	98.2	—	-71.1	—	-24	-14	24.3	2.1	18.16	0.826	0.082	0.003	0.087	0.0005	0.0013
QP4/2	P	L+V	0.06	89.5	—	-73.3	—	-25.3	-10.5	24	3.7	17.75	0.823	0.08	0.005	0.09	0.0004	0.001
QP4/3	P	L+V	0.08	97.8	—	-72.5	—	-24.3	-12.5	24.4	2.4	18.15	0.825	0.082	0.003	0.088	0.0005	0.0013
QP4/4	P	L+V	0.06	89.1	—	-72.4	—	-26.5	-19.3	21.1	6.1	17.82	0.835	0.069	0.009	0.086	0.0004	0.001

FI type	Origin	Number of phases	φ_V	T_h (°C)	P_h (MPa)	T_n(Ice) (°C)	T_e (°C)	T_m(Ice) (°C)	T_m(HH) (°C)	Salinity eq. *w*%		V_m (cm3/mol)	Bulk Composition					
										NaCl	$CaCl_2$		XH_2O	XNa	XCa	XCl	XCH_4	XN_2
QP4/5	P	L+V	0.07	102.3	—	-77.3	—	-24.2	-9.3	24.8	2.3	17.94	0.822	0.084	0.003	0.09	0.0004	0.0011
QP4/6	P	L+V	0.06	86.1	—	-71.2	—	-25.8	-5.5	24	4.5	17.73	0.82	0.08	0.006	0.093	0.0004	0.001
QP4/7	P	L+V	0.05	71.3	—	-67.9	—	-24.5	-14.3	24	2.6	17.86	0.828	0.081	0.004	0.088	—	—
QP4/8	P	L+V	0.1	128.7	—	—	—	-24.9	-5.5	24.9	3.1	19.05	0.82	0.084	0.004	0.092	—	—
QP4/9	P	L+V	0.1	113.2	—	—	—	-24.8	-12.5	24.1	3	18.15	0.824	0.081	0.004	0.089	0.0005	0.0013
QP4/10	P	L+V	0.06	93.1	—	—	—	-24.3	-15.5	24	2.4	17.79	0.828	0.081	0.003	0.087	0.0004	0.001
QP4/11	P	L+V	0.06	87.3	—	—	—	—	—	—	—	—	—	—	—	—	—	—
QP4/12	P	L+V	0.1	133	—	—	—	-24.7	-10.5	24.4	2.9	18.53	0.822	0.082	0.04	0.09	0.0006	0.0016
QP4/13	P	L+V	0.07	104.4	0.5	—	—	-26.7	-19	20.5	6.8	18.92	0.837	0.066	0.01	0.086	—	—
QP4/14	P	L+V	0.08	87.3	—	—	—	-24.3	—	—	22.5	19.3	0.876	—	0.041	0.083	—	—
QP4/15	P	L+V	0.07	—	—	—	—	—	-7.5	25.3	—	17.98	0.826	0.086	—	0.086	0.0004	0.0011
QP4/16	P	L+V	0.07	98.7	—	—	—	-24.5	-9.3	24.7	2.6	18.4	0.823	0.083	0.004	0.09	—	—
QP4/17	P	L+V	0.06	100.5	—	—	—	-24.5	-12.5	24.3	2.6	18.15	0.825	0.081	0.004	0.089	0.0005	0.0013
QP4/18	P	L+V	0.07	—	—	—	—	-24.7	-10.5	24.4	2.9	17.94	0.822	0.082	0.004	0.09	0.0004	0.0012
QP4/19	P	L+V	0.06	107	—	—	—	-24.7	-12.5	24.2	2.9	18.15	0.824	0.081	0.004	0.089	0.0004	0.0013
QP4/20	P	L+V	0.06	86.3	—	-68.6	—	-23.2	—	—	22.1	18	0.878	—	0.04	0.081	0.0004	0.001
QP4/21	P	L+V	0.06	87.5	—	—	—	—	—	—	—	—	—	—	—	—	—	—
QP4/22	P	L+V	0.07	112.7	—	—	—	-23	—	—	22	18.39	0.878	—	0.04	0.08	0.0005	0.0013
QP4/23	P	L+V	0.06	85.6	—	—	—	-23.6	—	—	22.2	19.02	0.878	—	0.041	0.081	—	—
QP4/24	P	L+V	0.08	84.7	—	—	—	—	—	—	—	—	—	—	—	—	—	—
QP4/25	P	L+V	0.06	80.5	—	—	—	—	—	—	—	—	—	—	—	—	—	—
QP4/26	P	L+V	0.06	91.4	0.6	—	—	-23.7	—	—	22.3	19.08	0.878	0.082	0.041	0.082	—	—
QPS3/1	PS	L+V	0.07	112	0.5	—	—	-23.9	—	—	22.4	19.29	0.877	—	0.041	0.082	—	—
QPS3/2	PS	L+V	0.07	145.5	0.5	—	—	-23.7	—	—	22.3	19.69	0.878	—	0.041	0.082	—	—
QPS3/3	PS	L+V	0.06	121	—	—	—	—	—	—	—	—	—	—	—	—	—	—
QPS3/4	PS	L+V	0.05	113.7	0.5	—	—	-23.4	—	—	22.1	19.3	0.878	—	0.041	0.081	—	—
QPS3/5	PS	L+V	0.1	98	—	—	—	-18.3*	—	—	—	—	—	—	—	—	—	—
QPS3/6	PS	L+V	0.1	107.5	—	—	—	-17*	—	—	—	—	—	—	—	—	—	—
QP5/1	P	L+V	0.04	49.3	—	—	—	—	—	—	—	—	—	—	—	—	—	—
QP5/2	P	L+V	0.06	83.9	—	—	—	-23.9	—	—	23.4	17.57	0.87	—	0.043	0.086	0.0001	0.001
QP5/3	P	L+V	0.05	73.4	—	—	—	-24.3	—	—	23.6	17.74	0.868	—	0.043	0.087	0.0001	0.0011
QP5/4	P	L+V	0.06	85.6	—	—	—	—	—	—	—	—	—	—	—	—	—	—
QP5/5	P	L+V	0.03	43.9	—	—	—	—	—	—	—	—	—	—	—	—	—	—

Fluid type	Origin	Number of phases	φ_V	T_h (°C)	P_h (MPa)	T_n(Ice) (°C)	T_e (°C)	T_m(Ice) (°C)	T_m(HH) (°C)	Salinity eq. *w*%		V_m (cm3/mol)	Bulk Composition					
										NaCl	$CaCl_2$		XH_2O	XNa	XCa	XCl	XCH_4	XN_2
QP5/6	P	L+V	0.05	69.9	—	—	—	—	—	—	—	—	—	—	—	—	—	—
QP5/7	P	L+V	0.05	67.2	—	—	—	—	—	—	—	—	—	—	—	—	—	—
QP5/8	P	L+V	0.04	47.2	—	—	—	—	—	—	—	—	—	—	—	—	—	—
QP5/9	P	L+V	0.06	91.2	—	—	—	—	—	—	—	—	—	—	—	—	—	—
QP5/10	P	L+V	0.05	—	—	-69.7	—	-24.2	—	—	22.5	17.83	0.876	—	0.041	0.082	—	—
QP5/11	P	L+V	0.05	—	—	-57.3	—	-10	—	—	14.2	18.23	0.926	—	0.025	0.05	—	—
QP5/12	P	L+V	0.06	—	—	-53.2	—	-8.7	—	—	13	18.49	0.932	—	0.023	0.045	—	—
QP5/13	P	L+V	0.07	—	—	-59.1	—	-20.9	—	—	21.9	18.2	0.879	—	0.04	0.08	0.0001	0.0014
QP5/14	P	L+V	0.06	—	—	-59.2	—	-19.4	—	—	20.3	18.12	0.89	—	0.037	0.073	—	—
QP5/15	P	L+V	0.06	81.9	—	—	—	-17.5	—	—	20	18.1	0.891	—	0.036	0.072	0.0001	0.0013
QP5/16	P	L+V	0.04	56	—	-81.4	—	-26.7	—	—	24.7	17.51	0.862	—	0.046	0.091	0.0001	0.001
QP5/17	P	L+V	0.04	57.2	—	—	—	—	—	—	—	—	—	—	—	—	—	—
QP5/18	P	L+V	0.07	50.5	0.6	-82.3	—	-27.2	—	—	23.7	18.77	0.869	—	0.044	0.088	—	—
QP5/19	P	L+V	0.07	48.1	0.6	-72.2	—	-23.4	—	—	22.1	18.69	0.878	—	0.041	0.081	—	—
QP5/20	P	L+V	0.06	86.3	—	—	—	—	—	—	—	—	—	—	—	—	—	—
QS1/1	S	L+V	0.06	91.1	0.6	—	—	-22.9	—	—	21.9	19.06	0.88	—	0.04	0.08	—	—
QS1/2	S	L+V	0.1	116.7	0.5	—	—	-23.2	—	—	22.1	19.33	0.879	—	0.04	0.081	—	—
QS1/3	S	L+V	0.1	—	—	—	—	-24	—	—	22.4	18.21	0.877	—	0.041	0.082	—	—
QS1/4	S	L+V	0.06	107.6	0.5	—	—	-22.9	—	—	21.9	19.23	0.88	—	0.04	0.08	—	—
QS1/5	S	L+V	0.06	104.1	0.5	—	—	-23.7	—	—	22.3	19.2	0.878	—	0.041	0.082	—	—
QS1/6	S	L+V	0.1	109	—	—	—	—	—	—	—	—	—	—	—	—	—	—
QS1/7	S	L+V	0.07	109.5	—	—	—	—	—	—	—	—	—	—	—	—	—	—
DOLOMITE+CALCITE - Quartz-carbonate veins																		
DolCal/1	P	L+V	0.08	142	0.5	—	—	-23.3	—	—	22.1	19.63	0.879	—	0.04	0.081	—	—
DolCal/2	P	L+V	0.07	134	0.4	—	—	-23.3	—	—	22.1	19.53	0.879	—	0.04	0.081	—	—
DolCal/3	P	L+V	0.07	147.3	—	—	—	—	—	—	—	—	—	—	—	—	—	—
DolCal/4	P	L+V	0.06	167.5	0.6	—	—	-22.8	—	—	—	19.72	0.88	—	0.04	0.08	—	—
DolCal/5	P	L+V	0.07	138.7	—	—	—	—	—	—	—	—	—	—	—	—	—	—
DolCal/6	P	L+V	0.06	163.3	0.6	—	—	-23.1	—	—	22	19.92	0.879	—	0.04	0.081	—	—
DolCal/7	P	L+V	0.06	136.5	0.5	—	—	-23.2	—	—	22.1	19.56	0.879	—	0.04	0.081	—	—
DolCal/8	P	L+V	0.06	136.3	—	—	—	—	—	—	—	—	—	—	—	—	—	—
DolCal/9	P	L+V	0.07	159.6	—	—	—	-24.2	—	—	22.5	19.88	0.876	—	0.041	0.082	—	—
DolCal/10	P	L+V	0.06	156.7	—	—	—	—	—	—	—	—	—	—	—	—	—	—

Fluid type	Origin	Number of phases	φ_V	T_h (°C)	P_h (MPa)	T_n(Ice) (°C)	T_e (°C)	T_m(Ice) (°C)	T_m(HH) (°C)	Salinity eq. *w*%		V_m (cm3/mol)	Bulk Composition					
										NaCl	$CaCl_2$		XH_2O	XNa	XCa	XCl	XCH_4	XN_2
DolCal/11	P	L+V	0.06	157.5	0.5	—	—	-24	—	—	22.4	19.85	0.877	—	0.041	0.082	—	—
DolCal/12	P	L+V	0.04	155.3	0.5	—	—	-24.1	—	—	22.4	19.82	0.877	—	0.041	0.082	—	—
DolCal/13	P	L+V	0.04	141.8	0.5	—	—	-23.2	—	—	22.1	19.63	0.879	—	0.04	0.081	—	—
DolCal/14	P	L+V	0.07	140.8	0.5	—	—	-23.5	—	—	22.2	19.62	0.878	—	0.041	0.081	—	—
DolCal/15	P	L+V	0.07	144.6	0.5	—	—	-23.7	—	—	22.3	19.67	0.877	—	0.041	0.082	—	—
DolCal/16	P	L+V	0.06	144.3	0.5	—	—	-23.3	—	—	22.1	19.66	0.879	—	0.04	0.081	—	—
DolCal/17	P	L+V	0.06	136.8	—	—	—	—	—	—	—	—	—	—	—	—	—	—
DolCal/18	P	L+V	0.1	151.4	—	—	—	—	—	—	—	—	—	—	—	—	—	—
DolCal/19	P	L+V	0.1	137.2	—	—	—	—	—	—	—	—	—	—	—	—	—	—
DolCal/20	P	L+V	0.06	160.5	—	—	—	—	—	—	—	—	—	—	—	—	—	—
DolCal/21	P	L+V	0.06	95	—	—	—	—	—	—	—	—	—	—	—	—	—	—
DolCal/22	P	L+V	0.1	175	—	—	—	—	—	—	—	—	—	—	—	—	—	—
DolCal/23	P	L+V	0.07	135.3	—	—	—	—	—	—	—	—	—	—	—	—	—	—
DolCal/24	P	L+V	0.08	133.8	—	—	—	—	—	—	—	—	—	—	—	—	—	—
DolCal/25	P	L+V	0.07	177	—	—	—	—	—	—	—	—	—	—	—	—	—	—
DolCal/26	P	L+V	0.07	182	—	—	—	—	—	—	—	—	—	—	—	—	—	—
DolCal/27	P	L+V	0.06	179	—	—	—	—	—	—	—	—	—	—	—	—	—	—
DolCal/28	P	L+V	0.07	176.6	—	—	—	—	—	—	—	—	—	—	—	—	—	—
DolCal/29	P	L+V	0.06	174	—	—	—	—	—	—	—	—	—	—	—	—	—	—
DolCal/30	P	L+V	0.06	180.2	—	—	—	—	—	—	—	—	—	—	—	—	—	—
DolCal/31	P	L+V	0.06	133.2	—	—	—	—	—	—	—	—	—	—	—	—	—	—
DolCal/32	P	L+V	0.07	161	0.6	-67.9	—	-23.8	—	—	22.3	19.89	0.877	—	0.041	0.082	—	—
DolCal/33	P	L+V	0.06	147	0.5	-71.5	—	-24.5	—	—	22.6	19.72	0.875	—	0.042	0.083	—	—
DolCal/34	P	L+V	0.06	167	0.6	-73.1	—	-24.3	—	—	22.5	19.98	0.876	—	0.041	0.083	—	—
DolCal/35	P	L+V	0.04	143	—	—	—	—	—	—	—	—	—	—	—	—	—	—
DolCal/36	P	L+V	0.04	149.2	—	—	—	—	—	—	—	—	—	—	—	—	—	—
DolCal/37	P	L+V	0.07	133.7	—	—	—	—	—	—	—	—	—	—	—	—	—	—